CREEP OF HAFNIUM DIBORIDE -20 VOL% SILICON CARBIDE AT 1500 °C IN AIR

THESIS

Glen E. Pry, Captain, USAF

AFIT-ENY-MS-18-M-286

DEPARTMENT OF THE AIR FORCE
AIR UNIVERSITY

AIR FORCE INSTITUTE OF TECHNOLOGY

Wright-Patterson Air Force Base, Ohio

AFIT-ENY-MS-18-M-286

CREEP OF HAFNIUM DIBORIDE -20 VOL% SILICON CARBIDE AT 1500 °C IN
AIR

THESIS

Presented to the Faculty

Department of Aeronautics and Astronautics

Graduate School of Engineering and Management

Air Force Institute of Technology

Air University

Air Education and Training Command

In Partial Fulfillment of the Requirements for the

Degree of Master of Science in Materials Science

Glen E. Pry III, BS, MBA

Captain, USAF

March 2018

AFIT-ENY-MS-18-M-286

CREEP OF HAFNIUM DIBORIDE -20 VOL% SILICON CARBIDE AT 1500 °C IN AIR

Glen E. Pry, BS, MBA

Captain, USAF

Committee Membership:

Marina B. Ruggles-Wrenn, PhD

Chair

Randall S. Hay, PhD

Member

Craig P. Przybyla, PhD

Member

AFIT-ENY-MS-18-M-286

Abstract

Refractory metal borides, commonly referred to as Ultra High Temperature Ceramics (UHTCs), exhibit a number of unique properties, such as extremely high melting temperature and hardness, chemical stability, high electrical and thermal conductivity and corrosion resistance. It has been demonstrated that the addition of SiC improves the oxidation resistance of ZrB_2- and HfB_2-based UHTCs above 1200°C by modifying the composition of the oxide scale. Addition of SiC retards the oxidation rate of ZrB_2 and HfB_2 by forming a protective layer of borosilicate glass. Creep deformation is one of the critical criterion for structural application of ceramics at elevated temperatures. Compression creep of HfB_2-20 vol% SiC was studied at 1500°C in air at stresses ranging from -50 to -200 MPa. Primary and secondary creep regimes were observed in all tests. Minimum creep rates were measured. Post-test examination of material microstructure with SEM was employed to characterize the evolution of oxide scale with time. Additional analysis using EDS and XRD revealed the elemental and crystallographic makeup of the oxide scale and provided evidence that supports the assumed creep mechanism, grain boundary sliding. Comparison of the results of this effort with those from prior work indicate that sustained compressive stress has little effect on the growth rate of oxide scale. Likewise, oxidation appears to have negligible influence on steady-state creep rates.

Table of Contents

List of Figures

List of Tables

CREEP OF HAFNIUM DIBORIDE -20 VOL% SILICON CARBIDE AT 1500 °C IN AIR

I. INTRODUCTION AND BACKGROUND

Refractory metal borides, commonly referred to as Ultra High Temperature Ceramics (UHTCs), exhibit a number of unique properties, such as extremely high melting temperature and hardness, chemical stability, high electrical and thermal conductivity and corrosion resistance. It has been demonstrated that the addition of SiC improves the oxidation resistance of ZrB_2- and HfB_2-based UHTCs above 1200°C by modifying the composition of the oxide scale. Addition of SiC retards the oxidation rate of ZrB_2 and HfB_2 by forming a protective layer of borosilicate glass. The addition of silicon carbide to a boride-based UHTC (e.g., hafnium-diboride) classifies the material as a ceramic matrix composite (CMC) and enables the material to significantly reduce oxidation rates at elevated temperature in an operational environment (exposed to oxygen). A detailed explanation of ceramics, UHTCs, oxidation and creep is essential in order to properly interpret prior research in this field.

1.1 Ceramics

Ceramics are inorganic, nonmetallic solids that are typically manufactured through high-temperature processing. Ceramic materials possess unique mechanical, thermal, electrical and chemical characteristics which make them desirable for a wide variety of applications [1, 2]. Structurally, ceramics are usually strong and brittle. However, they also exhibit excellent thermal and electrical insulation and corrosion resistance properties. Atomic bonding within ceramic materials can be either ionic, covalent or, most commonly, a combination of the two [3]. The significant variance in

1

bonding type and material composition enables ceramics to define a class of materials with a wide range of material properties and characteristics.

Generally, ceramics can be divided into two categories: traditional and engineering. Traditional ceramics are derived from common, naturally occurring raw materials such as clay and quartz sand; they are typically used in pottery and construction materials. Evidence suggests that humans have been utilizing traditional ceramics since at least 24,000 BC [4]. Engineering ceramics, the focus of this study, are developed through highly controlled, advanced manufacturing methods to achieve particular chemical compositions and material properties.

Engineering ceramics are often utilized for their high strength and resistance to corrosion, particularly at high temperatures. However, ceramics are difficult to manufacture. They are typically brittle and thus, subject to catastrophic failure with little notice (strain or elongation) [1, 5]. Due to their brittle nature, the slightest number of defects present in a ceramic material can lead to crack initiation and propagation under stress, leading to unpredictable, catastrophic failure. Unlike tougher materials, like metals, which exhibit identifiable signs prior to fracture (i.e., yielding or elongation), ceramics fracture with little to no identifiable warning signs. Poor fracture toughness, and therefore unpredictable failure modes, is one of the primary reasons ceramics are not more commonly utilized across industry as structural materials in applications in which safety is critical [1].

Engineering ceramics intended for use in high stress environments must be processed carefully to ensure high purity and eliminate as many internal defects as possible to reduce the risk of failure [1]. Unfortunately, extensive processing is expensive

and even the most technologically advanced material synthesis procedures cannot eliminate all internal defects within a monolithic ceramic material. Therefore, the risk of unpredictable catastrophic failure of an engineering ceramic cannot be entirely eliminated through processing alone.

1.2 Ultra-High Temperature Ceramics (UHTCs)

Ultra-high temperature ceramics are a subset of engineering ceramics with very high melting temperatures. They are able to operate at sustained temperatures between 1900-2500 °C without losing substantial structural integrity [6-12]. As of 2007 there were only 15 known materials in the world with melting temperature above 3000 °C [7] as shown in Figure 1.
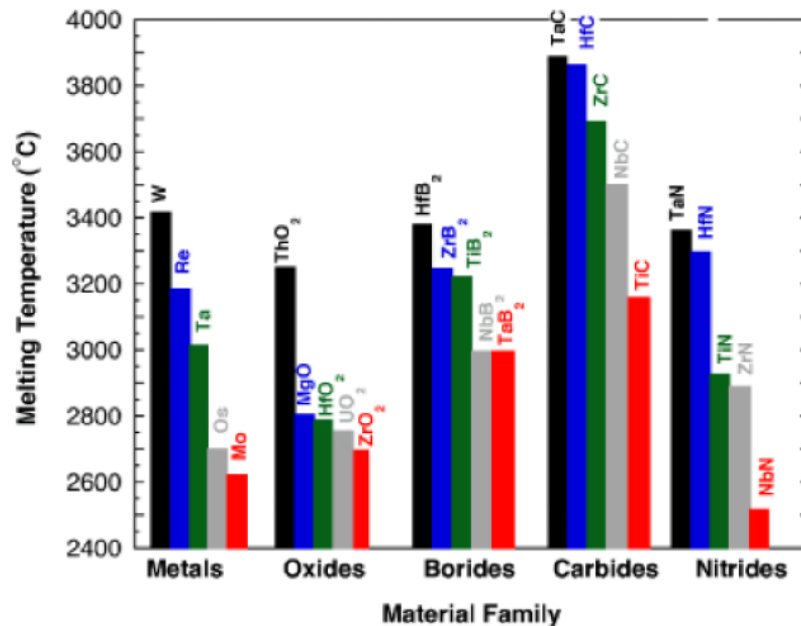
Figure 1. Melting temperatures of various materials, reproduced from Bowen [13], with permission from [7].

As shown in Figure 1, UHTCs are typically transition-metal based borides, carbides, nitrides or oxides. They exhibit melting temperatures in excess of 3000 °C, very high hardness, chemical stability, electrical and thermal conductivity, and oxidation resistance [7-12, 14-19].

Additives can be added to ceramics to improve more than just strength or fracture toughness. This research focuses on the effect of additives which alter creep and oxidation behavior within a ceramic, particularly the addition of silicon carbide (SiC) particles to the ultra-high temperature ceramic, hafnium-diboride (HfB_2). Kaufman and Clougherty identified HfB_2 as one of the most oxidation resistant materials for high temperature applications and proposed that the addition of SiC might further improve oxidation resistance [20]. Bargeron, Winder, and DeGregoria confirmed that SiC provides increased oxidation resistance when added to boride-based ceramics through the formation, at high temperatures, of a borosilicate glass oxygen diffusion barrier on the surface, limiting oxidation into the substrate [21, 22, 23].

DeGregoria has also shown that the addition of SiC particles to HfB_2 significantly alters the creep behavior of the ceramic at high temperatures. Notably, the addition of certain proportions of SiC to a HfB_2 matrix enables the HfB_2-SiC composite to deform significantly more than either of the individual constituents [23]. DeGregoria found that the addition of SiC significantly reduced the grain size of the HfB_2, more readily enabling grain boundary sliding and thus, allowing greater deformation under load. Eventually, as more SiC is added to the ceramic matrix, individual SiC grains begin to touch one another, forming a web-like network of SiC within the material. Once this network forms within the matrix, SiC begins to dominate the overall composite deformation. Figure 2

illustrates how the creep rates of pure HfB_2, and SiC are significantly lower than those of

HfB_2-SiC composite with certain amounts of SiC. The rise in creep rate is due to the

reduction in HfB_2 grain size caused by the introduction of SiC into the HfB_2 matrix. The

subsequent decrease in creep rate is explained through percolation theory. Percolation

theory postulates that additives create networks of point-to-point contacts within the

parent material. When enough contacts occur, generally due to increased volume fraction

of the additive, networks form which can greatly increase creep resistance of the

composite [24]. The curve in Figure 2 provides a visual representation of percolation

theory through the creep rate of a HfB_2 ceramic with increased SiC content. Creep rate

starts off at a value for pure HfB_2 then increases as grain size decreases due to the initial

introduction of the SiC additive. As the volume fraction of SiC increases, a network of

SiC contacts forms within HfB_2-SiC and drives down the composite's creep rate,

eventually reaching a value exhibited by SiC.
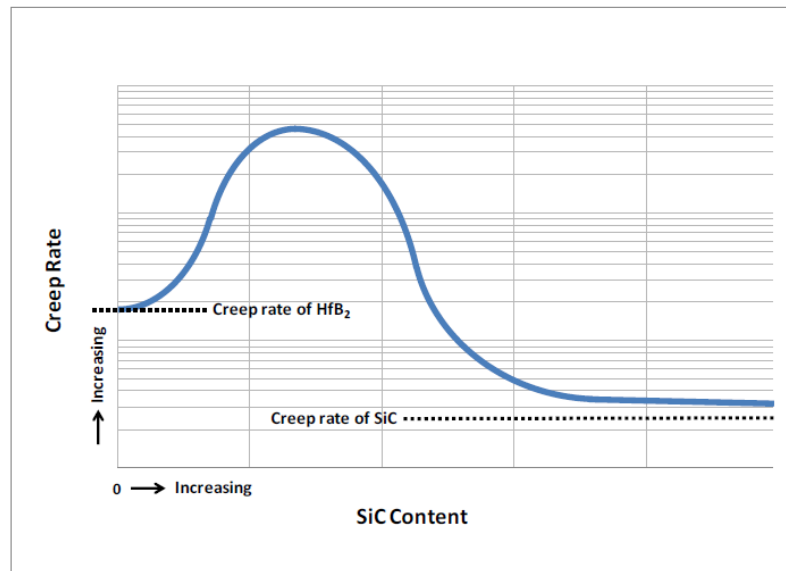
Figure 2. Creep rate of HfB_2 vs. SiC content, reproduced from DeGregoria [23].

1.3 Creep

While the ultra-high melting temperature capability of UHTCs is promising, the ceramic must also retain strength, toughness and creep resistance at the use temperatures. Creep deformation represents one of the critical criterion for structural application of ceramics at elevated temperatures.

Creep is the progressive deformation of a material under constant load [25]. In a standard creep test, a specimen is loaded to a desired tensile or compressive load. Then the load is held constant for a desired duration and deformation (or strain) is measured. The strain-time data collected during the test are plotted on a creep strain vs. time diagram, where creep regimes are identified. Primary creep regime is characterized by a decreasing strain rate. Primary creep is associated with changes in the material structure (e.g., grain size, dislocation structure, etc.) or with the redistribution of stresses. Of particular interest is the secondary or the steady-state creep regime characterized by a constant strain rate. In this regime, creep is viewed as the deformation of an invariant microstructure. Tertiary creep, characterized by an increasing strain rate, is associated with the initiation of the failure processes. Steady-state creep in polycrystals can proceed by dislocation mechanisms and by diffusional mechanisms. The diffusion can occur through the grains (Nabarro-Herring creep) as well as along grain boundaries (Coble creep). For a large number of creep mechanisms the steady-state creep rate can be expressed by Equation 1.

$$\dot{\varepsilon} = \frac{AD\mu b}{kT}\left(\frac{b}{d}\right)^m \left(\frac{\sigma}{\mu}\right)^n$$

Where: $D = D_o \exp\left(\frac{-Q}{RT}\right)$

$\dot{\varepsilon}$ – steady-state creep rate μ – shear modulus

A – dimensionless constant   k – Boltzmann constant

D – diffusion coefficient   T – absolute temperature

D_o – frequency factor   b – Burgers vector

Q – creep activation energy   d – grain size

R – the gas constant   m – grain size exponent

σ – applied stress   n – stress exponent

Equation 1. Governing equation for steady-state creep rate [26].

Equation 1 identifies a number of variables that affect the steady-state creep rate. The primary failure mode of ceramics under constant loading at high temperatures has been found to be grain boundary sliding [2], [27]. It can therefore be assumed that the failure mode of the UHTC specimens in this work will be controlled by grain boundary sliding. Appropriate UHTC compounds can be selected to minimize the variables that contribute to grain boundary sliding (grain size, dislocation diffusion and defect concentration) to help focus test efforts [1, 27]. The test material in this study was designed to possess equiaxed grains, with a random crystallographic orientation.

1.4 Oxidation

Oxidation is a chemical reaction, in which a substrate reacts with oxygen to form an oxide. In order for the oxide to form, the substrate must be reduced. In the case of a surface reaction, an oxide layer will form on the surface of the substrate. The oxide layer will limit further oxidation of the substrate beneath it provided the oxide layer is dense enough to prevent oxygen diffusion. While a thin oxide layer might improve properties of

a metal at low temperatures (i.e. environmental protection and increased hardness) it can be devastating to a material operating across large temperature variations. The oxide layer on the surface and the substrate (UHTC in this work) likely have different coefficients of thermal expansions. Under large changes in temperature (thermal shock), the oxide layer may separate or crack away from the substrate, re-exposing the substrate to the oxygen rich environment [21]. This cycle continues, leading to accelerated oxidation rates, substrate loss and eventual material failure [28].

The addition of SiC to HfB_2 has been shown to reduce oxidation in the substrate by reacting with oxygen at the surface to form a glass layer. The amorphous glass layer fills in any cracks that form within the substrate, preventing further oxidation and shielding the substrate from further structural damage [29]. Recently Parthasarathy et al. modeled oxidation kinetics in SiC-containing HfB_2 and ZrB_2 at temperatures ranging from 1200 to 2200 °C [30]. Model predictions agree well with limited experimental results in literature, including the results of baseline oxidation tests reported by DeGregoria [23]. A schematic representation of the Parthasarathy model for metal diborides with a SiC additive is given in Figure 3, where chemical reactions taking place during oxidation at elevated temperatures are also defined. Note the presence of the oxide layer (MeO_2) between the substrate (MeB_2) and the borosilicate (B_2O_3-SiO_2) glass on the surface. The borosilicate glass disperses throughout the oxide scale, filling in cracks and voids, encapsulating the substrate and effectively creating an oxide barrier.
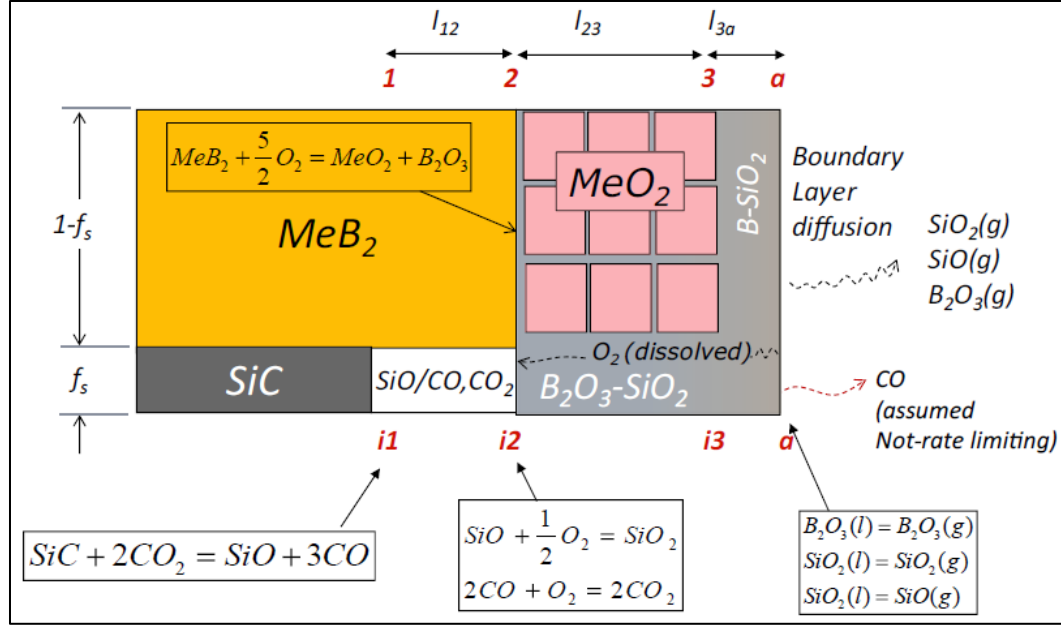
Figure 3: Model of an oxidized metal diboride with SiC copyright © 2011, The American Ceramic Society, Journal of the American Ceramic Society, used with permission [30].

Figure 4 shows microstructure of HfB_2-20%SiC heat treated at 1800°C [31]. Several regions can be readily seen in the SEM image in Figure 4. Region I, on the surface of the specimen, is a borosilicate glass layer. Region II shows the presence of hafnia (HfO_2) with borosilicate glass (B_2O_3-SiO_2) filling in voids. Region IV shows presence of hafnia with Si-O-C inclusions and some borosilicate glass. The regions included in the Parathasarathy's model (Figure 3) agree with the experimental findings seen in the SEM image.
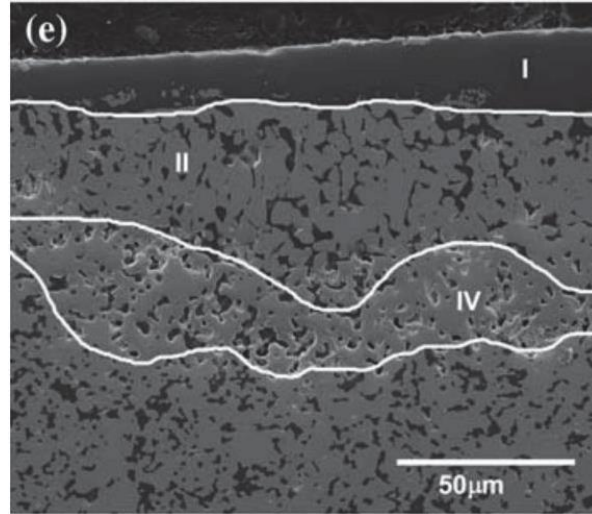
Figure 4. Oxidation of HfB2-20% SiC at 1800°C (I: SiO_2, II: SiO_2 filled HfO_2, IV: HfO_2 with Si-O-C inclusions), reproduced from [31] with permission.

1.5 Previous Research

Early experiments with UHTCs dating back to the 1970s focused primarily on ZrB_2-based ceramics. While it is recognized that experimental evaluation of mechanical properties and behavior of UHTCs is of critical importance, little has been reported on the mechanical behavior of UHTCs at elevated temperatures. Most studies that reported high-temperature mechanical properties for the diborides reported strength measurements obtained in four-point bending (three-point bending in some cases) at elevated temperatures. Notably, only a limited number of studies of the creep behavior of UHTCs have been reported in literature to-date. In most of these studies, creep rates were not measured directly but were estimated from flexure tests using strength of materials based calculations.

An ongoing research effort at AFIT aims to: (1) characterize and analyze high-temperature creep deformation, (2) identify controlling creep mechanisms of UHTCs at temperatures up to 1700°C, and (3) investigate an interaction between oxidation and

compression creep of UHTCs at temperatures up to 1700°C. Recent research efforts at AFIT successfully developed, constructed and validated a specialized facility for mechanical testing of small UHTC specimens in air and in argon at 1500-1700 °C [13, 22, 23]. Furthermore, a method to perform compression creep tests of small HfB_2 specimens in air and in argon at 1500-1700 °C was developed and validated [13, 22, 23]. A brief summary of mechanical testing efforts found in the literature for HfB_2 and ZnB_2 is presented in Table 1.

Table 1: Summary of high-temperature creep tests on HfB_2 and ZnB_2, adapted from Bowen [13].

Author	Year	Material	Mechanical Test Method	Temp (°C)	Stress (MPa)	Additives
Bowen	2017	HfB2	Uniaxial Compression	1500	75 to 100	0 to 30% SiC
DeGregoria	2015	HfB2	Uniaxial Compression	1500	25 to 75	0 to 30% SiC
Winder	2015	HfB2	Uniaxial Compression	1500	25 to 100	0 to 20% SiC
Gangireddy	2013	ZrB2	Flexural	1700-2200	20 to 50	30% SiC
Bird	2011	ZrB2	Flexural	1400-1820	16 to 97	20% SiC
Guo	2011	ZrB2	Flexural	1500-1600	19	30% SiC
Talmy	2008	ZrB2	Flexural	1200-1500	30 to 180	0 to 50% SiC
Melendez-Martinez	2001	ZrB2	Uniaxial Compression	1400-1600	47 to 472	0, 4% Ni
Kats	1981	ZrB2	Flexural	1700-2420	5 to 30	0 to 100% ZrC
Spivak	1973	ZrB2	Flexural	2052-2291	5 to 196	0 to 100% ZrN
Rhodes	1970	Both	Both	800-1800	172	0, 20% SiC

The AFIT specialized test facility integrates a servo-controlled testing machine (MTS model 810) equipped with hydraulic, water-cooled wedge grips, a custom built furnace resistance-heated by two $MoSi_2$ heating elements and a MELLEN PS400 temperature controller. An MTS Flex Test 40 digital controller is used for input signal generation and data collection. Accurate strain measurement is accomplished with an MTS uniaxial, high-temperature, low-contact force extensometer equipped with two sapphire extension rods that reach into the furnace and are in direct contact with the test

specimens. Two high purity single-crystal yttrium aluminum garnet (YAG, $Y_3Al_5O_{12}$) pushrods of 10-mm diameter are used to apply compressive stress to the specimen in the furnace hot zone. The pushrods are mounted in custom-built stainless steel fixtures, which are gripped in upper and lower water-cooled hydraulic wedge grips.

While developing the AFIT test facility Winder [22] observed a thermo-chemical interaction occurring between the HfB_2 test specimen and the SX YAG pushrods at 1500°C in air. Winder determined that single crystal YAG was not stable in the presence of HfB_2 at 1500°C in air. She proposed that single crystal YAG reacted with B_2O_3 gas formed during oxidation of HfB_2 and was reduced into YAM, $AlBO_2$ (g) and YBO_2 (g). The gases were adsorbed onto the HfO_2 scale; thus, forming various Y- and Al-containing deposits. Surface properties of the HfO_2 scale determined the nature and composition of the surface deposits. Winder also found that placing chemically stable aluminum oxide (alumina, Al_2O_3) spacers between the HfB_2 test specimen and the single crystal YAG rods eliminated undesirable chemical reactions [22]. Based on these findings, the AFIT test method was modified to include alumina (Al_2O_3) spacers between the HfB_2 test specimen and the single crystal YAG pushrods.

DeGregoria [23] investigated oxidation of HfB_2 and HfB_2–20% SiC at 1500°C in air for up to 90 h. DeGregoria also designed an experiment to assess the effects of compressive stress on oxidation of HfB_2-based UHTCs and successfully investigated the oxidation behavior of HfB_2-20% SiC under compressive stress (50 MPa) at 1500°C in air. Results revealed no significant effect of compressive stress (50 MPa) on oxidation of HfB_2-20% SiC. DeGregoria also discovered that the aluminum oxide spacers failed prematurely in tests where compressive loads exceeded 50 MPa [23]. Bowen was tasked

to explore a more resilient alternative to the aluminum oxide spacers so that creep tests could be accomplished at higher compressive loads. Bowen replaced the aluminum oxide crystal spacers (comprised of a randomly oriented, polycrystalline structure) with arbitrarily oriented, single crystal aluminum oxide spacers (aka. sapphire). Sapphire spacers with a random crystallographic orientation were shown to perform well. Compression creep tests could now be performed at 1500 °C with significantly higher compressive loads. Bowen was able to perform successful tests up to 100 MPa. Additionally, considerably longer test durations were now possible at lower stress levels [13]. This research builds on the lessons learned from Winder, DeGregoria and Bowen to perform creep tests of HfB_2-SiC at 1500°C at higher compressive loads and to achieve longer test durations. A more detailed description of the test set-up will be provided in Chapter II.

DeGregoria [23] conducted baseline oxidation tests of HfB_2-SiC coupons at 1500 °C in a controlled, air environment using a box furnace. Twelve coupons of each HfB_2 and HfB_2-20% SiC were exposed under zero stress at 1500°C in air for up to 90 h. The HfB_2 samples, devoid of the borosilicate glassy diffusion barrier afforded by the addition of SiC particles, oxidized completely within 6 hours at 1500 °C. The experimental results obtained for the HfB_2-20% SiC samples are summarized in Figure 5 [23].
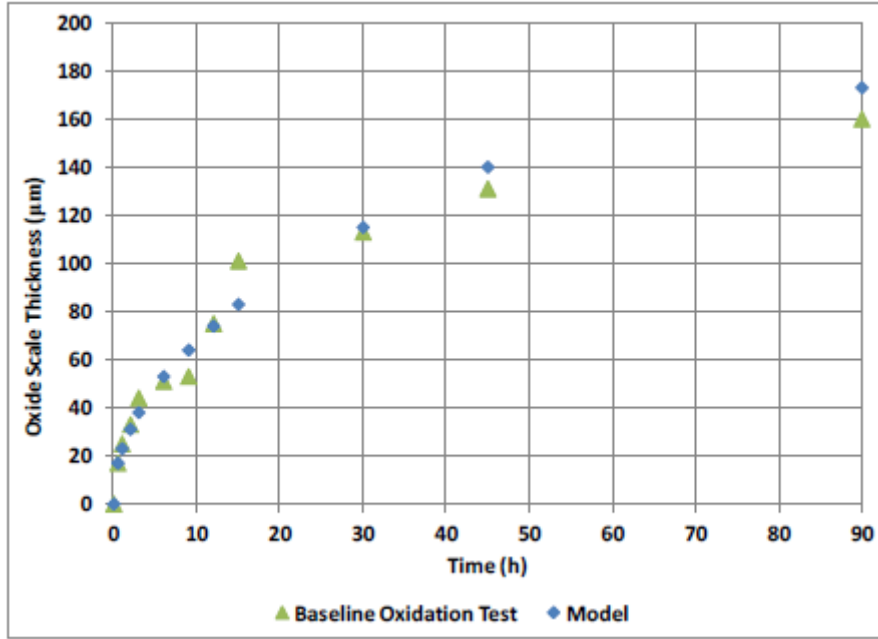
Figure 5. Oxide scale thickness vs time for HfB$_2$-20% SiC at 1500°C in air, experimental data from DeGregoria [23], model data from Parthasarathy et al. [30]

Experimental results obtained by DeGregoria [23] were compared with the predictions of the oxidation model proposed by Parthasarathy et al [30]. As shown in Figure 5, model predictions agreed well with the experimental data. DeGregoria also designed an experiment to assess effects of compressive stress on oxidation of HfB$_2$-based UHTCs at 1500°C. He investigated the oxidation behavior of HfB$_2$-20% SiC under compressive stress of 50 MPa at 1500°C in air. Sustained compressive stress of 50 MPa was found to have no significant effect on oxidation of HfB$_2$-20% SiC compared to experimental results for the baseline, unstressed specimen. However, the question remained whether oxidation behavior of HfB$_2$-20% SiC would be affected by sustained compressive stresses exceeding 50 MPa.

This research effort aims to examine compressive creep of HfB$_2$-20% SiC under compressive stresses exceeding 50 MPa for up to 20 h. Following creep test, specimens

14

will be sectioned and examined under SEM to elucidate the evolution of oxide scale under compressive stress with time. The results of this work will be compared with those of baseline oxidation tests under zero load reported by DeGregoria. We will determine whether a relationship exists between compressive stress and oxidation rates of HfB_2-20% SiC at 1500 °C in air. While previous research has shown that the addition of SiC has significant effects on oxidation and on creep behavior of HfB_2, this research will attempt to determine if there is an interaction between oxidation and creep.

In this work we will determine the minimum creep rates of HfB_2- 20% SiC at 1500°C in air. These results can be readily compared to the minimum creep rates of HfB_2- 20% SiC at 1500°C in an inert environment found by DeGregoria. Using the same AFIT experimental setup, test method, and test specimens from the same billet, facilitates a direct comparison between the results of current work and those reported previously by DeGregoria.

In this work we aim to determine:

i.) Minimum creep rates of HfB_2-20% SiC in air at 1500°C for various compressive creep stresses.

ii.) Effect of sustained compressive loading (compressive creep) on oxidation rate.

iii.) Effect of oxidation on minimum creep rate.

iv.) Effect of sustained compressive loading on preferred grain orientation.

The concepts described in this chapter provide a framework for understanding the background and purpose of this research. This research attempts to characterize the material properties of a specific UHTC, hafnium diboride (HfB_2), a material potentially capable of replacing traditional structural materials in ultra-high temperature applications.

15

A detailed description of the test material, experimental facility and test methods used in this work is provided in Chapter II.

II. RESEARCH METHODOLOGY

The AFIT specialized test facility was designed, built and validated by Winder [22]. Subsequently, both the experimental setup and the test methods were further improved by DeGregoria [23] and Bowen [13]. This chapter provides a brief description of the research material, experimental facility, test methods and procedures, and post-test analysis equipment and techniques used in this work. A detailed review of the general UHTC research methodology developed at AFIT is provided by DeGregoria [23].

2.1 Research Materials

The HfB_2-20 vol% SiC material used in this work was fabricated at the Air Force Research Laboratory's (AFRL) Materials and Manufacturing Directorate using commercially available HfB_2 (Cerac, Milwaukee Wisconsin) and SiC (Reade Advanced Materials, East Providence Rhode Island) powders. The HfB_2 powder had a purity of 99.5% and a mean particle size of 4.6 μm. The SiC powder was α-phase, 99.9% pure, with particle sizes between 0.03 μm and 3 μm. A Si_3N_4 grinding media in isopropanol was used to pre-mill the HfB_2 powder for 60 h, resulting in an average particle size of 1.3 μm. To process the HfB_2-20 vol% SiC bulk material, the appropriate amount of SiC powder by volume was added and the mixture was milled with Si_3N_4 for 18 h, followed by stirring, drying at room temperature, and dry milling for another 18 h. The mixture was sifted through an 80-mesh screen. 100 g of the mixture was loaded into a 40-mm

graphite die coated with BN and lined with graphite foil. The mixture was sintered using the spark plasma sintering (SPS) process with a heating and cooling rate of 50°C/min and a maximum temperature of 2100°C. The hold time at 2100°C was 10 min. A pressure of 40 MPa was applied during heating to 1600°C and held throughout the remainder of the sintering cycle. The pressure was released to 4 MPa during cool-down to 450°C. Near full density was achieved for HfB_2-20 vol% SiC. A detailed description of the material processing is given elsewhere [31, 32]. Note that the material tested in this research was from the same batch as that investigated by DeGregoria [23] and Bowen [13].

The sintered HfB_2-20 vol% SiC pucks were cut into test samples utilizing electric discharge machining. The nominal dimensions of the test specimens were 6.5 mm x 6.5 mm x 19 mm (see Figure 6). Note the two grooves machined on one side of the test specimen for placement of extensometer rods. After machining, all sample surfaces were polished to a 45-μm finish using diamond slurry to remove surface flaws. DeGregoria [23] sectioned representative as-machined scraps of HfB_2-20 vol% SiC and analyzed these samples using scanning electron microscopy (SEM) and energy dispersive x-ray spectroscopy (EDS) to determine the depth of damage and contamination from the machining process. Based on this analysis, the polishing depth for HfB_2-20 vol% SiC was set at 100 μm.
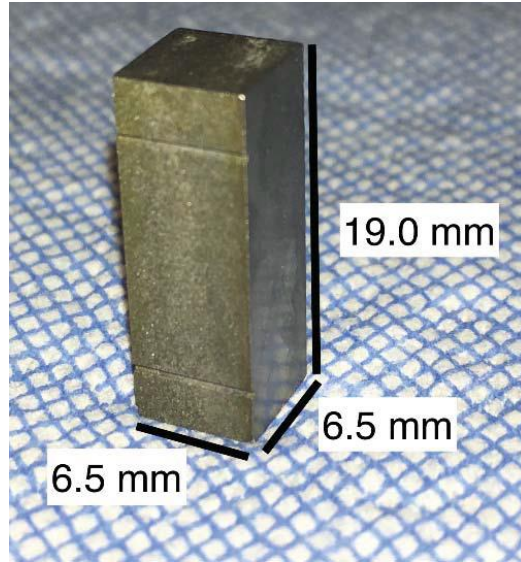
Figure 6. Test specimen geometry, reproduced from Bowen [13].

2.2 Experimental Arrangements

The test facility was designed to test small UHTC specimens in compression at temperatures of up to 1700°C in air or in argon. A detailed description of the test facility is provided by Winder [22] and DeGregoria [23]. A detailed description of lessons learned regarding alumina and sapphire spacers is provided by Bowen [13]. A brief summary of the experimental setup is offered below. The main components of the test setup are shown in Figure 7a.

AFIT specialized test facility includes:

- A Model 810 MTS testing machine (load capacity: 25 kN)

- A uniaxial load cell

- A custom built furnace with two $MoSi_2$ heating elements

- A Eurotherm 3504 temperature controller

18

- A MTS model 632.53E-14 axial high temperature extensometer with custom sapphire extension rods

- A FlexTest 40 Digital Controller for command signal generation and data acquisition

- A model NESLAB RTE 7 recirculation chiller used to keep the MTS wedge grips cool during test

- Cooling fans
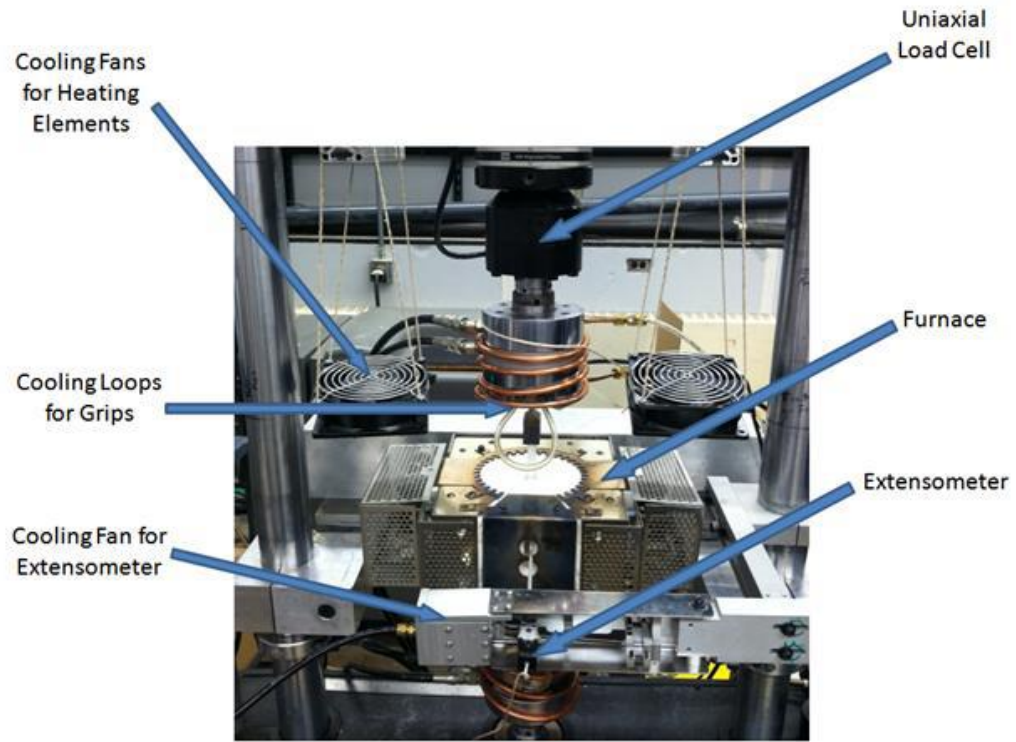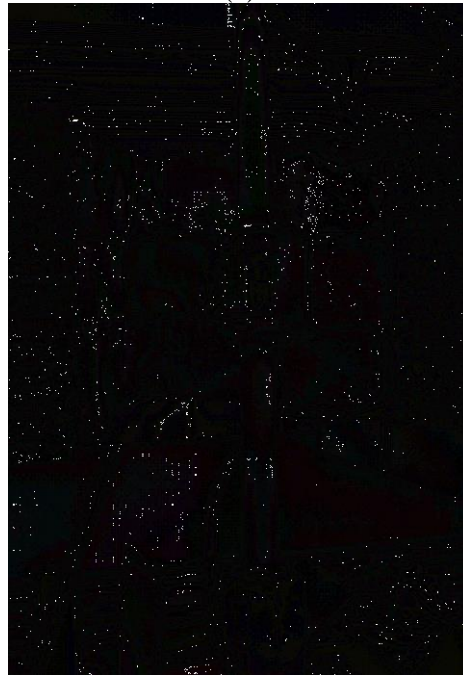
Figure 7: (a) Experimental setup, (b) specimen mounted in the experimental facility and ready for testing, reproduced from DeGregoria [23].

Figure 7b shows a test specimen mounted in the experimental facility and ready for testing. A schematic of the method developed at AFIT for testing small HfB_2 specimens in compression is shown in Figure 8. The test method employs: custom grip fixtures, single crystal YAG push rods, sapphire spacers and Pt foil between single crystal YAG pushrods and sapphire spacers. Note that the portion of the YAG rod inserted into the custom holder is also wrapped in copper foil to cushion the brittle YAG from the metal holder and to ensure an even, snug fit. The custom holders contain setscrews and spring loaded washers that tighten the holder onto the YAG rod while allowing enough flexibility to prevent fracture of the YAG rod due to thermal expansion. A detailed description of the custom holders is provided by Bowen [13]. The YAG rod is separated from the test specimen by platinum foil and sapphire spacers. The sapphire spacers are used to prevent thermo-chemical interaction between YAG and HfB_2. The platinum foil prevents bonding between the YAG rod and sapphire spacers. The chisel-shaped ends of the extensometer rods are placed in direct contact with the test specimen using the grooves cut into the HfB_2 test specimen. Such arrangement ensures direct contact strain measurement with the MTS high-temperature extensometer. Direct contact strain measurement permits an accurate evaluation of creep rate. The direct strain measurement is one of the advantages of the AFIT test method over flexural testing [22].
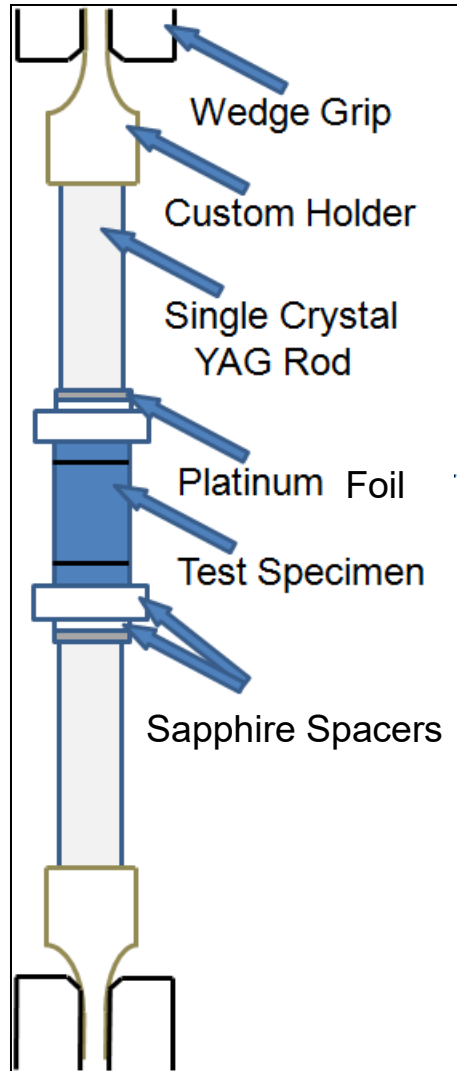
Figure 8: Schematic of the method for testing small HfB$_2$ specimens in compression, adapted from DeGregoria [23].

The nature of the prescribed load train requires precise alignment to ensure proper load transfer to the specimen and to avoid instability, uneven loading and premature test failure. To assist with alignment, a custom alignment tool designed by Bowen is utilized, ensuring that YAG rods, sapphire spacers and the test specimen are properly installed [13]. Figure 9 shows how proper alignment is achieved with the use of the alignment tool.
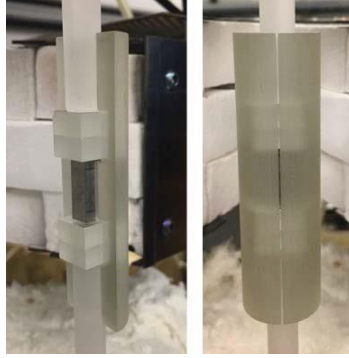
Figure 9. Custom load train alignment tool, open (left) and closed (right), reproduced from Bowen [13].

2.3 Test Procedure

The test procedure used in this work was developed and successfully employed by DeGregoria and later improved upon by Bowen [23, 13]. The test procedure was adapted slightly to meet the current test objectives by altering the creep load and test duration. A detailed account of the full test procedures is given in Appendix B.

Prior to testing, it was necessary to calibrate temperature to ensure the specimens were exposed to the desired 1500°C during test. The furnace temperature controller uses a non-contacting B-type thermocouple exposed to the ambient environment in the vicinity of the test specimen. During the calibration procedure, the test specimen is mounted in the load train and kept under zero load. A thermocouple probe is inserted into the test chamber to measure the temperature of the specimen. The temperature setting on the controller is gradually increased until the specimen temperature reaches the target test temperature of 1500°C±5°C. The calibration process was repeated 10 times to confirm the controller setting. Multiple furnace set points were explored between 1500° C and 1540° C. Ultimately, a set point of 1510° C was selected as the optimum setting to achieve a specimen temperature of 1500°C±5°C. The ±5°C temperature variation was deemed negligible as it represents less than 1% of the test temperature. During all tests, a

23

specimen was heated to test temperature at a rate of 0.5°C/min and held at 1500° C for 1 h prior to loading.

The MTS configuration file initially developed by DeGregoria and later modified by Bowen was used in this work [23, 13]. The configuration file, "Temperature.cfg", is listed in the test procedure detailed in Appendix B. The following data was recorded for the entire duration of each test: time (s), strain (m/m), displacement (mm), force (N), force command (N), temperature (° C) and temperature command (° C). For each test, specimens were loaded to the creep stress at a rate of 0.5 MPa/s and unloaded to zero load at the same rate at the completion of the creep test.

2.4 Microstructural Examination Procedure

Once high temperature creep tests were accomplished, each specimen was examined under an optical microscope and SEM to evaluate the oxide scale. Preliminary inspection under the optical microscope provided a baseline for SEM examination and insight into the general condition of the specimen surface. The optical microscope used for this research was a Zeiss Discovery V12 with SteREO and AxioVision software (AxioVs40 V 4.8.2.0). Once the optical microscopy was complete, each sample was prepared for either SEM or XRD examination. Some specimens exhibiting interesting surface deposits were subject to XRD analysis prior to SEM examination. Note that XRD analysis required minimal specimen preparation. A Rigaku Ultima IV X-Ray Diffractometer was used to perform XRD analysis. The open source Rietveld refinement program, MAUD was used to determine phase fractions from the x-Ray diffraction patterns.

2.4.1 Sample Preparation for Examination under SEM

The basic specimen preparation steps for examination under SEM include mounting, sectioning, polishing and the application of a surface treatment to avoid surface charging effects (which can provide a poor quality image). Specimens were mounted using a two-stage epoxy resin to ensure the brittle oxide scale on the specimen surface remained intact for examination. The epoxy consisted of two parts EpoThin 2 Epoxy Resin (20-3440-128) to one part EpoThin 2 Epoxy Hardener (20-3442-064). The mixture was stirred to ensure even mixing and to prevent air bubbles from forming. The specimens were then placed into a 1-in diameter mold coated with a releasing agent and the epoxy resin was poured into the mold. The mounted specimens were then placed under partial vacuum for 10 min to eliminate air bubbles in the epoxy and left overnight to cure.

Once the mounted specimens were fully cured, they were labeled then sectioned using a Buehler IsoMet™ 1000 saw. The samples were sectioned along the plane normal to the specimen longitudinal axis to reveal the cross section. Due to the brittle nature of the HfB_2-SiC specimens, gentle pressure was used during cutting to avoid fracture. A low concentration diamond blade was used at 275 RPM with a force of approximately 150g.

Samples were polished by hand using successively course diamond slurries on Piano DGD or VerduTex polishing cloths until a surface finish of 0.25 μm was reached. Each specimen required slightly different polishing steps depending on the depth of scratches introduced during cutting. Typical polishing steps are listed in Table 2. After each step in Table 2, the mounted specimen was inspected using an optical microscope to ensure even, uniform polishing and subsequently rinsed in an ultrasonic alcohol bath to

remove any residual debris. Following rinse, the samples were blown dry using nitrogen

gas prior to moving on to the next polishing step.

Table 2: Polishing steps.

	Surface	Grit Size	Time	Spin Type	Base Speed	Pressure (Estimate-Induced by Hand)
1	Piano DGD	35 μm	5 min or until planar and diamond saw marks are eliminated	Contra	150 rpm	10 lbs
2	Piano DGD	15 μm	5:00 min	Contra	150 rpm	10 lbs
3	VerduTex	9 μm	5:00 min	Contra	150 rpm	10 lbs
4	VerduTex	6 μm	5:00 min	Contra	150 rpm	10 lbs
5	VerduTex	3 μm	3:00 min	Contra	150 rpm	10 lbs
6	VerduTex	1 μm	3:00 min	Contra	150 rpm	10 lbs
7	VerduTex	0.25 μm	3:00 min	Contra	150 rpm	10 lbs

Once the specimens were polished to a 0.25 μm finish, both copper tape and a

conductive coating were installed onto the sample to prevent surface charging during

SEM examination. During SEM inspection, the specimen is irradiated with electrons. If

the specimen fails to adequately conduct the bombarding electrons away from its surface,

the subsequent electron buildup deteriorates the SEM image quality. The conductive

coating and copper tape provide a path for electrons to dissipate away from the specimen

surface, enabling higher quality imaging. The conductive coating was iridium based and

was applied using a Vacuum Desk IV sputter coating machine. Once the copper tape and

iridium sputter coat was applied, sample preparation was complete. Figure 10 shows a

specimen fully prepared for SEM imaging.
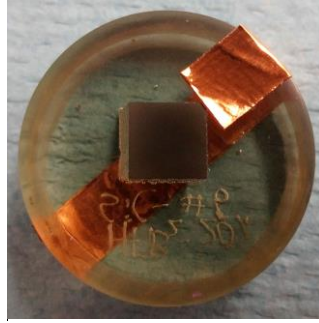
Figure 10. Specimen HfB$_2$-20%SiC-6 prepared for SEM examination.

2.4.2 Microstructural Examination of Specimen with SEM and XRD

A primary research objective was to evaluate the oxide scale formed on the specimen under sustained compressive stress at 1500°C in air. Examination of the oxide scale formed on HfB$_2$-20% SiC specimens tested in creep will provide insight into the interaction between creep and oxidation processes. DeGregoria [23] reported measurements of the oxide scale thickness obtained for HfB$_2$-20% SiC specimens in baseline oxidation tests under zero stress at 1500°C in air. Comparison of the oxide scale thickness measurements obtained under compressive stress in this work to those obtained by DeGregoria in baseline oxidation tests is of particular interest. Hence, an effort was made to ensure consistency in the oxide scale measurement methods used in this work with the methods used by DeGregoria.

SEM imaging was used due to the high resolution achieved at the magnification required to accurately measure oxide scale thickness. All SEM images were generated using FEI Quanta 650 SEM (AFRL/RX). Images were captured such that the entire oxide scale was shown in the micrograph. For each specimen, up to 24 images were taken around the perimeter of the sample to ensure that a comprehensive representation of the oxide scale was recorded. SEM can only provide gray scale imagery of the specimen

27

surface. Therefore, composition analysis was performed on each sample to confirm the elemental composition of the oxide scale. Composition analysis was accomplished via energy-dispersive X-ray spectroscopy (EDS) using an FEI Quanta 650 with an EDAX Octane Super 60mm^2 detector at AFRL/RX.

General test procedures and setup were developed by Winder, DeGregoria and Bowen as described previously [22, 23, 13]. However, the minor modifications made during this effort led to the discovery of new information. Through analysis of the data collected, conclusions can be made regarding (i) whether creep loading has an impact on oxidation rate and (ii) whether oxidation has an effect on the creep rate of HfB$_2$-20% SiC at 1500 °C in air.

III. RESULTS AND ANALYSIS

Seven compressive creep tests were performed in this work using the methodology detailed in chapter II. Table 3 provides a summary of testing conditions.

Table 3: Summary of compression creep tests performed at 1500 °C in air.

Specimen	Composition (% by Volume)	Compressive Stress (MPa)	Test Duration (h)	Reason for Test Termination
HfB2-20SiC-4	20% SiC	150	8.05	Spacer/ YAG Rod Failure
HfB2-20SiC-5	20% SiC	100	10	Run Out
HfB2-20SiC-6	20% SiC	75	10	Run Out
HfB2-20SiC-9	20% SiC	150	6.03	Spacer Failure
HfB2-20SiC-10	20% SiC	50	20	Run Out
HfB2-20SiC-11	20% SiC	75	18	Spacer/ YAG Rod Failure
HfB2-20SiC-12	20% SiC	200	0	Spacer Failure on Load-up

3.1 Compression Creep Tests - Summary and Analysis

As mentioned in section 1.5, the replacement of alumina spacers with sapphire spacers within the load train enabled testing at higher compressive stresses for longer durations. As indicated in Table 3, four of the seven tests performed were terminated prematurely due to either spacer or YAG rod failure. Figure 11 shows the damage incurred on the upper sapphire spacers and upper YAG rod following a test performed at 150 MPa in air at 1500°for 8.05 h.

Figure 11. Failed YAG rods and sapphire spacers used in a creep test of specimen HfB_2-20SiC-4 performed at 150 MPa for 8.05 hours.

As seen in Figure 11, both spacers located between the upper YAG pushrod and the test specimen failed catastrophically. The upper YAG rod also failed near the base in contact with the spacers, with cracks propagating to the portion encapsulated by the custom grip. In tests where both YAG rod and spacer failed, it is not possible to determine which component failed first. However, prior work indicates that spacer failure likely occurred first. While four tests ended due to spacer or YAG rod failure, these tests were performed with higher stress levels than those accomplished in prior work. Furthermore, longer test durations were achieved. The use of sapphire spacers in place of alumina spacers undoubtedly permits creep testing at higher compressive creep stresses for longer durations, validating Bowen's work.

This effort focused on HfB_2-SiC specimens containing 20% SiC in order to more readily compare results with those obtained by DeGregoria in baseline oxidation tests for HfB_2-20% SiC specimens. Test results obtained in the current effort are plotted in Figure 12 together with those reported by DeGregoria [23] and Winder [22] for HfB_2-20% SiC specimens.
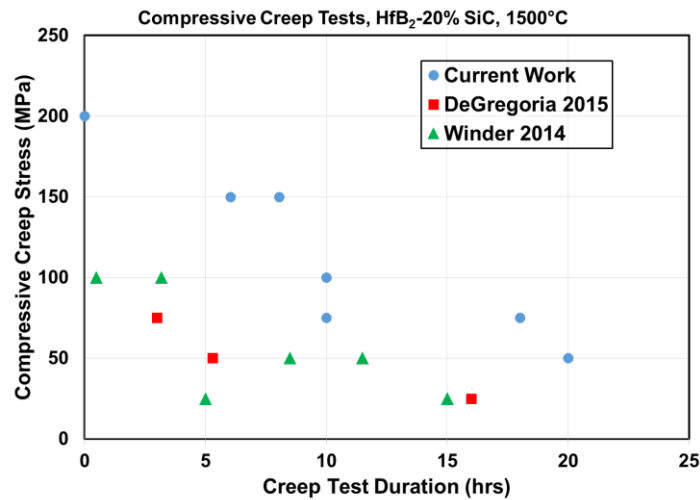
Figure 12. Compressive creep stress vs. creep test duration performed for HfB_2-20% SiC at 1500°C in air. Data from [22] and [23] is included for comparison.

30

As illustrated in Figure 12, longer test durations were achieved at compressive stresses of 50, 75, and 100 MPa in this work than in previous research efforts. Compared to prior work, test durations for compressive creep stresses up to 75 MPa increased by at least 74% and up to 600%. Additionally, two successful creep tests were performed at 150 MPa. At higher compressive stress levels, the specimen is expected to reach steady state-creep more rapidly. Then the steady-state creep rate can be determined.

The creep strain vs. time curves produced during this effort are shown in Figure 13. Two tests were performed at each 75 and 150 MPa. As expected, the two creep strain curves obtained at 75 MPa overlap. The same observation can be made for the two creep strain curves obtained at 150 MPa. As expected, compressive creep strain rates increase with increasing compressive creep stresses.
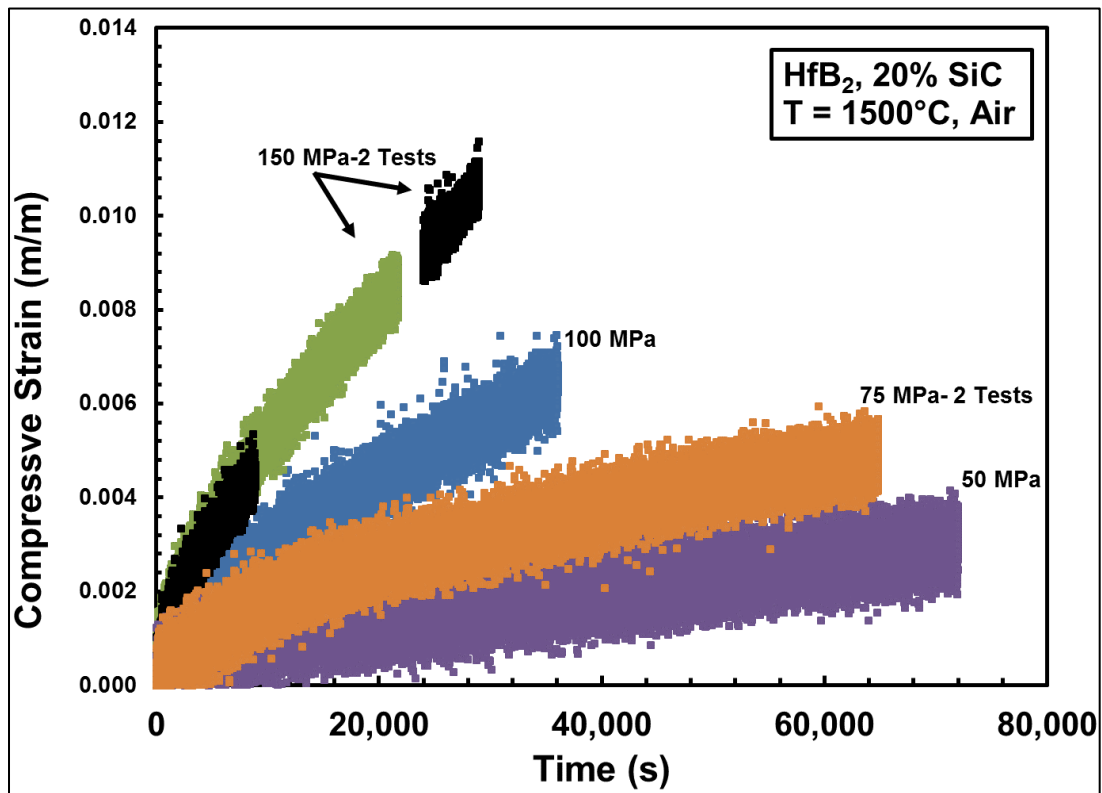
Figure 13. Compressive creep strain vs. time curves obtained for HfB$_2$- 20% SiC specimens at 1500°C in air.

The creep curves in Figure 13 exhibit primary and secondary (or steady-state) creep regimes. Minimum creep rate was determined in all tests. The minimum creep rate is found by calculating the slope of the linear portion of the creep curve. Higher compressive creep strains and longer test durations achieved in this work ensure that the steady-state creep regime is in fact reached, which was not always the case in prior tests of much shorter duration. See, for example, Figure 14, where the compressive creep curve obtained for HfB_2- 20% SiC at 75 MPa at 1500°C in air in this work is compared to that obtained by DeGregoria [23] for HfB_2- 20% SiC at 75 MPa at 1500°C in argon. The striking dissimilarity between the two data sets in Figure 14 is the duration of the tests. The test in air ran for 10 h while the test in argon was terminated after 3 h due to spacer failure. Results in Figure 14 demonstrate that the steady-state creep was reached during the 10-h test performed at 1500 °C in air, but not during the 3-h test performed at 1500°C in argon. While the minimum creep rate could be calculated for both tests, only the 10-h test provided sufficient data to determine the steady-state creep rate. Note that the minimum creep rate determined for the 3-h test performed in argon was 3.09 x 10^{-7} s^{-1} while the 10-h test in air yielded a lower steady-state creep rate of 1.34 x 10^{-7} s^{-1}. Results in Figure 14 also reveal that nearly identical data were produced during the first 3 h of creep in both air and argon tests. Hence it is likely that had the test in argon been allowed to proceed to reach steady-state creep, a steady-state creep rate close to 1.34 x 10^{-7} s^{-1} would have been produced.
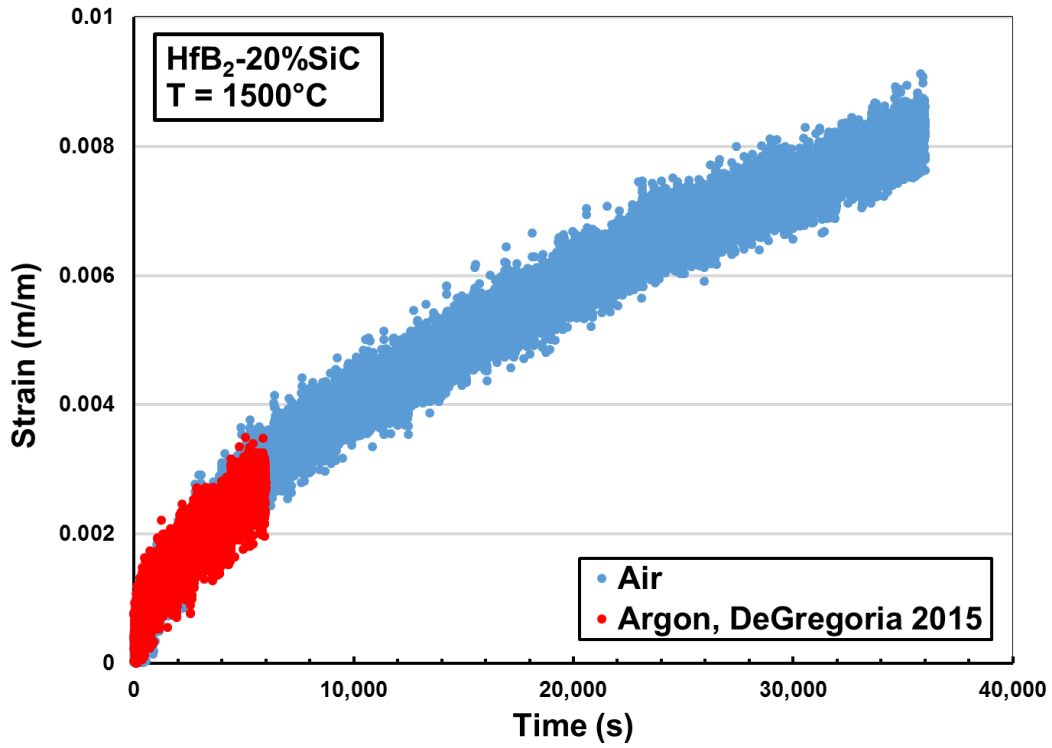
Figure 14. Creep curves obtained for HfB$_2$-20% SiC at 75 MPa in air and in argon. Data in argon from DeGregoria [23]. Note the importance of test duration for ensuring that steady-state creep has been reached.

Table 4 summarizes the steady state creep rates calculated for each test conducted at 1500°C in air during the current effort.

Table 4. Steady state creep rates obtained for HfB$_2$-20% SiC in compression creep tests performed at 1500° C in air.

Specimen	Compressive Stress (MPa)	Test Duration (h)	Steady-State Creep Rate (s^{-1})
HfB2-20SiC-10	50	20	2.87 x10^{-8}
HfB2-20SiC-6	75	10	1.34 x10^{-7}
HfB2-20SiC-11	75	18	3.85 x10^{-8}
HfB2-20SiC-5	100	10	1.23x10^{-7}
HfB2-20SiC-9	150	6.03	2.91 x10^{-7}
HfB2-20SiC-4	150	8.05	2.66 x10^{-7}

Steady-state creep rate as a function of the applied compressive stress for HfB_2-20% SiC at 1500°C in air is shown Figure 15, where the results obtained by DeGregoria [23] at 1500°C in argon are included for comparison. Note that the same test equipment and test method were used in this work and in the prior effort [23]. Furthermore, the HfB_2-20% SiC test material came the same batch, thus ensuring that material with the same grain size was tested in both efforts. Note that for the longer-term tests performed in air during this effort, the steady-state creep regime was achieved. Hence the minimum creep rate is the steady-state creep rate. However, because the steady-state creep regime was not always reached in tests of shorter duration performed in argon, only the minimum creep rate could be calculated. The minimum creep rate can be greater than or equal to the steady-state creep rate.

Notably, the minimum creep rates obtained in argon at compressive stresses of 50 and 75 MPa are higher than those obtained in air for the same compressive creep stresses. Recall that tests performed in argon at 50 and 75 MPa were terminated after 5.3 and 3 h, respectively. The steady-state creep regime was not reached in these tests. Hence only the minimum creep rate could be determined. Conversely the tests performed in air continued for 20 h at 50 MPa, and for 10 and 18 h at 75 MPa. In these tests, the steady-state creep regime was reached and the steady-state creep rate was determined. By definition of the creep regimes, the minimum creep rate is always greater than or equal to the steady-state creep rate. Hence the minimum creep rates obtained in argon are higher than the steady-state creep rates obtained in air. We believe that similar steady-state creep rates would be obtained in air and in argon if creep tests of longer duration were accomplished in argon.

Given the relatively limited data in argon, further testing in argon would be required to reach a definitive conclusion.
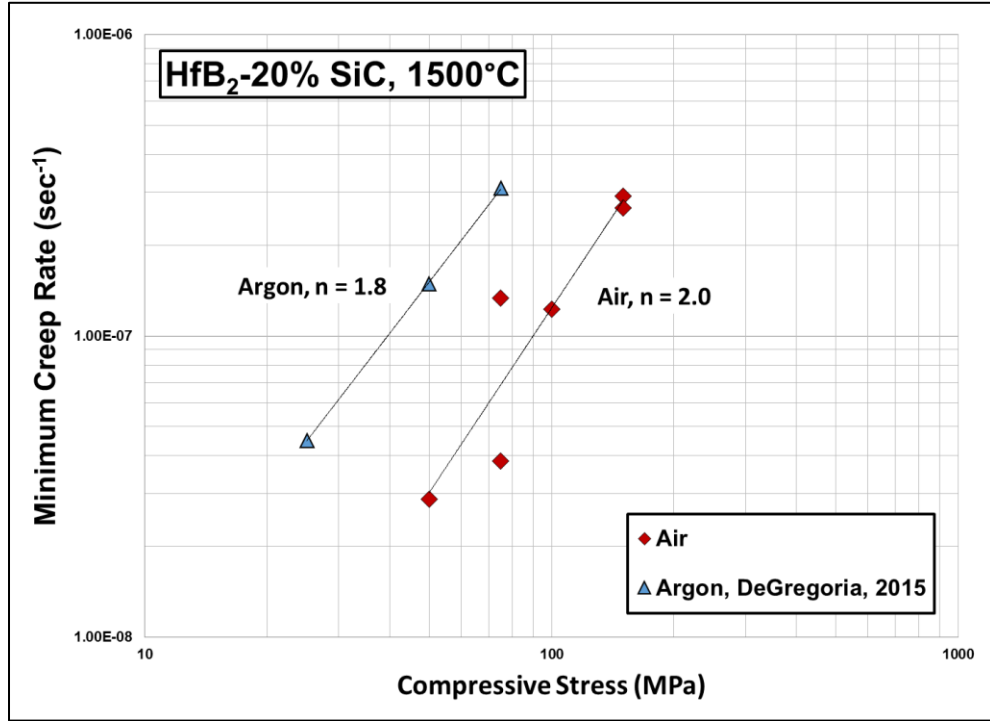
Figure 15. Minimum creep rate vs compressive stress for HfB_2- 20% SiC at 1500°C in air and in argon. Data in argon from DeGregoria [23].

As expected, the minimum creep rate increases with increasing compressive creep stress. Fitting the experimental results (obtained in either air or argon) in Figure 15 with a temperature-independent Norton-Bailey equation of the form:

$$\dot{\varepsilon} = A\sigma^n$$

yields the stress exponents, n = 2.0 in air and n = 1.8 in argon. Note that the stress exponents obtained in air are close to those obtained in argon.

Microstructural examination of the tested specimens presented in the following section reveals that the largest oxide scale thickness obtained in this work is approximately 100 μm. Assuming that an oxide scale has zero load-bearing capacity, the presence of a 100-μm thick oxide scale reduces the load-bearing cross-sectional area of the test specimen from 6.5 mm x 6.5 mm to 6.1 mm x 6.1 mm. A compressive load applied to produce the creep stress of 75 MPa at the start of the test will cause the stress to increase to ~85 MPa as the 100-μm thick oxide scale forms and the load-bearing cross-sectional area is reduced. A progressively increasing stress would result in increasing creep rates. Again, performing creep tests of longer duration at 1500°C in argon would provide greater insight into the effect of oxidation on creep rates.

3.2 Oxidation of HfB$_2$-20 % SiC Under Compressive Stress at 1500°C in Air

The post-test microstructure of all specimens tested in this work was examined using an optical microscope in order to elucidate the surface features. Optical micrographs are shown in Appendix A. Following optical microscopy, specimens were mounted, sectioned and polished for SEM and EDS analysis as described in chapter II. Twenty four SEM images were taken at regular intervals around the perimeter of each sectioned specimen in order to capture oxide scale thickness. Then an average oxide scale thickness was calculated for each specimen. Winder and DeGregoria noted that oxidation behavior was markedly different near the corners of tested HfB$_2$ specimens [22, 23]. Therefore, in this work, measurements were not taken within 1 mm of the corners to ensure that the anomalous scale growth near the edges did not affect the average oxide scale calculation. Figure 16 presents a typical SEM image used for measuring oxide scale thickness in this work.
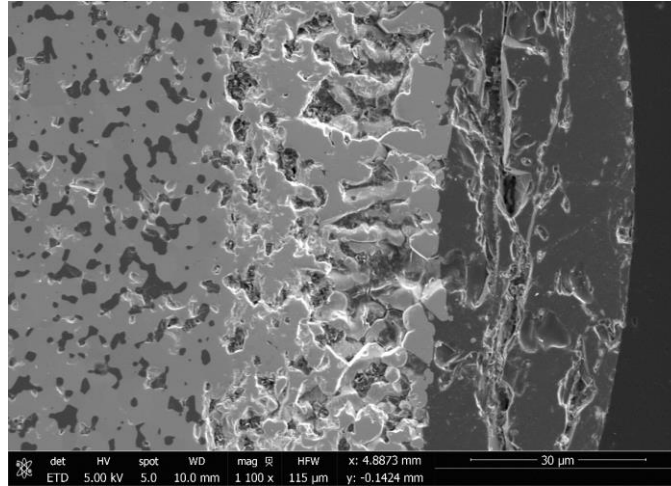
Figure 16. A typical SEM image used to measure the oxide scale thickness. Specimen HfB$_2$-20SiC-5, creep stress = 100 MPa, test duration = 10 h.

The SEM micrograph in Figure 16 shows three distinct regions: the HfB$_2$-20%SiC parent material on the left, a lighter grey, hafnium oxide layer in the middle, and a dark grey, borosilicate glassy region on the right. To ensure the direct comparison with the results from prior work, the oxide scale was measured using the methodology employed by Winder, DeGregoria and Bowen [22, 23, 13]. In this work, the oxide scale thickness measurement includes borosilicate glass, hafnium oxide, and SiC-depleted regions when present. For each specimen 190-260 scale thickness measurements were taken and an average value of the scale thickness was calculated. The average values of the oxide scale thicknesses values found in this work are summarized in Table 5. Note that creep test duration (time under sustained compressive load) provided in Table 5 does not include a 1-h soak at 1500°C prior to load up or a 1- to 2-h cool down period following test termination.

Table 5. Summary of Oxide Scale Thickness of HfB$_2$-20%SiC Specimens Tested in Compression Creep at 1500°C in Air

Specimen	Creep Stress (Mpa)	Creep Duration (h)	Average Oxide Scale Thickness (µm)	Standard Deviation	Number of Measurements	Min Thickness (µm)	Max Thickness (µm)
HfB2-20SiC-10	50	20	97	27.52	231	29.86	172.61
HfB2-20SiC-6	75	10	65.99	18.35	239	18.97	102.37
HfB2-20SiC-11	75	18	82.85	34.84	190	28.03	150.36
HfB2-20SiC-5	100	10	89.83	21.35	260	50.92	168.15
HfB2-20SiC-9	150	6.11	57.33	13.19	239	28.06	94.86
HfB2-20SiC-4	150	11.7	100.36	22.71	239	40.14	214.01

Figure 17 represents the results of an EDS line scan performed on the specimen HfB$_2$-20SiC-5 shown in Figure 16. Recall that specimen HfB$_2$-20SiC-5 was subjected to compressive stress of 100 MPa for 10 h at 1500°C in air. The EDS analysis confirms the elemental composition of the three different regions formed during the creep test.
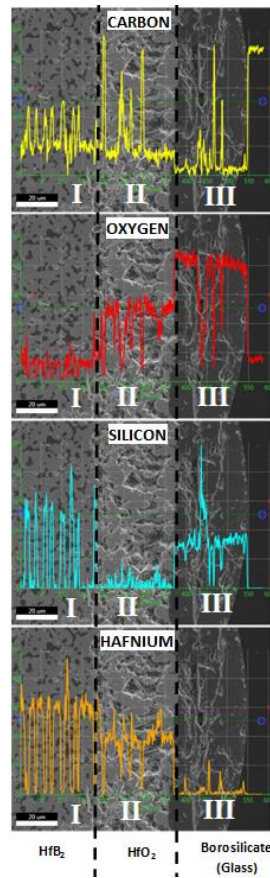
Figure 17. EDS line scan of specimen HfB$_2$-20SiC-5 (creep stress = 100 MPa, test duration = 10 h.)

The intensity of the peaks in Figure 17 reflects the presence of each element in the test specimen. Three distinct regions (I, II and III) can be readily identified in Figure 17: region I - HfB_2-SiC, region II - HfO_2 and B_2O_3-SiO_2 filling the voids, and region III - B_2O_3-SiO_2. It is recognized that boron is difficult to detect with EDS due to its light atomic weight, therefore the EDS analysis was limited to detecting the levels of the remaining elements: carbon, oxygen, silicon and hafnium. The EDS results indicate that region I contains primarily Hf, Si, and C with minimal levels of O, as expected. The composition of this region is consistent with that of an untested HfB_2-20%SiC specimen. Region II is comprised primarily of hafnium and oxygen, consistent with the expectations of HfO_2. Region II also shows depleted levels of silicon. Depletion of silicon in region II is consistent with the chemical reactions taking placed during oxidation of the HfB_2-20%SiC specimen per Parthasarathy et al (see Figure 3). Silicon is leached from the oxide layer to form the borosilicate glass on the surface of the specimen. Notably, region III contains elevated levels of silicon and carbon and virtually no hafnium, indicating that this region is comprised primarily of borosilicate glass (B_2O_3+SiO_2). Overall, the EDS analysis confirms that the material tested in this work exhibits the same oxidation behavior as that reported previously by Winder, DeGregoria and Bowen. Furthermore, the regions I, II, and III formed during oxidation under sustained compressive stress in this work agree with those postulated in the oxidation model by Parthasarathy et al [30].

The average oxide scale thickness calculated in this work was plotted vs. time in Figure 18, where the results obtained by DeGregoria [23] under zero load and under compressive stress of 50 MPa are included for comparison. The experimental results in

39

Figure 18 are also compared to the predictions of the oxidation model by Parthasarathy et al [30] for HfB_2-20% SiC. Note that the oxidation model does not account for the material being subjected to sustained stress.
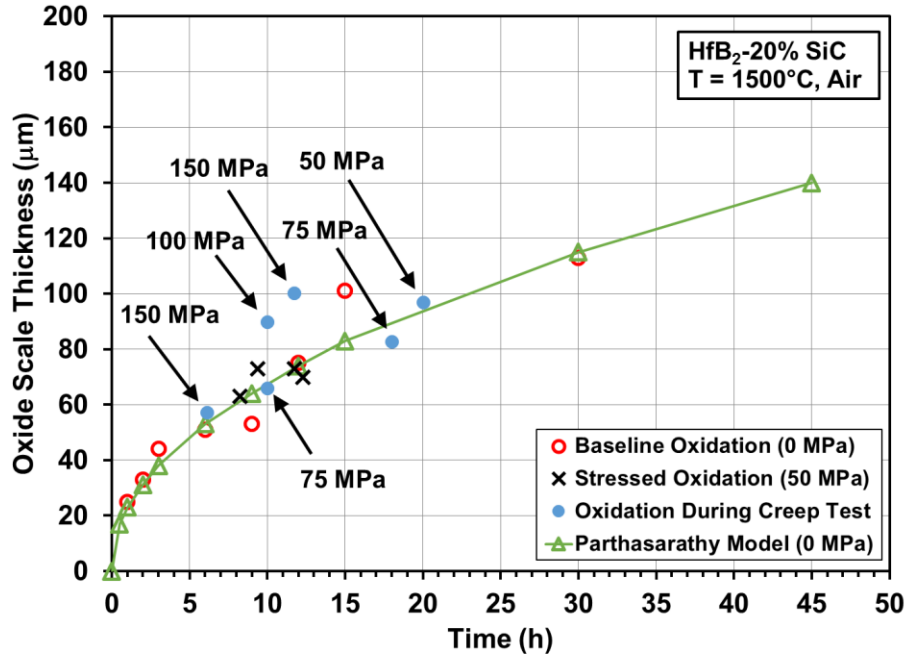
Figure 18. Average oxide scale thickness vs. time for HfB_2-20% SiC at 1500°C in air. Results at 0 MPa (baseline oxidation) and at 50 MPa (stressed oxidation) from DeGregoria [23]. Experimental results are compared with predictions of the oxidation model by Parthasarathy et al [30].

The results of baseline oxidation tests and stressed oxidation tests reported by DeGregoria agree well with the predictions of the Parthasarathy oxidation model. The results of current work compare reasonably well with those obtained by DeGregoria. Note that two data points (corresponding to 100 MPa and 150 MPa) somewhat exceed the predictions of the oxidation model. However, the discrepancy is likely due to data scatter. Furthermore, note that these two data points lie within 3 standard deviations of the baseline oxidation results reported by DeGregoria.

The results in Figure 18 suggest that sustained compressive stress (50-150 MPa) does not significantly affect the oxidation rate of HfB_2-20% SiC at 1500°C in air. The same conclusion was reached by DeGregoria [23]. It appears that there is no interaction between creep and oxidation processes for the stresses and durations tested.

3.2.1 Analysis of Surface Deposits

During post-test examination under optical microscope, interesting scale formations were observed on the surface of several specimen. The following features were noted: (i) apparent bubble bursts, (ii) white, scaly deposits where the sapphire extensometer rods or the sapphire spacers were in contact with the specimen, and (iii) slight brown discoloration. Similar features were observed and reported by Winder [22], DeGregoris [23], and Bowen [13]. In addition, three visually dissimilar scales formed on the surface of three of the test specimen. Figure 19 shows the three different types of scale formed on the surface of specimen HfB_2-20SiC-9.
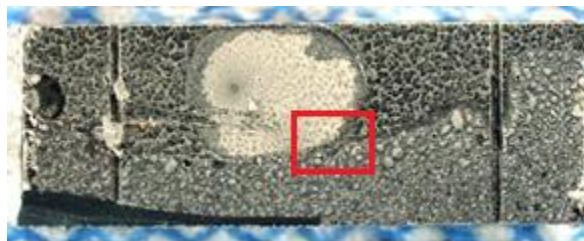
Figure 19: Post-test optical micrograph of HfB_2-20SiC-9 specimen showing three different types of scale formation: (i) a large white spot, apparently formed after a borosilicate bubble burst while at elevated temperature,(ii) a darker scale covering the upper region and (iii) a lighter scale covering the majority of the surface. The red square indicates the region selected for SEM and EDS analysis.

While it's unknown why different types of scale formed on the surface of the specimen, EDS and XRD analysis provided insight into the elemental makeup and crystallographic structure of each scale type. The region enclosed by red square in Figure

19 includes the three types of scale formed on the surface of the specimen HfB$_2$-20SiC-9.

This region was selected for the SEM examination (see Figure 20) and the EDS analysis.

Figure 21 shows higher magnification images of each type of scale formation.
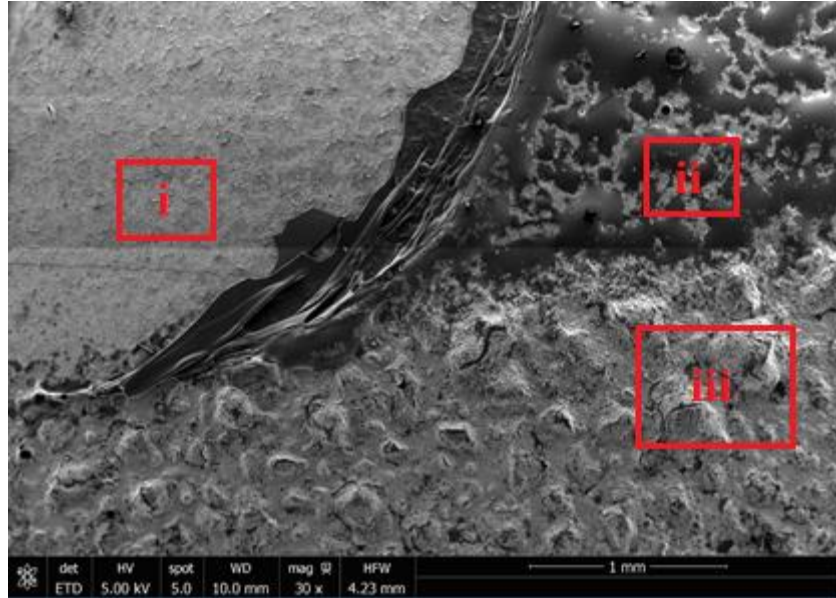
Figure 20. An SEM micrograph of specimen HfB$_2$-20SiC-9 showing 3 different types of scale formation: (i) a large white spot from Figure 19 assumed to have formed after a borosilicate bubble burst, (ii) a darker tinted scale covering the upper region of the specimen surface from Figure 19, and (iii) a lighter tinted scale covering the majority of the specimen surface from Figure 19.

(i)
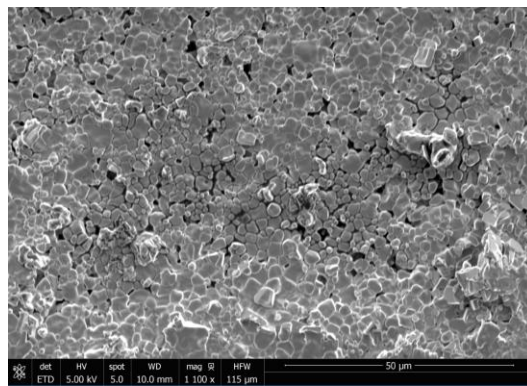
<center>(ii)   (iii)</center>
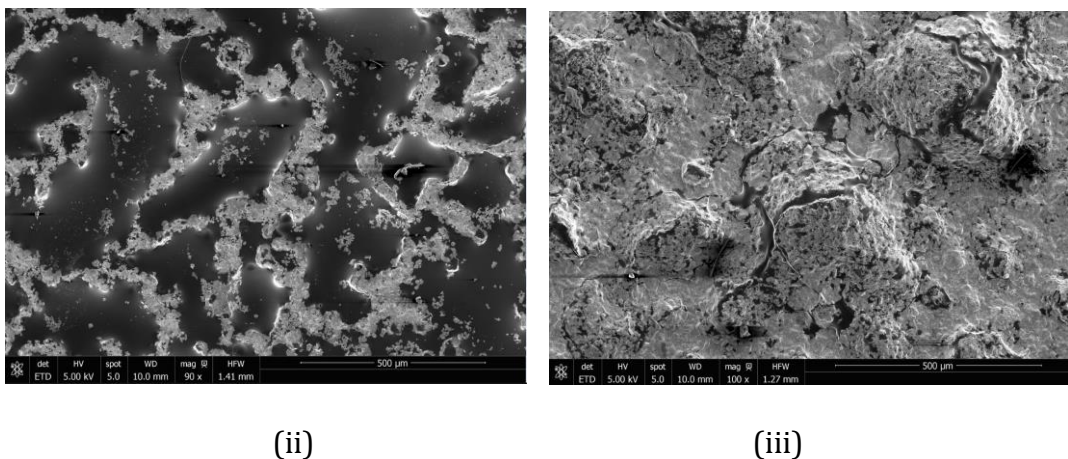
Figure 21. Higher magnification images of the three areas outlined in red in Figure 20: (i) Area 1, part of the large white spot from Figure 19 assumed to have formed after a borosilicate glass bubble burst, (ii) Area 2, a darker tinted scale covering the upper region of the specimen surface in Figure 19, and (iii) Area 3, a lighter tinted scale covering the majority of the specimen surface in Figure 19.

The EDS spot analysis was performed on Areas 1-3 shown in Figures 20 and 21 to determine the elemental composition of each type of scale. Results obtained for Area 1 are shown in Figure 22. Figure 21(i) shows overall microstructure of Area 1. We note a well ordered, crystalline structure containing multiple, small voids. Visibly missing in this region is the expected amorphous borosilicate glass which, at 1500°C, typically acts as a liquid flowing across the surface, filling in cracks and voids. As seen in Figure 22, the EDS analysis of this region detected significant amounts of hafnium and oxygen only, indicating the presence of HfO_2. Interestingly, silicon is missing entirely from this region, which likely contributes to the lack of borosilicate glass on the surface. Considering Area 1 appears to be located within the remains of a bubble-burst region, it's possible that the liquid glass was dispelled from this region after a bubble burst, redepositing the glass around the perimeter of the region. It's assumed that bubbles are formed under the liquid glass as gasses, through a series of chemical reactions described by Parthasarathy [30],

<center>43</center>

then escape from the oxide scale and find their way to the surface. Once a sufficient

amount of gas has coalesced under the glassy layer, a bubble forms and eventually bursts,

exposing a small area of the oxide layer to the environment.
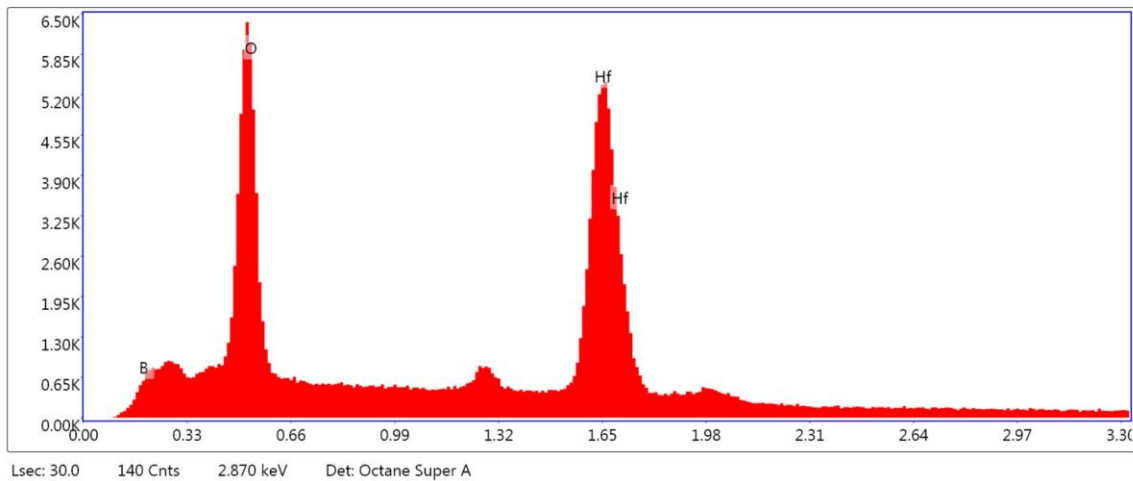
Figure 22. Area 1 EDS analysis indicating that hafnium and oxygen are the most prominent elements present in this region. Note that silicon was not detected in this region.

EDS analysis for Area 2 is shown in Figure 23.
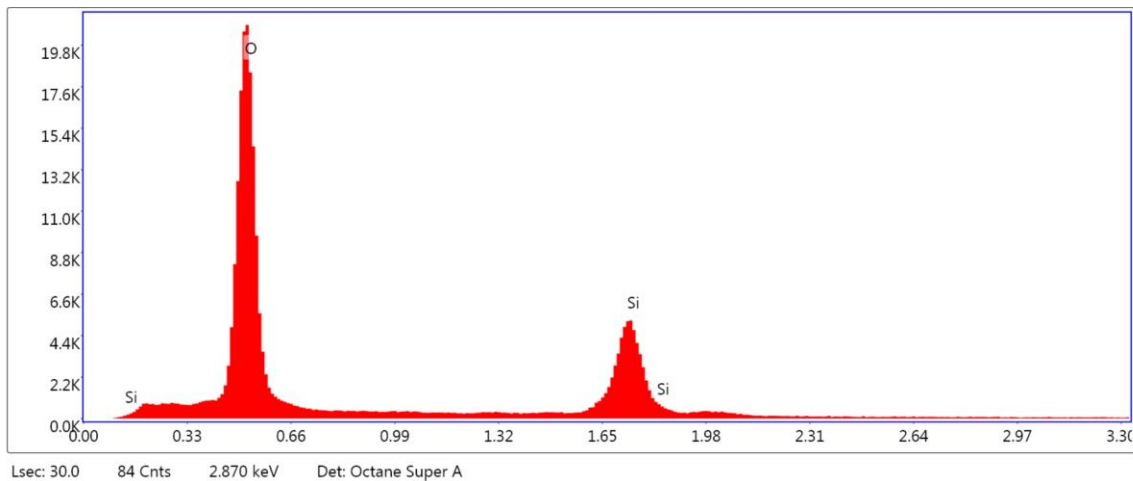
Figure 23. Area 2. EDS analysis indicating that silicon and oxygen are the most prominent elements present in this region. Note hafnium was not detected in this region.

Figure 21(ii) shows overall microstructure of Area 2. We observe a predominantly dark tinted, amorphous region interlaced with thin bands of lighter tinted, crystalline material. As expected, the EDS analysis in Figure 23 shows the presence of silicon and oxygen. Given that the EDS equipment used in this work was unable to detect boron, it is most likely that the visibly amorphous material is borosilicate glass ($B_2O_3+SiO_2$). It's unknown whether the thin bands of crystalline material shown in Figure 21(ii) are comprised of SiC or if the EDS detector wasn't able to resolve the presence of hafnium. Based on the examination and the EDS analysis we conclude that the surface of Area 2 is dominated by an amorphous silicate glass.

The EDS analysis for Area 3 is shown in Figure 24.
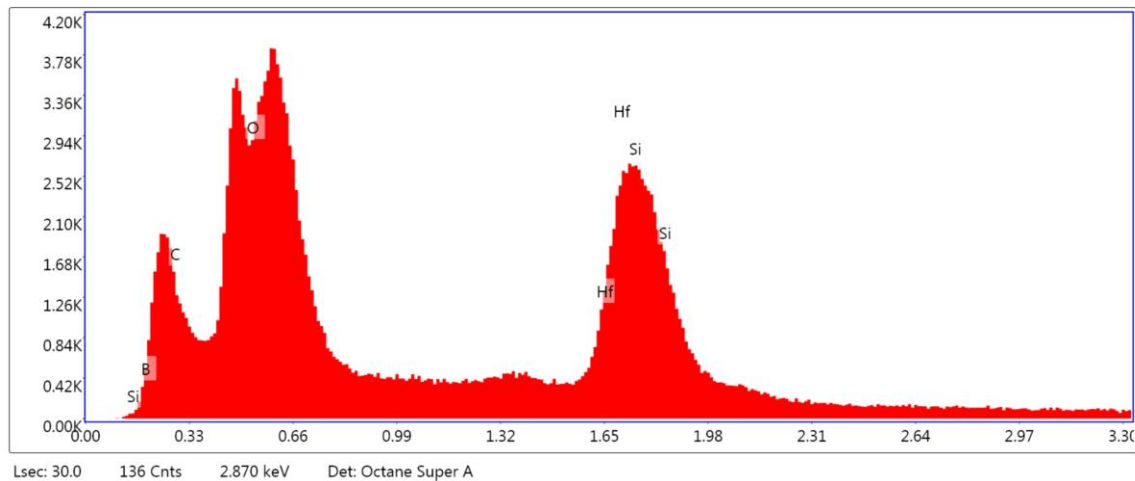
Figure 24: Area 3 EDS analysis indicating the presence of silicon, hafnia and oxygen in this region.

Figure 21(iii) shows overall microstructure of Area 3. We note a lighter tinted crystalline material covering the majority of the surface with a darker tinted, amorphous material filling in cracks and voids. The EDS analysis summarized in Figure 24 indicates the presence of silicon, carbon, hafnium and oxygen. It is most likely that the white

crystalline phase is comprised of hafnia (HfO_2) while the dark, amorphous material is comprised of borosilicate glass ($B_2O_3 + SiO_2$).

The EDS analysis (Figures 22-24) confirmed the presence of Si, C, Hf, and O on the specimen surface and dispelled any theories that additional elements contributed in the formation of these three different types of scales. Area 1 was comprised primarily of pure hafnia. The darker scale in Area 2 was comprised primarily of borosilicate glass. The lighter colored scale in Area 3 was comprised primarily of hafnia with borosilicate glass filling in cracks and voids. Additional EDS analysis was performed on specimen HfB_2-20SiC-6 and results were virtually identical to the results presented above. The EDS analysis of specimen HfB_2-20SiC-6 is summarized in Appendix D. The XRD analysis was also performed to characterize the crystalline structures of the different types of scales formed on the surface of specimens HfB_2-20SiC-6 and HfB_2-20SiC-9. The results of the XRD analysis are presented in Appendix C.

3.3 Effect of Compressive Stress on Preferred Grain Orientation of HfB_2-20% SiC at 1500°C

A secondary objective of this work was to assess whether sustained compressive stress had an effect on preferred grain orientation of the test specimen. The as-processed material had equiaxed grains distributed in a random orientation. The material was processed at AFRL/RX and was delivered to AFIT in the form of a puck. Test specimen were cut from the puck using EDM. DeGregoria found that as long as the test specimens are cut from the center portion of the puck, grain size and orientation remain consistent, and unaffected by bulk diffusion or deformation induced near the edges of the pucks. Because the virgin test specimens had a randomly distributed grain orientation, the XRD

analysis of a specimen subjected to sustained compressive stress can reveal whether a preferred grain orientation was induced during compression creep test. Recent findings reported in literature indicate that the prevalent creep mechanism occurring in HfB_2-SiC under uniaxial loading is grain boundary sliding. The specimens tested in this work produced compressive creep strains reaching 1.2%. If this strain was a result of grain boundary sliding and not bulk diffusion, the XRD analysis should show that no preferred orientation was induced through compression creep testing.

XRD analysis is able to determine whether a preferred orientation exists within a sample by comparing relative peak height or area obtained from a 2Ө scan with the expected relative intensity from a standard of the same material with no preferred orientation. The open source XRD analysis software is then used to perform additional analysis to determine the direction of preferred orientation and to generate a unit-less variable known as multiples of random distribution (MRD) which indicates the relative amount of preferred grain orientation within the sample. The MRD scale ranges from 1 to infinity. An MRD value of 1 indicates that the ratio of peak intensities measured within the sample align perfectly with the known standard of a randomly distributed grain orientation. Conversely, an MRD score of infinity represents a perfectly oriented crystal structure or single crystal. In order to determine whether constant compressive loading induced a preferred grain orientation, both an untested specimen (HfB_2-20SiC-15) and a tested specimen (HfB_2-20SiC-9) were subject to XRD analysis. Specimen HfB_2-20SiC-15 was manufactured in the same lot as all the other tested specimens in this work and should provide consistent results to any other untested HfB_2-20%SiC specimen. Specimen HfB_2-20SiC-9 was chosen to represent the tested specimens because it was

exposed to the highest compressive load and produced significant strain during testing.

Recall specimen HfB_2-20SiC-9 was subject to 150 MPa for a duration of 6.03 hours and

experienced approximately 1% strain prior to test termination. If any of the tested

specimens in this work had a preferred orientation induced by sustained loading, analysis

of specimen HfB_2-20SiC-9 should provide an indication. Table 6 provides the MRD

values calculated for both the untested and tested specimens. XRD analysis was

performed on 3 separate, mutually orthogonal sides of each specimen to ensure

completeness. The subscripts in the MRD_{xxx} labels within Table 6 indicate miller indices,

the crystallographic planes the measured preferred orientation is aligned with. For

example, side 1 of the untested specimen has an MRD value of 1.13, oriented with the

110 plane. Appendix C shows the pole diagrams generated to ascertain the MRD values

and miller indices.

Table 6. MRD values for an untested specimen and a tested specimen of HfB_2-20%SiC.
The tested specimen was subject to a sustained compressive stress of 150 MPa for 6.03 h
in air at 1500°C

	Untested Specimen HfB_2-20SiC-15	Tested Specimen HfB_2-20SiC-9
Side 1	MRD_{110} 1.13	MRD_{110} 1.14
Side 2	MRD_{002} 1.12	MRD_{002} 1.16
Side 3	MRD_{200} 1.14	MRD_{110} 1.15

The MRD values calculated for the untested specimen indicate there was a slight

orientation induced from the manufacturing process. While the MRD values for the tested

specimen are slightly higher than the values for the untested specimen, the small disparity

indicates that no significant preferred orientation was caused by sustained compressive

loading. The small differences in MRD values may simply be a result of variance in the

48

manufacturing process. These results cannot conclusively prove that the controlling creep mechanism during compressive testing was grain boundary sliding. However, it can be said with confidence that sustained compressive loading of HfB$_2$-20% SiC at 1500°C in does not significantly alter the preferred grain orientation for compressive stresses up to 150 MPa.

IV. CONCLUSIONS

The series of creep tests performed in this work were of significant importance due to higher compressive stresses and longer test durations compared to those achieved in prior work. Determination of the steady-state creep rate is critical to identifying creep mechanisms operating in the material. To determine the steady-state creep rate, the duration of creep test must be sufficiently long to ensure that the steady-state (or secondary) creep regime has been reached. When a creep test is terminated early it may not be clear whether the steady-state creep regime has been achieved. In that case only the minimum creep rate can be determined, which is by definition greater than or equal to the steady-state creep rate. Performing creep tests at higher compressive stresses broadens the range of applied stresses for which the steady-state creep rate is determined and thereby provides better insight into the controlling creep mechanisms. Additionally, the sought-after steady-state creep regime is typically reached sooner in tests performed with higher applied stress levels.

Creep strain vs. time curves obtained in this work compare favorably with those generated in previous work by DeGregoria [23] and Winder [22] for HfB_2-20% SiC specimens. Due to longer duration of the tests performed in this work, it was possible to determine the steady-state creep rates rather than the minimum creep rates as was frequently the case in prior efforts. Notably, the steady-state creep rates determined in this work were lower than minimum creep rates found in prior work. Yet the steady-state creep rates obtained for HfB_2-20%SiC at 1500°C in air in this effort were comparable to the minimum creep rates obtained by DeGregoria in short-duration tests performed at 1500°C in argon. The difference between the two sets of creep rates was negligible,

suggesting that the presence of an oxidizing environment does not have a significant effect on creep of HfB_2-20% SiC at 1500°C. Further testing at higher creep stresses and for longer durations in both air and argon is recommended in order to gain more confidence regarding the effect of an oxidizing environment on creep of HfB_2-SiC UHTCs.

Average oxide scale thickness values measured in this work are consistent with those obtained by DeGregoria [23] during baseline (zero load) oxidation tests and in 50 MPa compressive creep tests. In addition, the oxide scale growth in HfB_2-20% SiC was characterized in terms of the Parathasarathy oxidation model. The model was employed to predict the evolution of the oxide scale with time at 1500°C in air. The Parathasarathy oxidation model does not account for the presence of the sustained compressive load. Yet the model predictions compared well with the experimental results produced in this work. Hence we conclude that the presence of the sustained compressive load does not have a significant effect on the oxidation of HfB_2-20% SiC. Baseline oxidation tests at zero load of HfB_2-10% and HfB_2-30% SiC compositions are recommended. Further creep testing at higher stresses and for longer durations (exceeding 10 hours) of HfB_2-10%, HfB_2-20%, and HfB_2-30% SiC compositions at 1500°C in air are also recommended. The results of such tests would provide important insight into the possible interaction between creep and oxidation processed for the HfB_2-SiC UHTCs.

EDS and XRD analysis of oxide scale of dissimilar appearance confirmed that silicon, oxygen, hafnium, carbon and boron were responsible for the formation of all scales. The different appearance of surface scales is attributed to different amounts of amorphous borosilicate glass.

51

Lastly, XRD analysis of a tested specimen and an untested specimen provided insight into whether sustained compressive loading induces a preferred grain orientation. Analysis showed that a specimen subjected to compressive stress of 150 MPa for 6.03 h did not exhibit a significant change in preferred grain orientation compared to an untested specimen. Future efforts may consider examining the same specimen prior to and after creep testing for more consistent results. Additionally, higher compressive loads and longer durations would provide more conclusive results regarding whether a preferred orientation is induced under sustained compressive stress.

Optical Micrographs
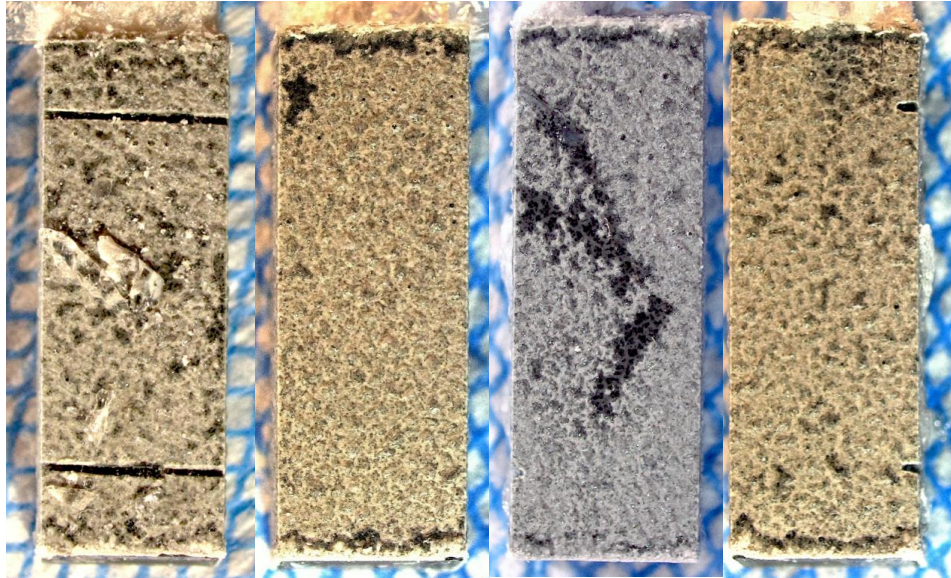
Figure 25. Post-test optical micrographs of specimen HfB$_2$-20%SiC-4 subject to 150 MPa for 8.05 hours. Test was terminated for spacer and YAG rod failure. Note presence of crystalline sapphire from spacers fused to the top and face of the specimen.
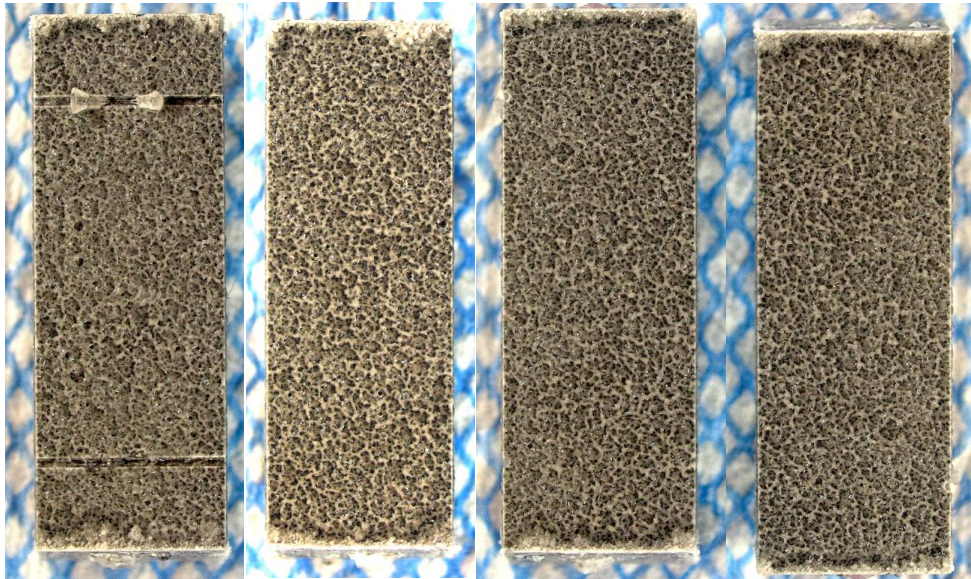
Figure 26. Post-test optical micrographs of specimen HfB$_2$-20%SiC-5 subject to 100 MPa for 10 hours. Test ran to planned duration with no complications. Note presence of crystalline sapphire from extensometer rods fused into the grooves cut into the face of the specimen.
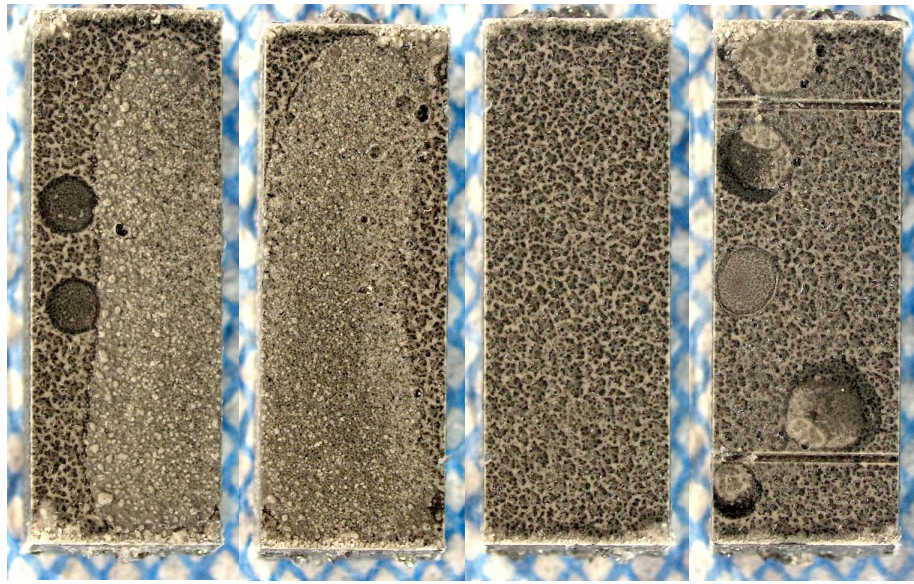
Figure 27. Post-test optical micrographs of specimen HfB$_2$-20%SiC-6 subject to 75 MPa for 10 hours. Test ran to planned duration with no complications. Note presence of apparent bubble burst formations. It is unknown why some specimens exhibit these bubble bursts and others do not. Also not the presence of the two visually dissimilar oxide scale formed on two of the sides of this specimen.
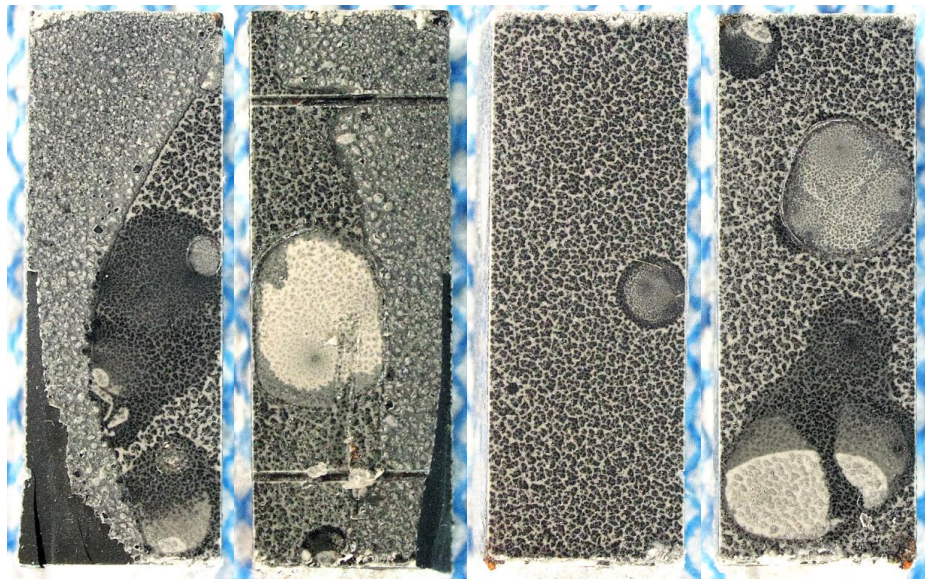
Figure 28. Post-test optical micrographs of specimen HfB$_2$-20%SiC-9 subject to 150 MPa for 6.03 hours. Test was terminated due to spacer failure. Note that the material was cracked at one corner. It is assumed that the spacer failure resulted in this damage. Also note the presence of bubble burst formations and dissimilar oxide scales.
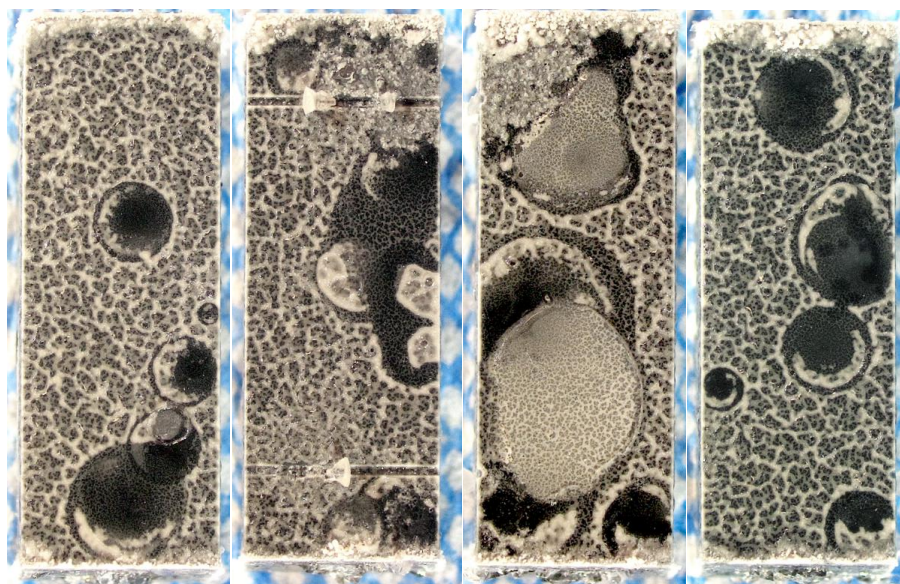
Figure 29. Post-test optical micrographs of specimen HfB$_2$-20%SiC-10 subject to 50 MPa for 20 hours. Test ran to planned duration with no complications. Note the presence of crystalline sapphire remnants from the sapphire extensometer rods in the grooves cut into the face of the specimen. Also not presence of bubble burst formations.
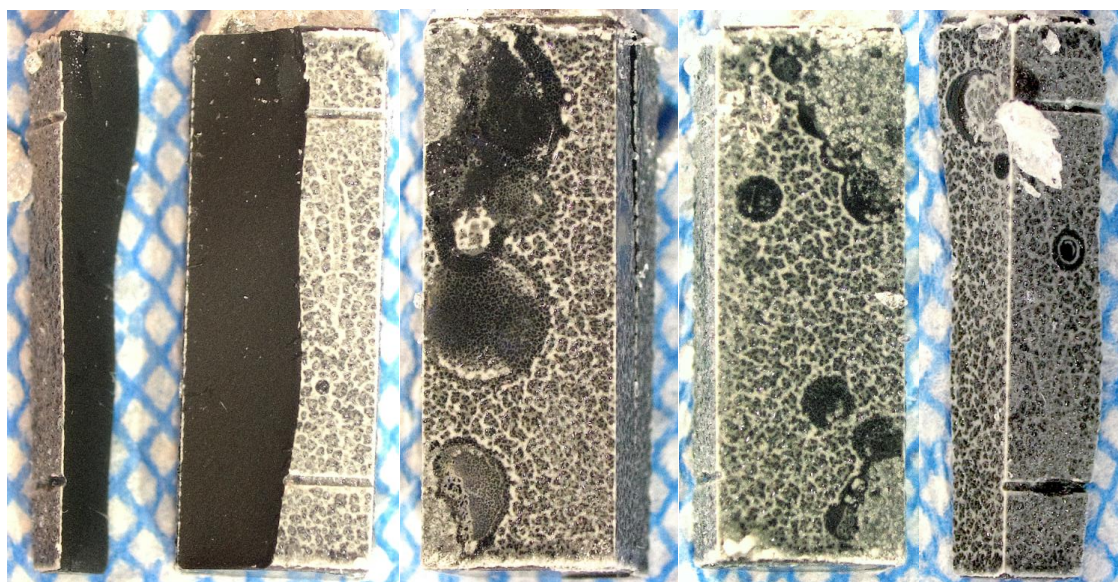
Figure 30. Post-test optical micrographs of specimen HfB$_2$-20%SiC-11 subject to 75 MPa for 18 hours. Test was terminated due to spacer and YAG rod failure. The specimen was sheared down the middle. It is assumed that this was caused by catastrophic failure of the sapphire spacer and YAG rod. Creep data shows sudden failure, not tertiary creep.
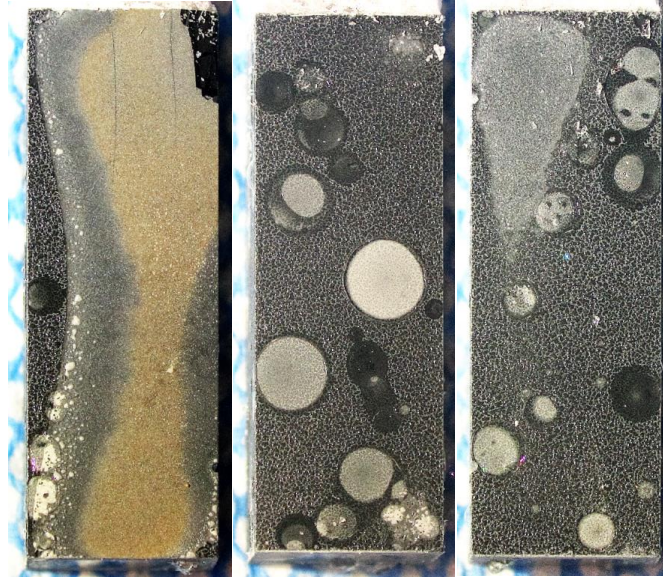
Figure 31. Post-test optical micrographs of specimen HfB$_2$-20%SiC-12 subject to 200 MPa for 0 hours. Test failed during loadup prior to reaching 200 MPa. The oxide scale that has developed to this point is due to the 1 hour temperature soak prior to load up and the 1-2 hour cool down period. EDS confirms that the noticeable brownish hue is due to the presence of alumina. After failure, the specimen was displaced from its normal position within the load train and came to rest on its face on the bottom of the alumina furnace. The face in contact with the alumina surface developed this brown scale. It's believed that the grey smudge present in the third photo is due to amorphous glass bumping against something in the furnace as the specimen came dislodged from its standard position. Note the specimen is cracked in several places. It's believed this was caused by spacer or YAG rod failure.
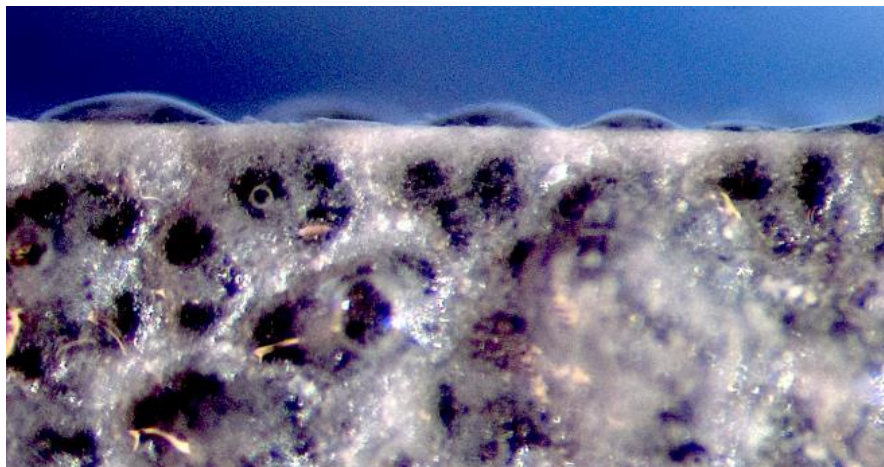
Figure 32. Post-test optical micrographs of specimen HfB$_2$-20%SiC-5 subject to 100 MPa for 10 hours. Notice the uneven, glassy scallops that develop across the surface of the specimen. Light colored oxide scale is visible beneath the glossy, glass surface.
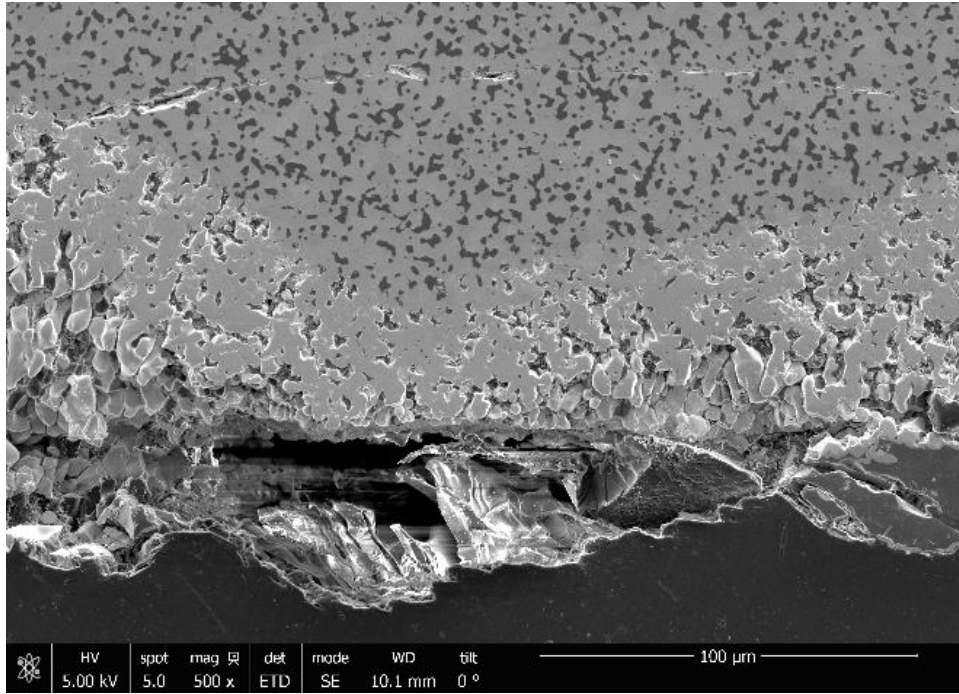
Figure 33. SEM Micrograph of HfB$_2$-20%SiC-4 oxide scale. Test ran at 150 MPa for 8.05 hours at 1500°C in air.
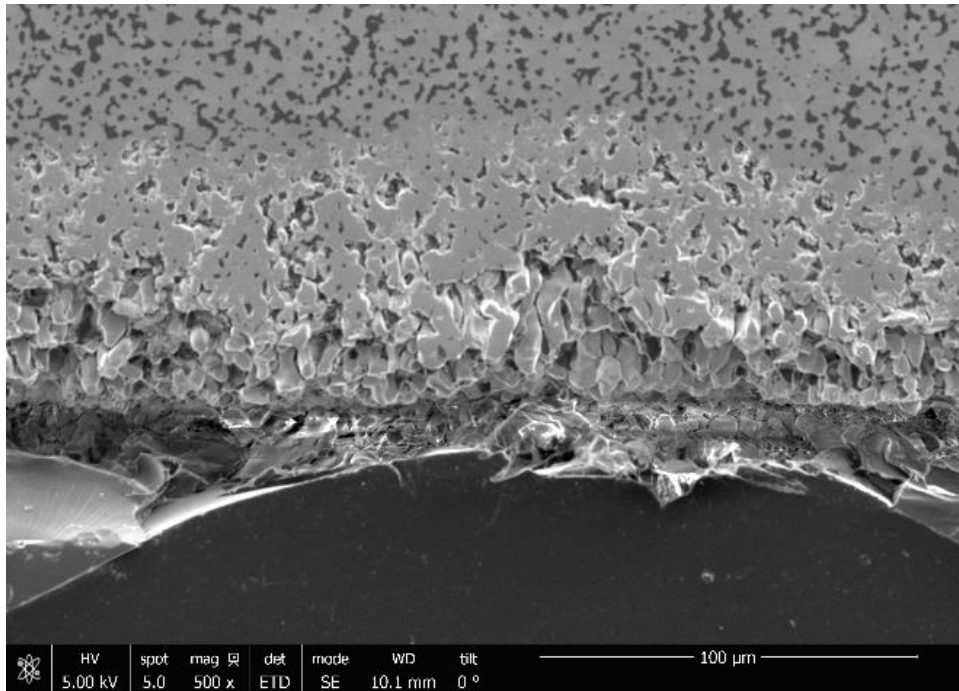
Figure 34. SEM Micrograph of HfB$_2$-20%SiC-4 oxide scale. Test ran at 150 MPa for 8.05 hours at 1500°C in air.
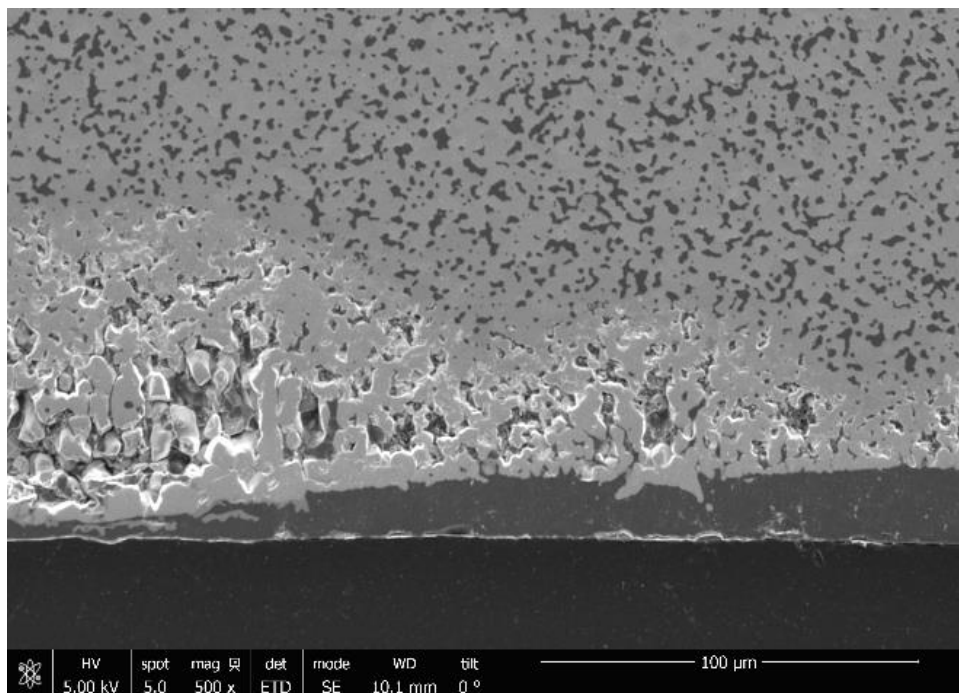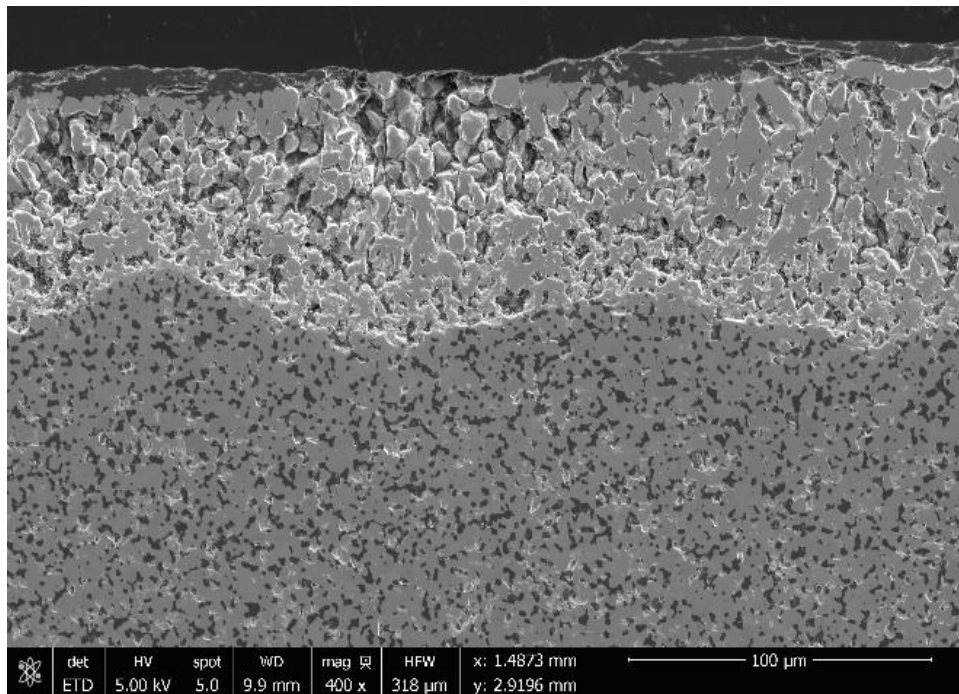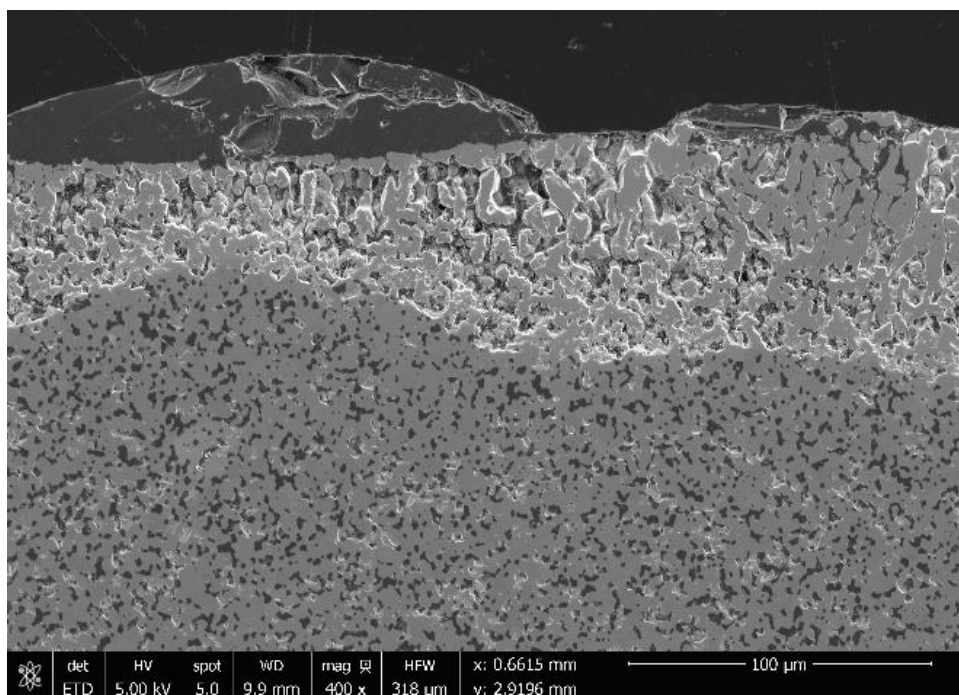
Figure 35. SEM Micrograph of HfB$_2$-20%SiC-4 oxide scale. Test ran at 150 MPa for 8.05 hours at 1500°C in air.
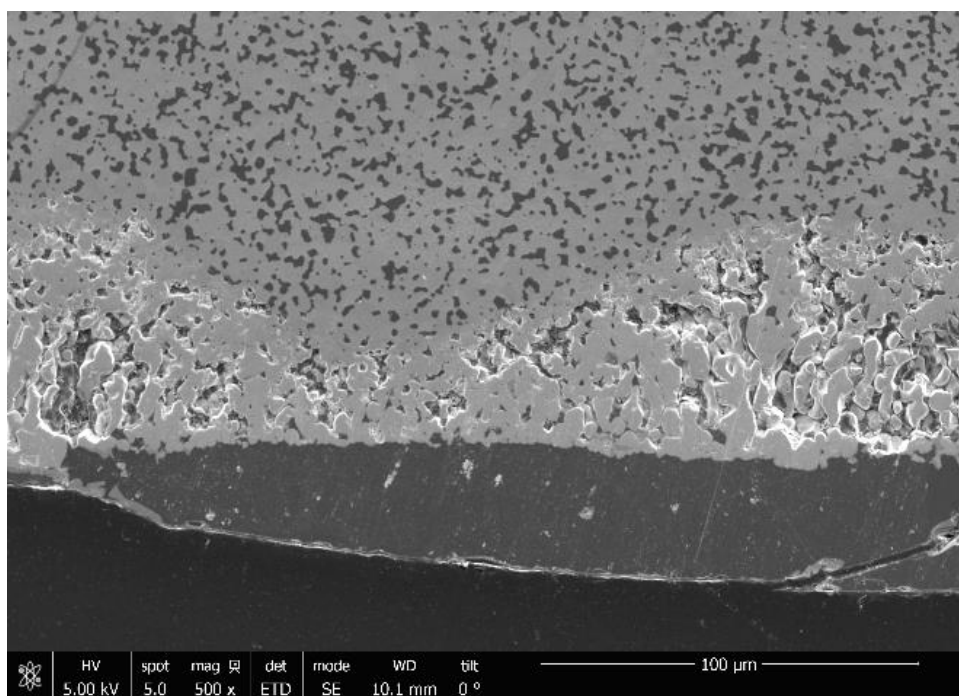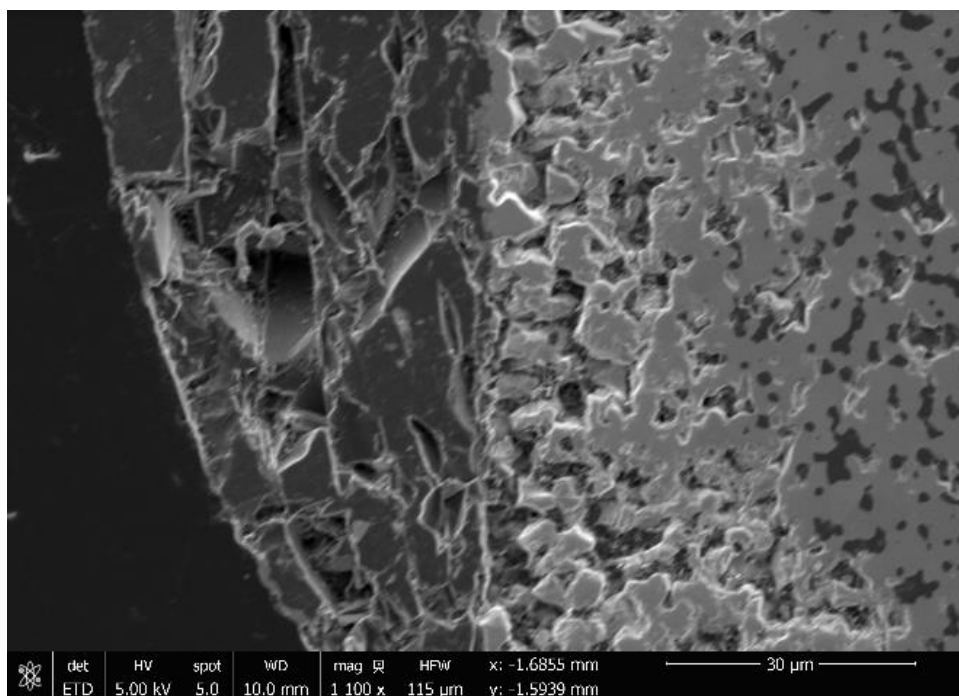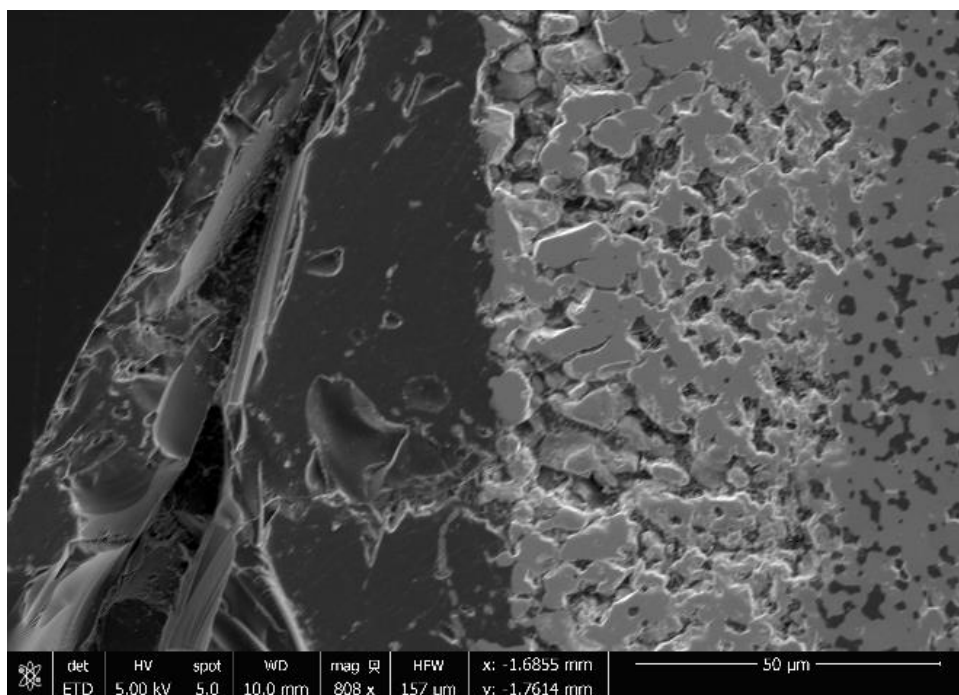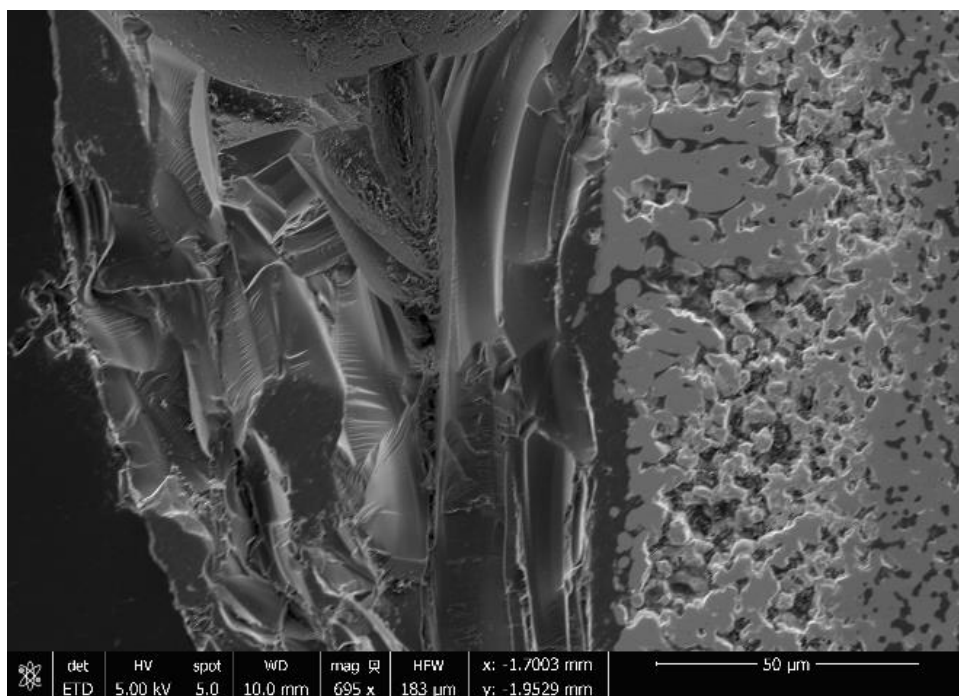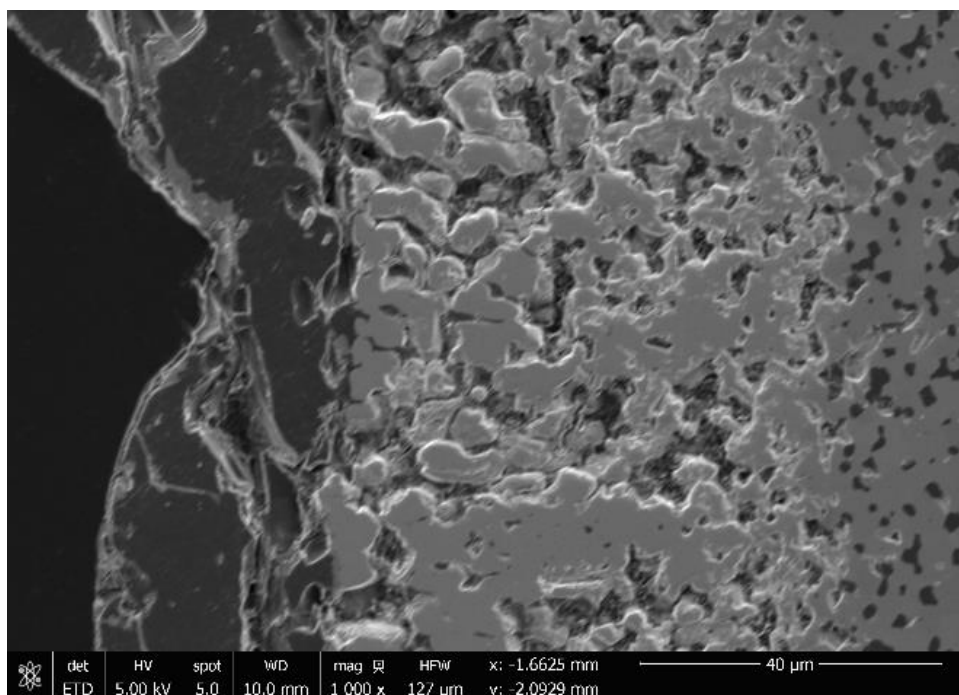

Figure 36. SEM Micrograph of HfB$_2$-20%SiC-4 oxide scale. Test ran at 150 MPa for 8.05 hours at 1500°C in air.
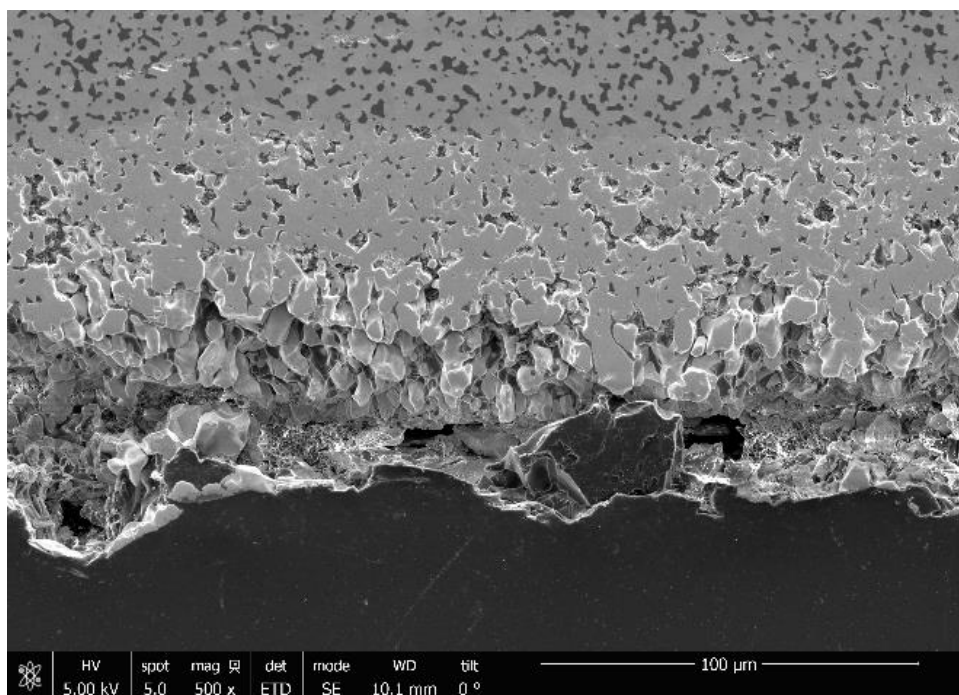
Figure 37. SEM Micrograph of HfB$_2$-20%SiC-4 oxide scale. Test ran at 150 MPa for 8.05 hours at 1500°C in air.
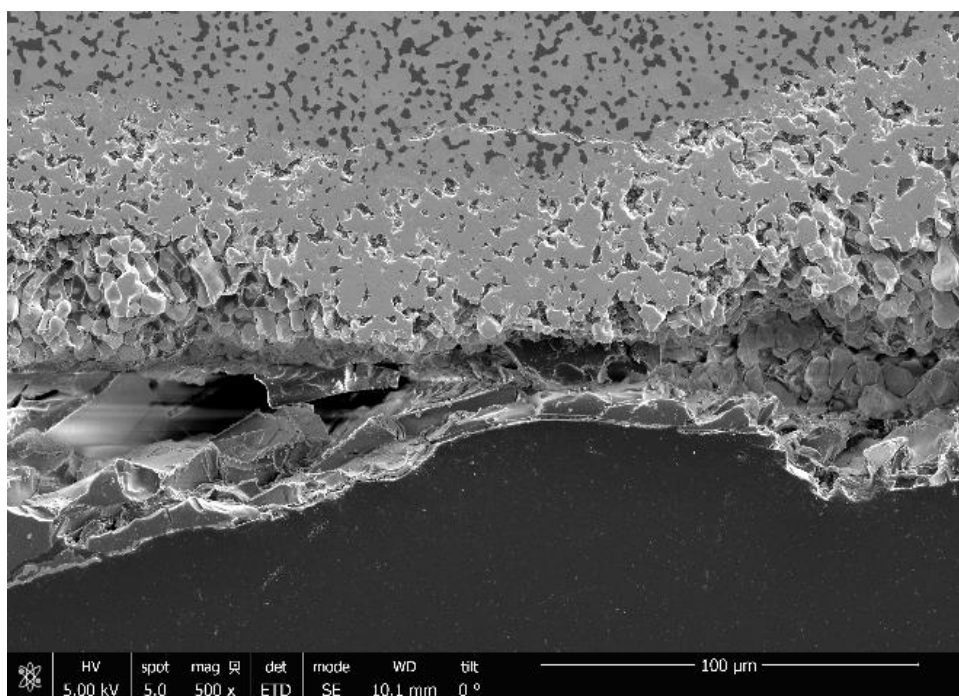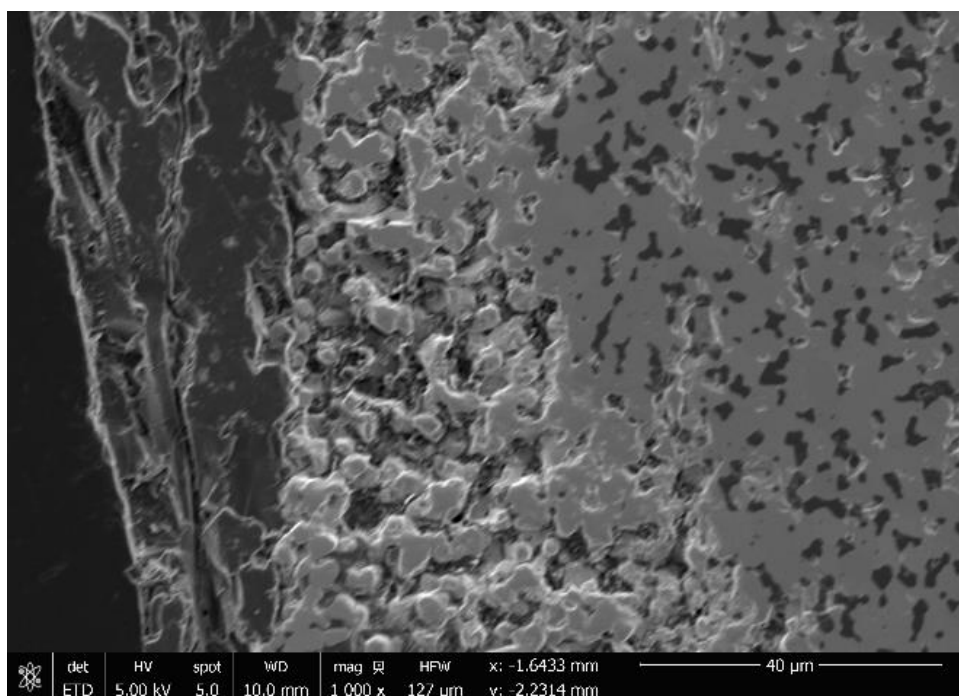

Figure 38. SEM Micrograph of HfB$_2$-20%SiC-4 oxide scale. Test ran at 150 MPa for 8.05 hours at 1500°C in air.
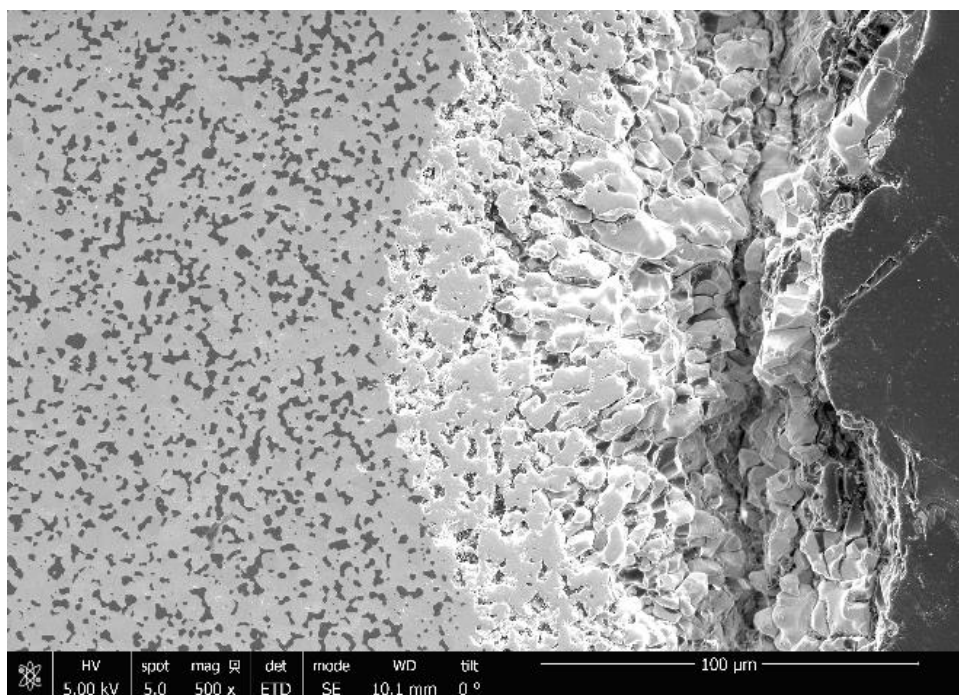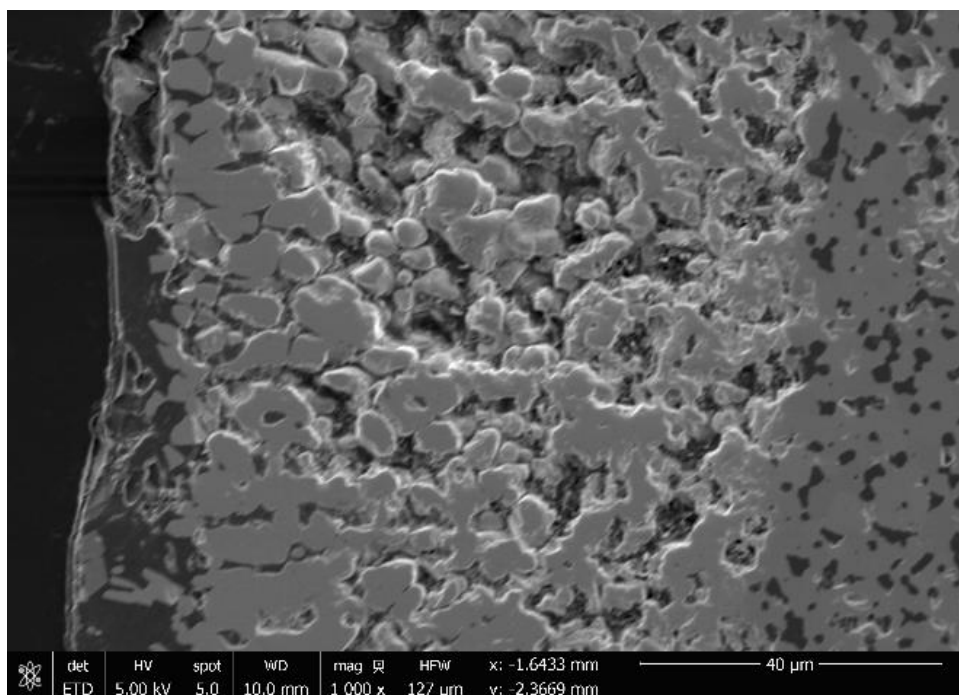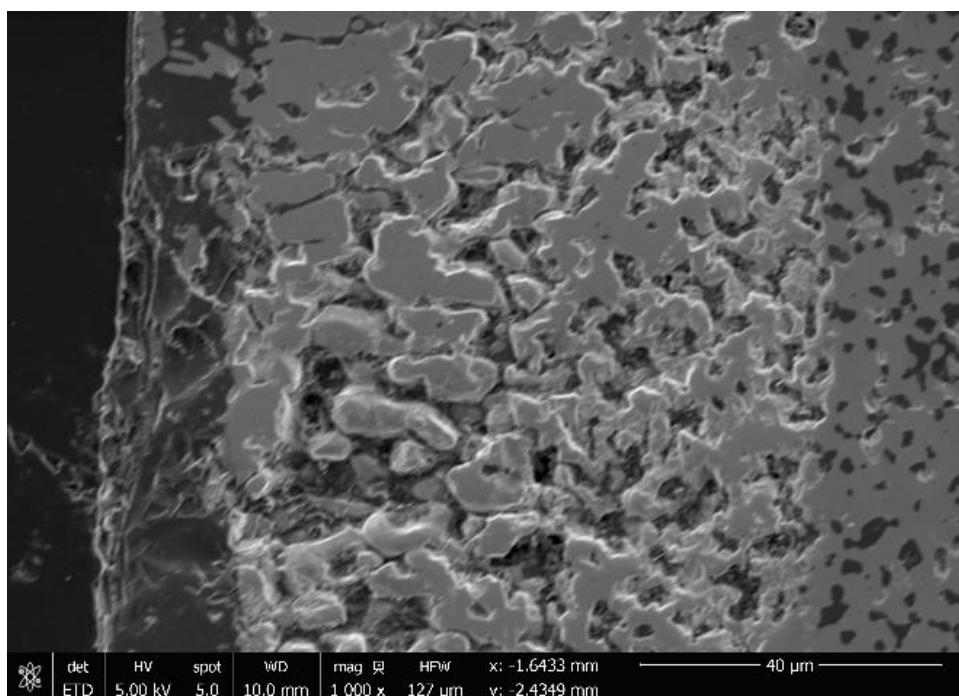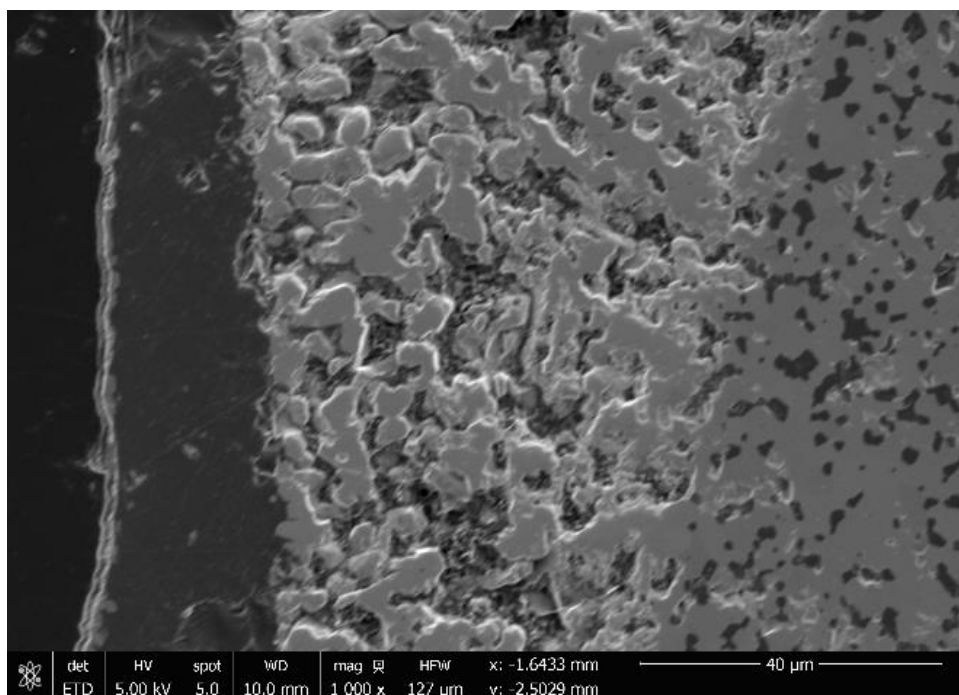
Figure 39. SEM Micrograph of HfB$_2$-20%SiC-4 oxide scale. Test ran at 150 MPa for 8.05 hours at 1500°C in air.
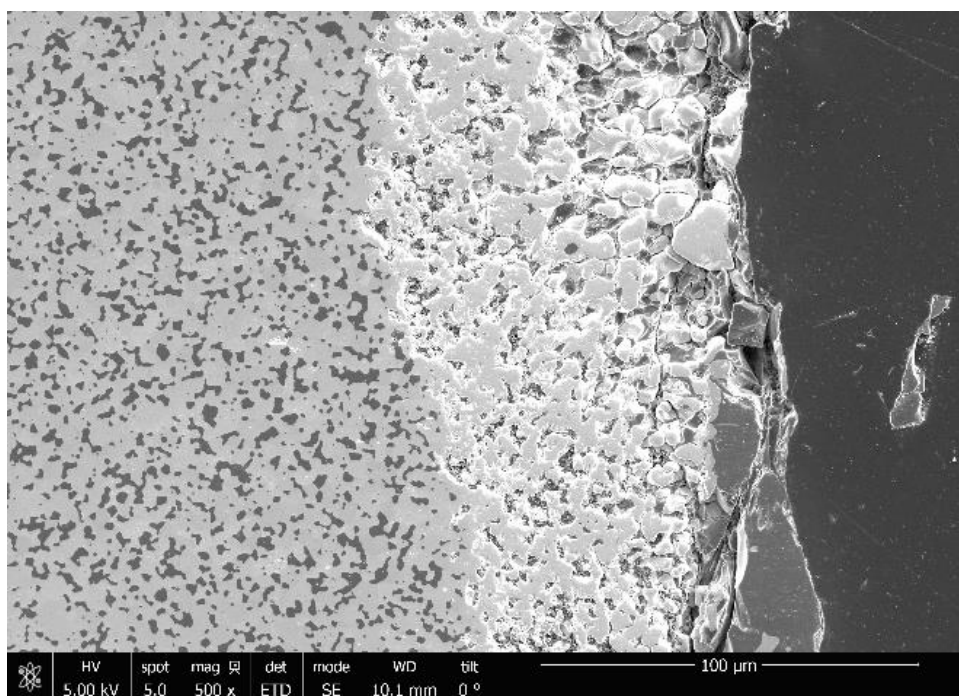
Figure 40. SEM Micrograph of HfB$_2$-20%SiC-4 oxide scale. Test ran at 150 MPa for 8.05 hours at 1500°C in air.

60
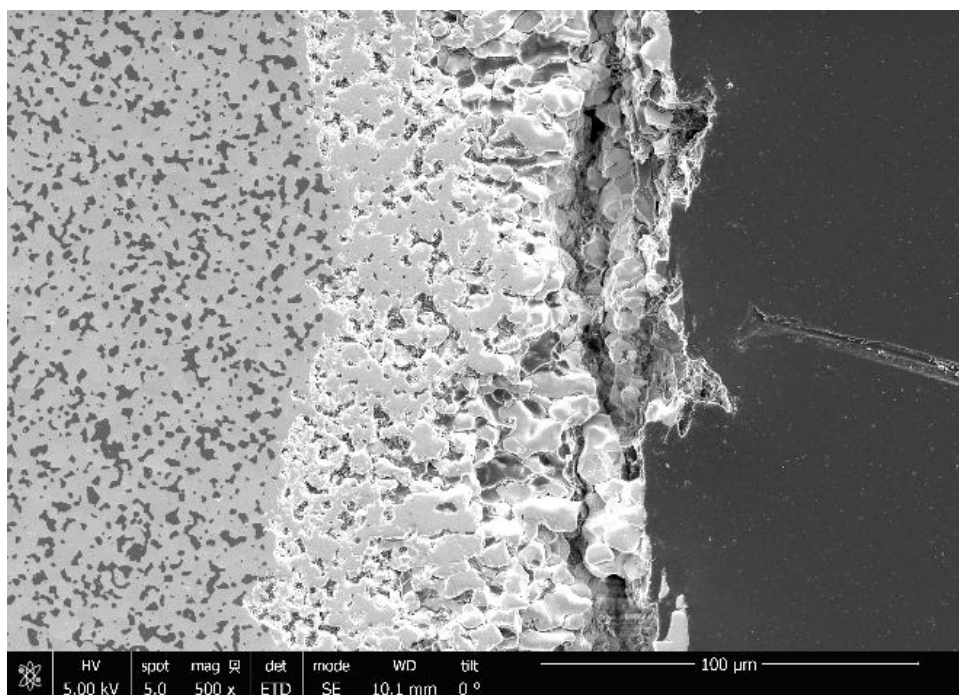
Figure 41. SEM Micrograph of HfB$_2$-20%SiC-4 oxide scale. Test ran at 150 MPa for 8.05 hours at 1500°C in air.
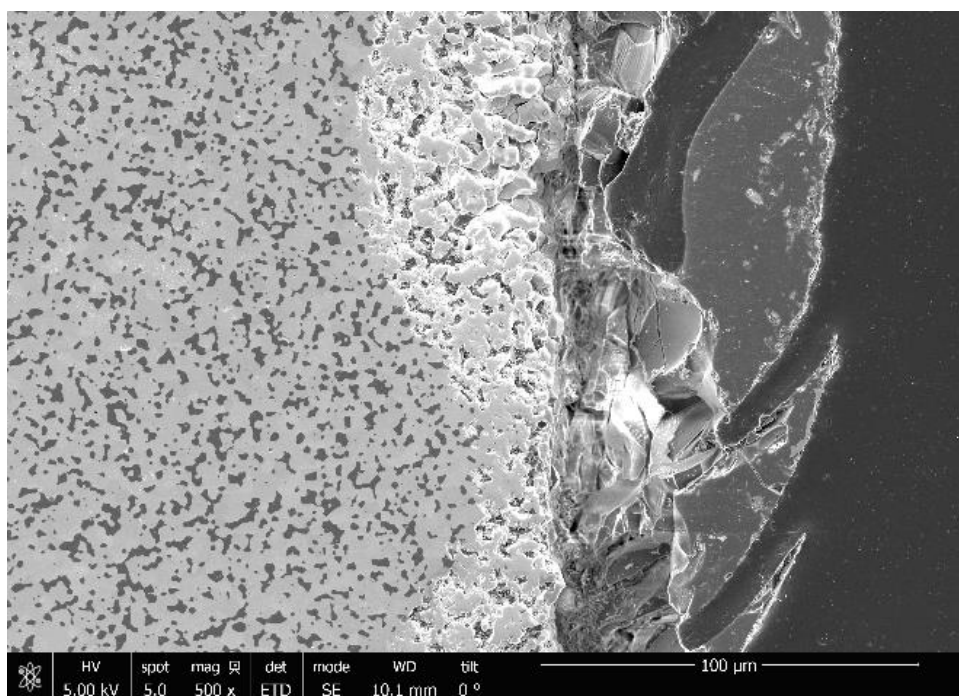
Figure 42. SEM Micrograph of HfB$_2$-20%SiC-4 oxide scale. Test ran at 150 MPa for 8.05 hours at 1500°C in air.
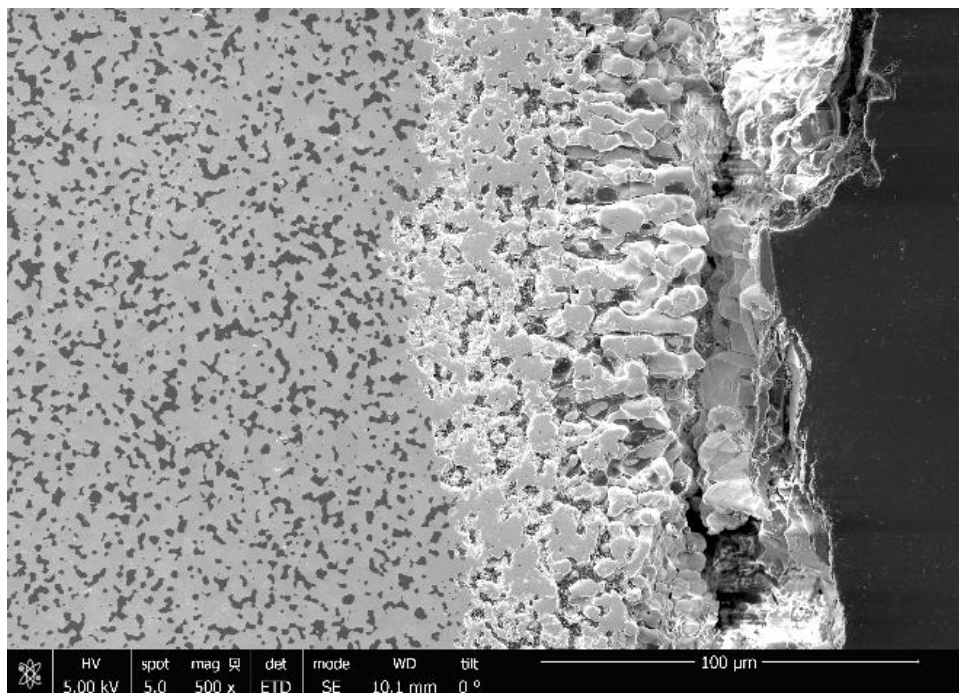
Figure 43. SEM Micrograph of HfB$_2$-20%SiC-4 oxide scale. Test ran at 150 MPa for 8.05 hours at 1500°C in air.
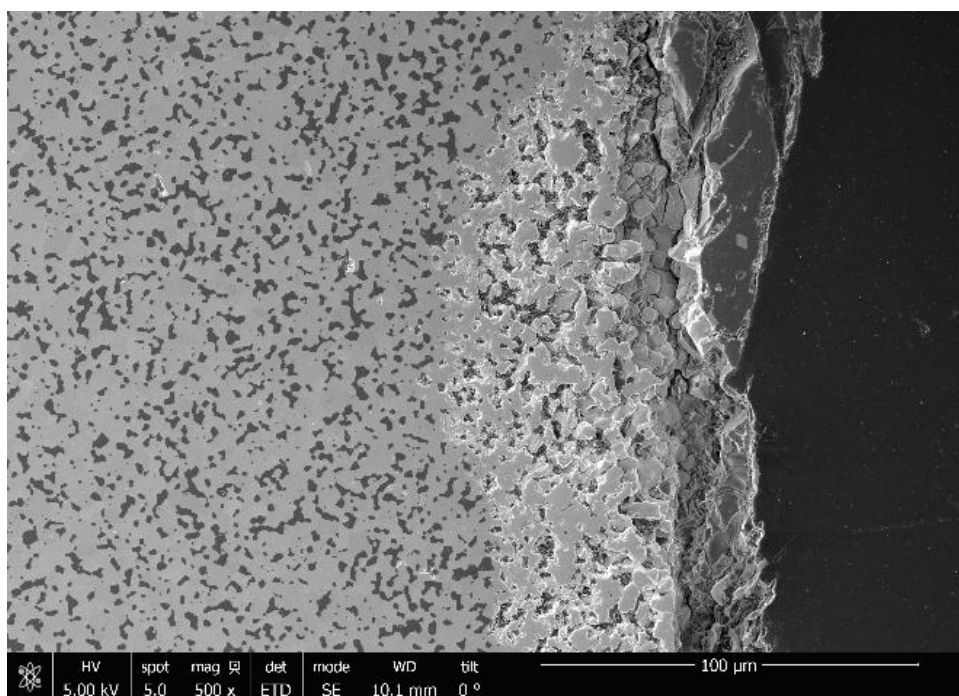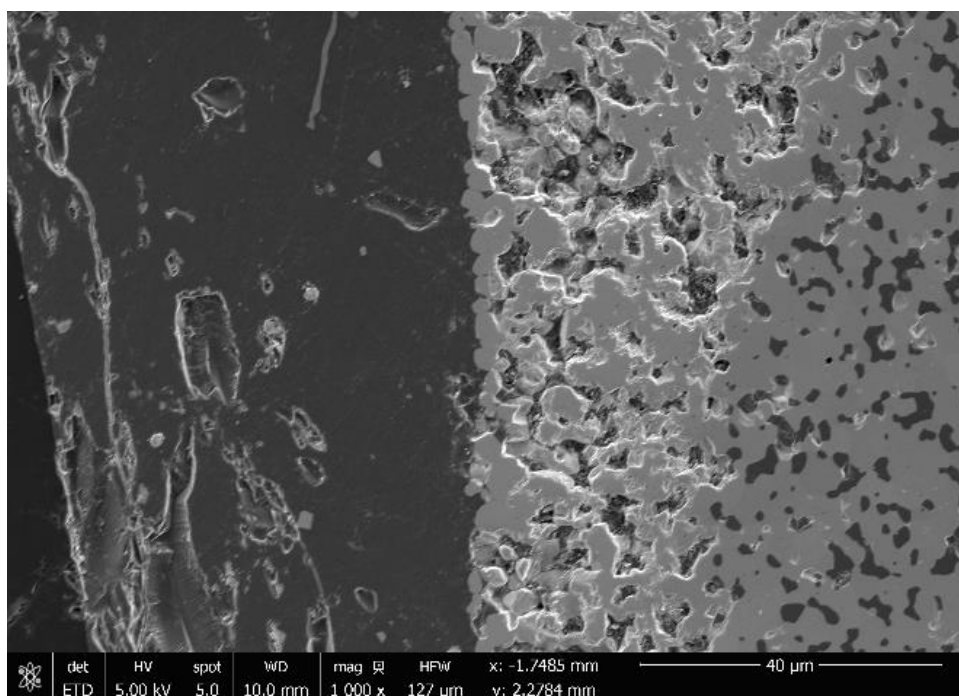

Figure 44. SEM Micrograph of HfB$_2$-20%SiC-4 oxide scale. Test ran at 150 MPa for 8.05 hours at 1500°C in air.
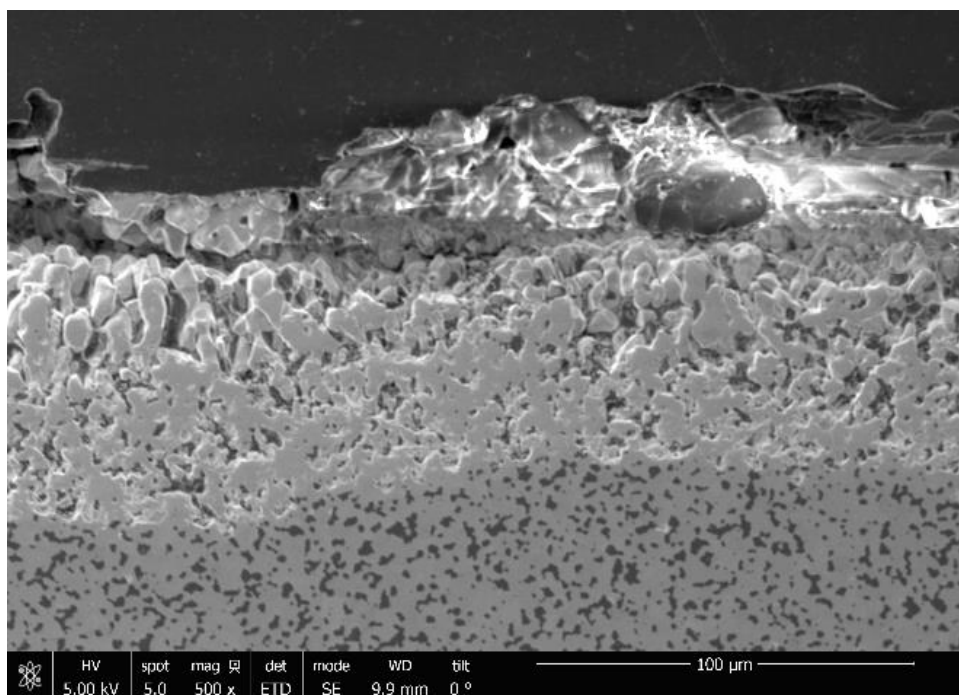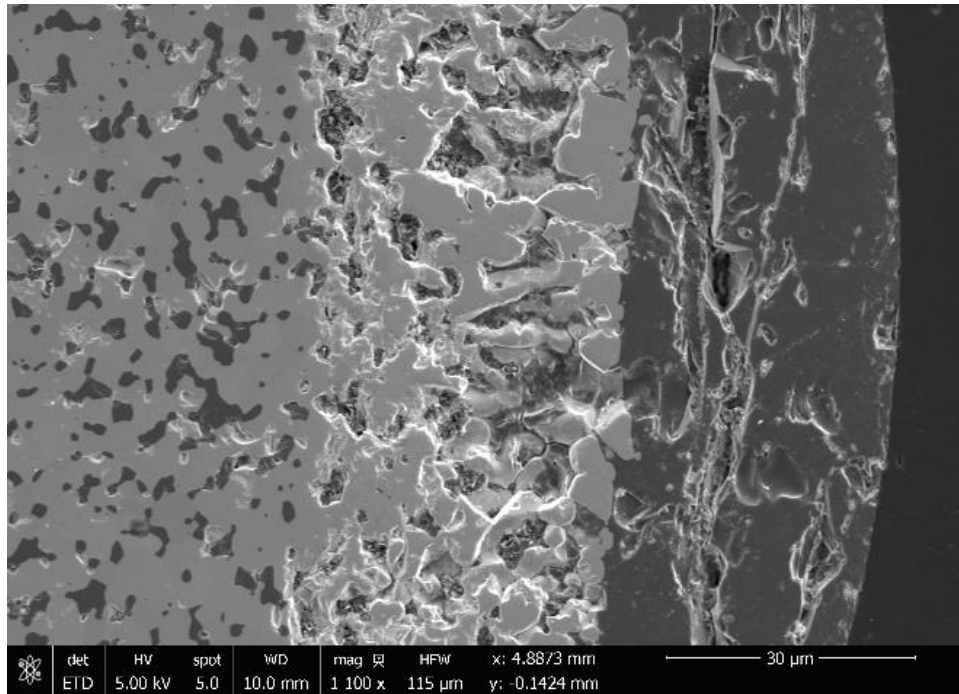
Figure 45. SEM Micrograph of HfB$_2$-20%SiC-4 oxide scale. Test ran at 150 MPa for 8.05 hours at 1500°C in air.
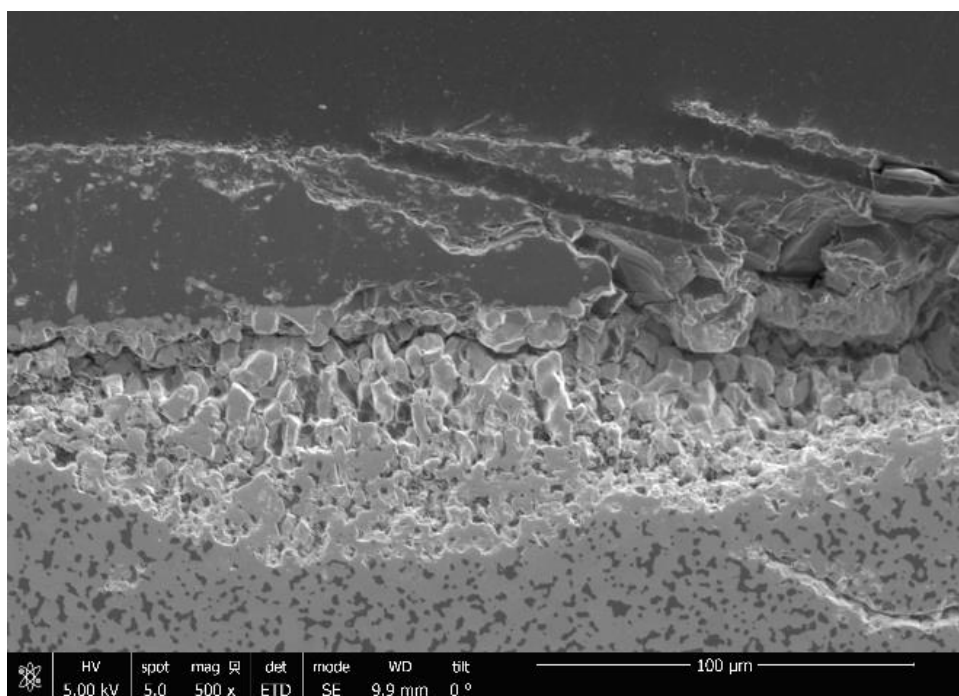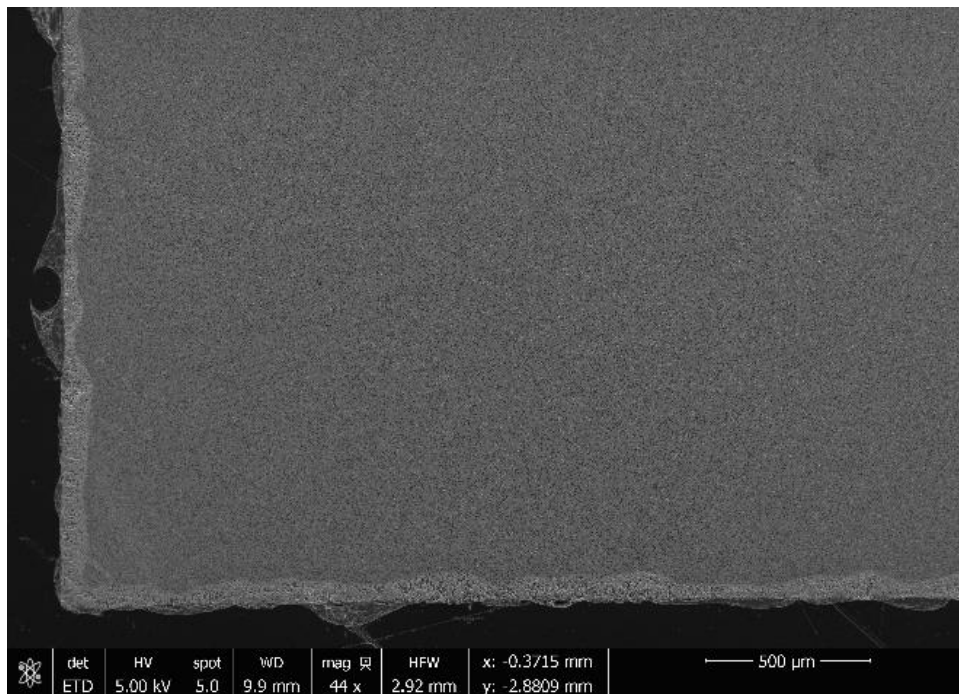

Figure 46. SEM Micrograph of HfB$_2$-20%SiC-4 oxide scale. Test ran at 150 MPa for 8.05 hours at 1500°C in air.
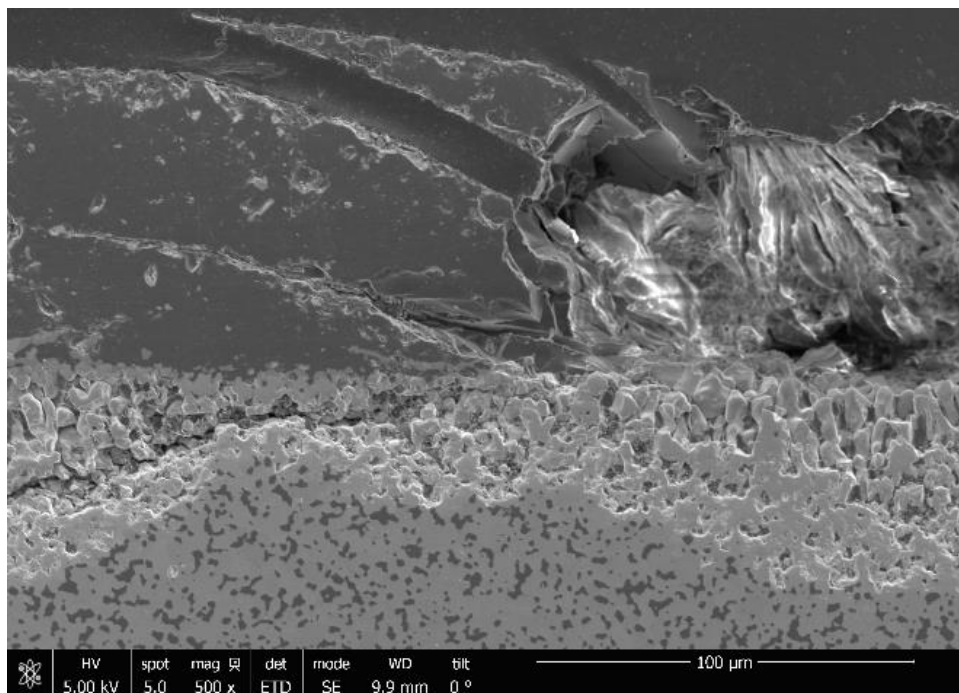
Figure 47. SEM Micrograph of HfB$_2$-20%SiC-4 oxide scale. Test ran at 150 MPa for 8.05 hours at 1500°C in air.
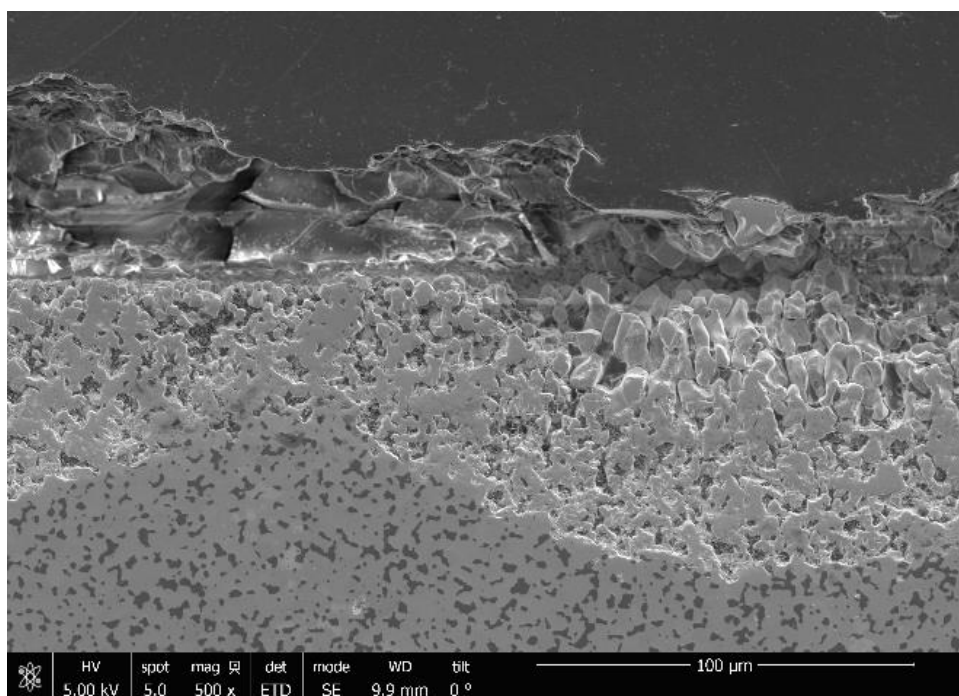
Figure 48. SEM Micrograph of HfB$_2$-20%SiC-4 oxide scale. Test ran at 150 MPa for 8.05 hours at 1500°C in air.
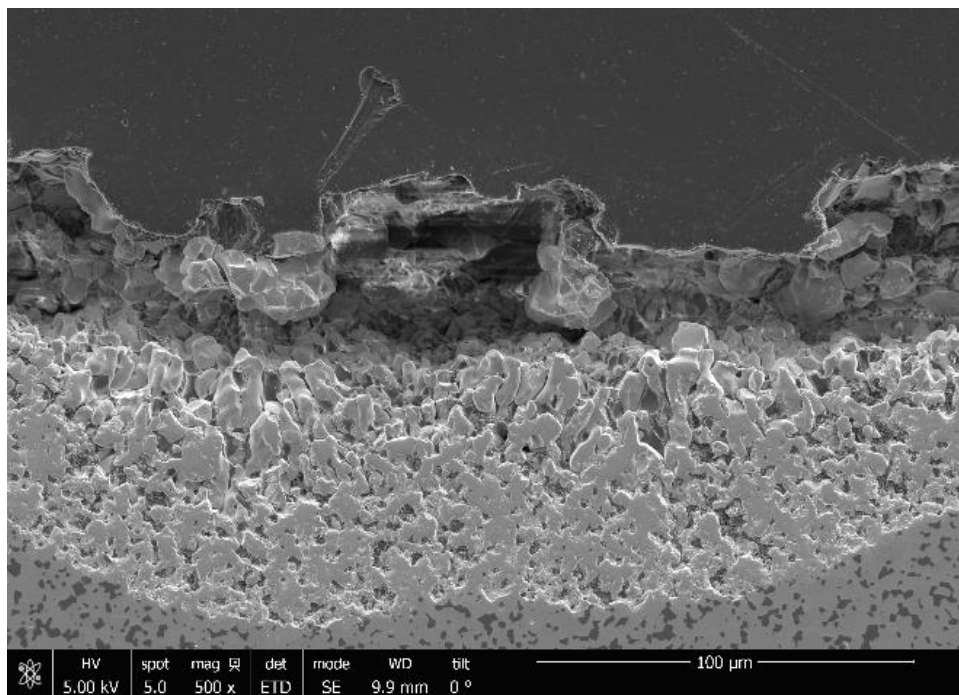
Figure 49. SEM Micrograph of HfB$_2$-20%SiC-4 oxide scale. Test ran at 150 MPa for 8.05 hours at 1500°C in air.
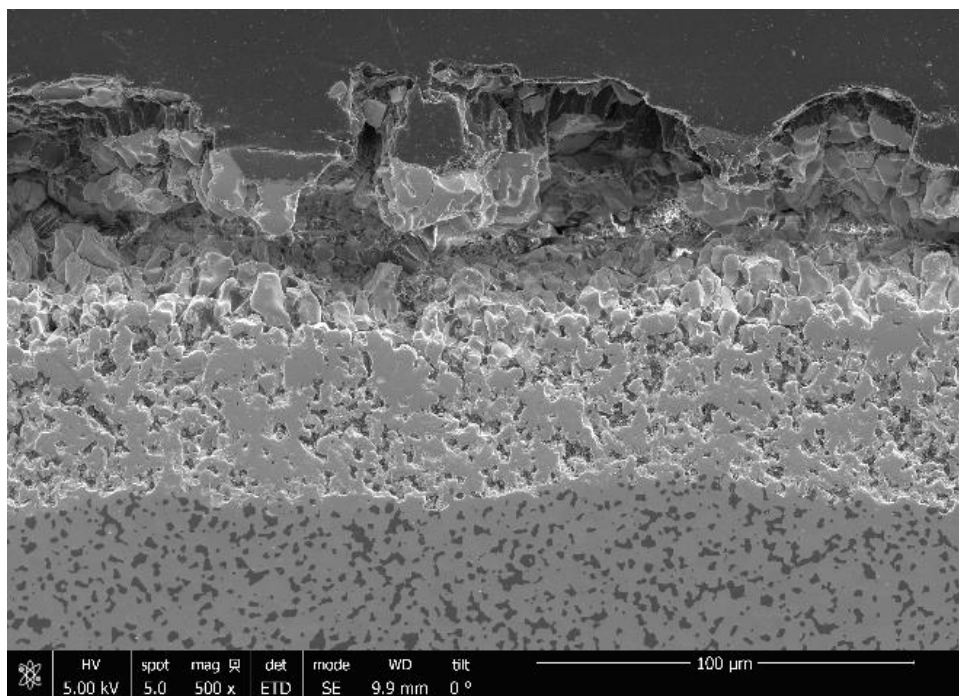
Figure 50. SEM Micrograph of HfB$_2$-20%SiC-4 oxide scale. Test ran at 150 MPa for 8.05 hours at 1500°C in air.
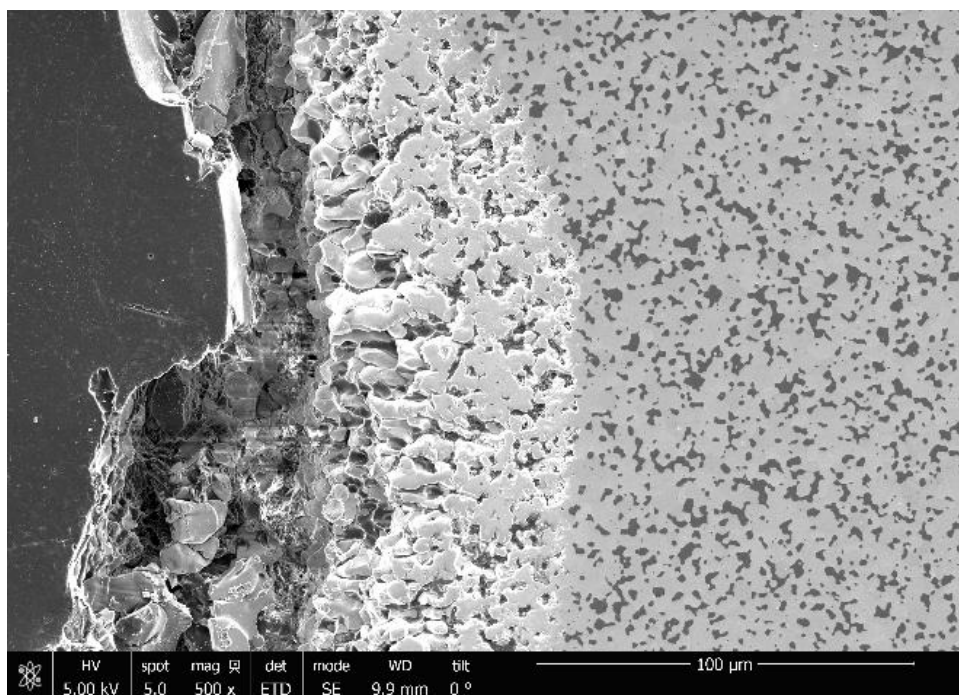
Figure 51. SEM Micrograph of HfB$_2$-20%SiC-4 oxide scale. Test ran at 150 MPa for 8.05 hours at 1500°C in air.
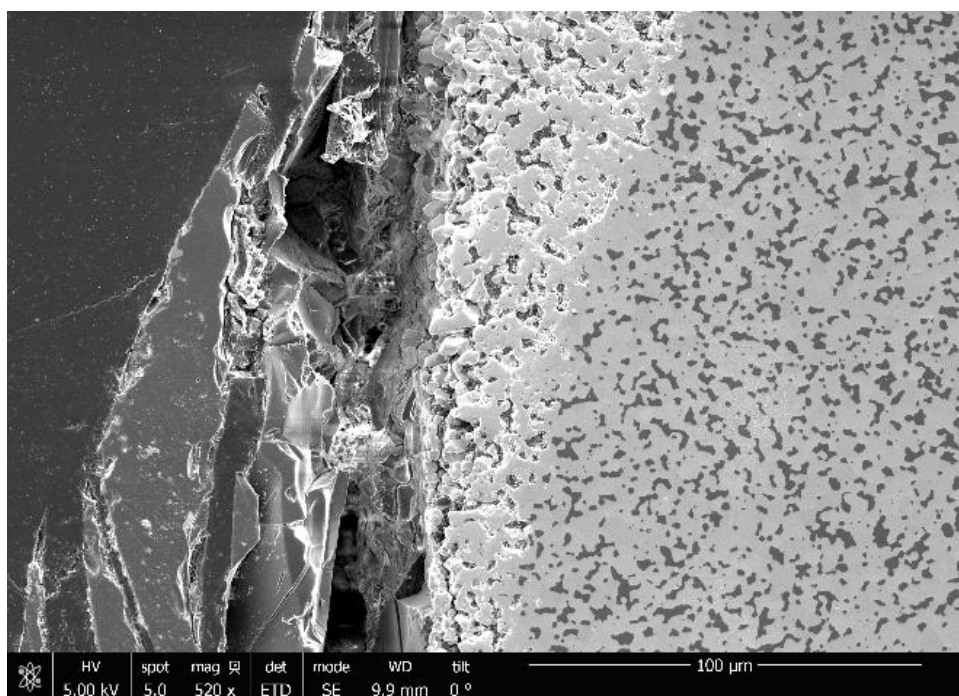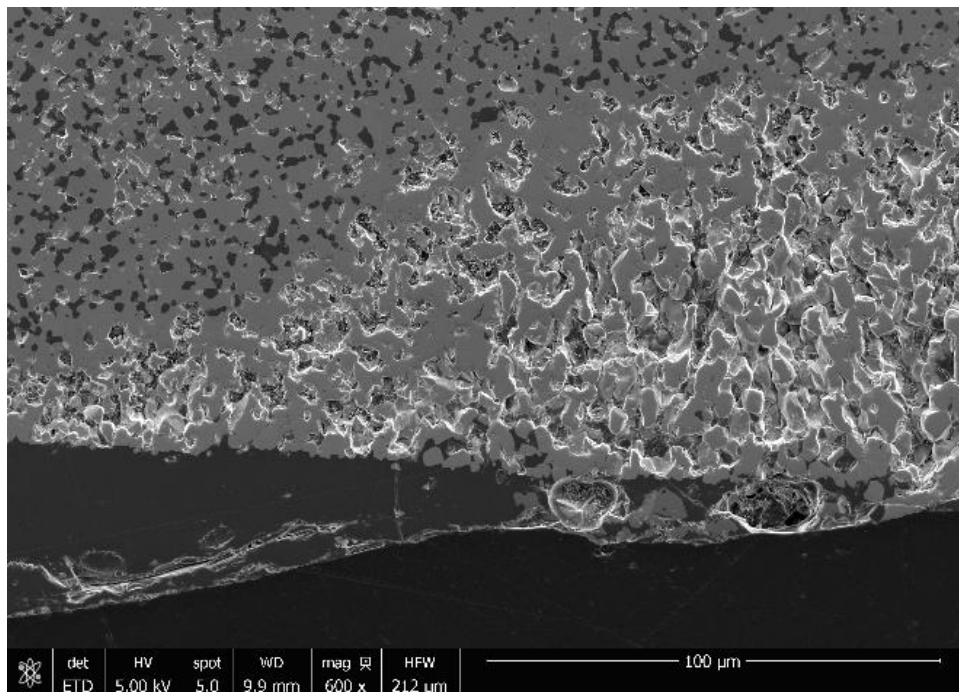

Figure 52. SEM Micrograph of HfB$_2$-20%SiC-4 oxide scale. Test ran at 150 MPa for 8.05 hours at 1500°C in air.
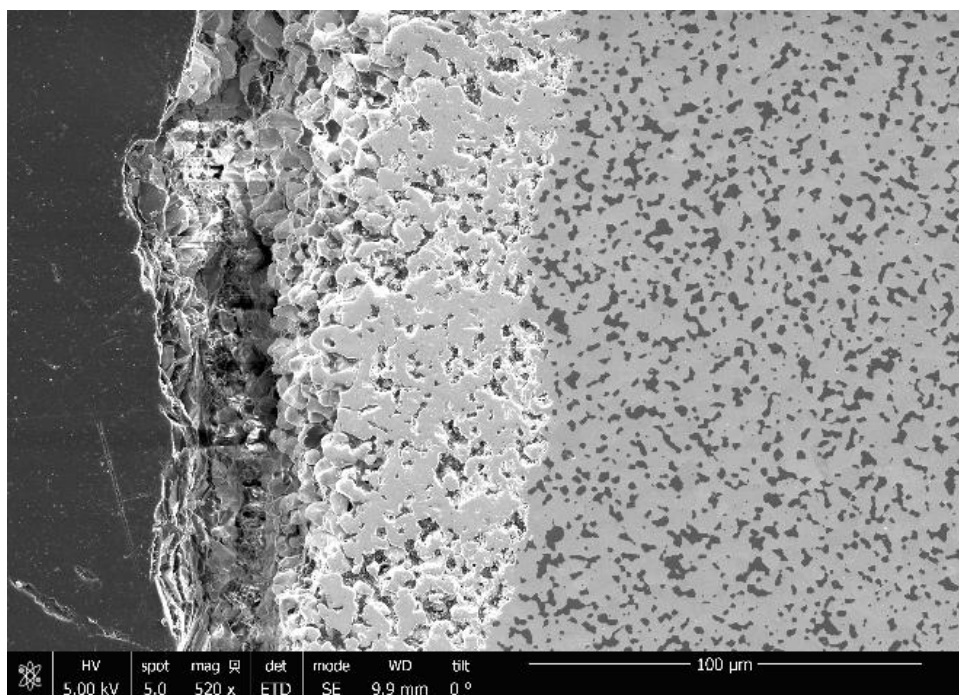
Figure 53. SEM Micrograph of HfB$_2$-20%SiC-4 oxide scale. Test ran at 150 MPa for 8.05 hours at 1500°C in air.
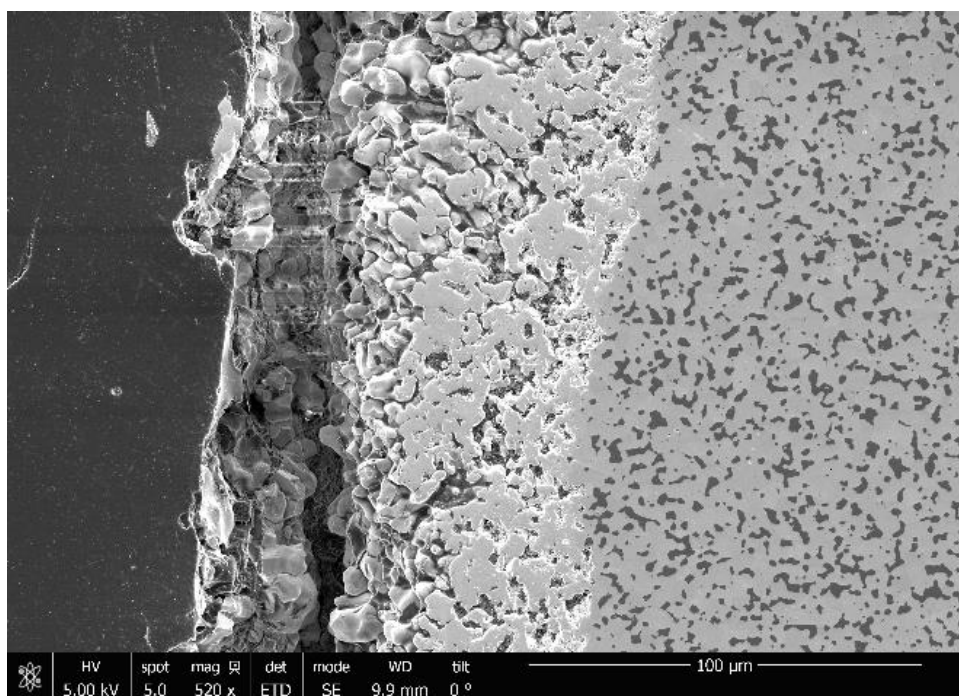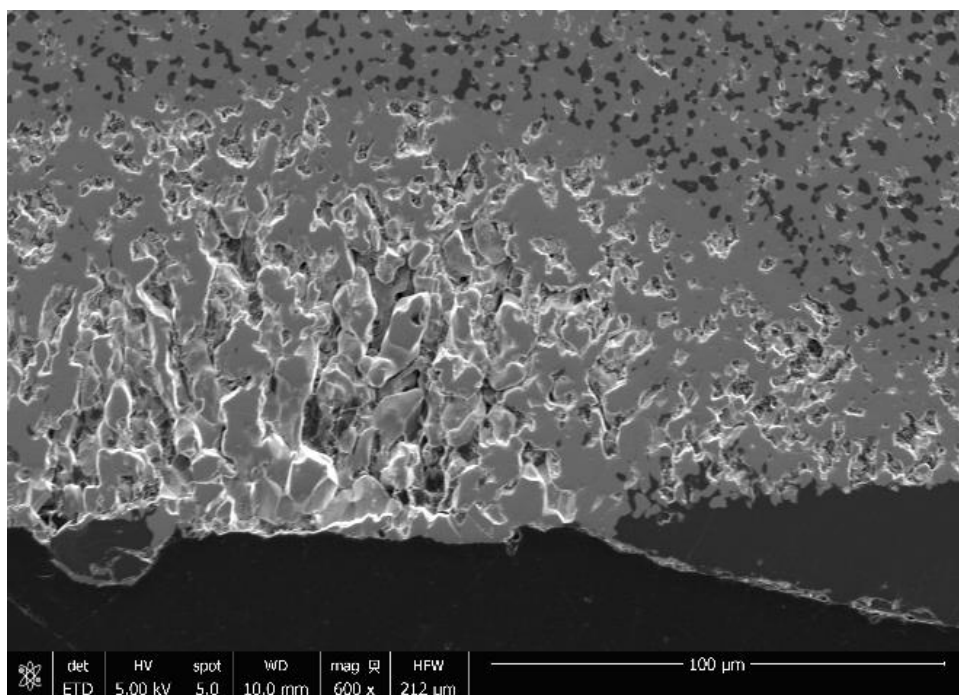

Figure 54. SEM Micrograph of HfB$_2$-20%SiC-4 oxide scale. Test ran at 150 MPa for 8.05 hours at 1500°C in air.
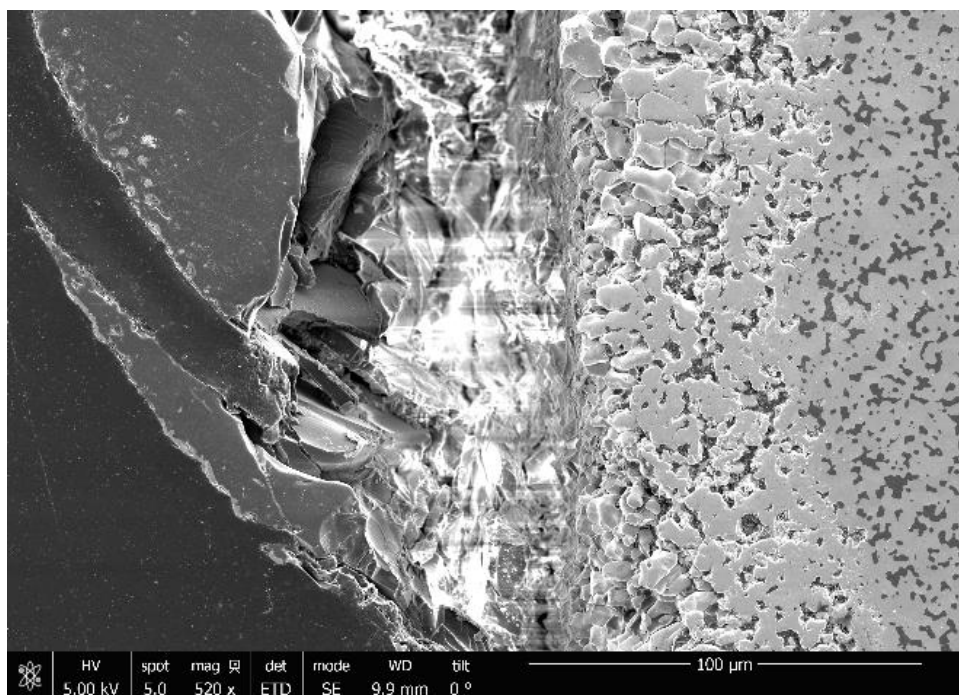
Figure 55. SEM Micrograph of HfB$_2$-20%SiC-4 oxide scale. Test ran at 150 MPa for 8.05 hours at 1500°C in air.
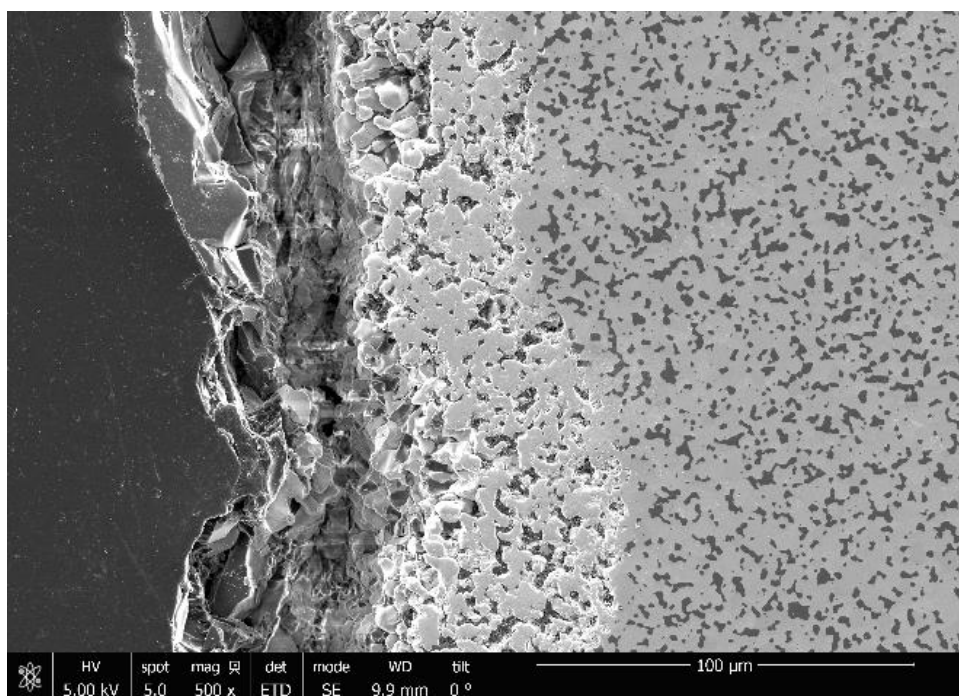
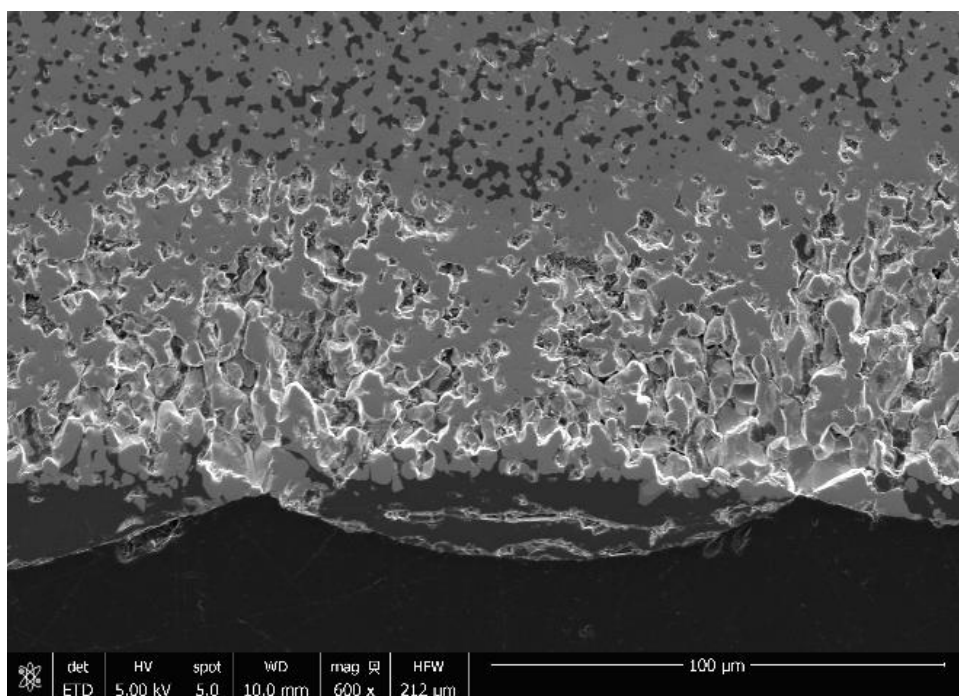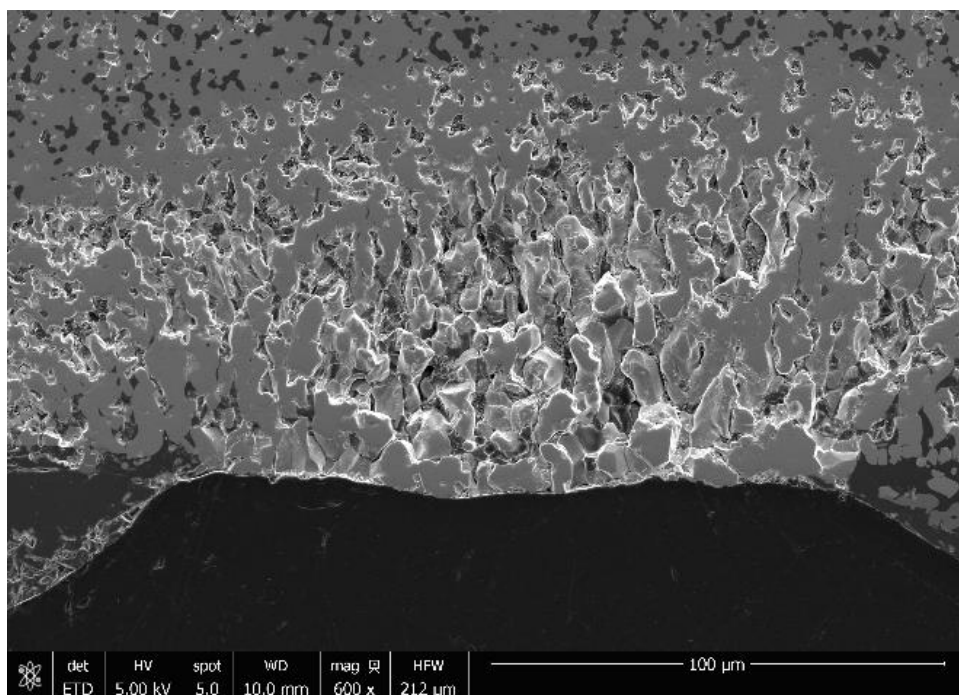Figure 56. SEM Micrograph of HfB$_2$-20%SiC-4 oxide scale. Test ran at 150 MPa for 8.05 hours at 1500°C in air.
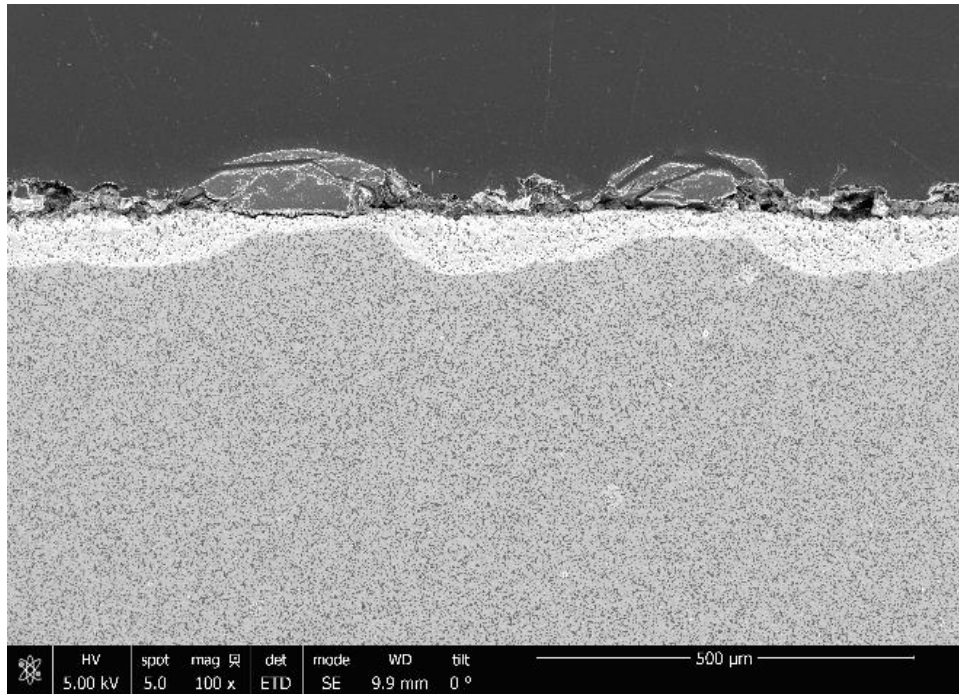
Figure 57. SEM Micrograph of HfB$_2$-20%SiC-4 oxide scale. Test ran at 150 MPa for 8.05 hours at 1500°C in air. Note that the thickness of the oxide scale (light grey) is directly related to the thickness of the glassy deposit on the surface. The thicker the glassy layer, the thinner the oxide scale. This represents how borosilicate glass is an effective oxidation barrier for the HfB$_2$-20% SiC substrate.
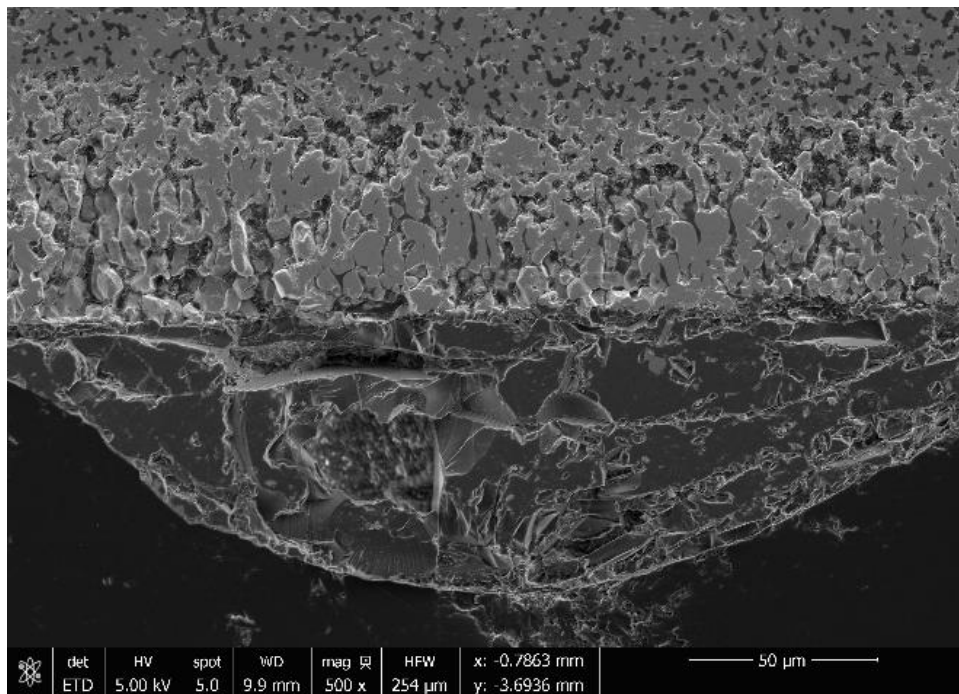
Figure 58. SEM Micrograph of HfB$_2$-20%SiC-5 oxide scale. Test ran at 100 MPa for 10 hours at 1500°C in air.
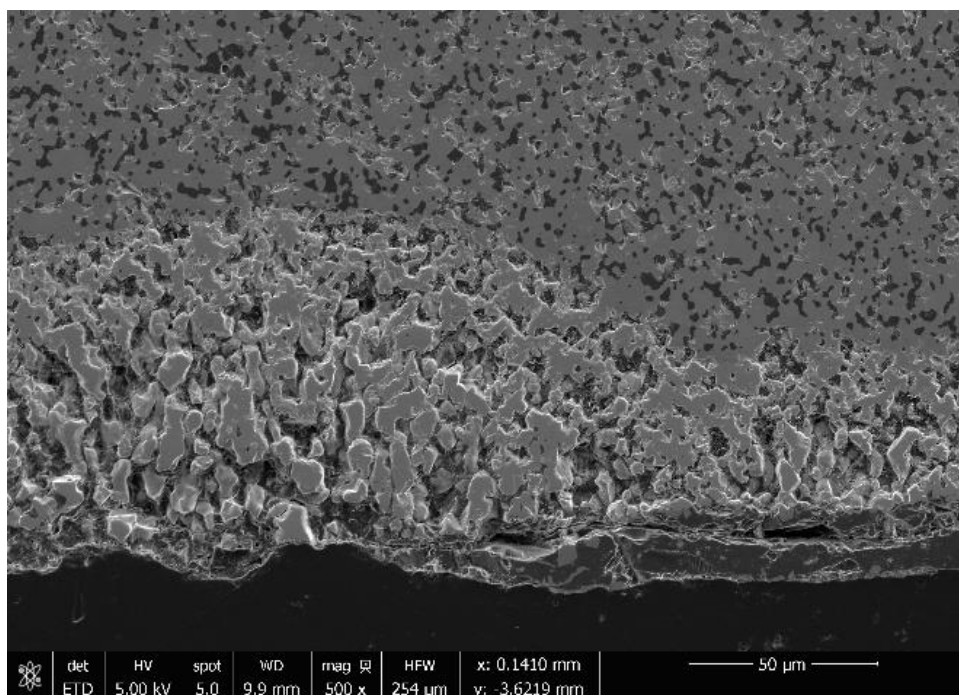
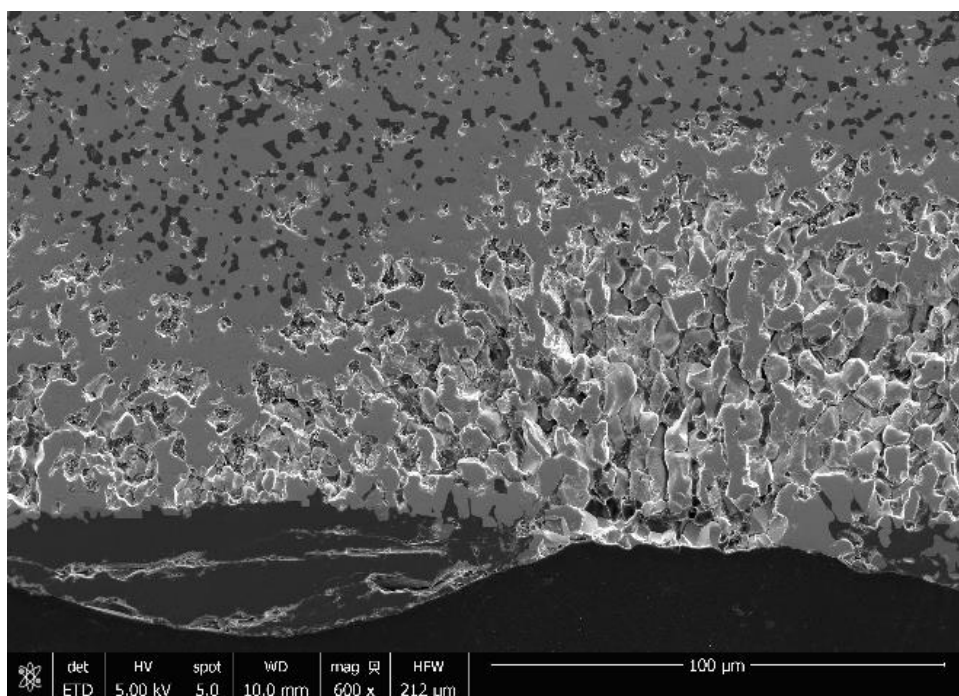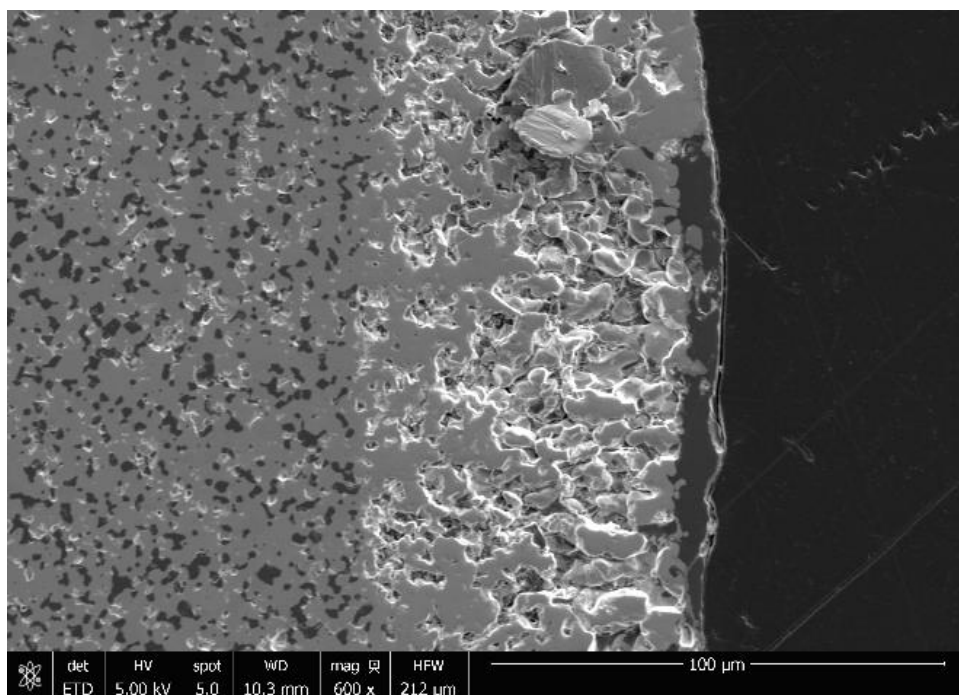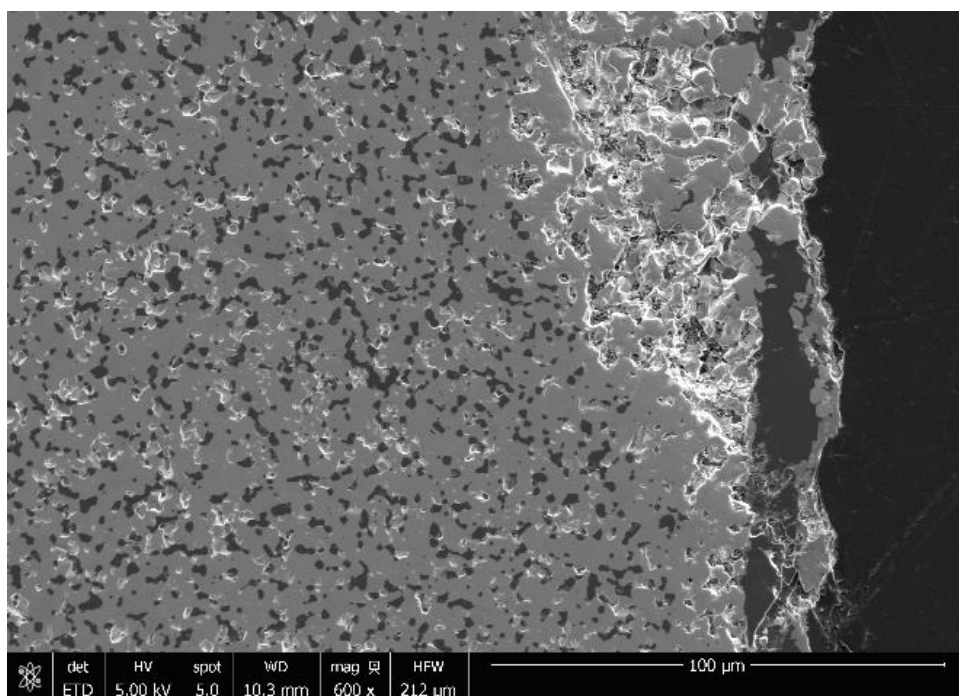Figure 59. SEM Micrograph of HfB$_2$-20%SiC-5 oxide scale. Test ran at 100 MPa for 10 hours at 1500°C in air.
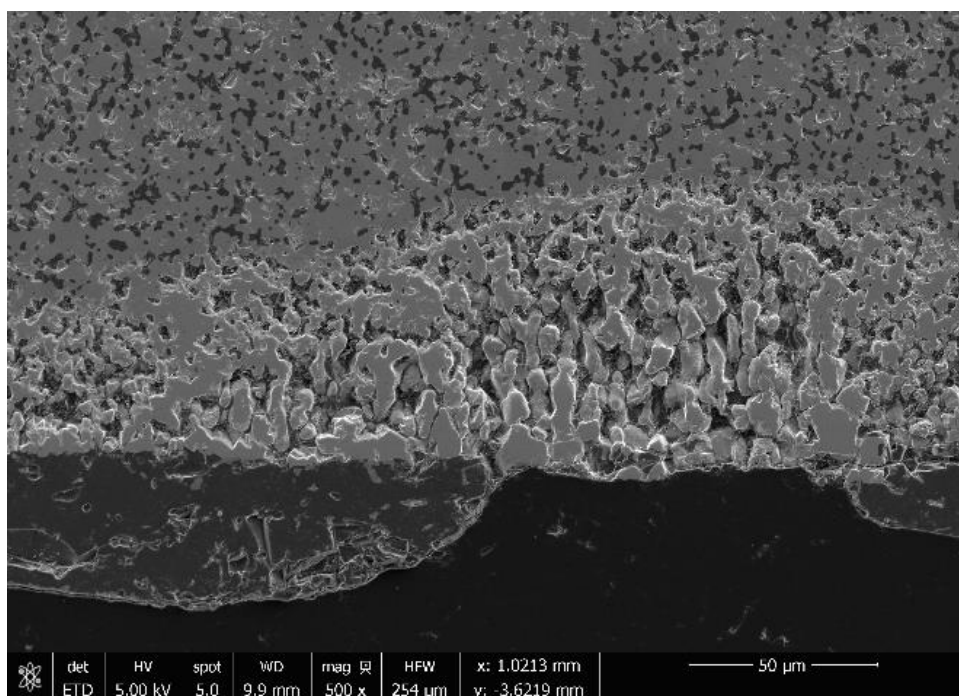
Figure 60. SEM Micrograph of HfB$_2$-20%SiC-5 oxide scale. Test ran at 100 MPa for 10 hours at 1500°C in air.
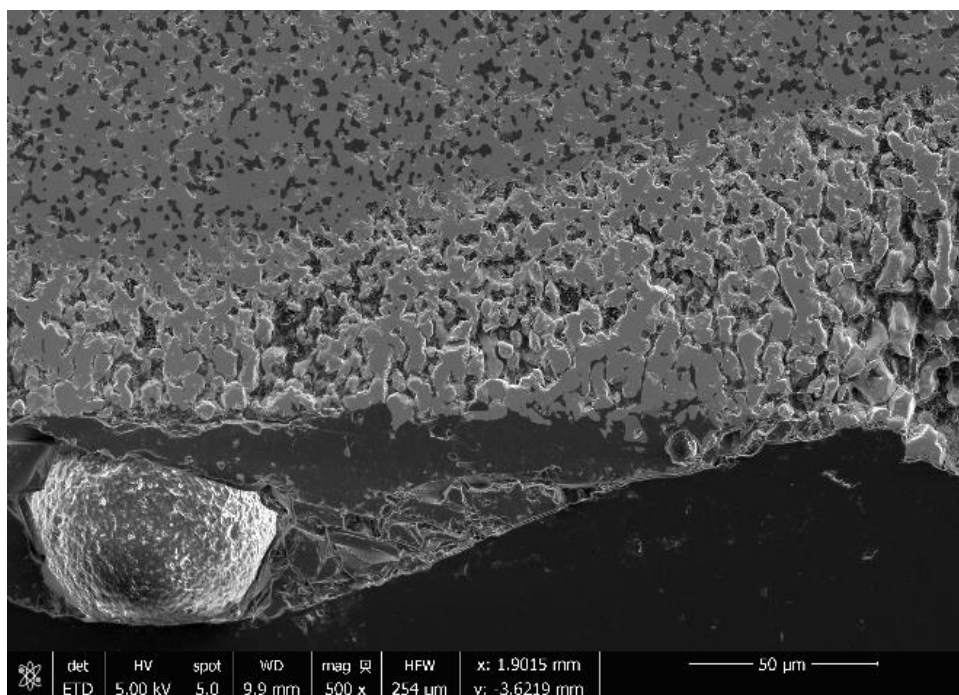
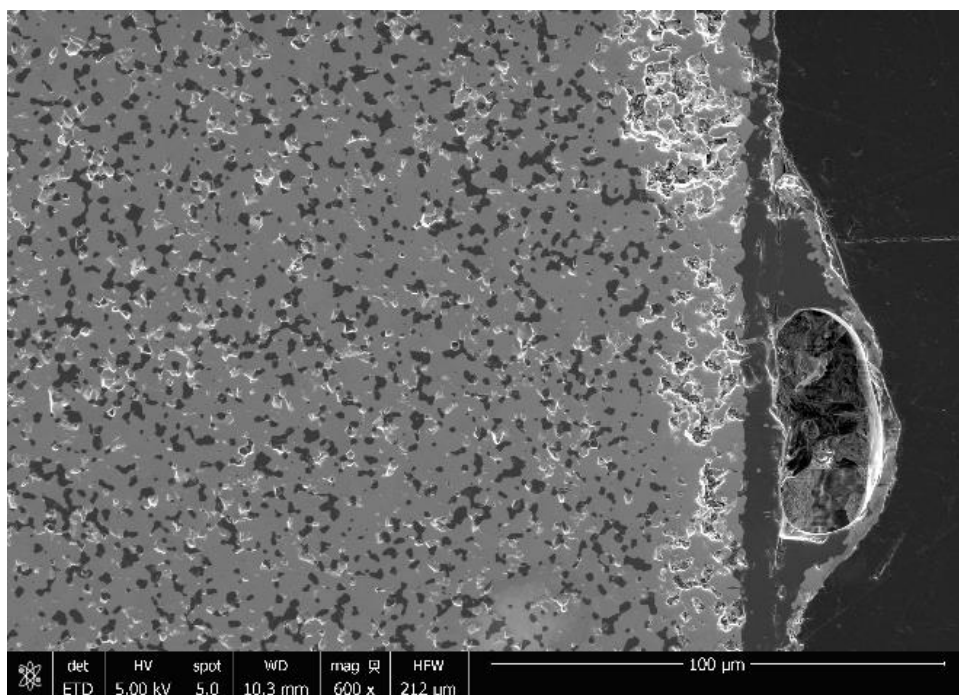Figure 61. SEM Micrograph of HfB$_2$-20%SiC-5 oxide scale. Test ran at 100 MPa for 10 hours at 1500°C in air.
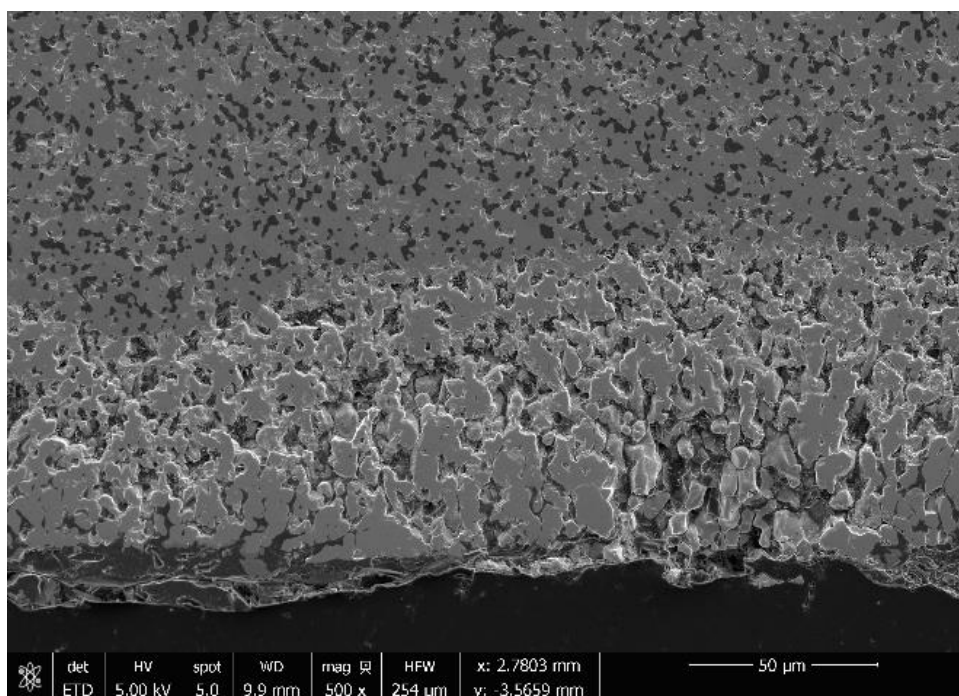
Figure 62. SEM Micrograph of HfB$_2$-20%SiC-5 oxide scale. Test ran at 100 MPa for 10 hours at 1500°C in air.
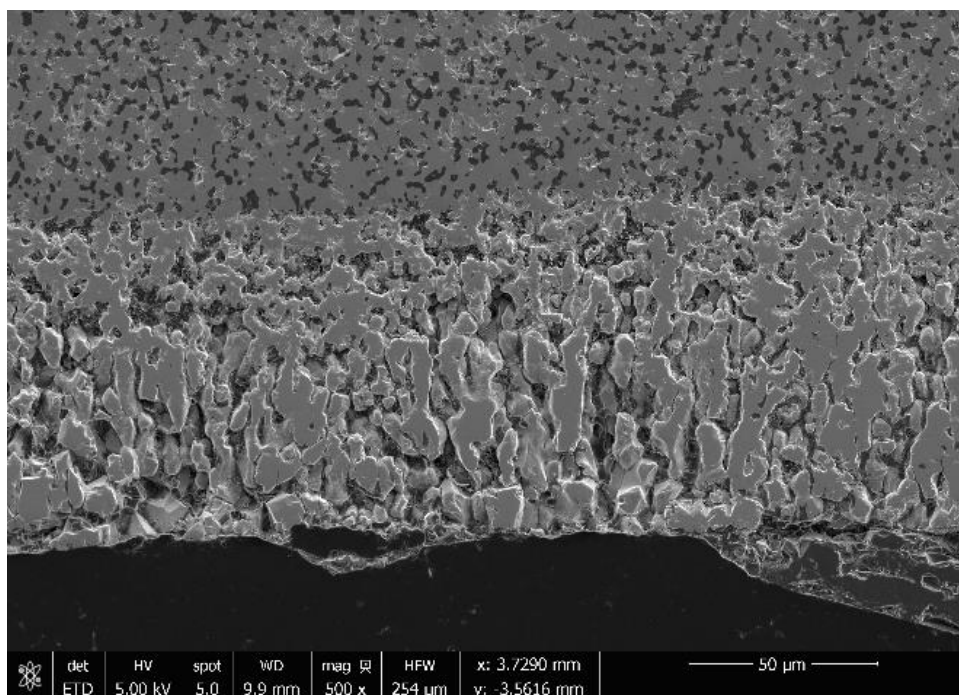
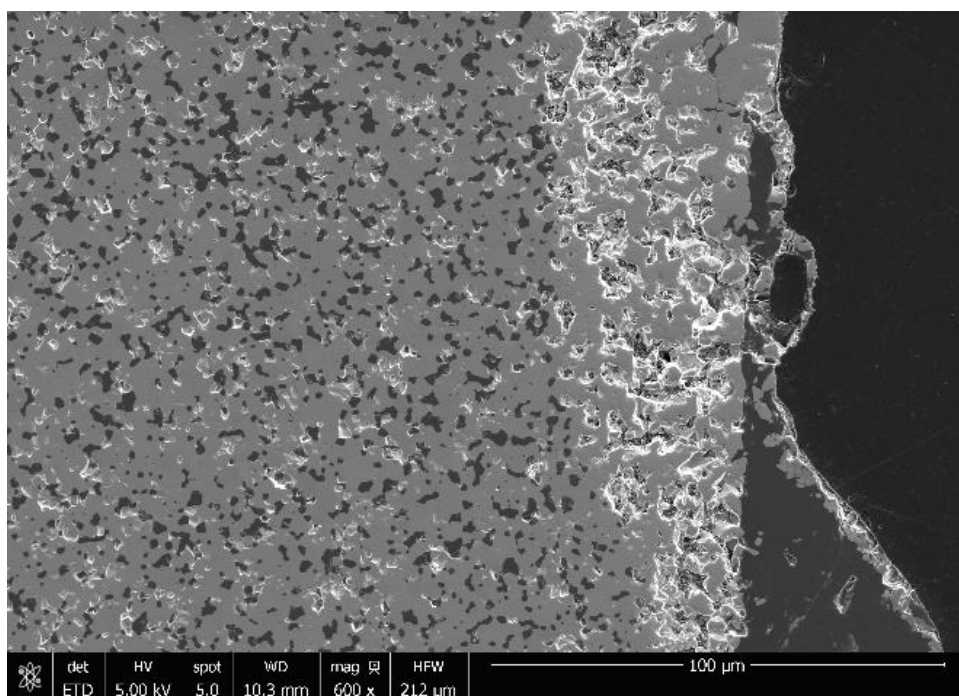Figure 63. SEM Micrograph of HfB$_2$-20%SiC-5 oxide scale. Test ran at 100 MPa for 10 hours at 1500°C in air.
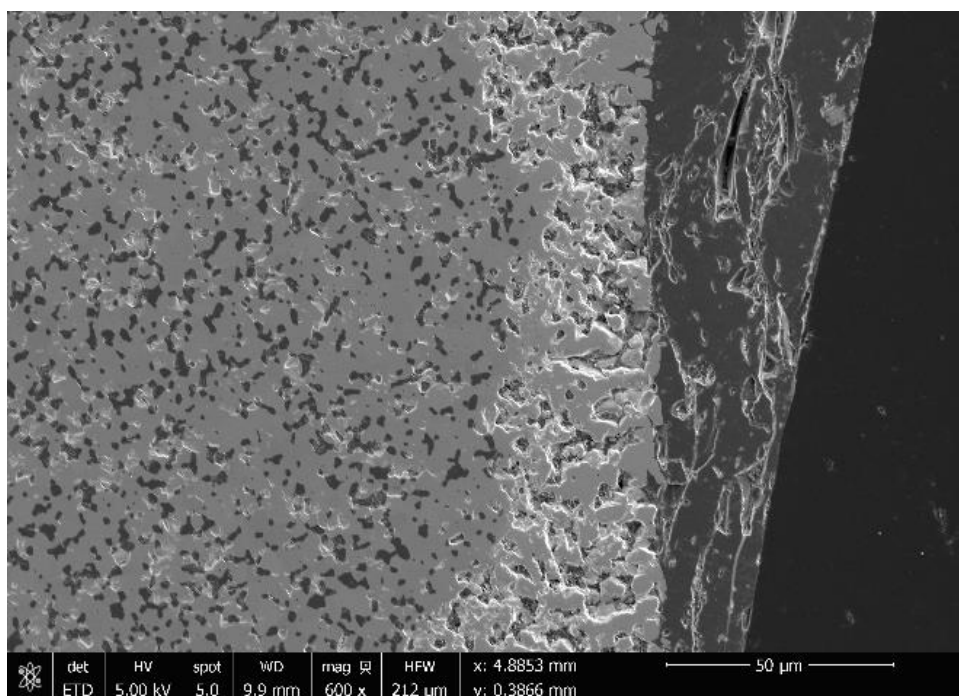
Figure 64. SEM Micrograph of HfB$_2$-20%SiC-5 oxide scale. Test ran at 100 MPa for 10 hours at 1500°C in air.
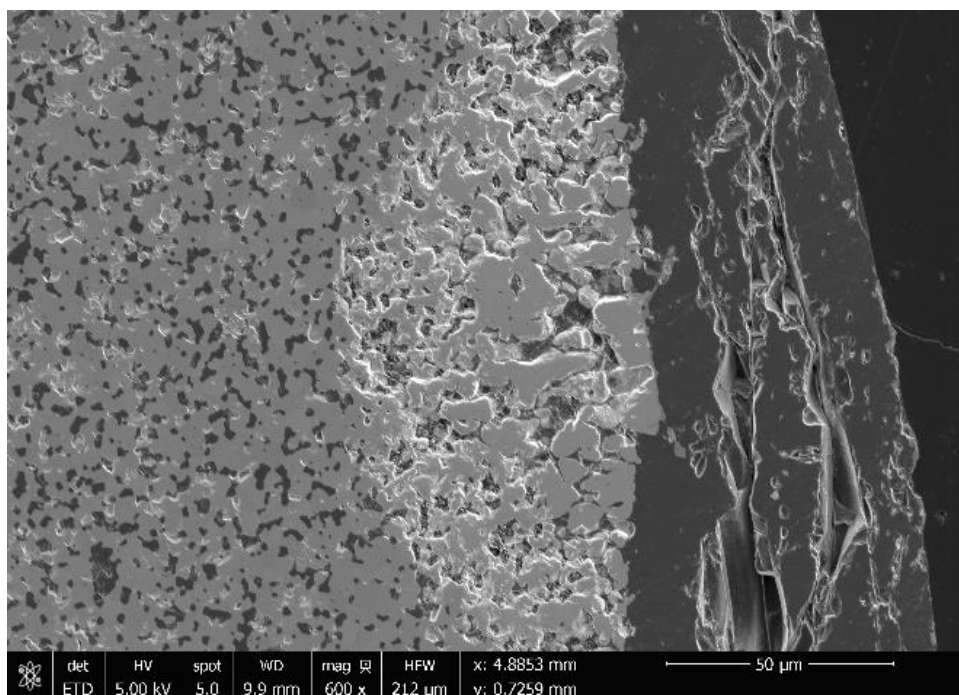
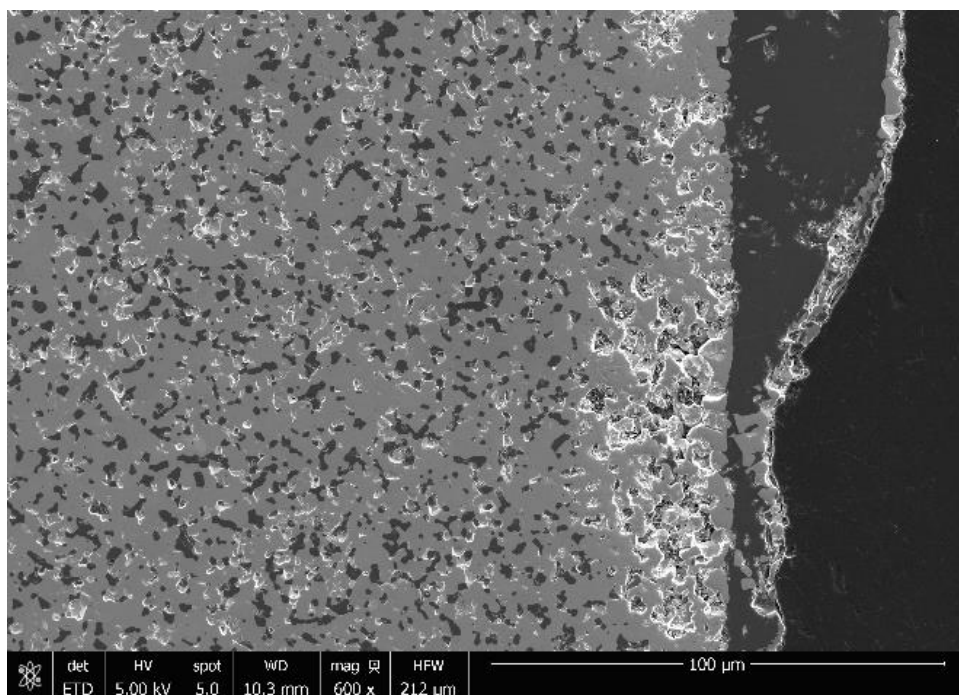Figure 65. SEM Micrograph of HfB$_2$-20%SiC-5 oxide scale. Test ran at 100 MPa for 10 hours at 1500°C in air.
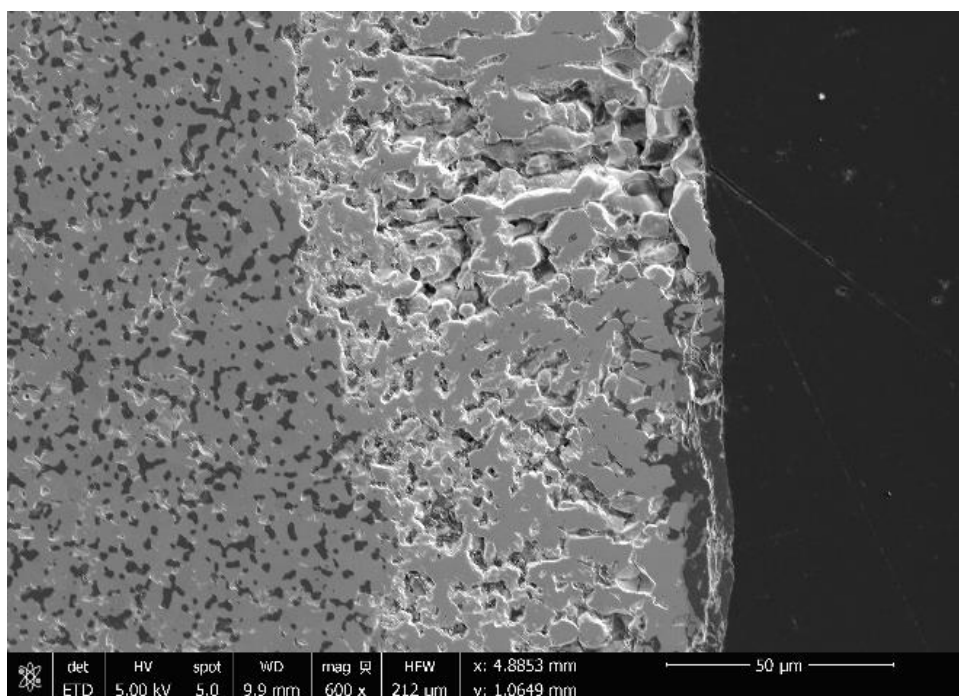
Figure 66. SEM Micrograph of HfB$_2$-20%SiC-5 oxide scale. Test ran at 100 MPa for 10 hours at 1500°C in air.
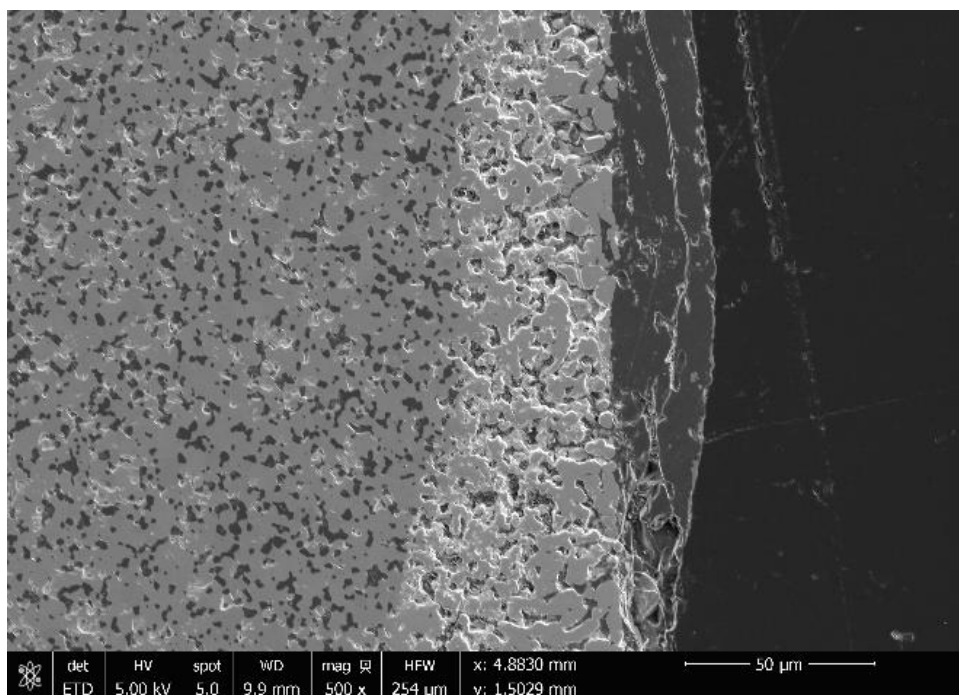
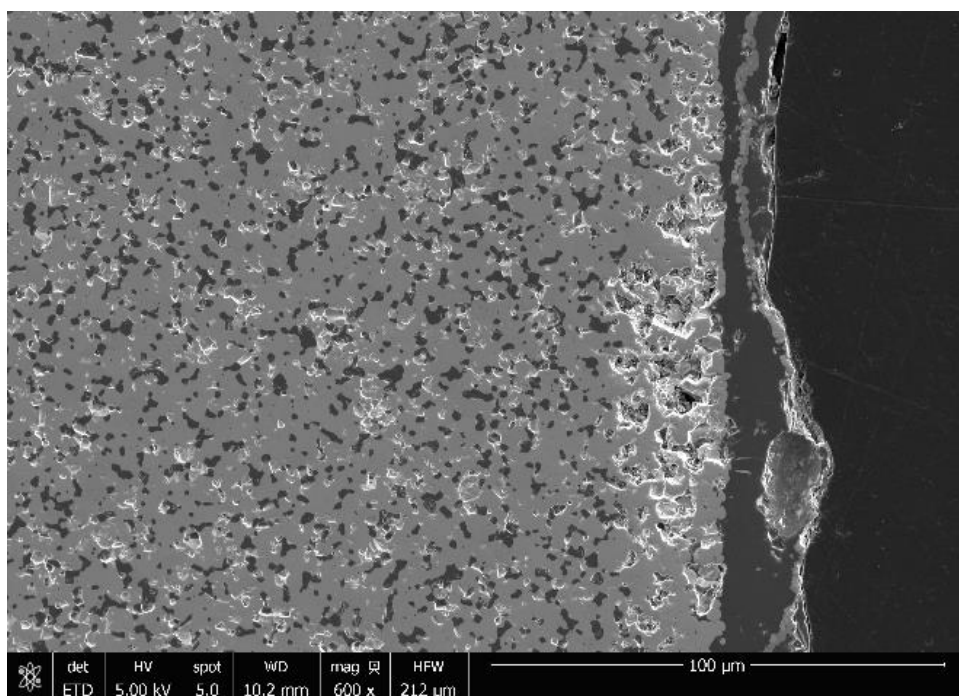Figure 67. SEM Micrograph of HfB$_2$-20%SiC-5 oxide scale. Test ran at 100 MPa for 10 hours at 1500°C in air.
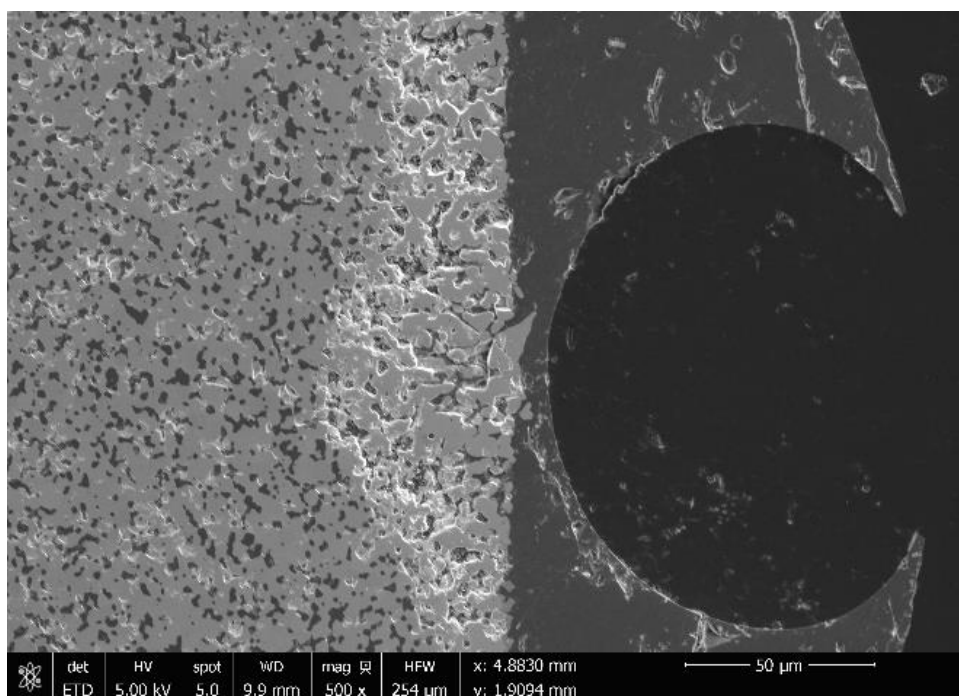
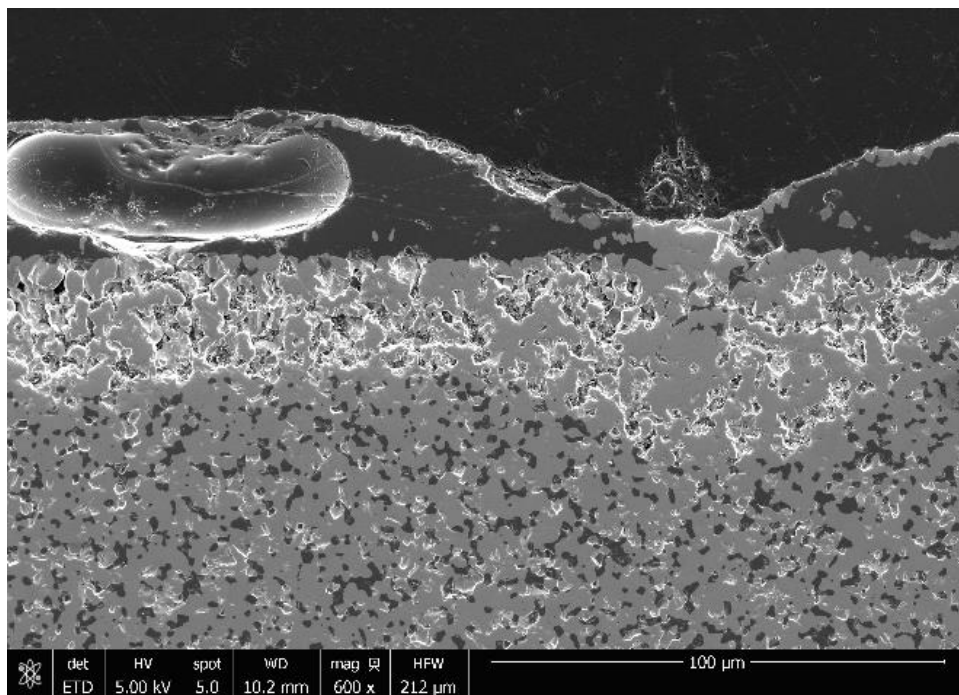Figure 68. SEM Micrograph of HfB$_2$-20%SiC-5 oxide scale. Test ran at 100 MPa for 10 hours at 1500°C in air.
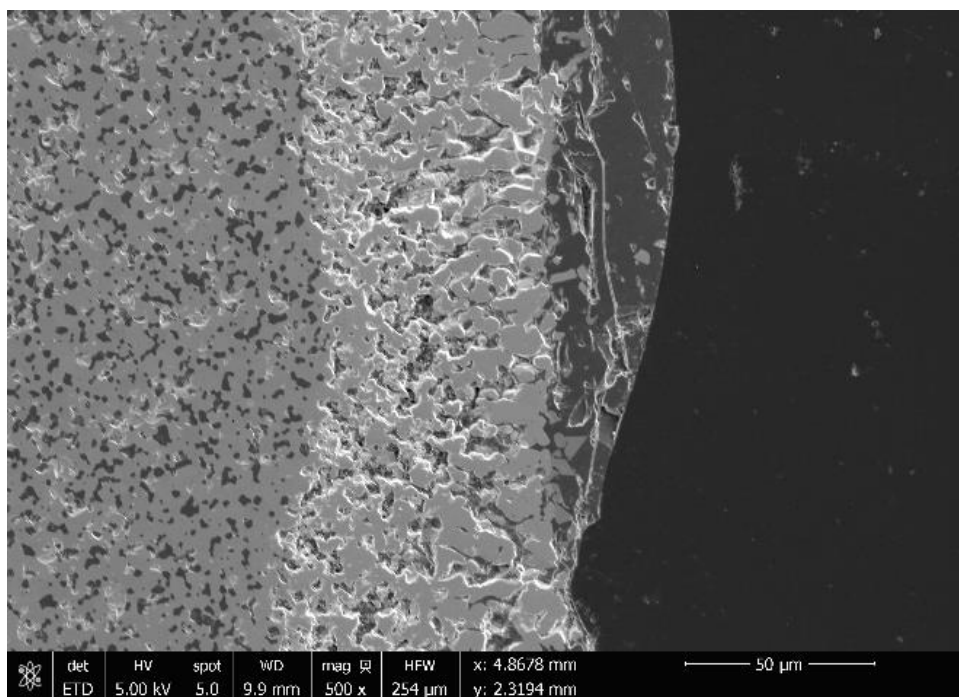
Figure 69. SEM Micrograph of HfB$_2$-20%SiC-5 oxide scale. Test ran at 100 MPa for 10 hours at 1500°C in air.
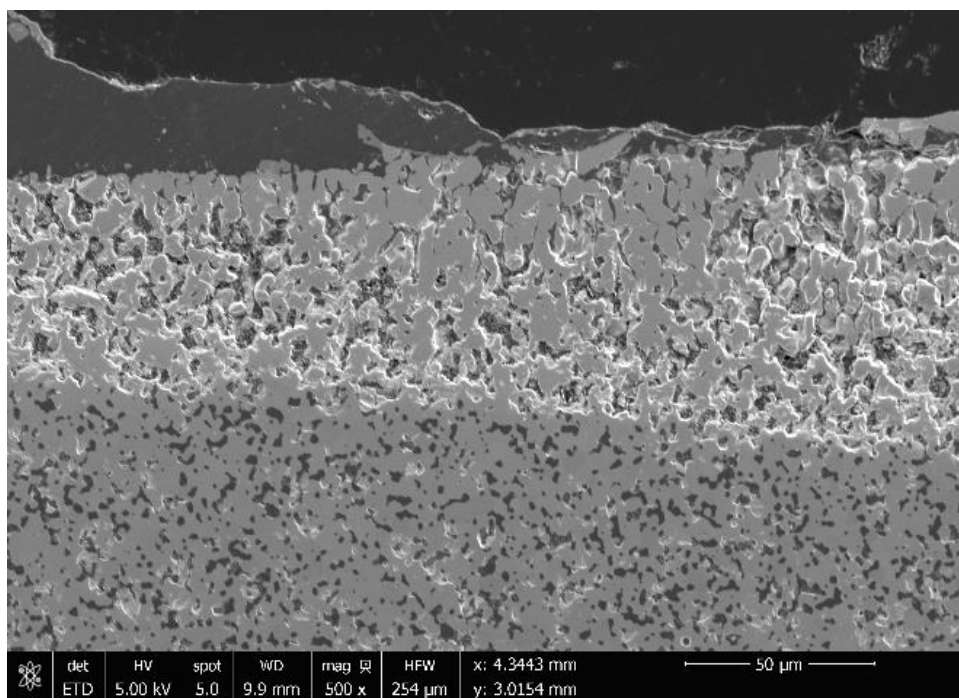
Figure 70. SEM Micrograph of HfB$_2$-20%SiC-5 oxide scale. Test ran at 100 MPa for 10 hours at 1500°C in air.
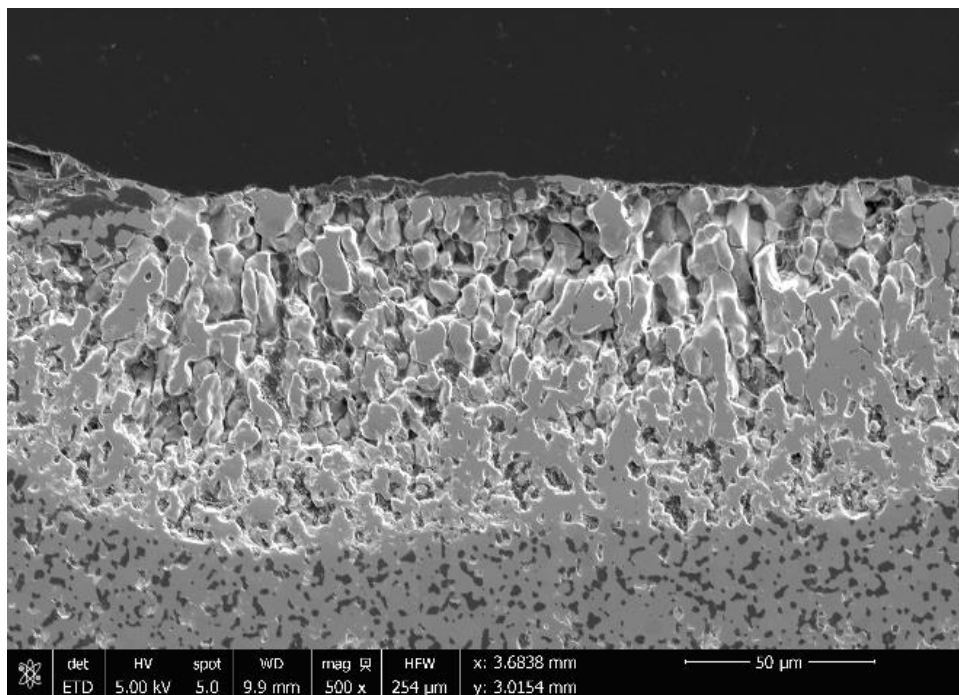
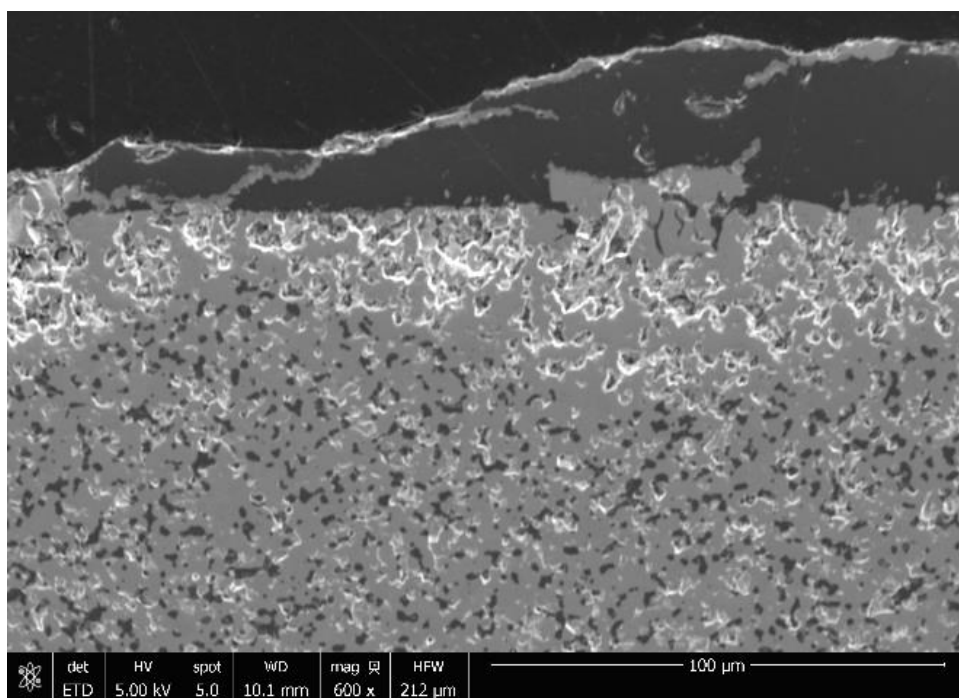Figure 71. SEM Micrograph of HfB$_2$-20%SiC-5 oxide scale. Test ran at 100 MPa for 10 hours at 1500°C in air.
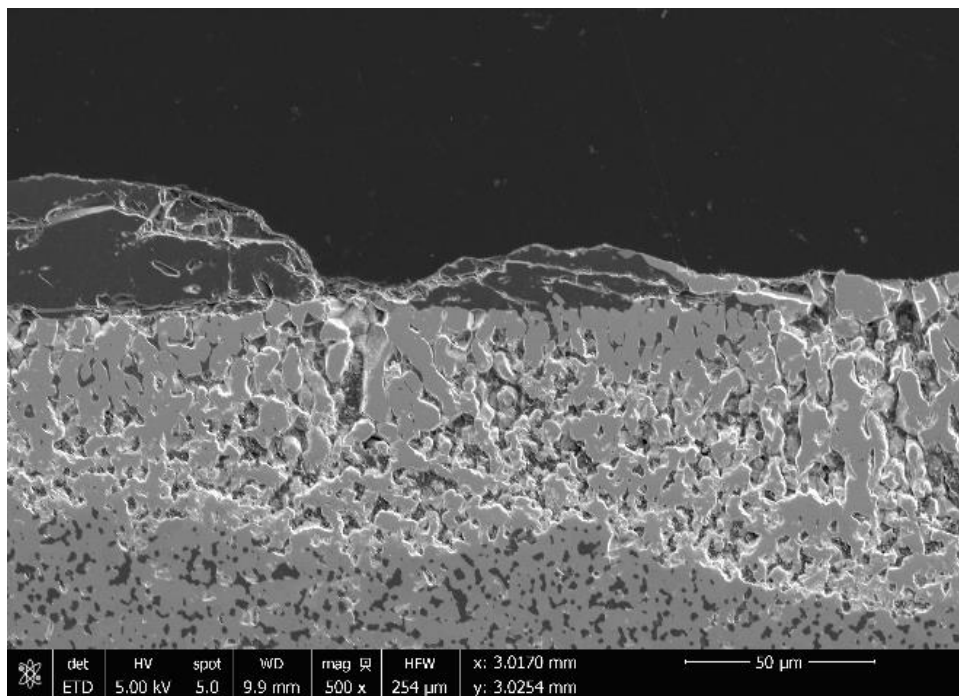
Figure 72. SEM Micrograph of HfB$_2$-20%SiC-5 oxide scale. Test ran at 100 MPa for 10 hours at 1500°C in air.
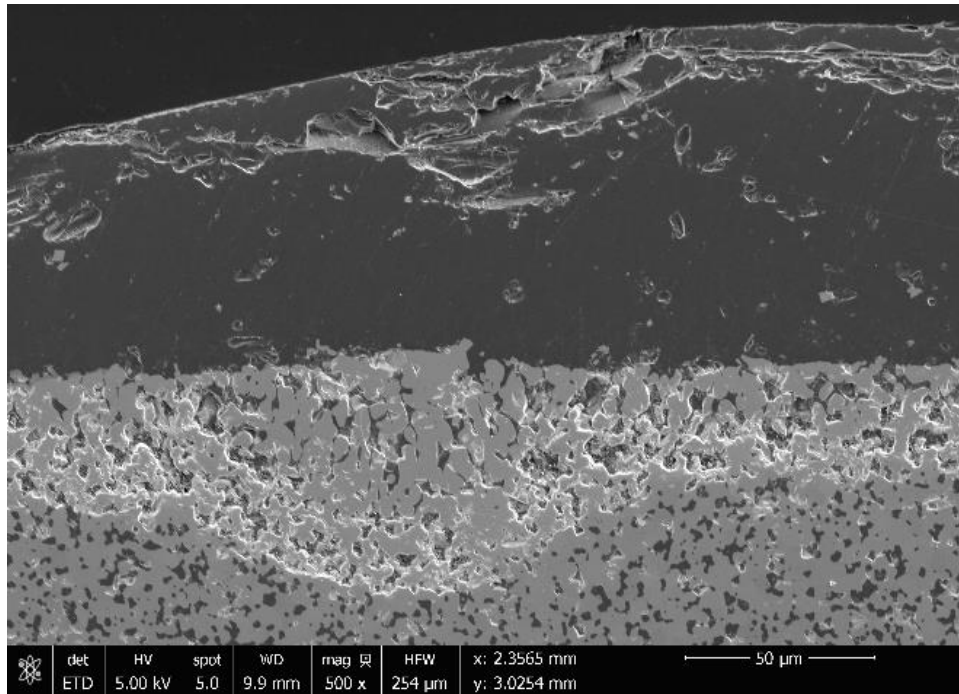
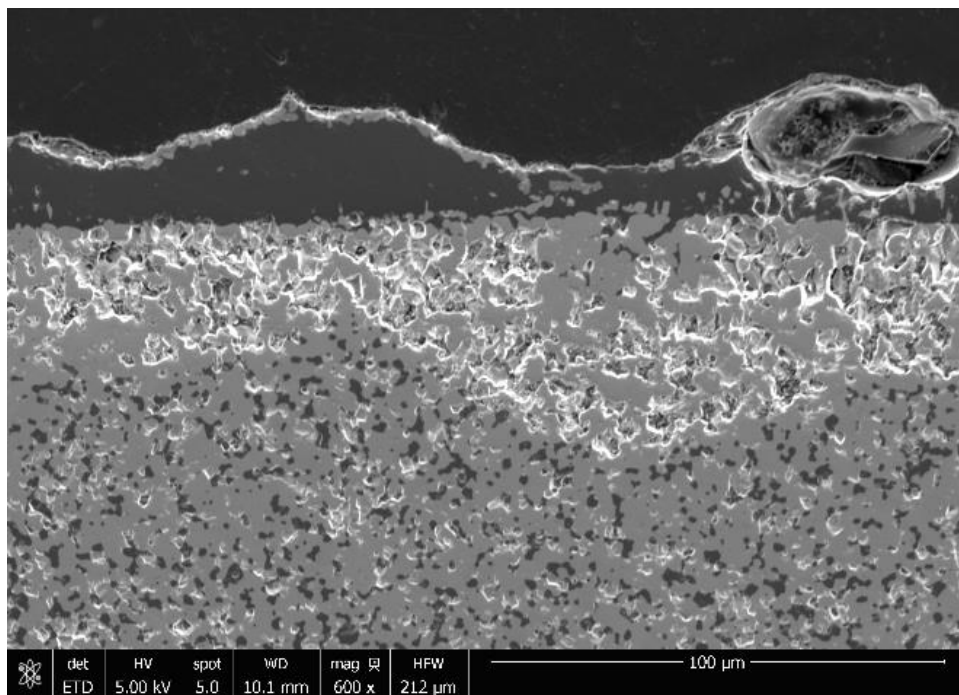Figure 73. SEM Micrograph of HfB$_2$-20%SiC-5 oxide scale. Test ran at 100 MPa for 10 hours at 1500°C in air.

Figure 74. SEM Micrograph of HfB$_2$-20%SiC-5 oxide scale. Test ran at 100 MPa for 10 hours at 1500°C in air.

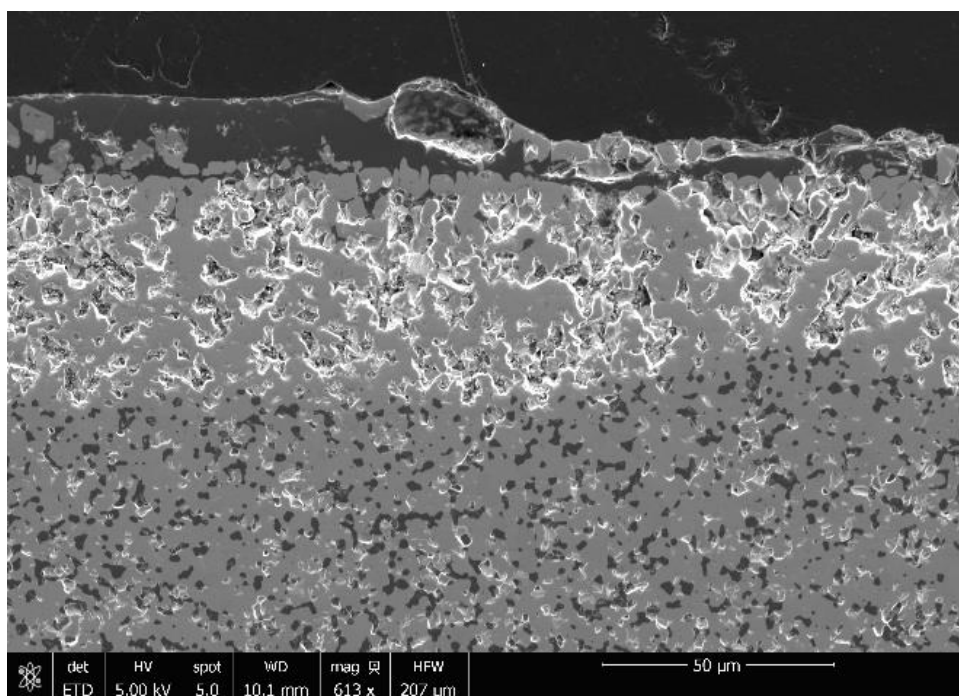Figure 75. SEM Micrograph of HfB$_2$-20%SiC-5 oxide scale. Test ran at 100 MPa for 10 hours at 1500°C in air.

Figure 76. SEM Micrograph of HfB$_2$-20%SiC-5 oxide scale. Test ran at 100 MPa for 10 hours at 1500°C in air.

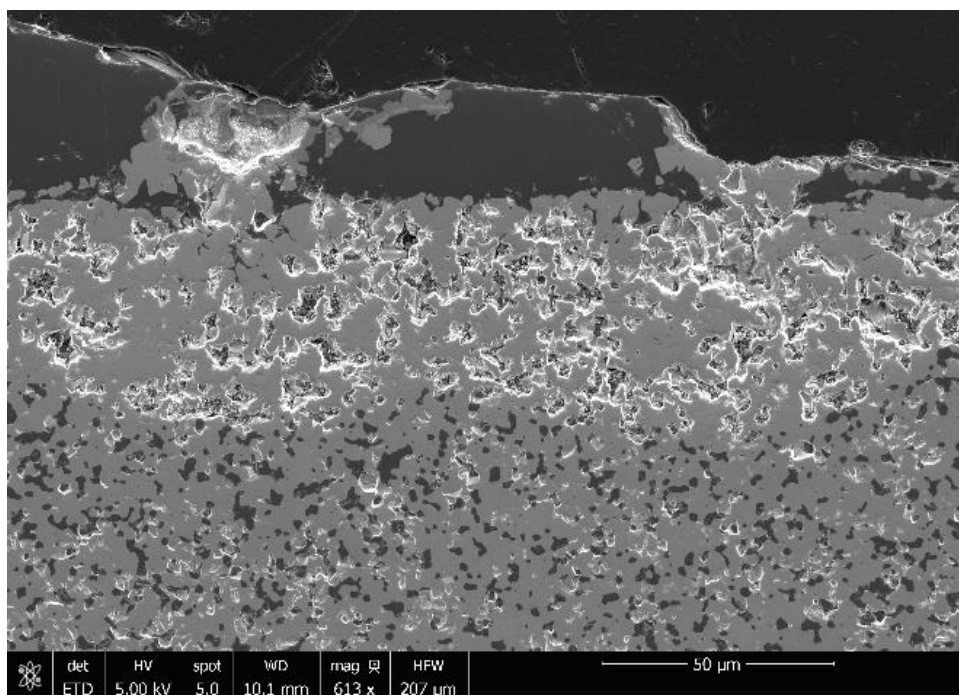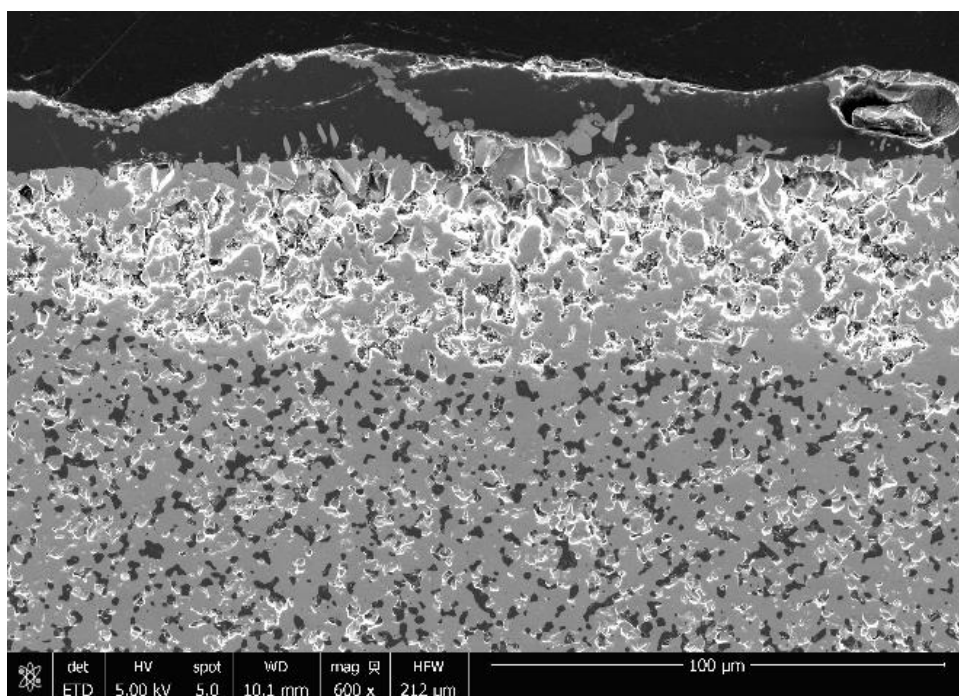Figure 77. SEM Micrograph of HfB$_2$-20%SiC-5 oxide scale. Test ran at 100 MPa for 10 hours at 1500°C in air.

Figure 78. SEM Micrograph of HfB$_2$-20%SiC-5 oxide scale. Test ran at 100 MPa for 10 hours at 1500°C in air.

Figure 79. SEM Micrograph of HfB$_2$-20%SiC-5 oxide scale. Test ran at 100 MPa for 10 hours at 1500°C in air.

Figure 80. SEM Micrograph of HfB$_2$-20%SiC-5 oxide scale. Test ran at 100 MPa for 10 hours at 1500°C in air.

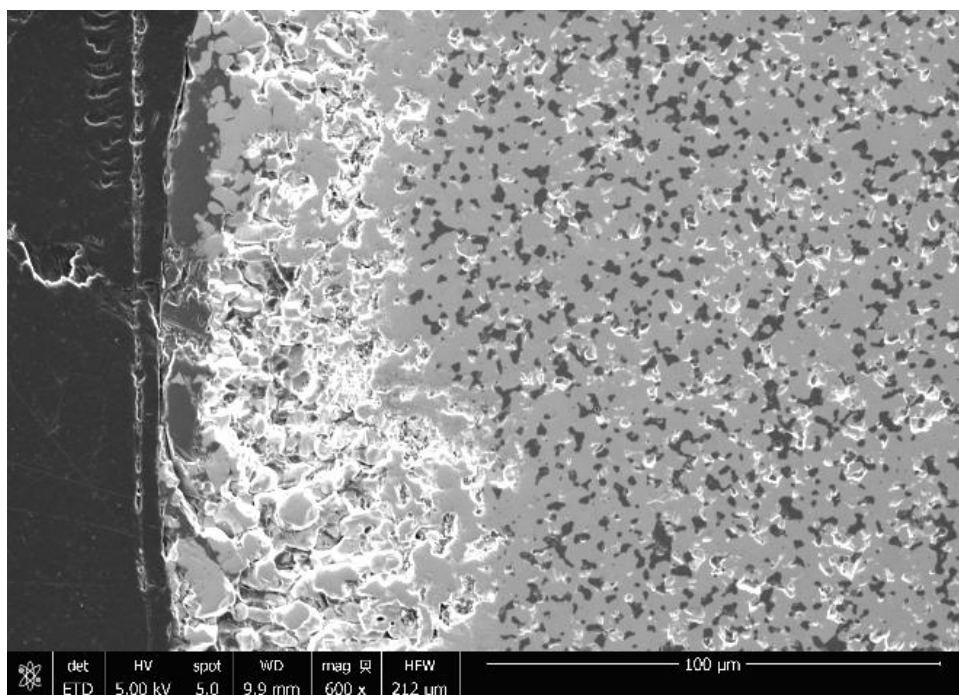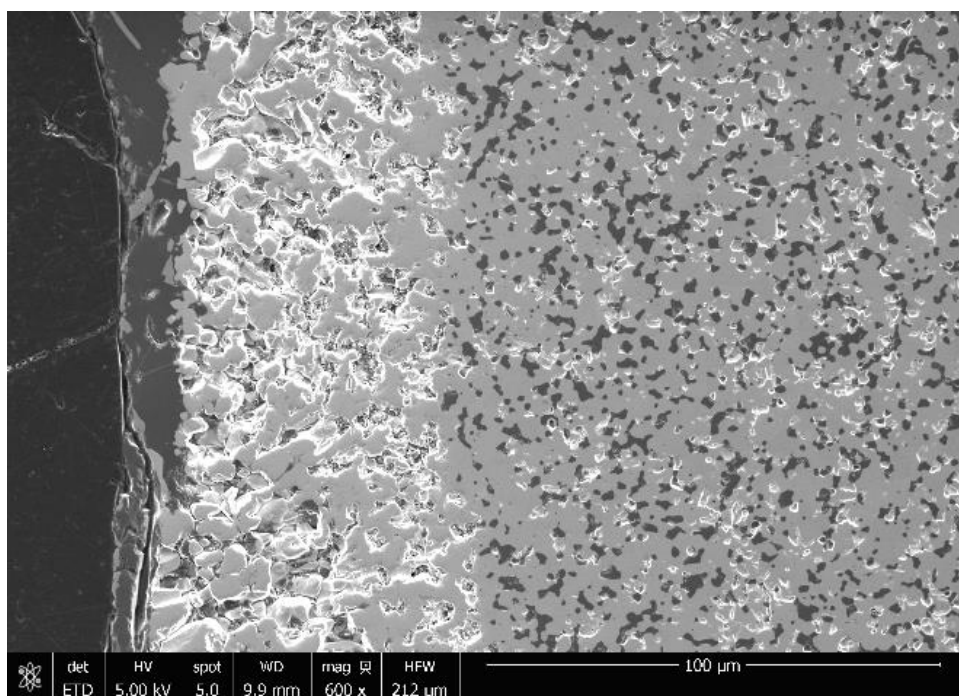Figure 81. SEM Micrograph of HfB$_2$-20%SiC-5 oxide scale. Test ran at 100 MPa for 10 hours at 1500°C in air.

Figure 82. SEM Micrograph of HfB$_2$-20%SiC-5 oxide scale. Test ran at 100 MPa for 10 hours at 1500°C in air.
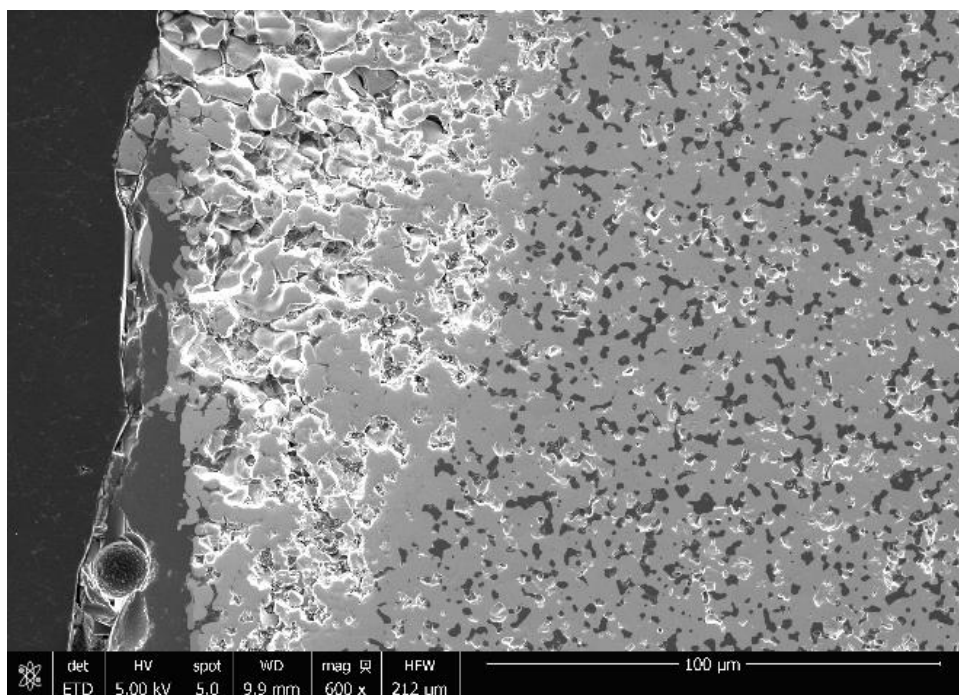
Figure 83. SEM Micrograph of HfB$_2$-20%SiC-5 oxide scale. Test ran at 100 MPa for 10 hours at 1500°C in air.

Figure 84. SEM Micrograph of HfB$_2$-20%SiC-5 oxide scale. Test ran at 100 MPa for 10 hours at 1500°C in air.

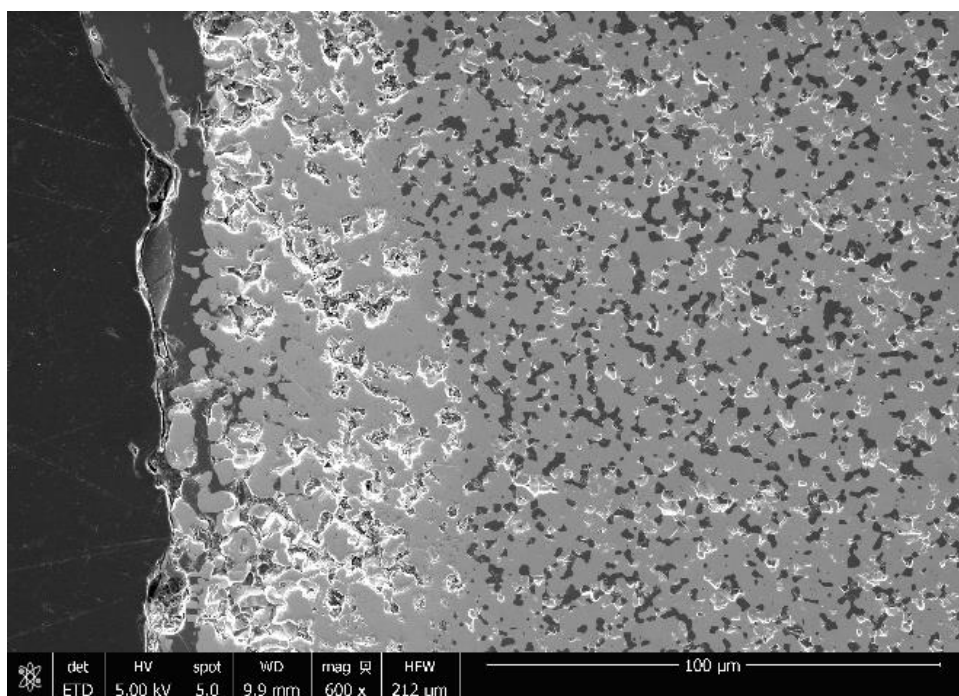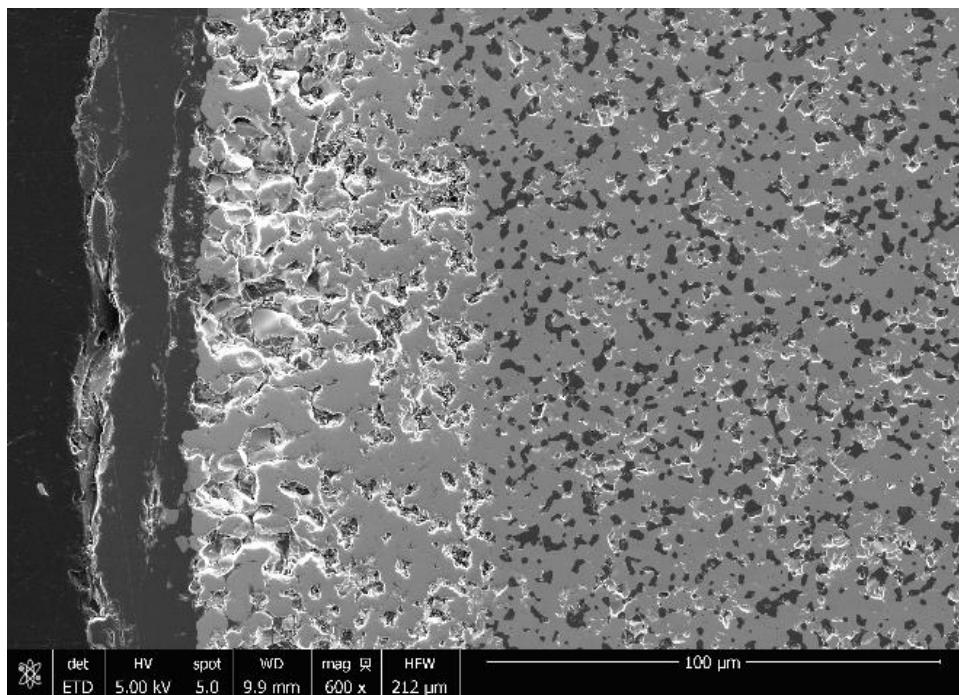Figure 85. SEM Micrograph of HfB$_2$-20%SiC-5 oxide scale. Test ran at 100 MPa for 10 hours at 1500°C in air.

Figure 86. SEM Micrograph of HfB$_2$-20%SiC-5 oxide scale. Test ran at 100 MPa for 10 hours at 1500°C in air. Note presence of air bubbles under glass scale. Also notice negligible corner effects on oxidation thickness. Corner effects are much more prevalent for 0% SiC specimen according to Bowen and DeGregoria.
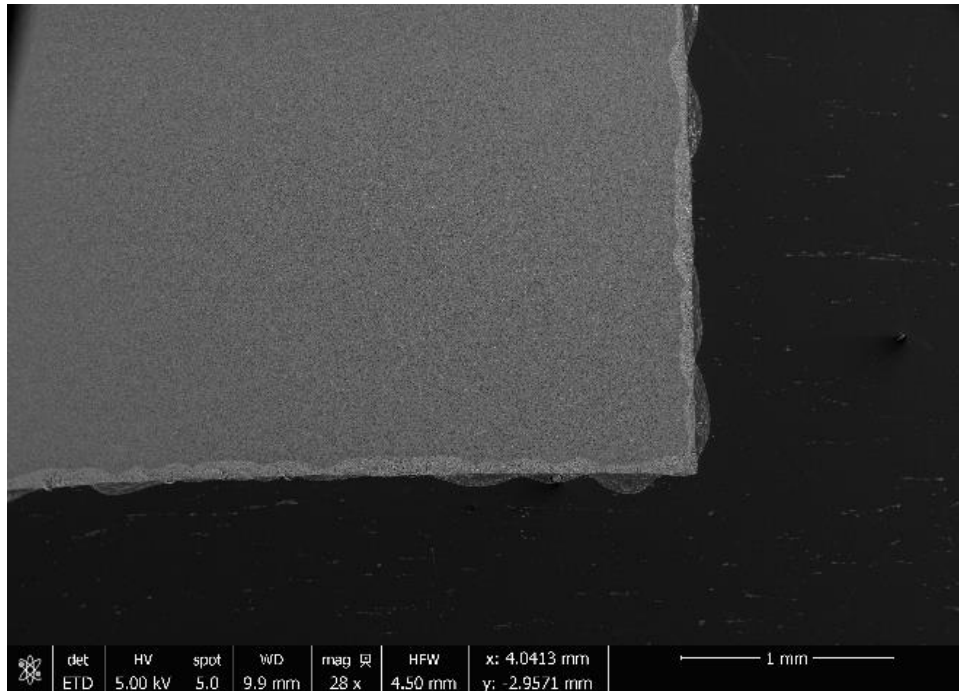
Figure 87. SEM Micrograph of HfB$_2$-20%SiC-5 oxide scale. Test ran at 100 MPa for 10 hours at 1500°C in air. Also notice negligible corner effects on oxidation thickness. Corner effects are much more prevalent for 0% SiC specimen according to Bowen and DeGregoria.
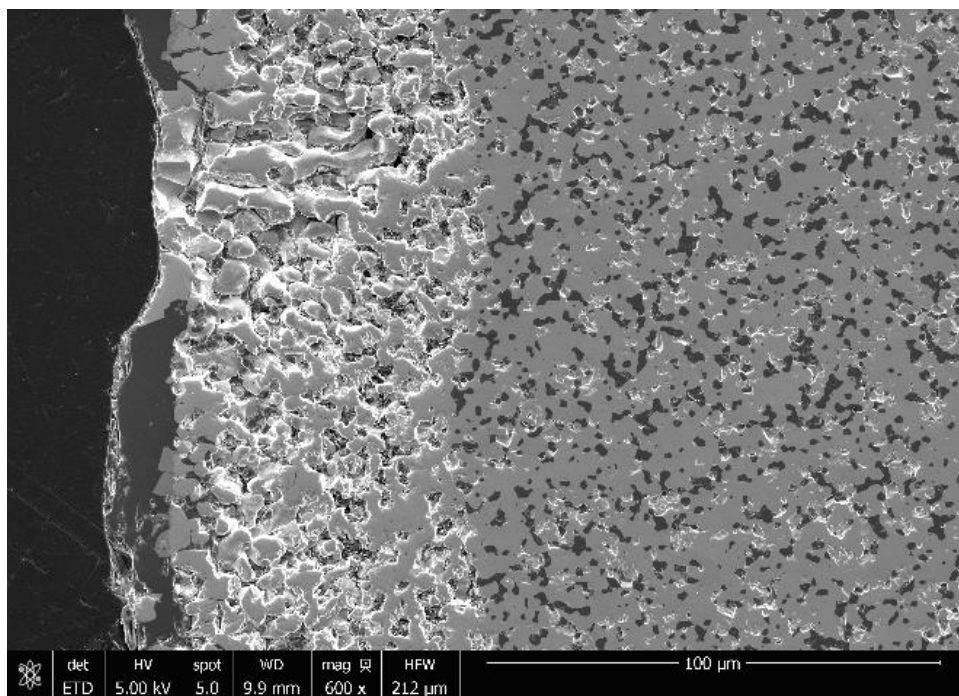

Figure 88. SEM Micrograph of HfB$_2$-20%SiC-6 oxide scale. Test ran at 75 MPa for 10 hours at 1500°C in air.

Figure 89. SEM Micrograph of HfB$_2$-20%SiC-6 oxide scale. Test ran at 75 MPa for 10 hours at 1500°C in air.

Figure 90. SEM Micrograph of HfB$_2$-20%SiC-6 oxide scale. Test ran at 75 MPa for 10 hours at 1500°C in air.
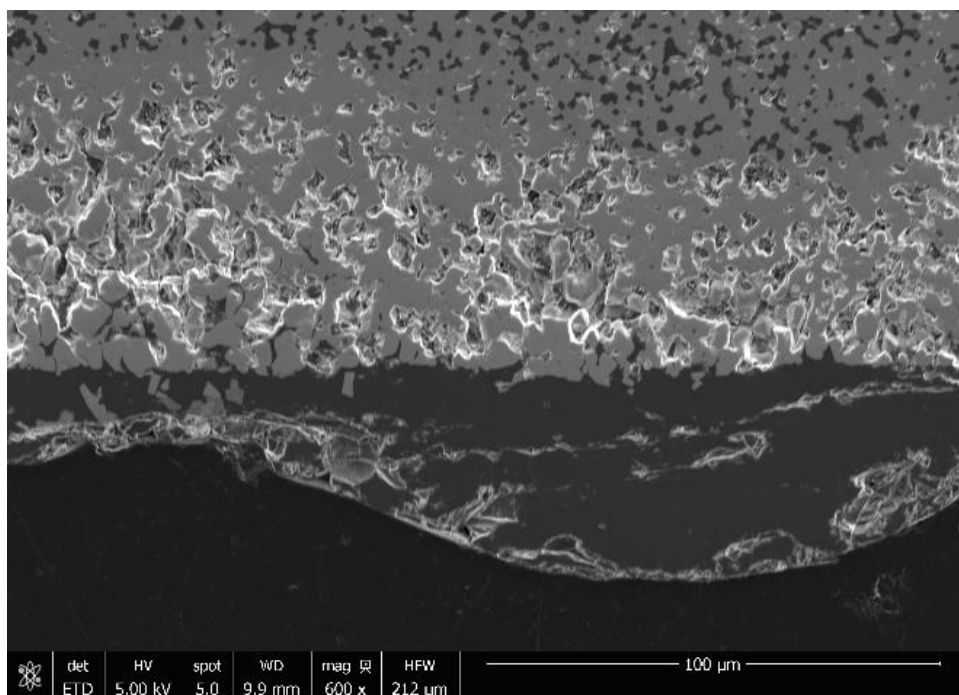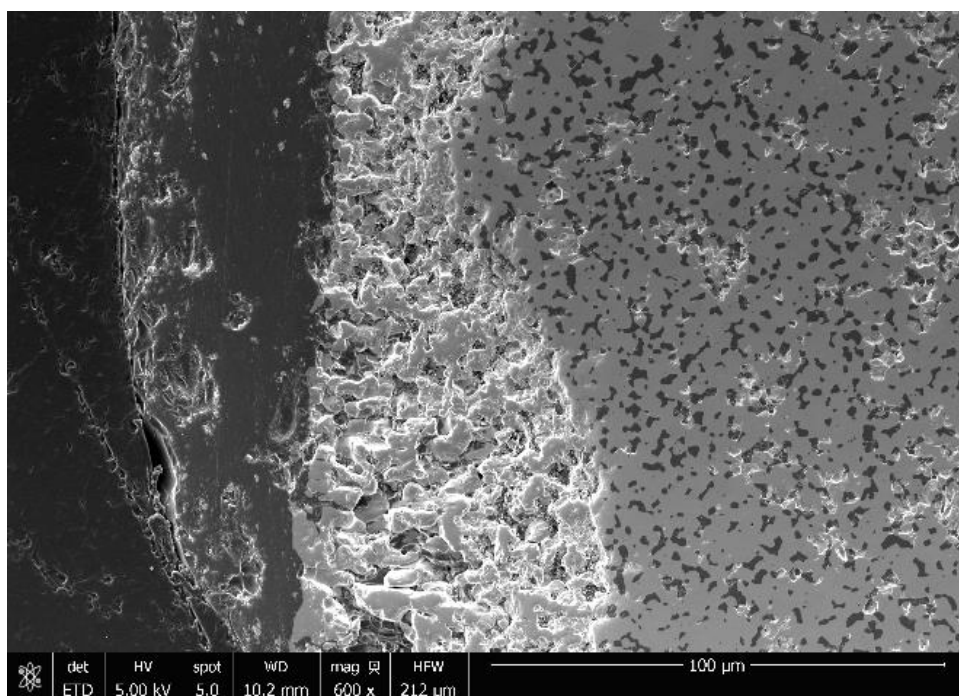
Figure 91. SEM Micrograph of HfB$_2$-20%SiC-6 oxide scale. Test ran at 75 MPa for 10 hours at 1500°C in air.

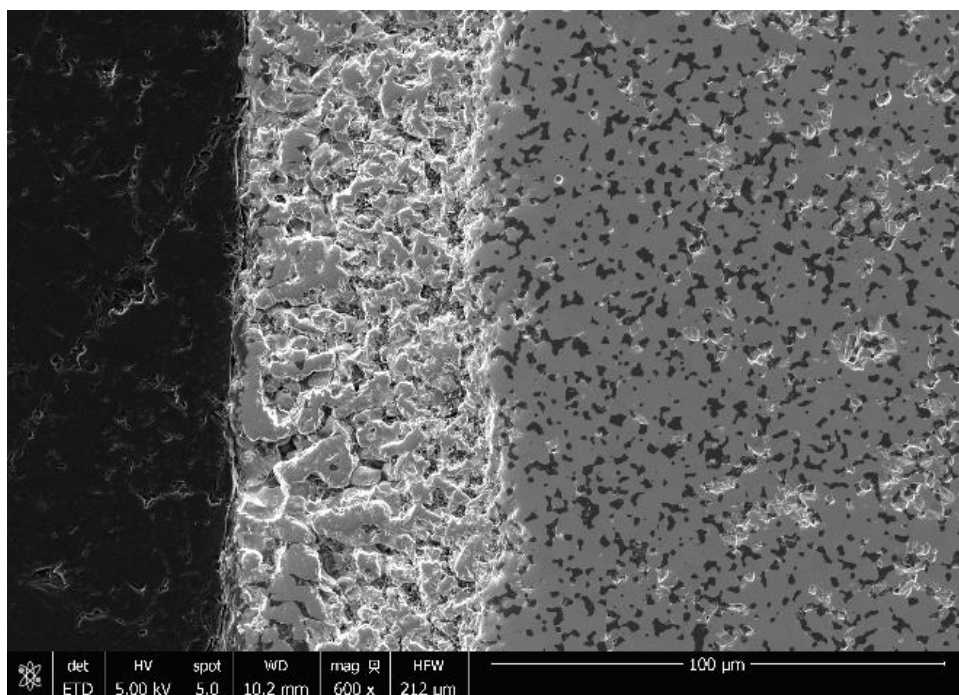Figure 92. SEM Micrograph of HfB$_2$-20%SiC-6 oxide scale. Test ran at 75 MPa for 10 hours at 1500°C in air.

Figure 93. SEM Micrograph of HfB$_2$-20%SiC-6 oxide scale. Test ran at 75 MPa for 10 hours at 1500°C in air.

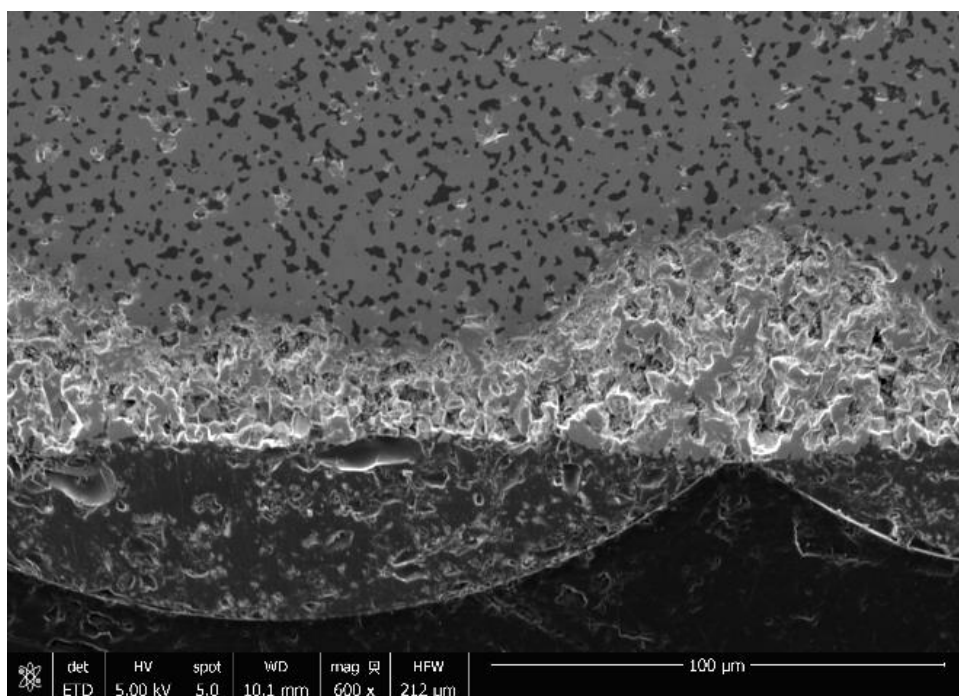Figure 94. SEM Micrograph of HfB$_2$-20%SiC-6 oxide scale. Test ran at 75 MPa for 10 hours at 1500°C in air.

Figure 95. SEM Micrograph of HfB$_2$-20%SiC-6 oxide scale. Test ran at 75 MPa for 10 hours at 1500°C in air.

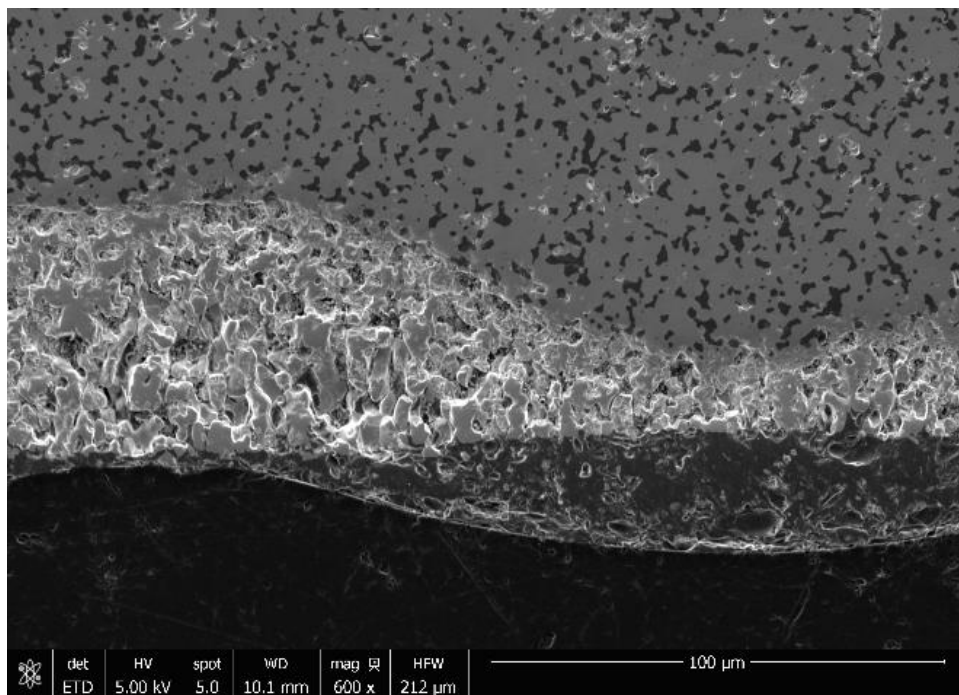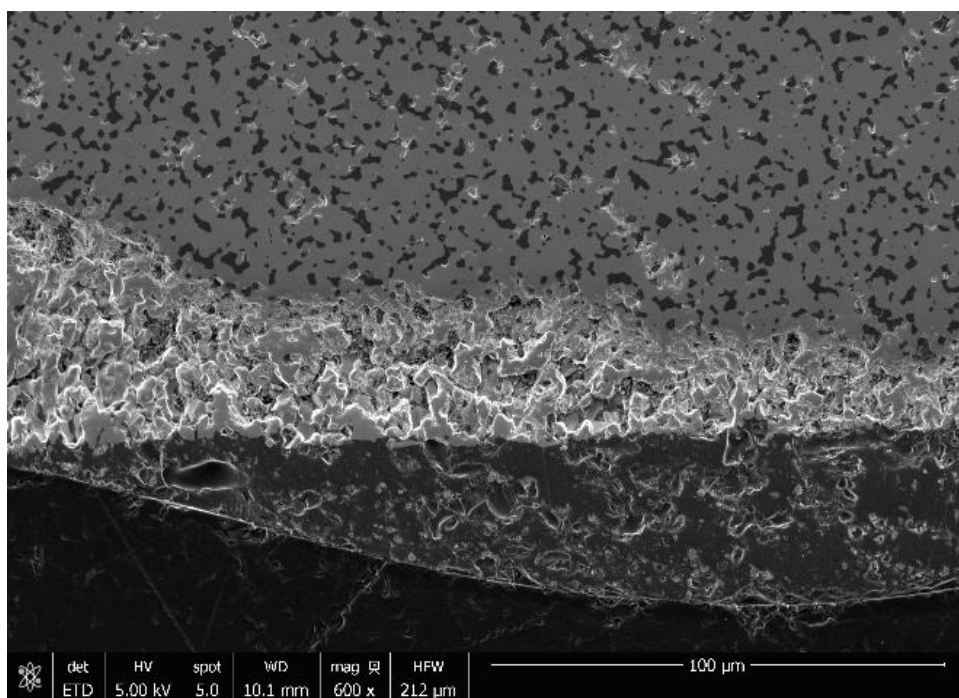Figure 96. SEM Micrograph of HfB$_2$-20%SiC-6 oxide scale. Test ran at 75 MPa for 10 hours at 1500°C in air.

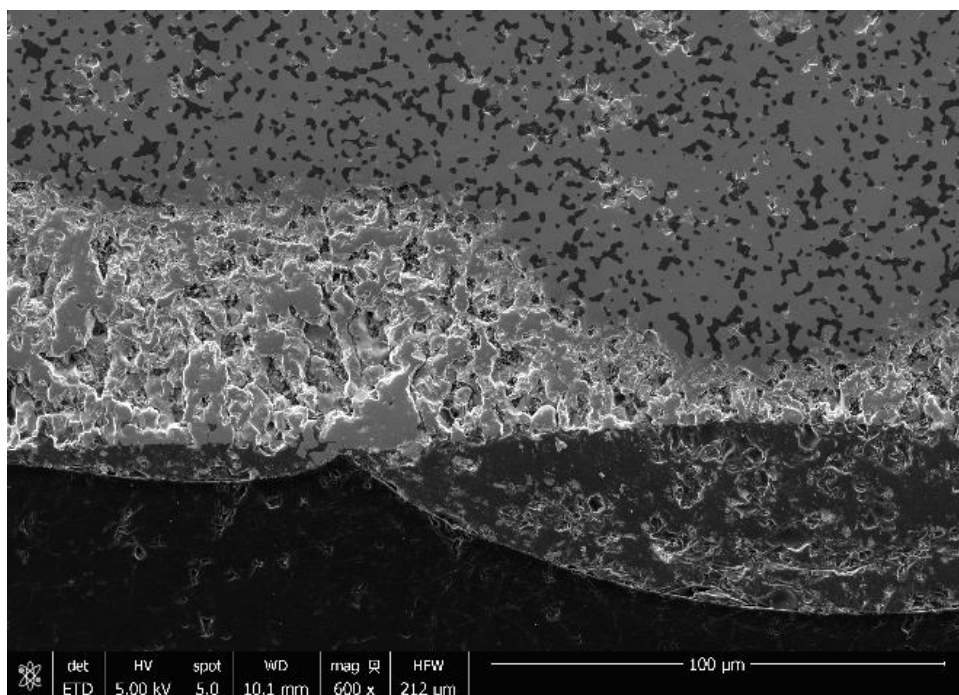Figure 97. SEM Micrograph of HfB$_2$-20%SiC-6 oxide scale. Test ran at 75 MPa for 10 hours at 1500°C in air.

Figure 98. SEM Micrograph of HfB$_2$-20%SiC-6 oxide scale. Test ran at 75 MPa for 10 hours at 1500°C in air.

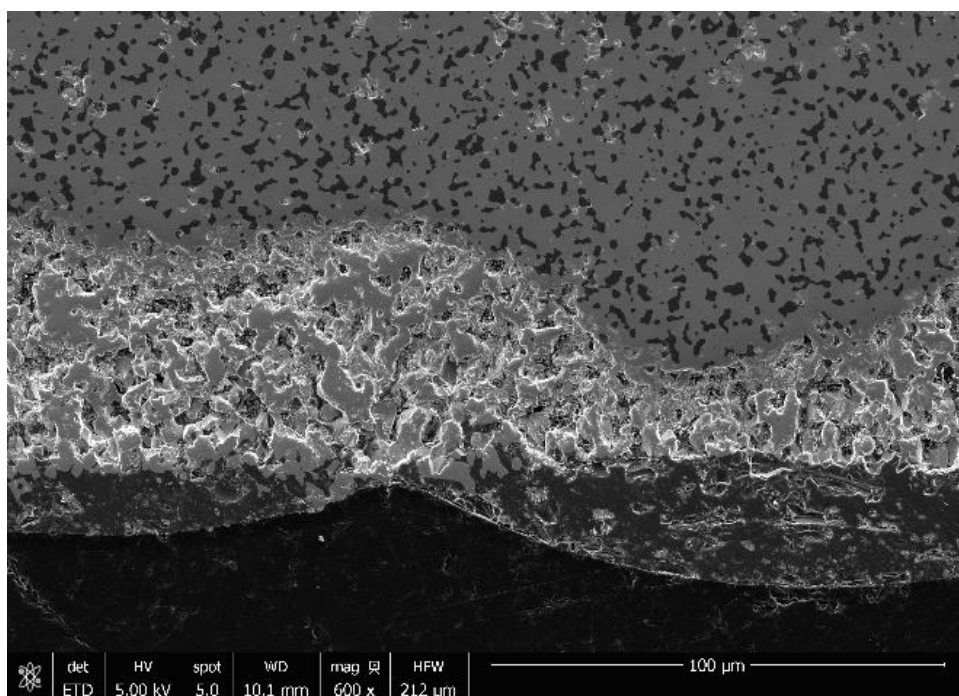Figure 99. SEM Micrograph of HfB$_2$-20%SiC-6 oxide scale. Test ran at 75 MPa for 10 hours at 1500°C in air.

Figure 100. SEM Micrograph of HfB$_2$-20%SiC-6 oxide scale. Test ran at 75 MPa for 10 hours at 1500°C in air.

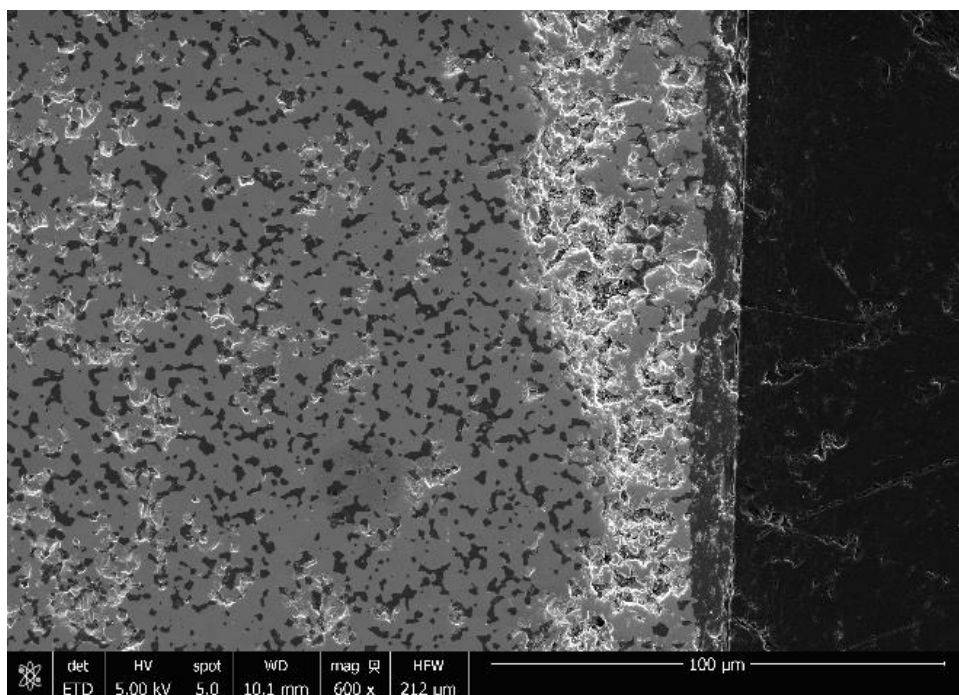Figure 101. SEM Micrograph of HfB$_2$-20%SiC-6 oxide scale. Test ran at 75 MPa for 10 hours at 1500°C in air.

Figure 102. SEM Micrograph of HfB$_2$-20%SiC-6 oxide scale. Test ran at 75 MPa for 10 hours at 1500°C in air.

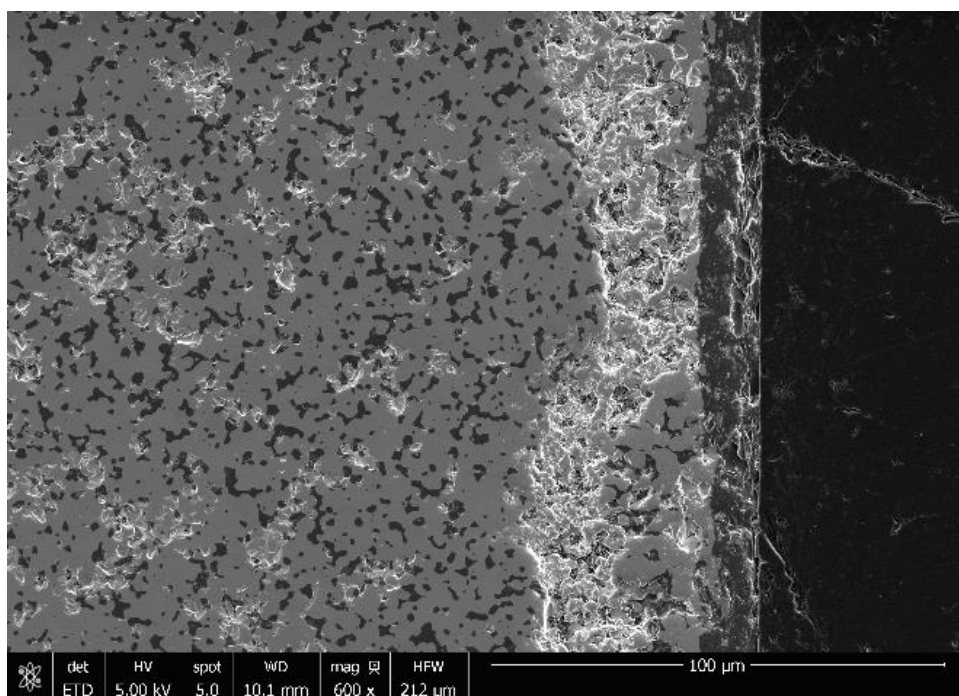Figure 103. SEM Micrograph of HfB$_2$-20%SiC-6 oxide scale. Test ran at 75 MPa for 10 hours at 1500°C in air.

Figure 104. SEM Micrograph of HfB$_2$-20%SiC-6 oxide scale. Test ran at 75 MPa for 10 hours at 1500°C in air.

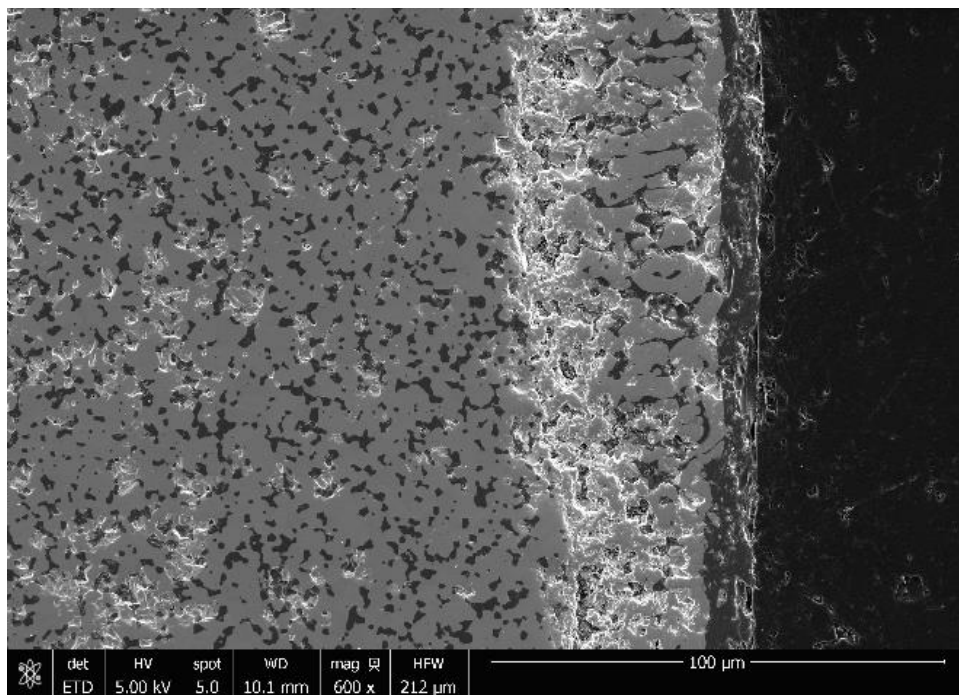Figure 105. SEM Micrograph of HfB$_2$-20%SiC-6 oxide scale. Test ran at 75 MPa for 10 hours at 1500°C in air.

Figure 106. SEM Micrograph of HfB$_2$-20%SiC-6 oxide scale. Test ran at 75 MPa for 10 hours at 1500°C in air.

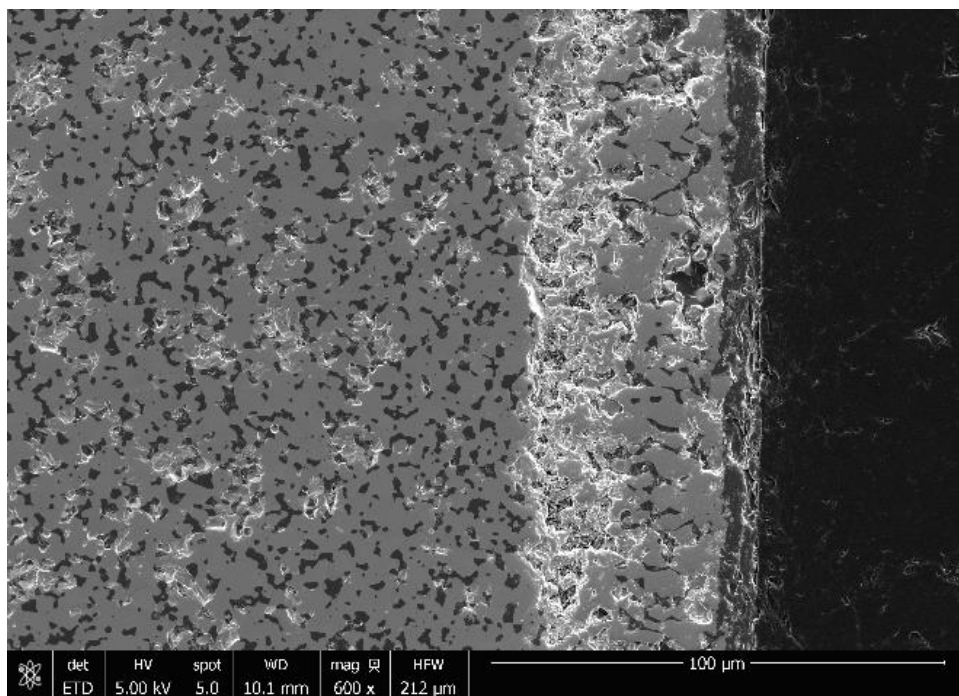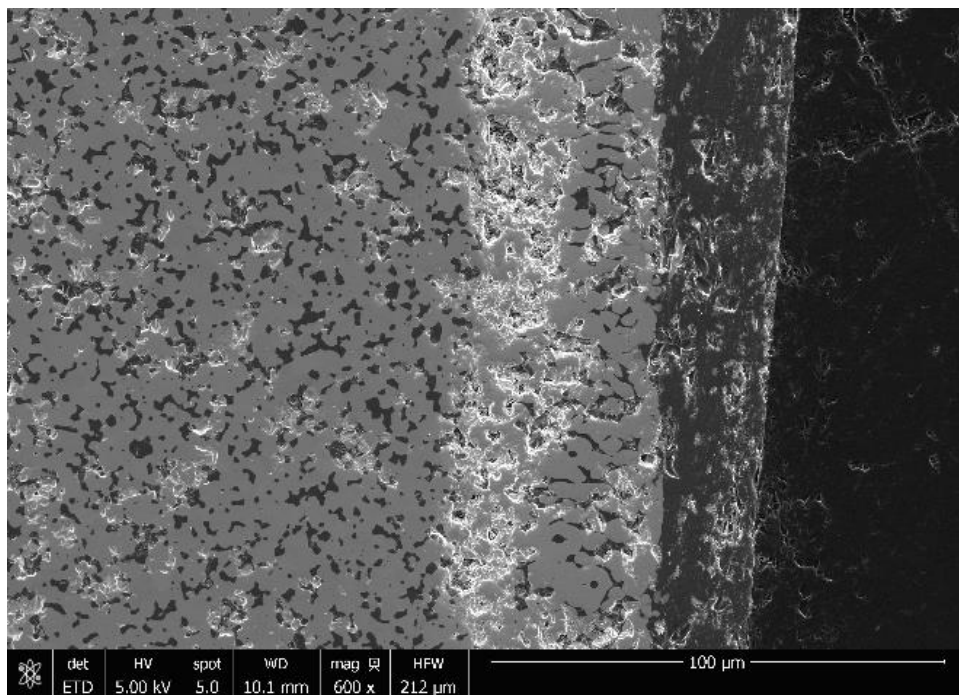Figure 107. SEM Micrograph of HfB$_2$-20%SiC-6 oxide scale. Test ran at 75 MPa for 10 hours at 1500°C in air.

Figure 108. SEM Micrograph of HfB$_2$-20%SiC-6 oxide scale. Test ran at 75 MPa for 10 hours at 1500°C in air.

Figure 109. SEM Micrograph of HfB$_2$-20%SiC-6 oxide scale. Test ran at 75 MPa for 10 hours at 1500°C in air.

Figure 110. SEM Micrograph of HfB$_2$-20%SiC-6 oxide scale. Test ran at 75 MPa for 10 hours at 1500°C in air.

Figure 111. SEM Micrograph of HfB$_2$-20%SiC-6 oxide scale. Test ran at 75 MPa for 10 hours at 1500°C in air.

Figure 112. SEM Micrograph of HfB$_2$-20%SiC-9 oxide scale. Test ran at 150 MPa for 6.03 hours at 1500°C in air.

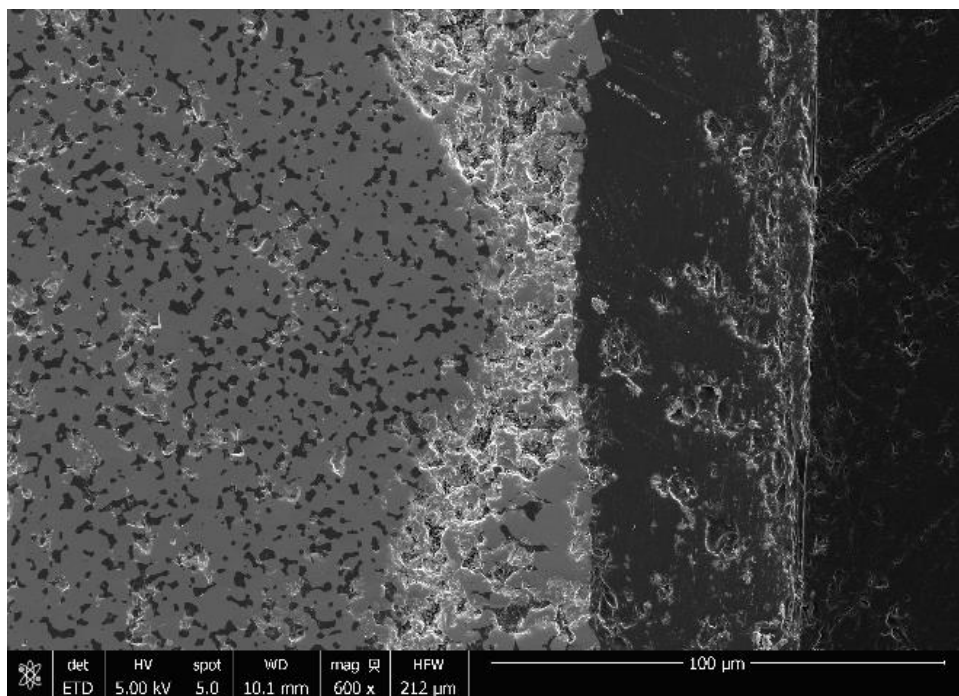Figure 113. SEM Micrograph of HfB$_2$-20%SiC-9 oxide scale. Test ran at 150 MPa for 6.03 hours at 1500°C in air.

Figure 114. SEM Micrograph of HfB$_2$-20%SiC-9 oxide scale. Test ran at 150 MPa for 6.03 hours at 1500°C in air.
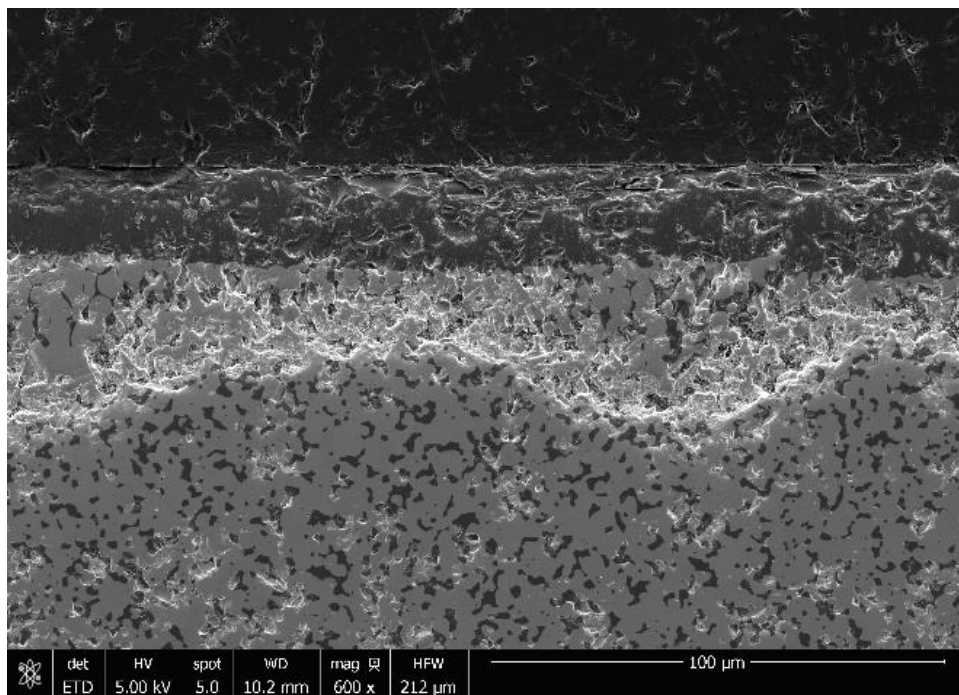
Figure 115. SEM Micrograph of HfB$_2$-20%SiC-9 oxide scale. Test ran at 150 MPa for 6.03 hours at 1500°C in air.
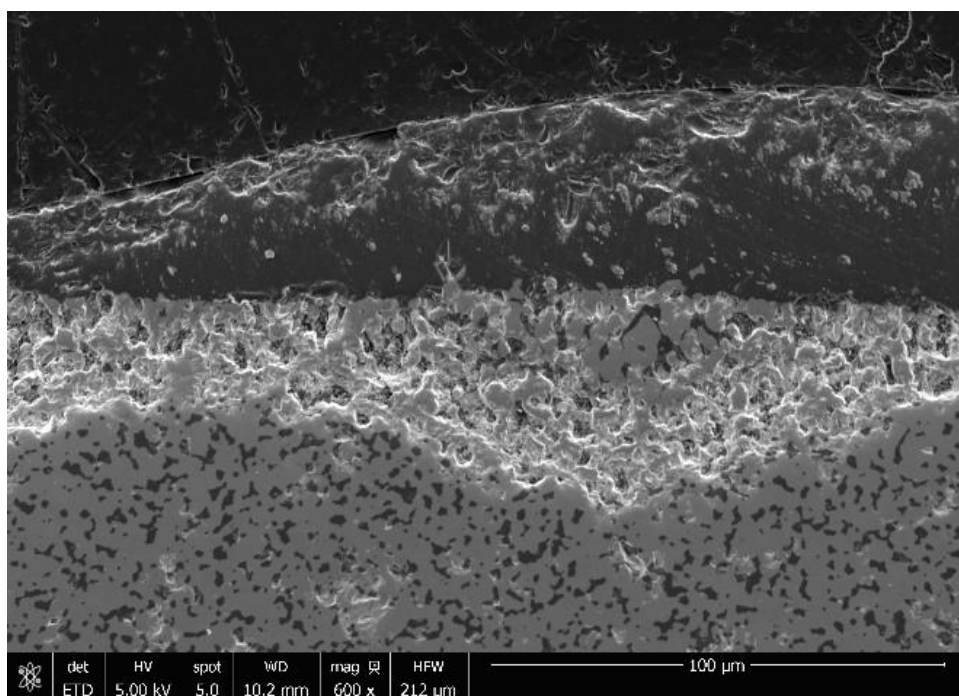

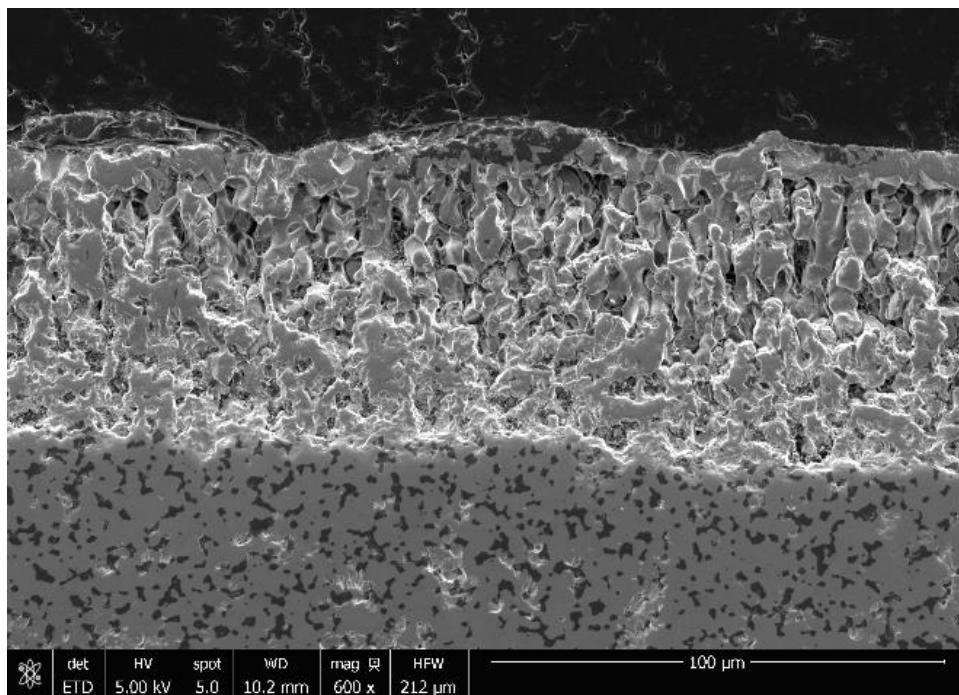Figure 116. SEM Micrograph of HfB$_2$-20%SiC-9 oxide scale. Test ran at 150 MPa for 6.03 hours at 1500°C in air.

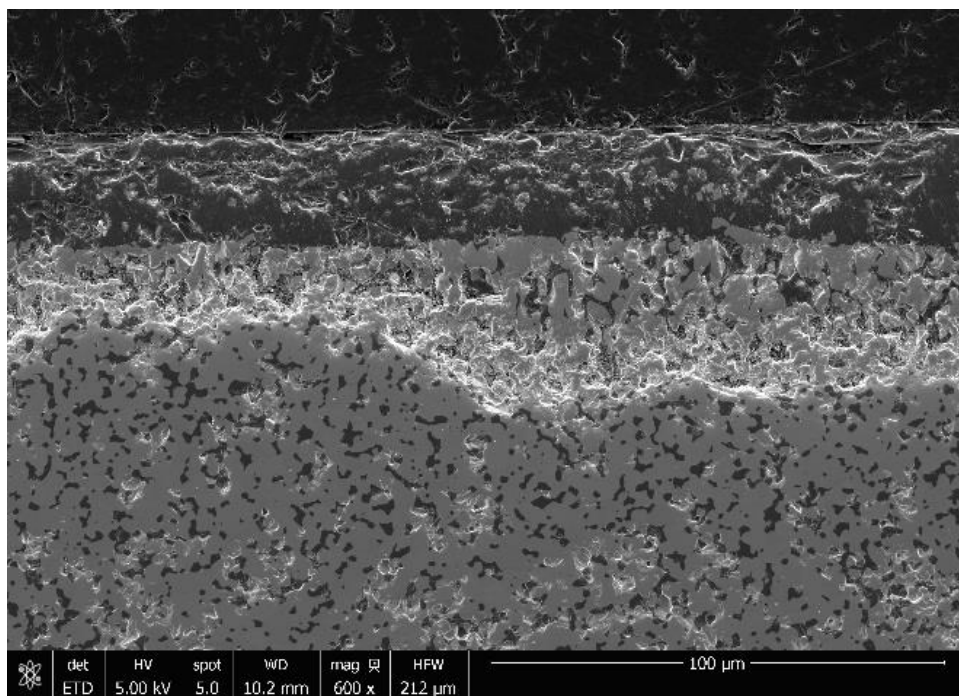Figure 117. SEM Micrograph of HfB$_2$-20%SiC-9 oxide scale. Test ran at 150 MPa for 6.03 hours at 1500°C in air.

Figure 118. SEM Micrograph of HfB$_2$-20%SiC-9 oxide scale. Test ran at 150 MPa for 6.03 hours at 1500°C in air.

Figure 119. SEM Micrograph of HfB$_2$-20%SiC-9 oxide scale. Test ran at 150 MPa for 6.03 hours at 1500°C in air.

Figure 120. SEM Micrograph of HfB$_2$-20%SiC-9 oxide scale. Test ran at 150 MPa for 6.03 hours at 1500°C in air.
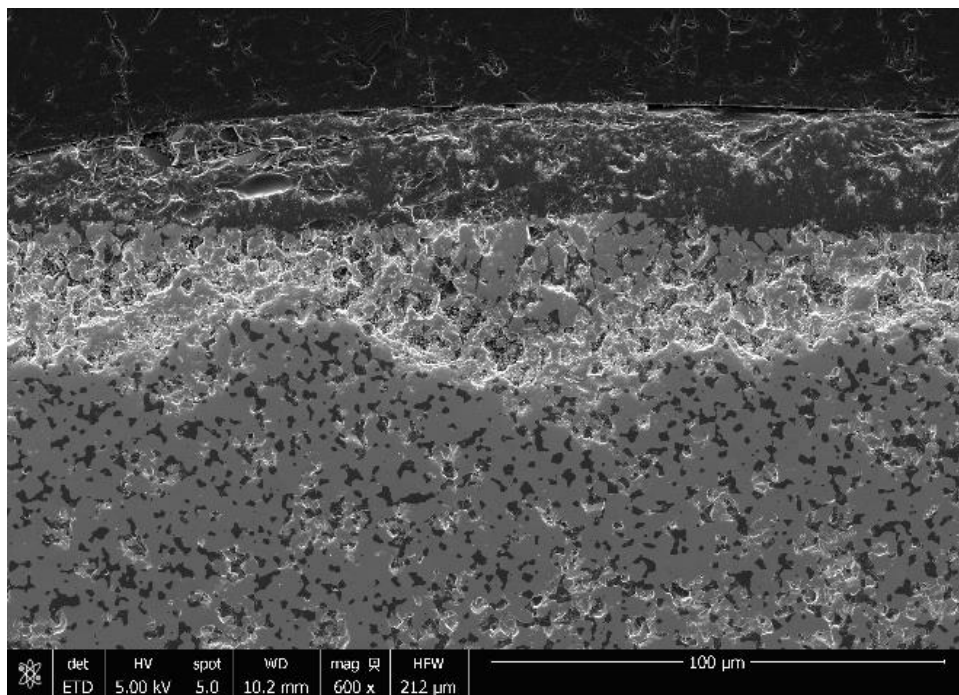
Figure 121. SEM Micrograph of HfB$_2$-20%SiC-9 oxide scale. Test ran at 150 MPa for 6.03 hours at 1500°C in air.
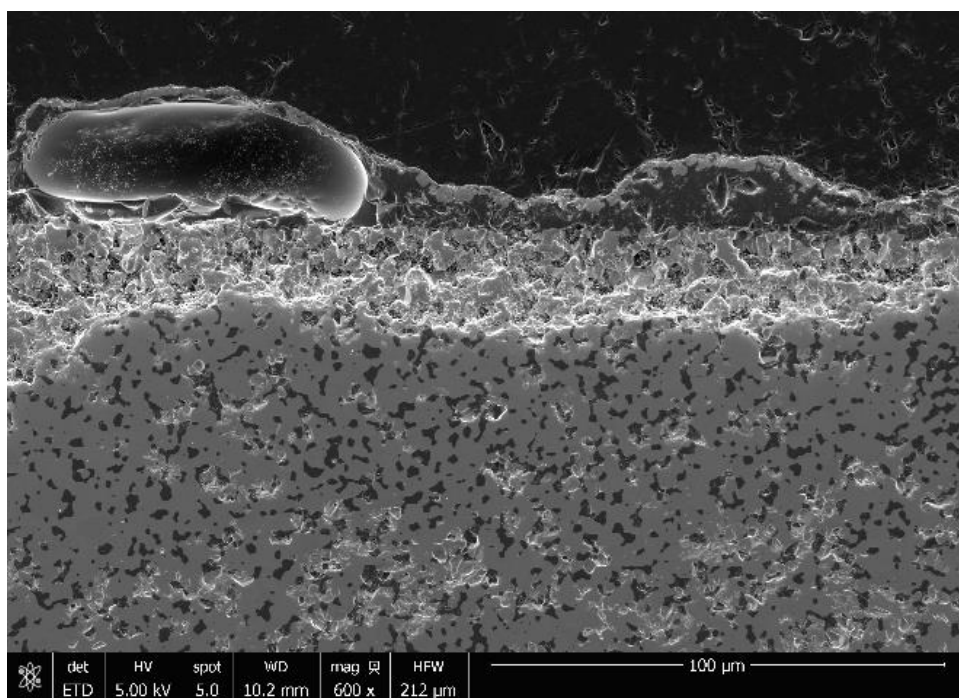

Figure 122. SEM Micrograph of HfB$_2$-20%SiC-9 oxide scale. Test ran at 150 MPa for 6.03 hours at 1500°C in air.

Figure 123. SEM Micrograph of HfB$_2$-20%SiC-9 oxide scale. Test ran at 150 MPa for 6.03 hours at 1500°C in air.
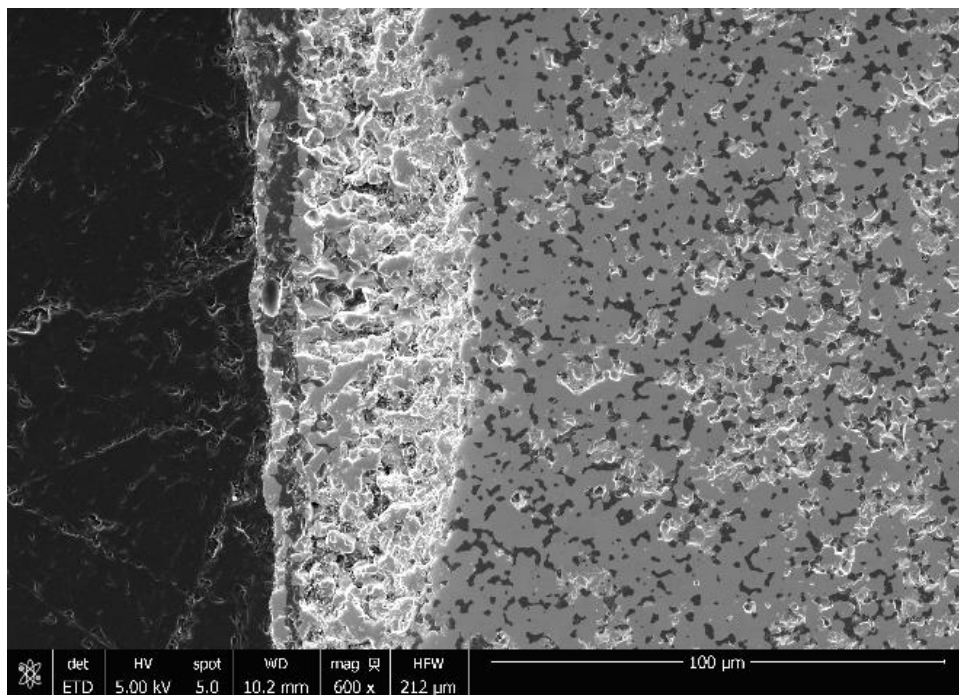

Figure 124. SEM Micrograph of HfB$_2$-20%SiC-9 oxide scale. Test ran at 150 MPa for 6.03 hours at 1500°C in air.

Figure 125. SEM Micrograph of HfB$_2$-20%SiC-9 oxide scale. Test ran at 150 MPa for 6.03 hours at 1500°C in air.
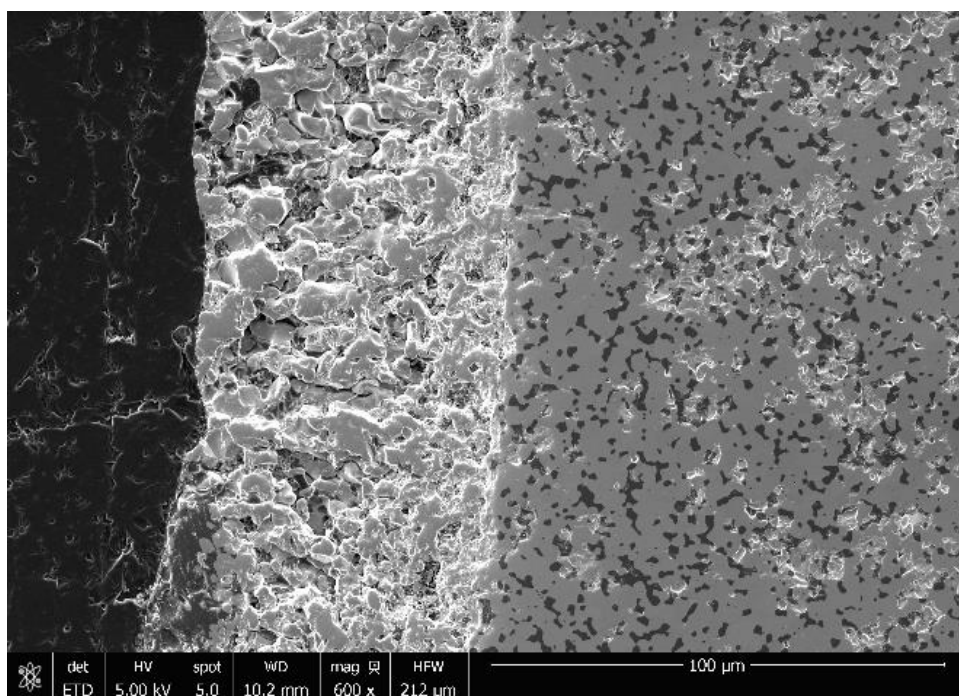

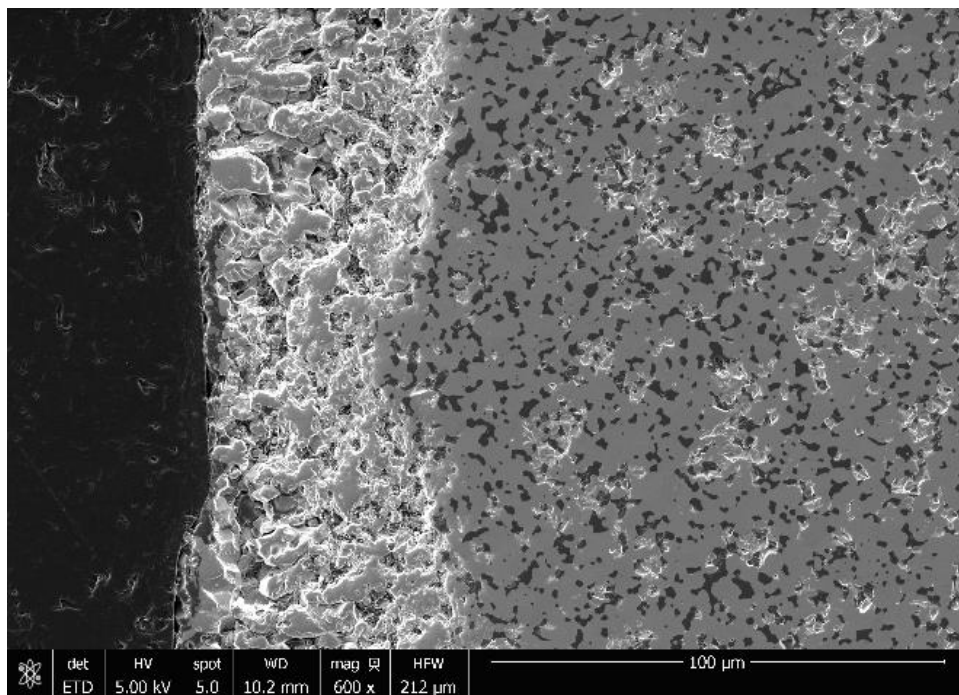Figure 126. SEM Micrograph of HfB$_2$-20%SiC-9 oxide scale. Test ran at 150 MPa for 6.03 hours at 1500°C in air.

Figure 127. SEM Micrograph of HfB$_2$-20%SiC-9 oxide scale. Test ran at 150 MPa for 6.03 hours at 1500°C in air.

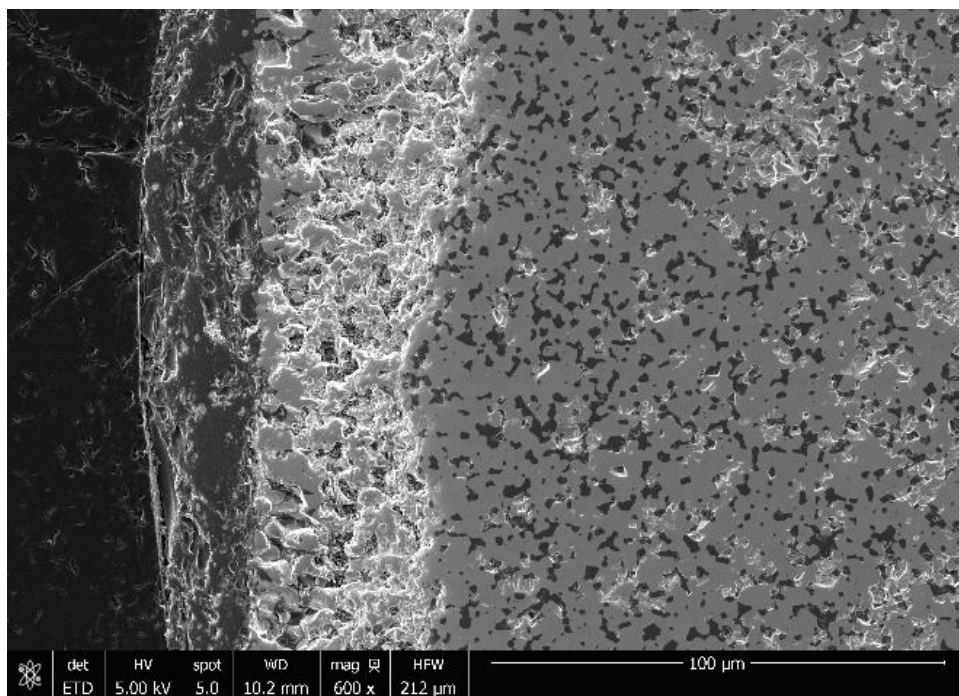Figure 128. SEM Micrograph of HfB$_2$-20%SiC-9 oxide scale. Test ran at 150 MPa for 6.03 hours at 1500°C in air.

Figure 129. SEM Micrograph of HfB$_2$-20%SiC-9 oxide scale. Test ran at 150 MPa for 6.03 hours at 1500°C in air.

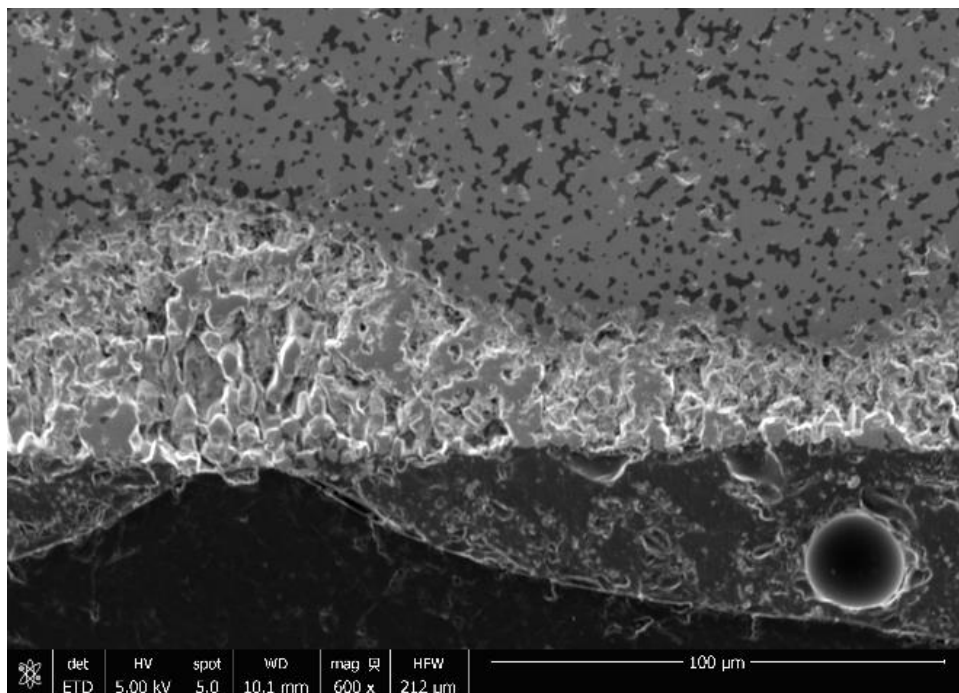Figure 130. SEM Micrograph of HfB$_2$-20%SiC-9 oxide scale. Test ran at 150 MPa for 6.03 hours at 1500°C in air.

Figure 131. SEM Micrograph of HfB$_2$-20%SiC-9 oxide scale. Test ran at 150 MPa for 6.03 hours at 1500°C in air.

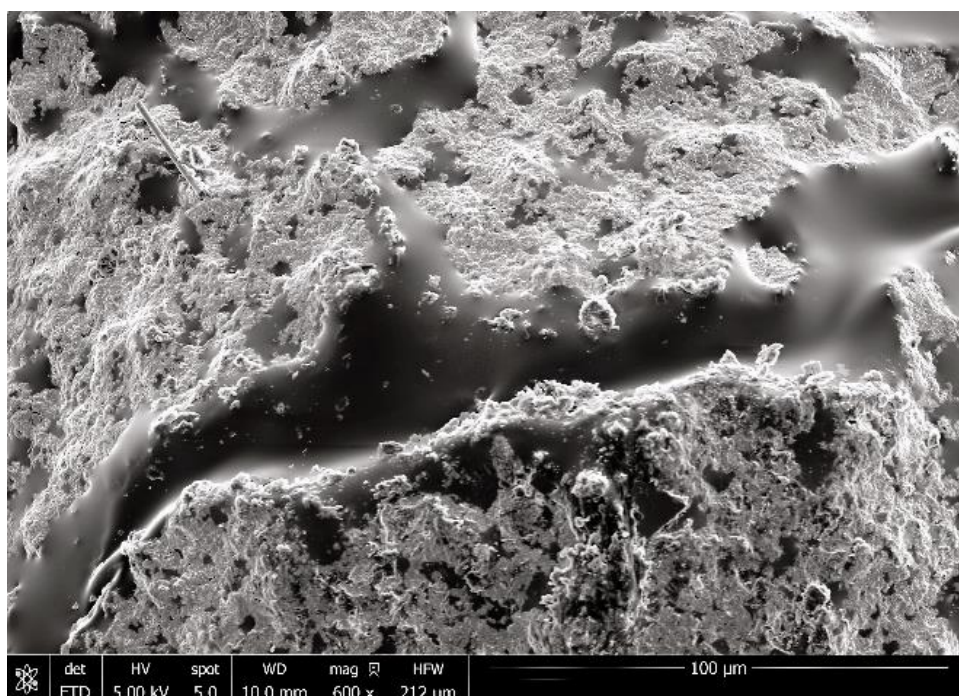Figure 132. SEM Micrograph of HfB$_2$-20%SiC-9 oxide scale. Test ran at 150 MPa for 6.03 hours at 1500°C in air.

Figure 133. SEM Micrograph of HfB$_2$-20%SiC-9 oxide scale. Test ran at 150 MPa for 6.03 hours at 1500°C in air.

Figure 134. SEM Micrograph of HfB$_2$-20%SiC-9 oxide scale. Test ran at 150 MPa for 6.03 hours at 1500°C in air.

Figure 135. SEM Micrograph of HfB$_2$-20%SiC-9 oxide scale. Test ran at 150 MPa for 6.03 hours at 1500°C in air.

Figure 136. SEM Micrograph of HfB$_2$-20%SiC-9 oxide scale. Test ran at 150 MPa for 6.03 hours at 1500°C in air. Note the white hafnia scale with amorphous borosilicate glass filling in cracks and voids.
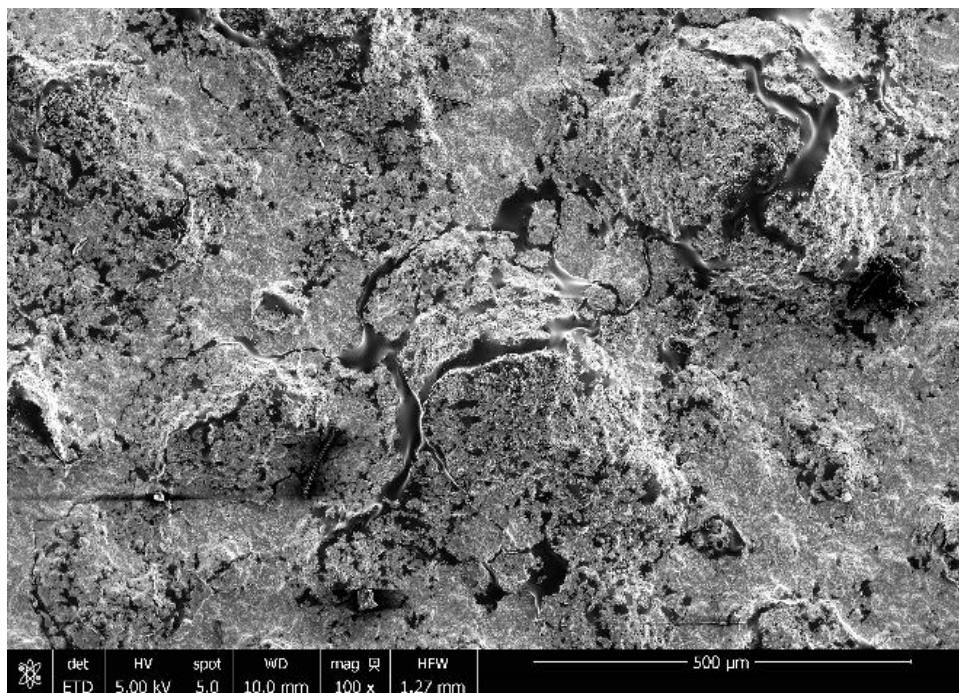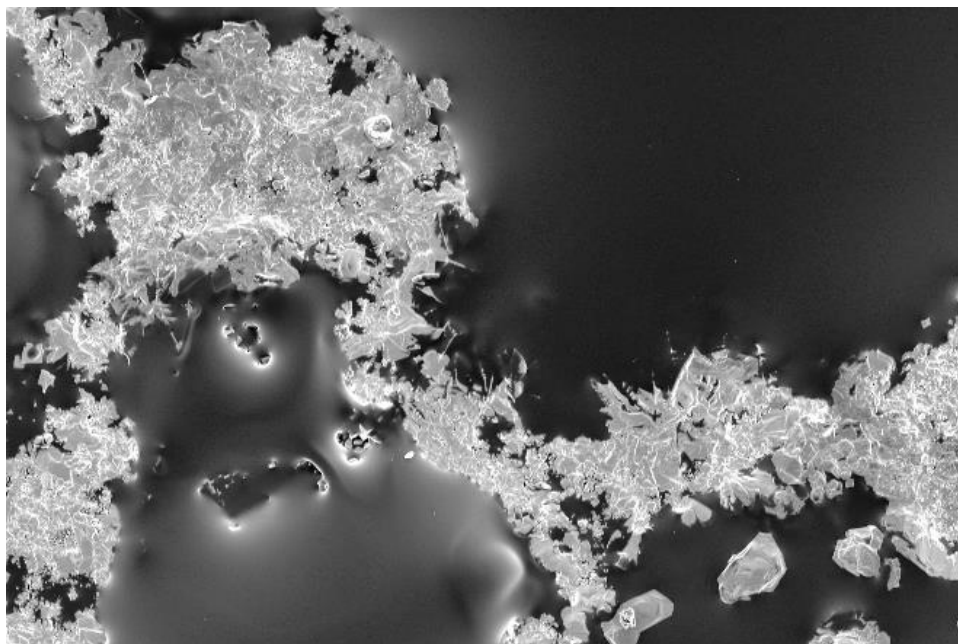
Figure 137. SEM Micrograph of HfB$_2$-20%SiC-9 oxide scale. Test ran at 150 MPa for 6.03 hours at 1500°C in air. Note the white hafnia scale with amorphous borosilicate glass filling in cracks and voids.

Figure 138. SEM Micrograph of HfB$_2$-20%SiC-9 oxide scale. Test ran at 150 MPa for 6.03 hours at 1500°C in air. Note large regions of dark, amorphous borosilicate glassy areas intermixed with crystalline hafnia scale.
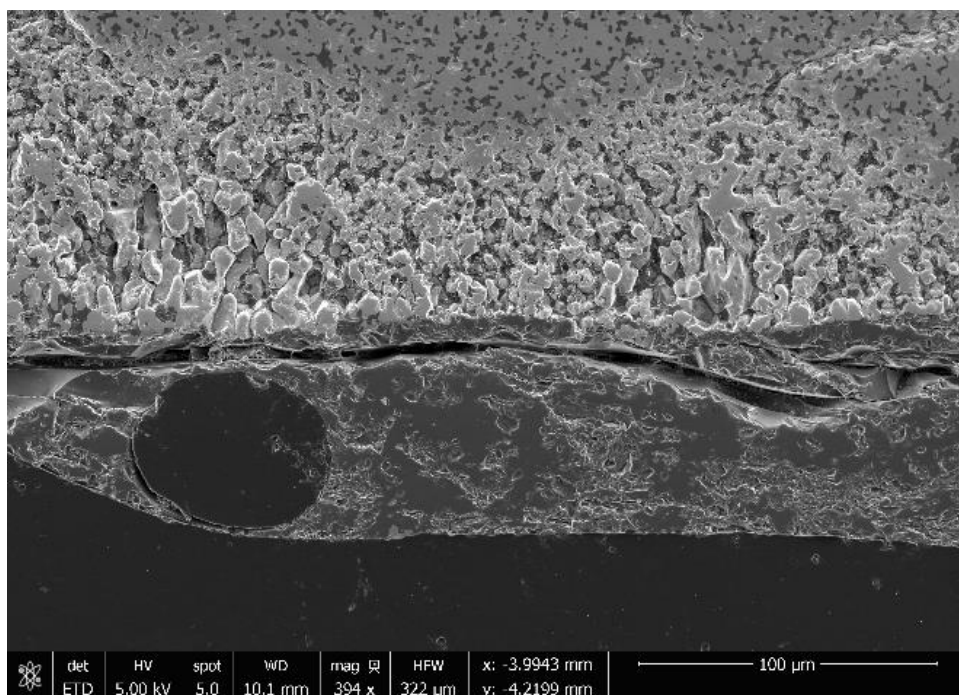
Figure 139. SEM Micrograph of HfB$_2$-20%SiC-10 oxide scale. Test ran at 50 MPa for 20 hours at 1500°C in air.
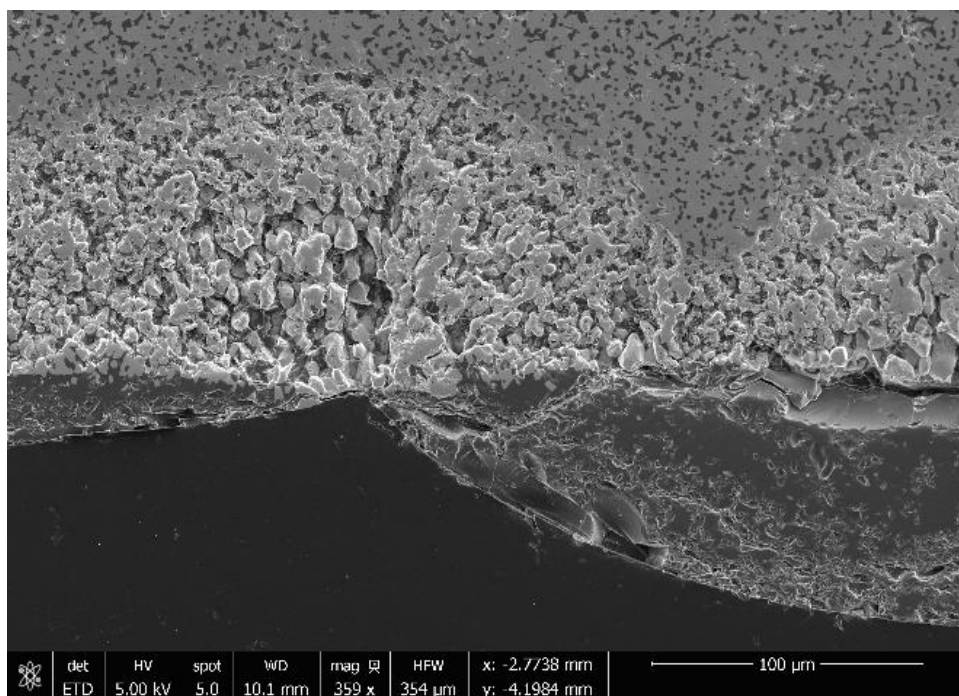

Figure 140. SEM Micrograph of HfB$_2$-20%SiC-10 oxide scale. Test ran at 50 MPa for 20 hours at 1500°C in air.
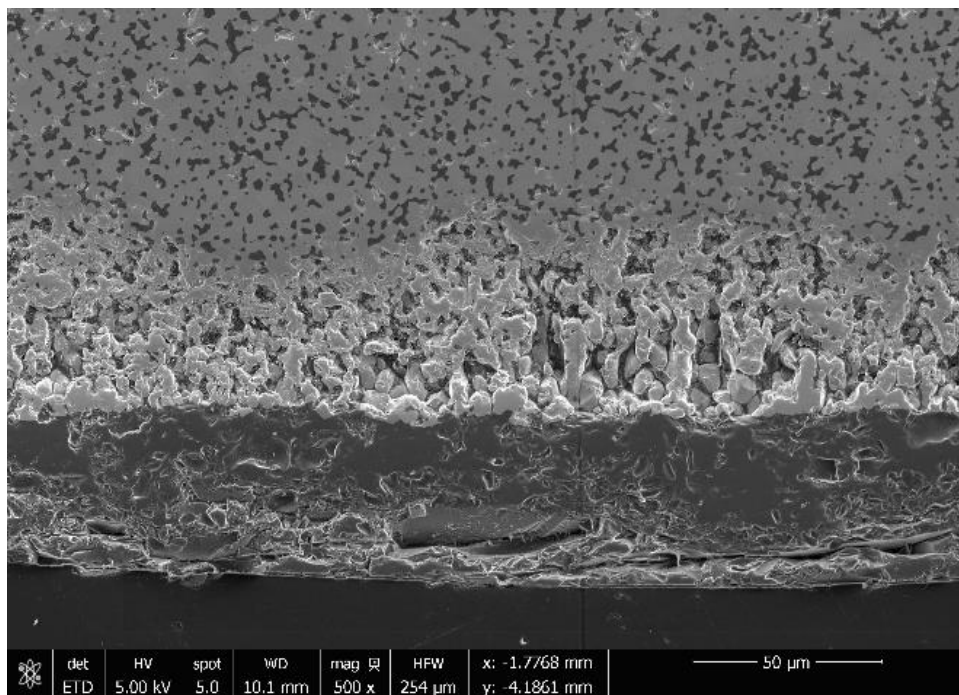
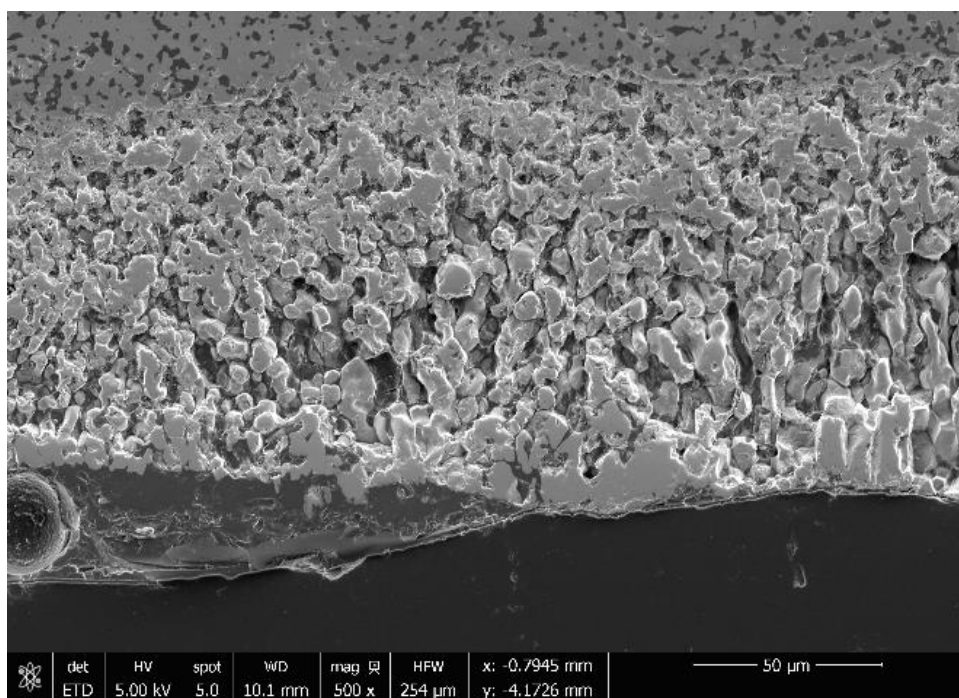Figure 141. SEM Micrograph of HfB$_2$-20%SiC-10 oxide scale. Test ran at 50 MPa for 20 hours at 1500°C in air.

Figure 142. SEM Micrograph of HfB$_2$-20%SiC-10 oxide scale. Test ran at 50 MPa for 20 hours at 1500°C in air.

Figure 143. SEM Micrograph of HfB$_2$-20%SiC-10 oxide scale. Test ran at 50 MPa for 20 hours at 1500°C in air.

Figure 144. SEM Micrograph of HfB$_2$-20%SiC-10 oxide scale. Test ran at 50 MPa for 20 hours at 1500°C in air.
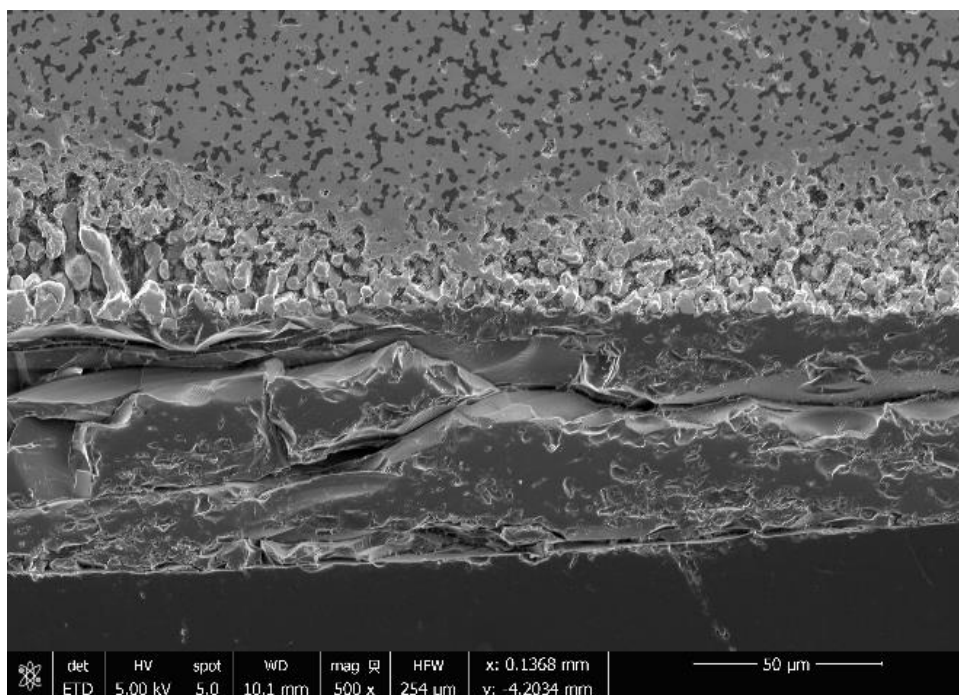
Figure 145. SEM Micrograph of HfB$_2$-20%SiC-10 oxide scale. Test ran at 50 MPa for 20 hours at 1500°C in air.
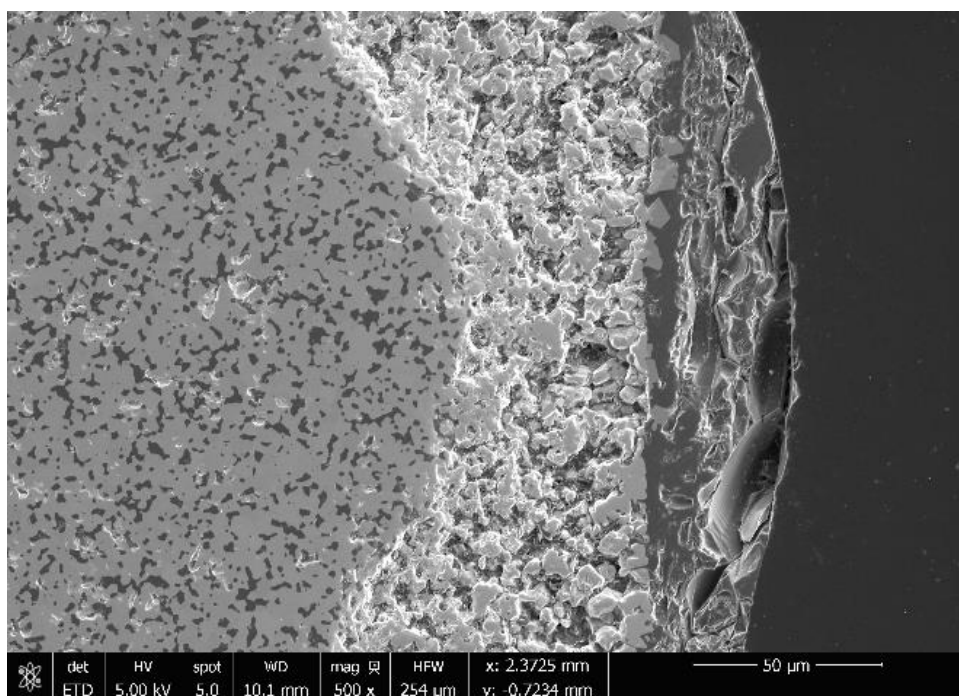

Figure 146. SEM Micrograph of HfB$_2$-20%SiC-10 oxide scale. Test ran at 50 MPa for 20 hours at 1500°C in air.

Figure 147. SEM Micrograph of HfB$_2$-20%SiC-10 oxide scale. Test ran at 50 MPa for 20 hours at 1500°C in air.

Figure 148. SEM Micrograph of HfB$_2$-20%SiC-10 oxide scale. Test ran at 50 MPa for 20 hours at 1500°C in air.
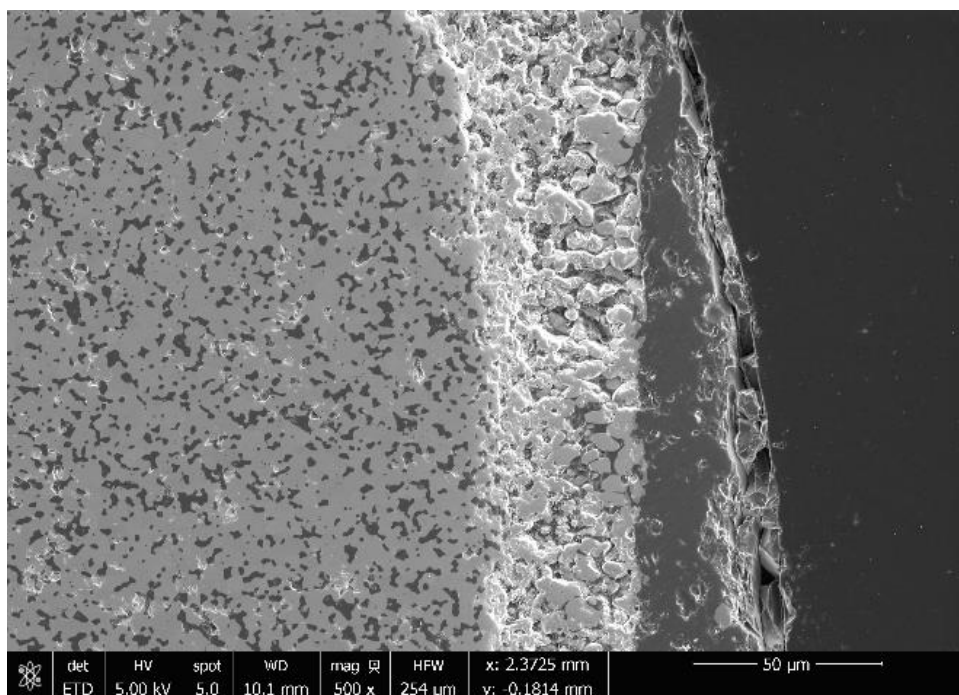
Figure 149. SEM Micrograph of HfB$_2$-20%SiC-10 oxide scale. Test ran at 50 MPa for 20 hours at 1500°C in air.
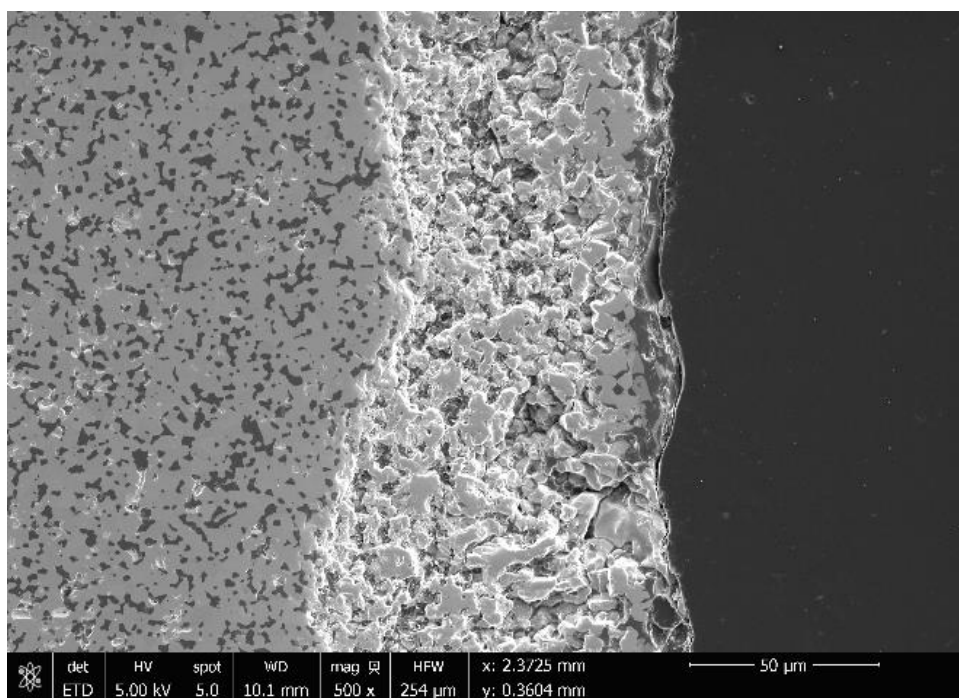

Figure 150. SEM Micrograph of HfB$_2$-20%SiC-10 oxide scale. Test ran at 50 MPa for 20 hours at 1500°C in air.
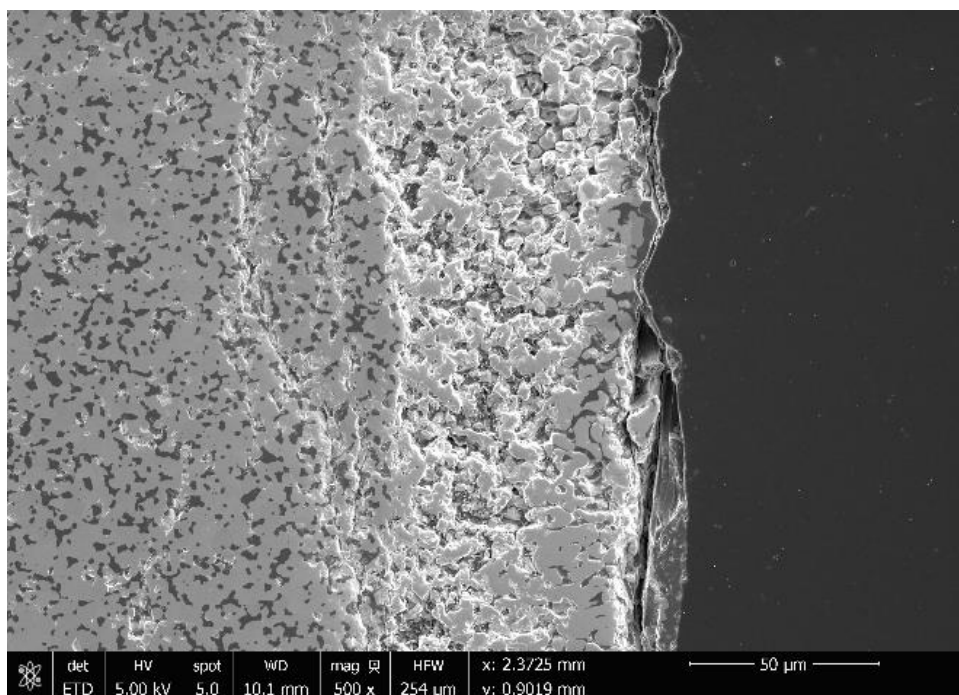
Figure 151. SEM Micrograph of HfB$_2$-20%SiC-10 oxide scale. Test ran at 50 MPa for 20 hours at 1500°C in air.

Figure 152. SEM Micrograph of HfB$_2$-20%SiC-10 oxide scale. Test ran at 50 MPa for 20 hours at 1500°C in air.
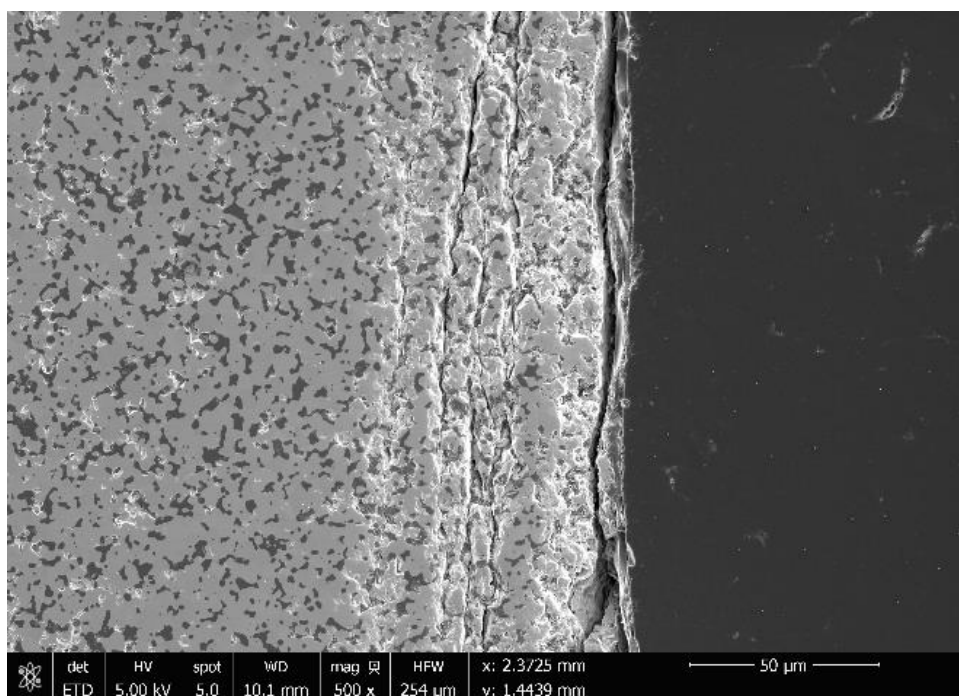
Figure 153. SEM Micrograph of HfB$_2$-20%SiC-10 oxide scale. Test ran at 50 MPa for 20 hours at 1500°C in air.

Figure 154. SEM Micrograph of HfB$_2$-20%SiC-10 oxide scale. Test ran at 50 MPa for 20 hours at 1500°C in air.
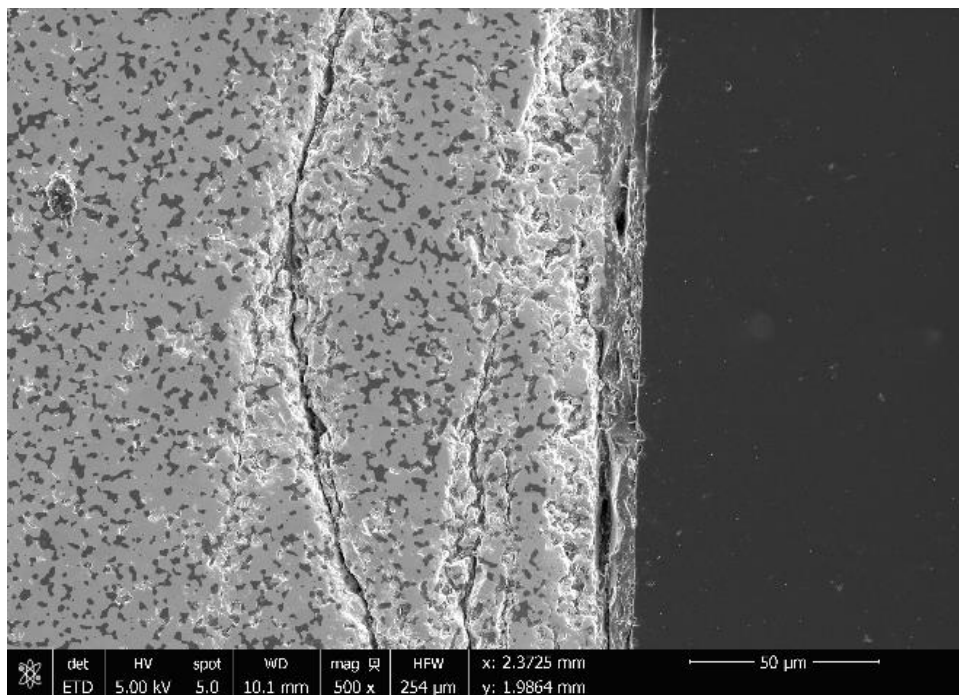
Figure 155. SEM Micrograph of HfB$_2$-20%SiC-10 oxide scale. Test ran at 50 MPa for 20 hours at 1500°C in air.

Figure 156. SEM Micrograph of HfB$_2$-20%SiC-10 oxide scale. Test ran at 50 MPa for 20 hours at 1500°C in air.
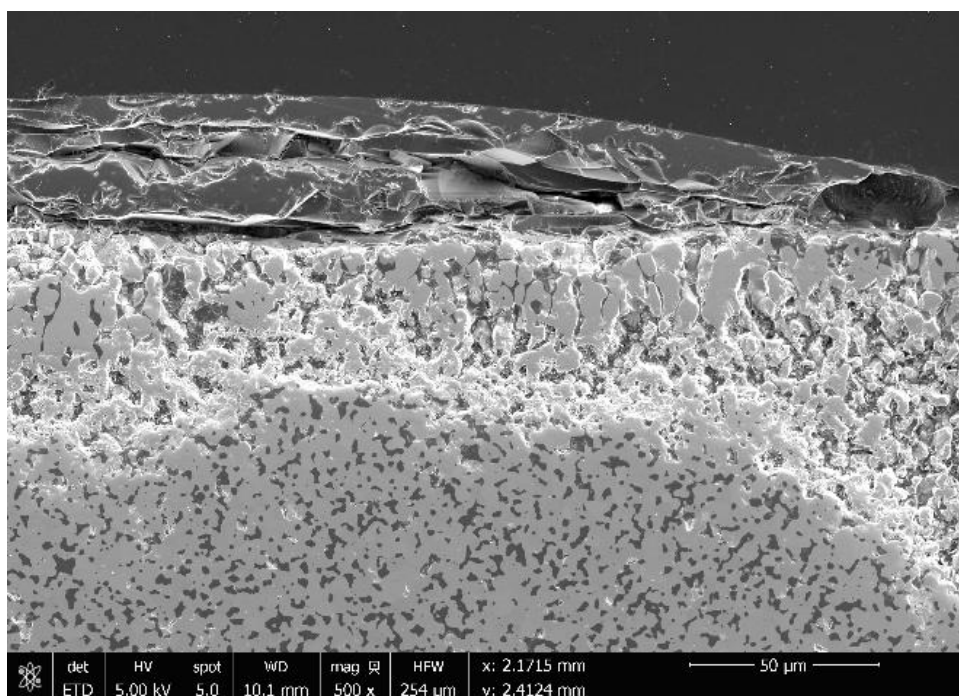
Figure 157. SEM Micrograph of HfB$_2$-20%SiC-10 oxide scale. Test ran at 50 MPa for 20 hours at 1500°C in air.

Figure 158. SEM Micrograph of HfB$_2$-20%SiC-10 oxide scale. Test ran at 50 MPa for 20 hours at 1500°C in air.
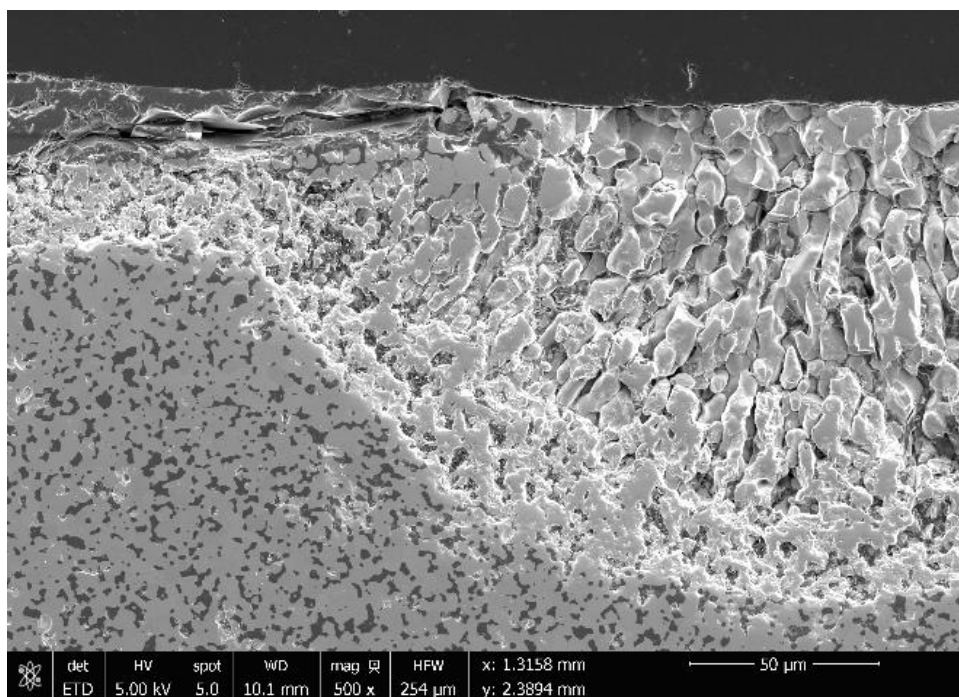
Figure 159. SEM Micrograph of HfB$_2$-20%SiC-10 oxide scale. Test ran at 50 MPa for 20 hours at 1500°C in air.

Figure 160. SEM Micrograph of HfB$_2$-20%SiC-10 oxide scale. Test ran at 50 MPa for 20 hours at 1500°C in air.

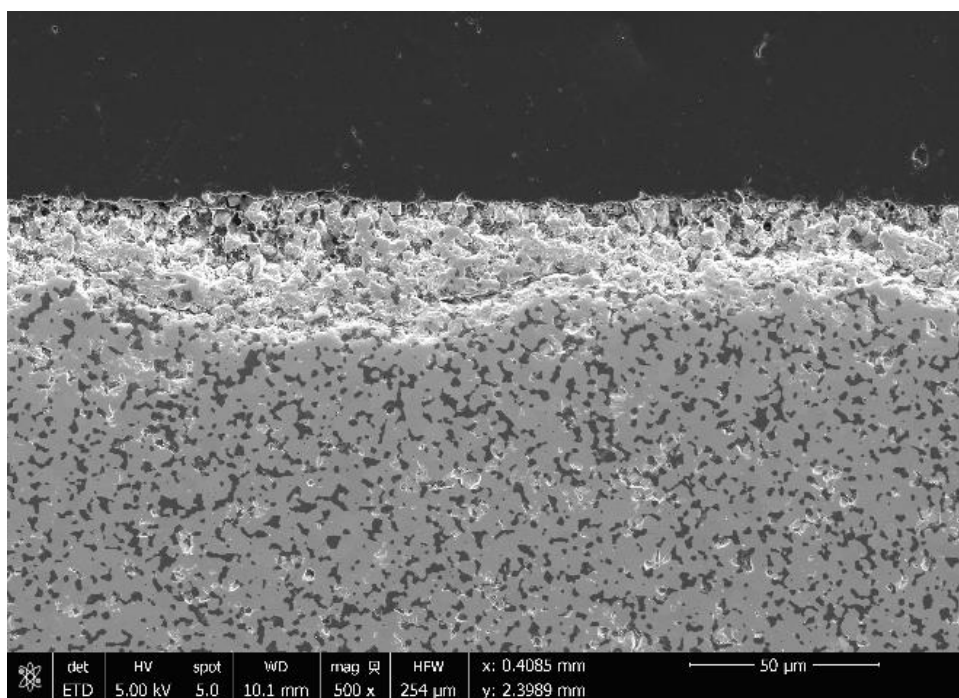Figure 161. SEM Micrograph of HfB$_2$-20%SiC-10 oxide scale. Test ran at 50 MPa for 20 hours at 1500°C in air.

Figure 162. SEM Micrograph of HfB$_2$-20%SiC-10 oxide scale. Test ran at 50 MPa for 20 hours at 1500°C in air.
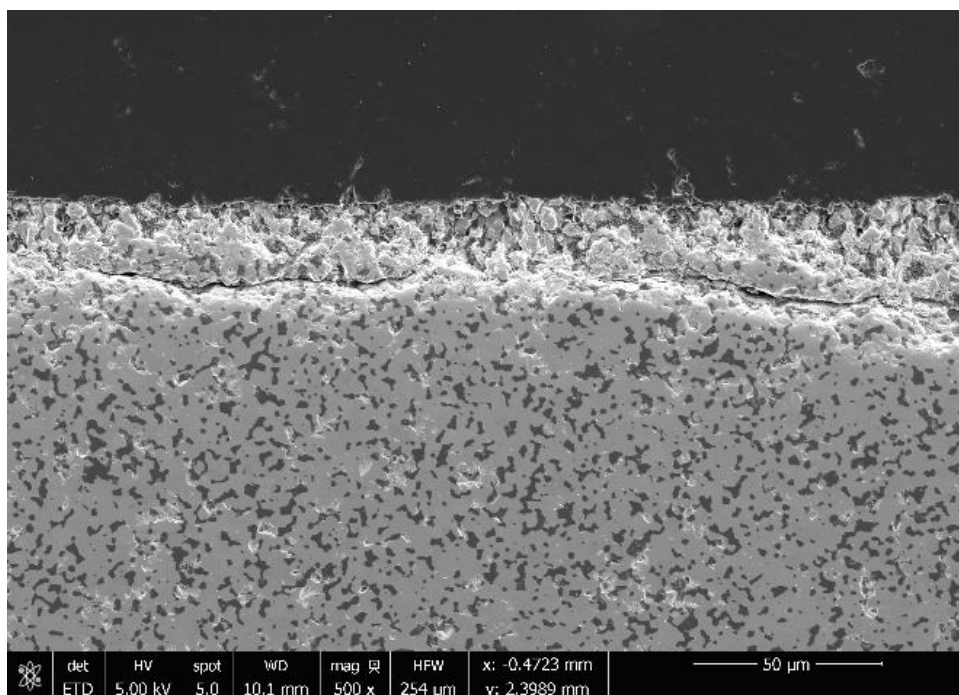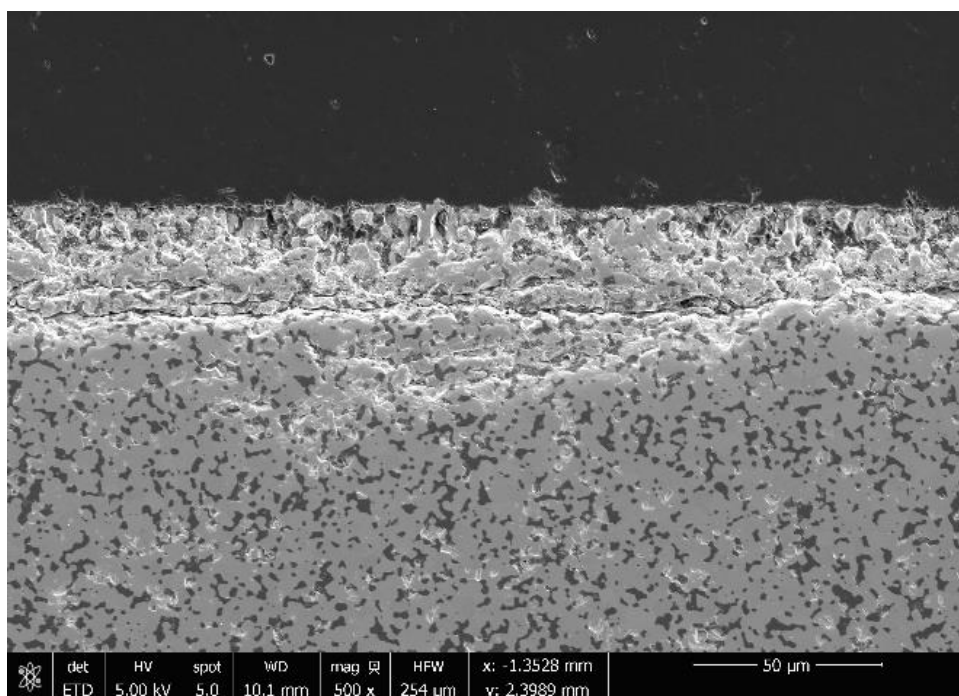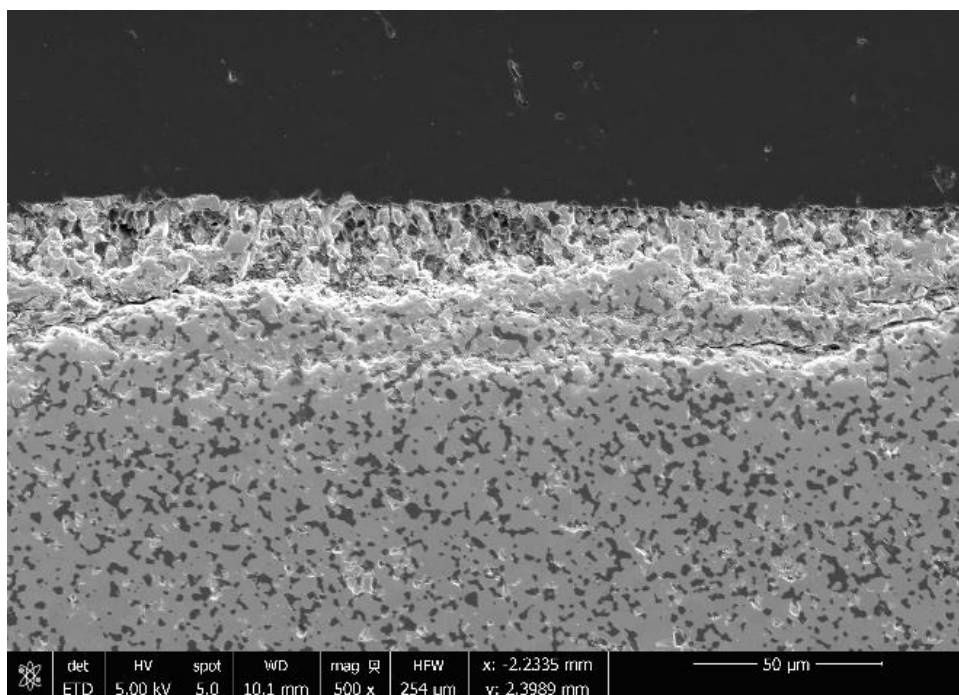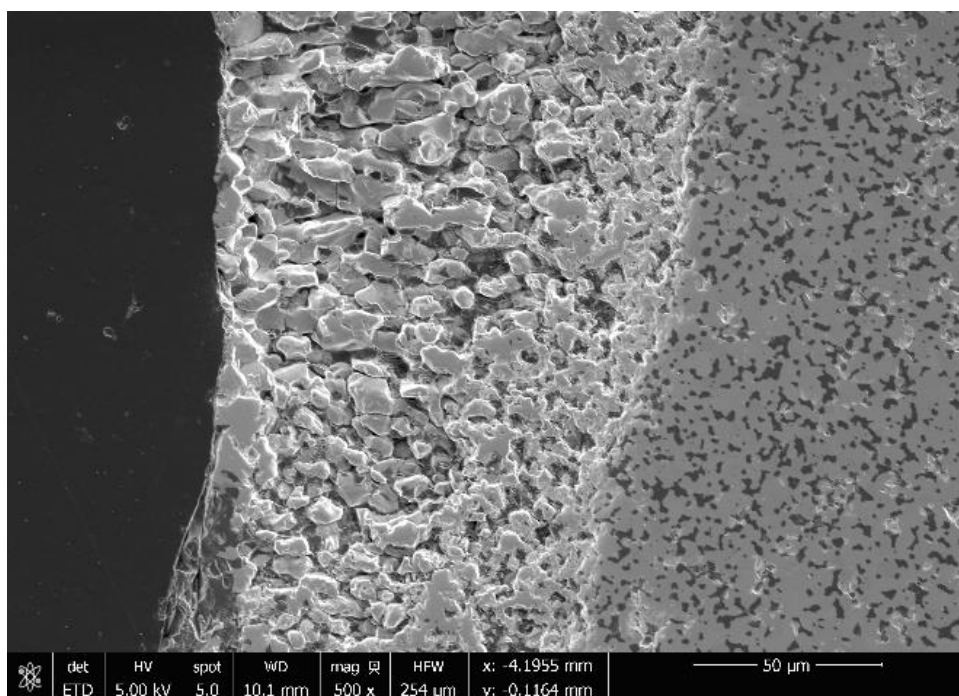
Figure 163. SEM Micrograph of HfB$_2$-20%SiC-11 oxide scale. Test ran at 75 MPa for 18 hours at 1500°C in air.

Figure 164. SEM Micrograph of HfB$_2$-20%SiC-11 oxide scale. Test ran at 75 MPa for 18 hours at 1500°C in air.

Figure 165. SEM Micrograph of HfB$_2$-20%SiC-11 oxide scale. Test ran at 75 MPa for 18 hours at 1500°C in air.

Figure 166. SEM Micrograph of HfB$_2$-20%SiC-11 oxide scale. Test ran at 75 MPa for 18 hours at 1500°C in air.
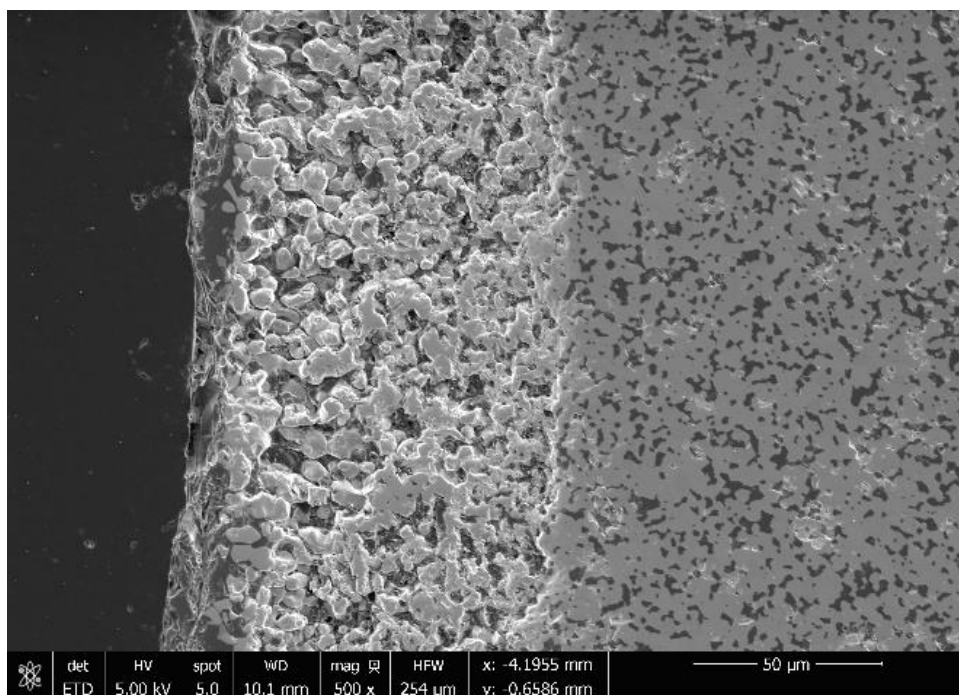
Figure 167. SEM Micrograph of HfB$_2$-20%SiC-11 oxide scale. Test ran at 75 MPa for 18 hours at 1500°C in air.

Figure 168. SEM Micrograph of HfB$_2$-20%SiC-11 oxide scale. Test ran at 75 MPa for 18 hours at 1500°C in air.

Figure 169. SEM Micrograph of HfB$_2$-20%SiC-11 oxide scale. Test ran at 75 MPa for 18 hours at 1500°C in air.

Figure 170. SEM Micrograph of HfB$_2$-20%SiC-11 oxide scale. Test ran at 75 MPa for 18 hours at 1500°C in air.
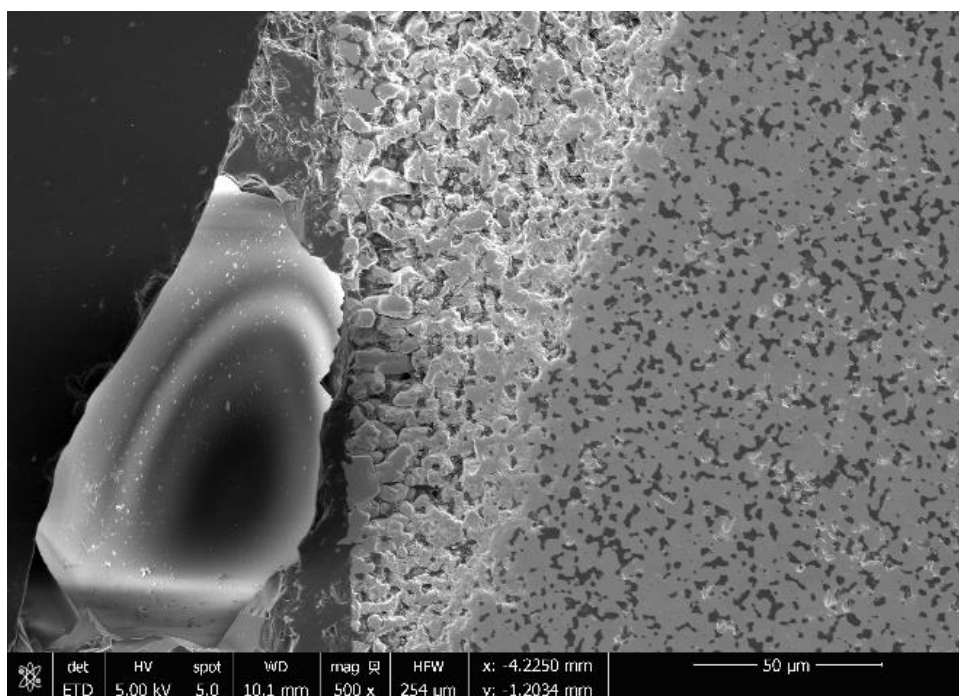
Figure 171. SEM Micrograph of HfB$_2$-20%SiC-11 oxide scale. Test ran at 75 MPa for 18 hours at 1500°C in air.

Figure 172. SEM Micrograph of HfB$_2$-20%SiC-11 oxide scale. Test ran at 75 MPa for 18 hours at 1500°C in air.
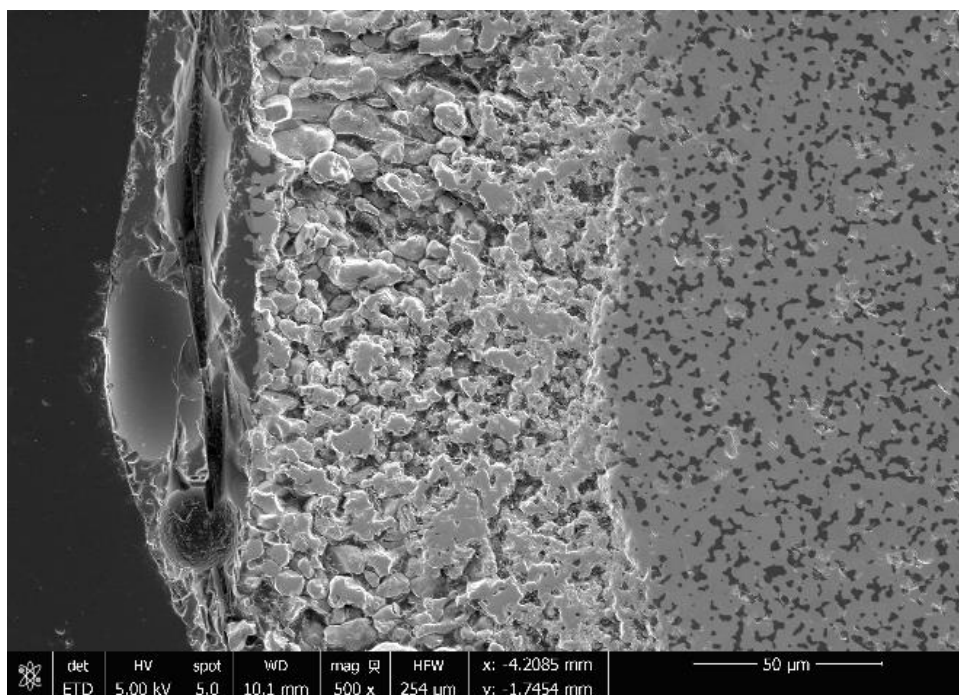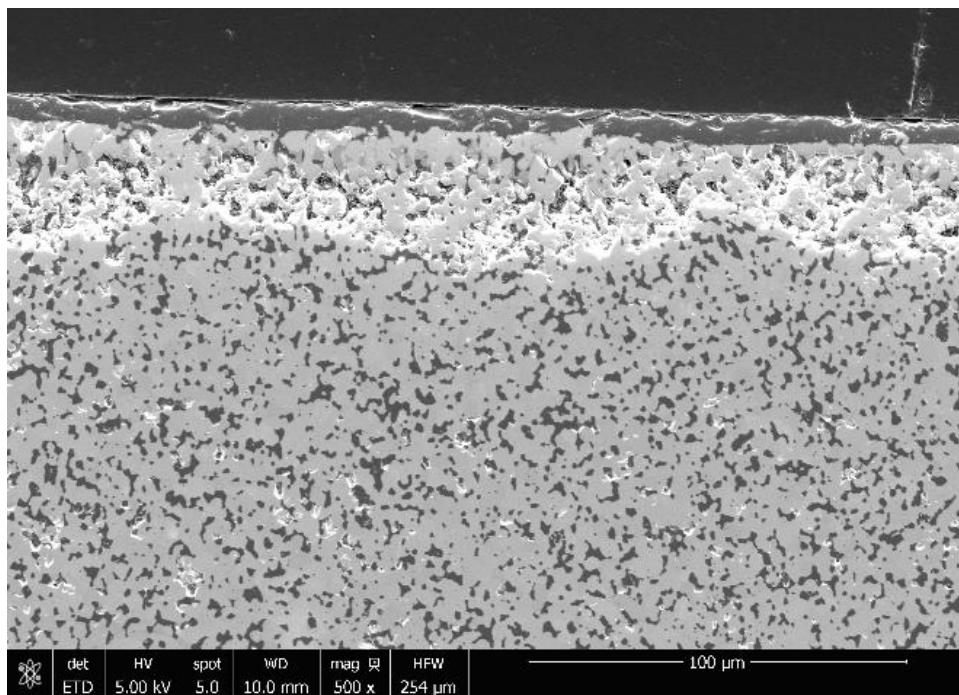
Figure 173. SEM Micrograph of HfB$_2$-20%SiC-11 oxide scale. Test ran at 75 MPa for 18 hours at 1500°C in air.
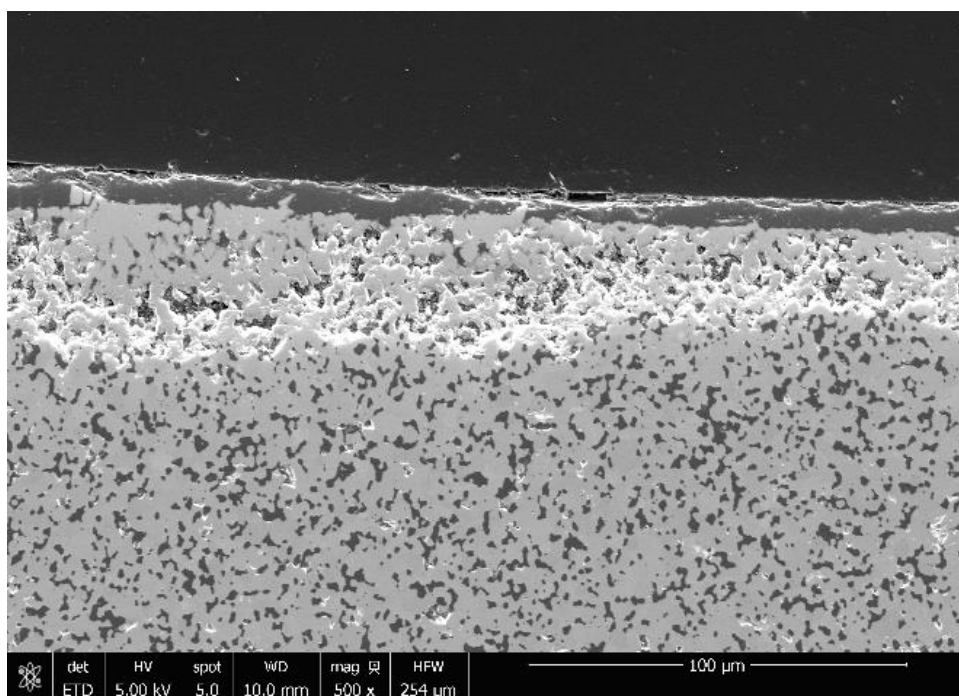
Figure 174. SEM Micrograph of HfB$_2$-20%SiC-11 oxide scale. Test ran at 75 MPa for 18 hours at 1500°C in air.
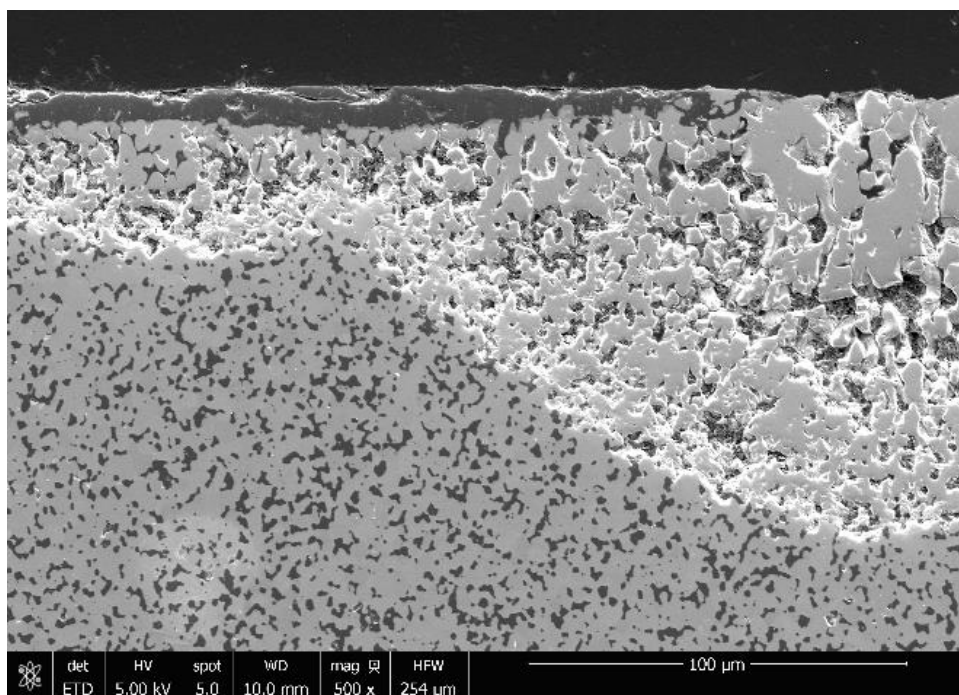
Figure 175. SEM Micrograph of HfB$_2$-20%SiC-11 oxide scale. Test ran at 75 MPa for 18 hours at 1500°C in air.
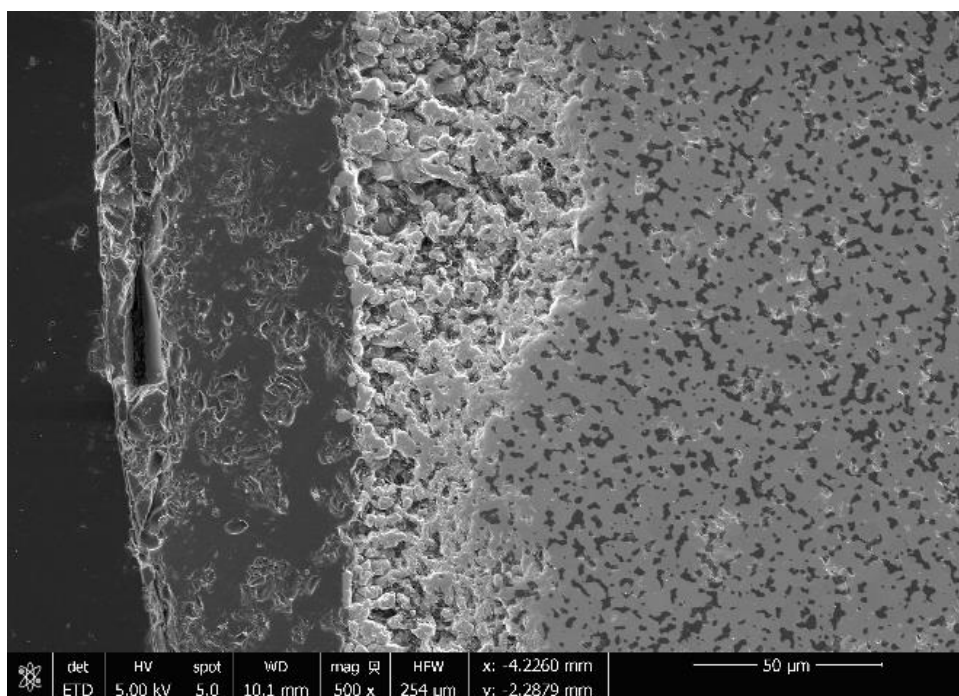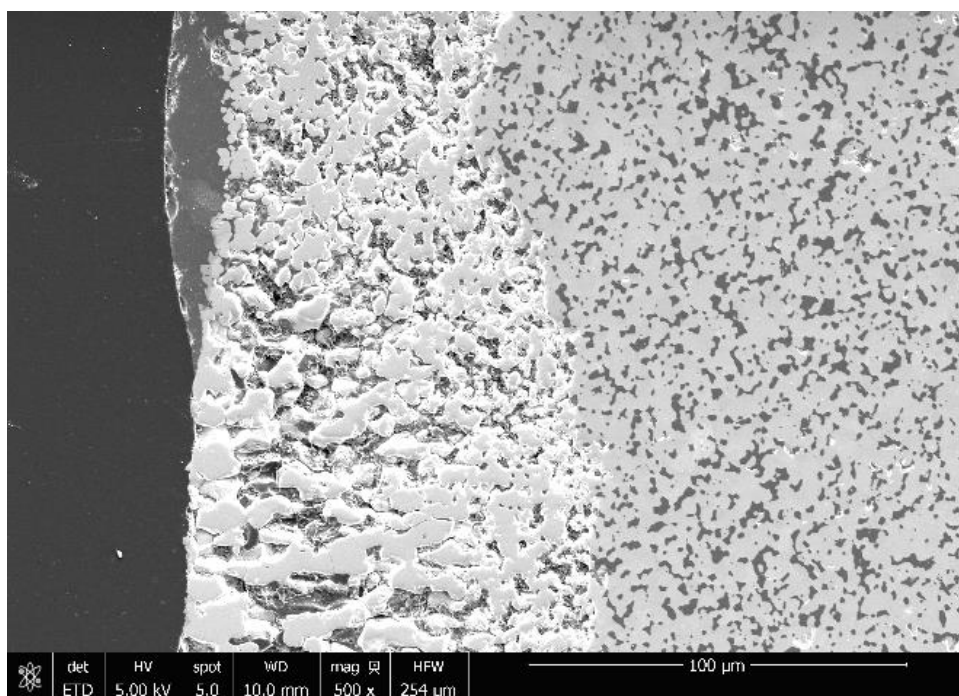

Figure 176. SEM Micrograph of HfB$_2$-20%SiC-11 oxide scale. Test ran at 75 MPa for 18 hours at 1500°C in air.
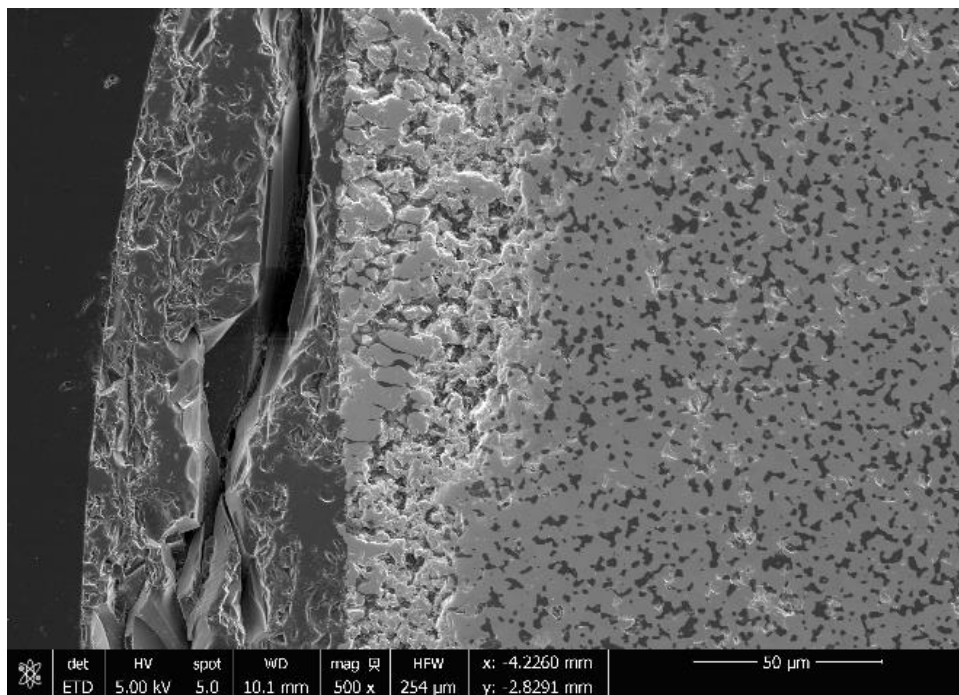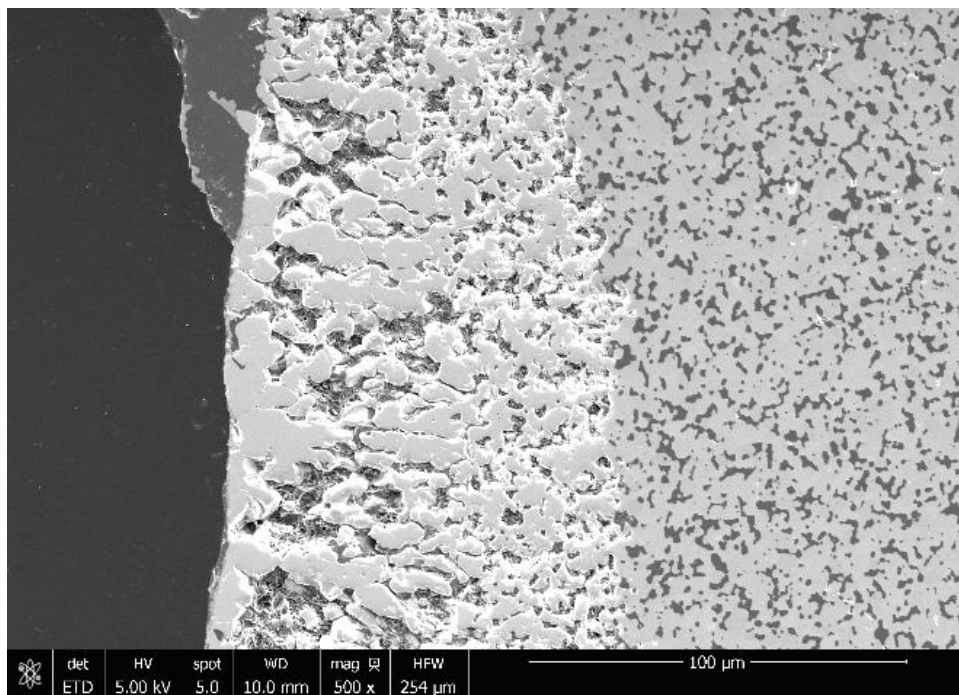
Figure 177. SEM Micrograph of HfB$_2$-20%SiC-11 oxide scale. Test ran at 75 MPa for 18 hours at 1500°C in air.
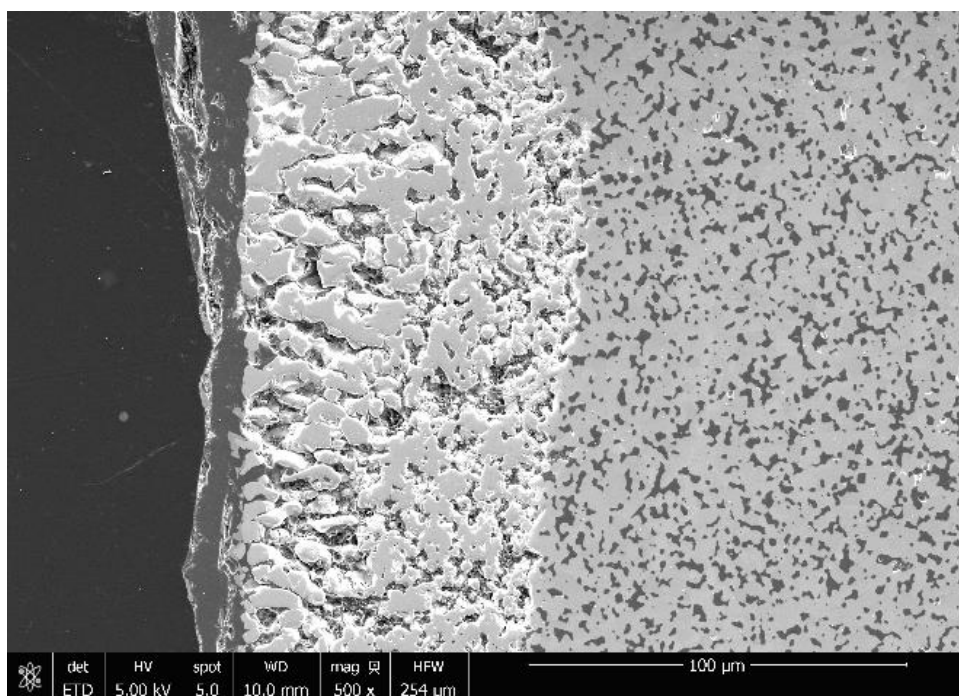
Figure 178. SEM Micrograph of HfB$_2$-20%SiC-11 oxide scale. Test ran at 75 MPa for 18 hours at 1500°C in air.
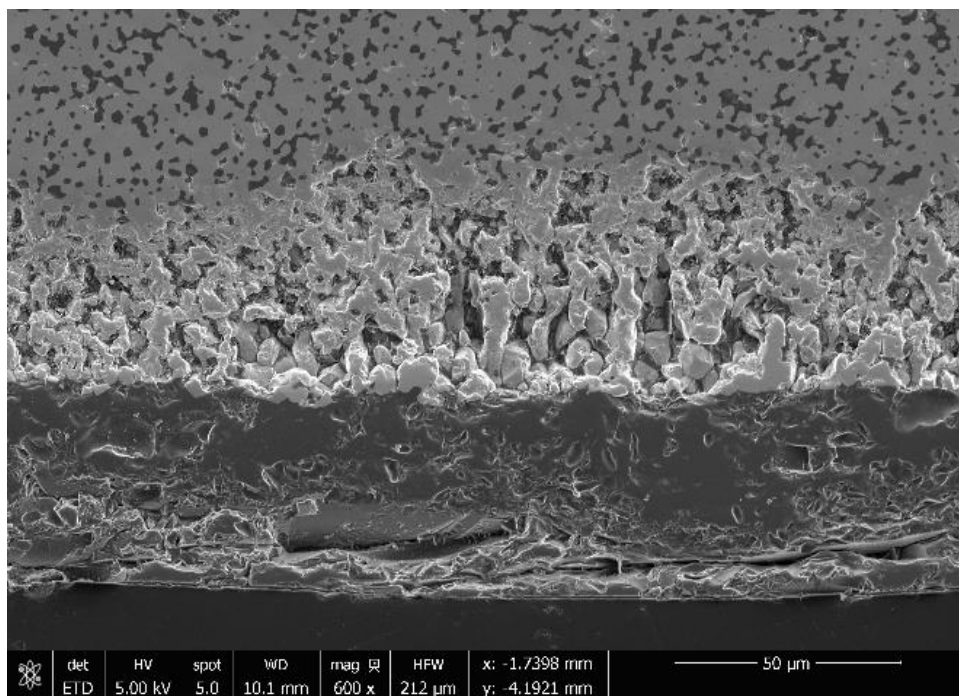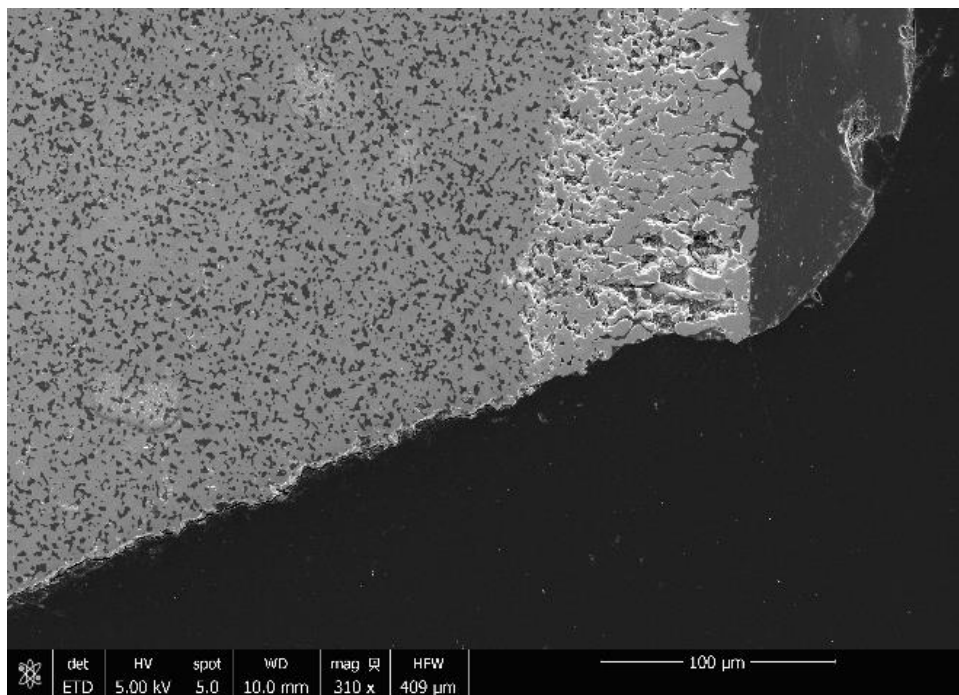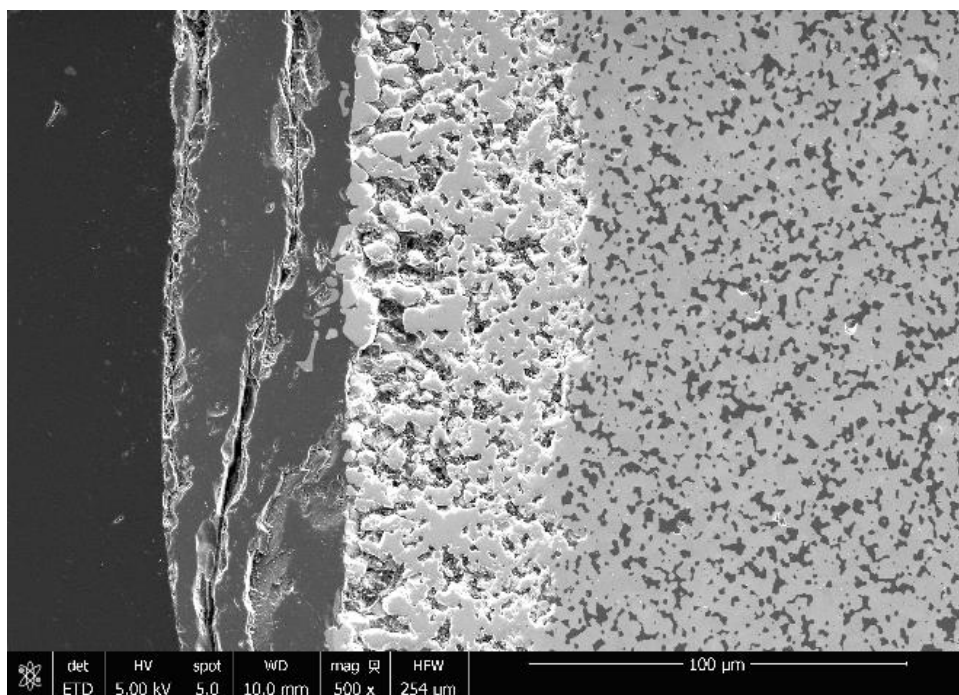
Figure 179. SEM Micrograph of HfB$_2$-20%SiC-11 oxide scale. Test ran at 75 MPa for 18 hours at 1500°C in air.
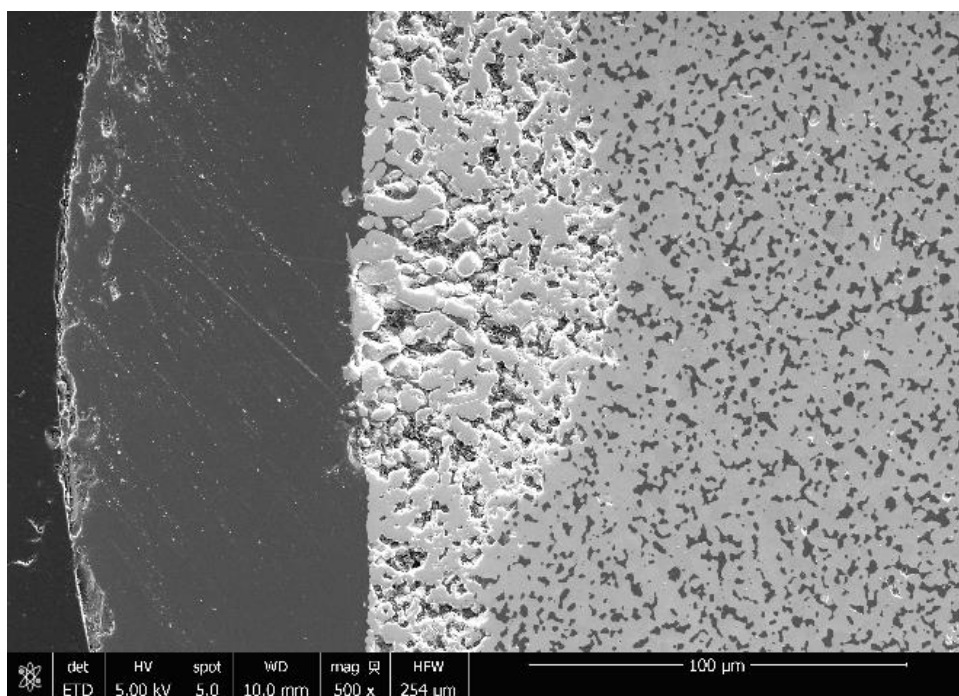
Figure 180. SEM Micrograph of HfB$_2$-20%SiC-11 oxide scale. Test ran at 75 MPa for 18 hours at 1500°C in air.
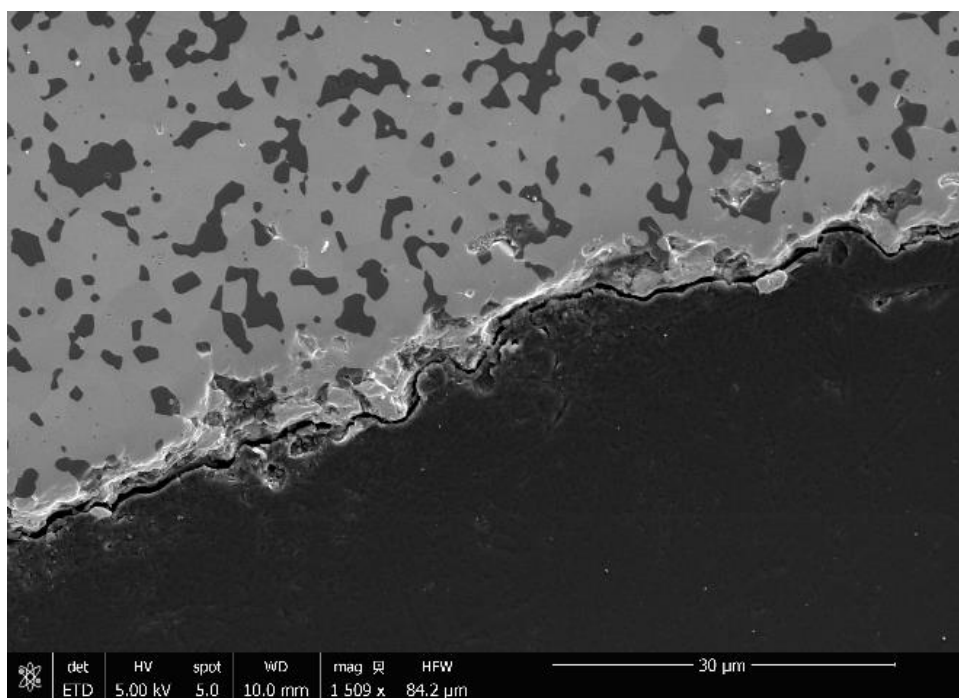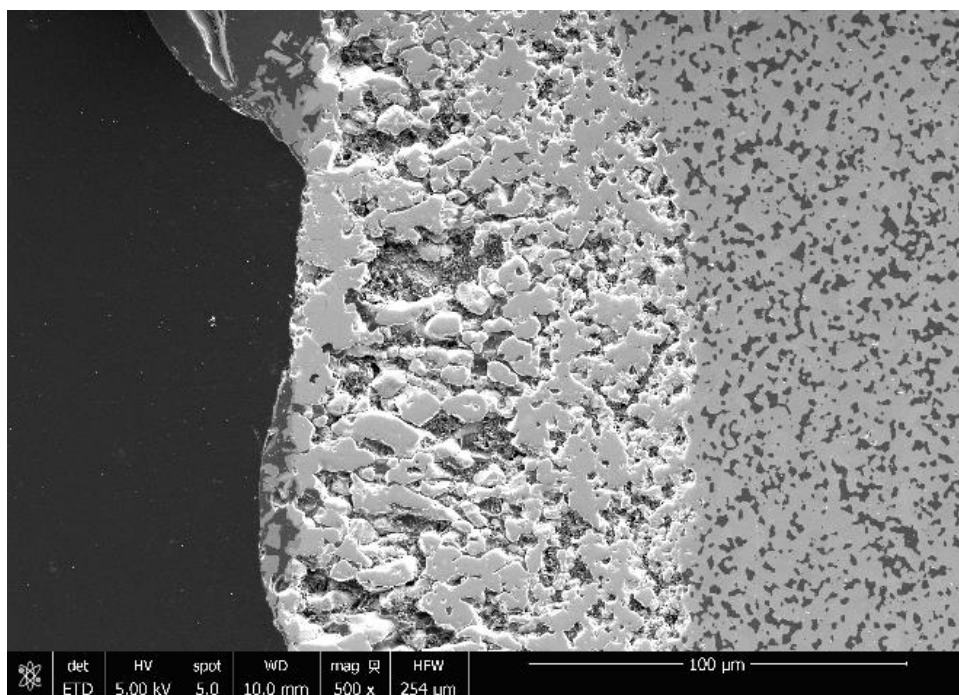
Figure 181. SEM Micrograph of HfB$_2$-20%SiC-11 oxide scale. Test ran at 75 MPa for 18 hours at 1500°C in air.
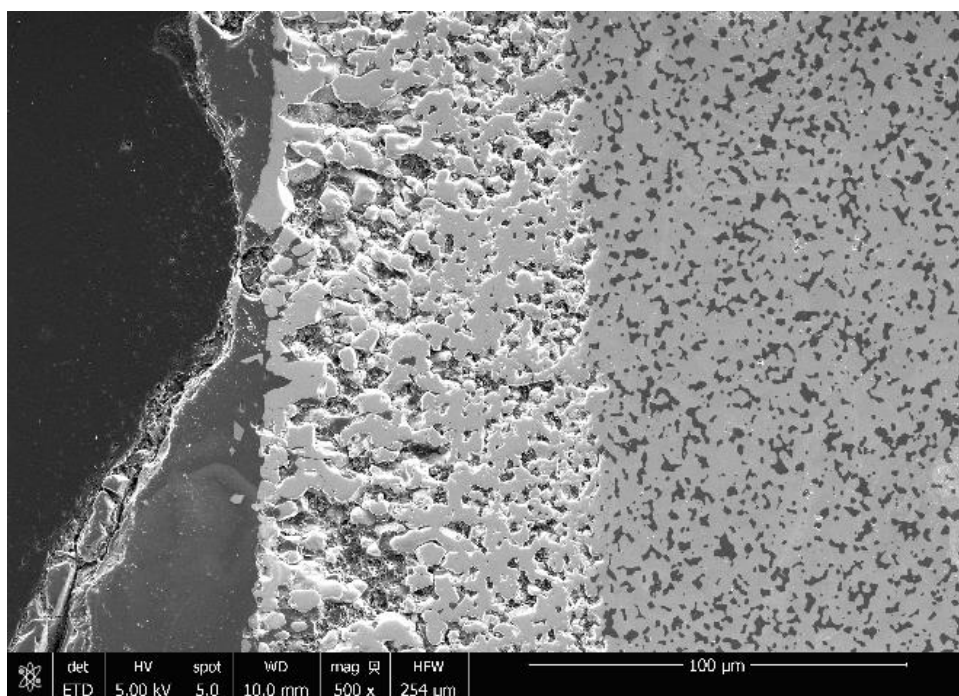
Figure 182. SEM Micrograph of HfB$_2$-20%SiC-11 oxide scale. Test ran at 75 MPa for 18 hours at 1500°C in air.
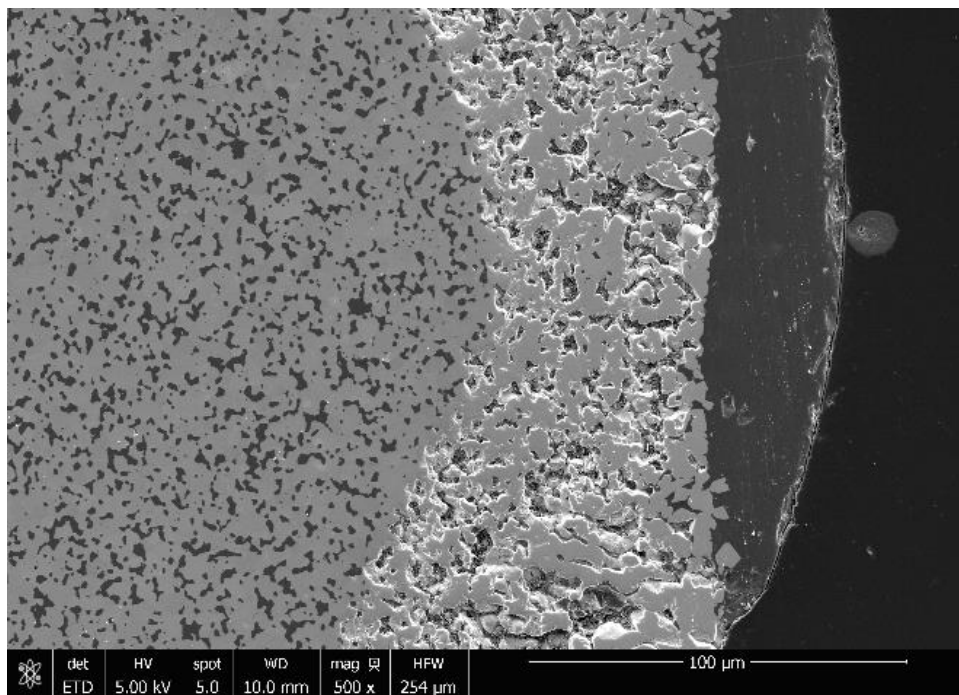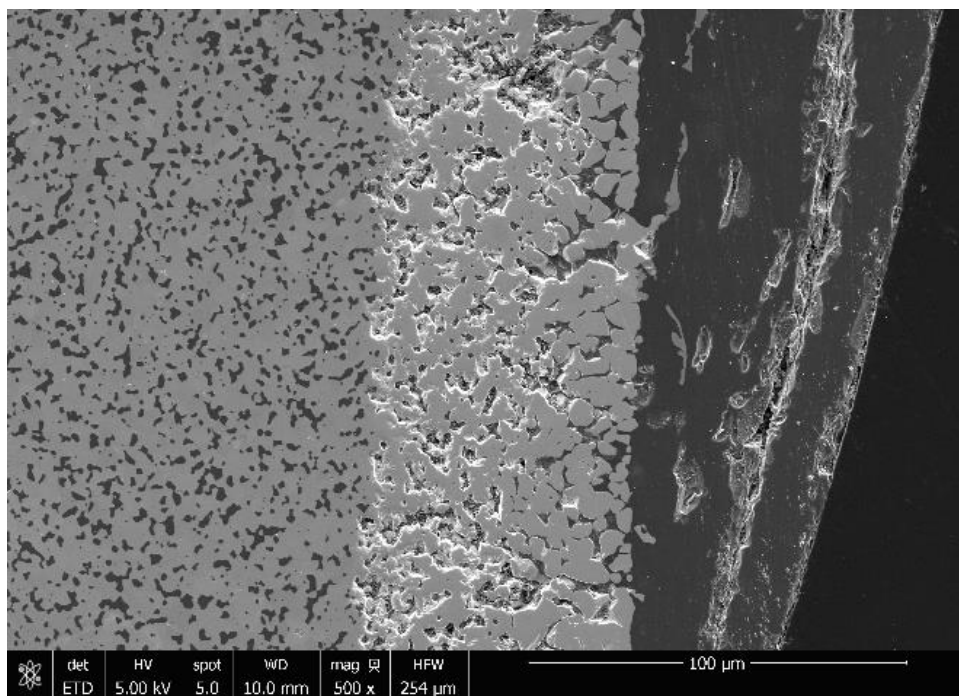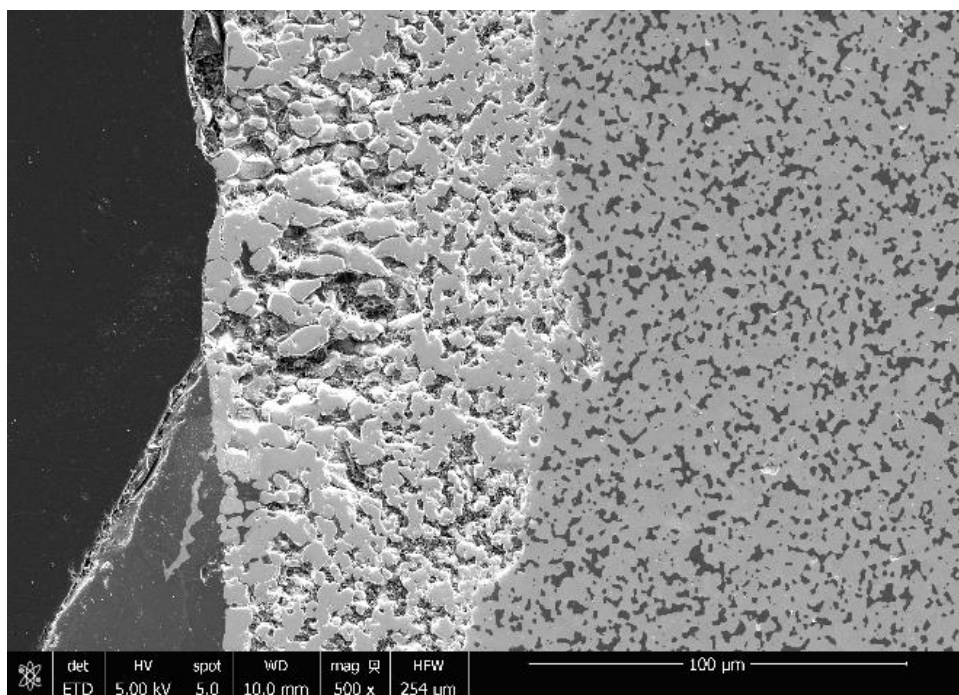
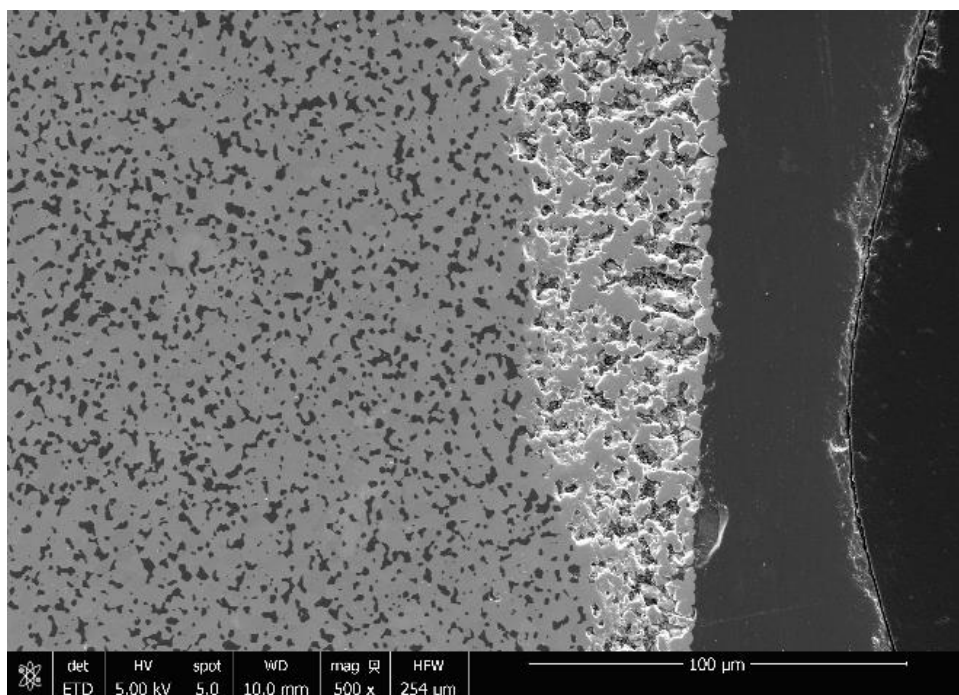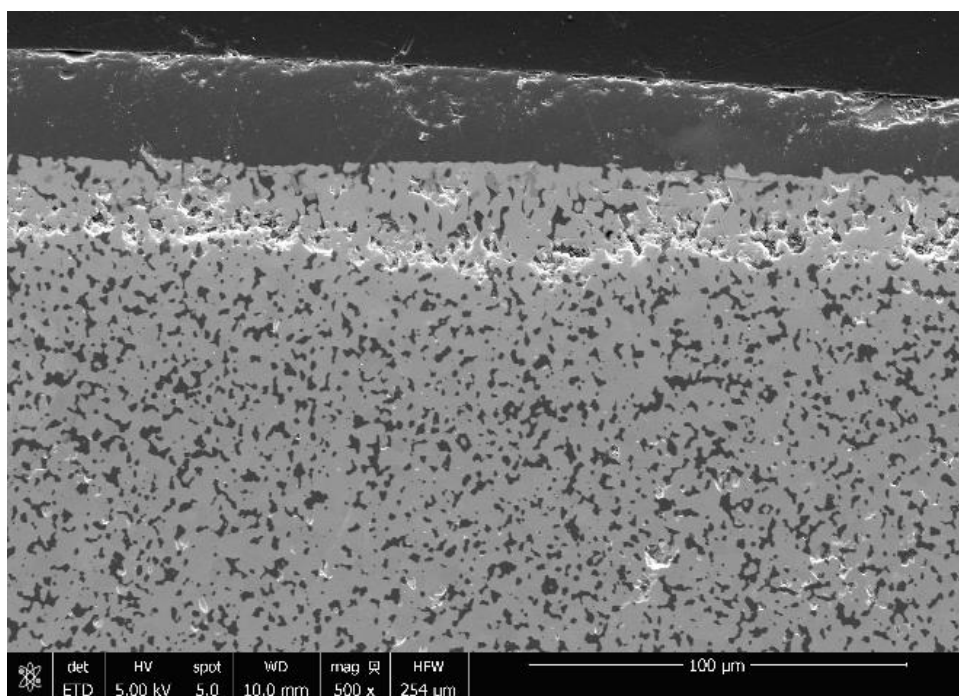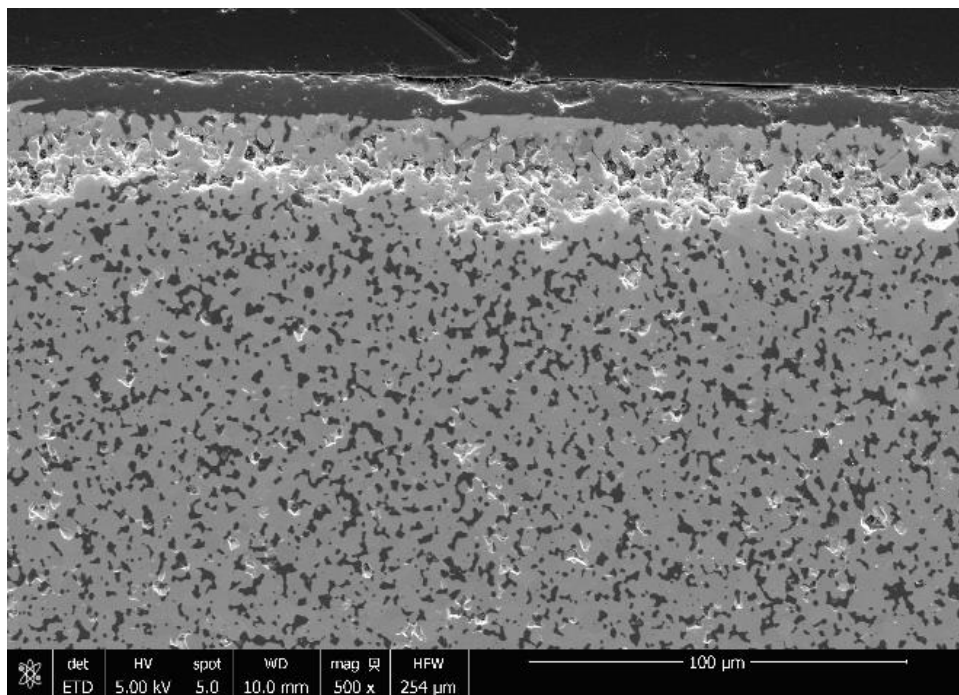Figure 183. SEM Micrograph of HfB$_2$-20%SiC-11 oxide scale. Test ran at 75 MPa for 18 hours at 1500°C in air.
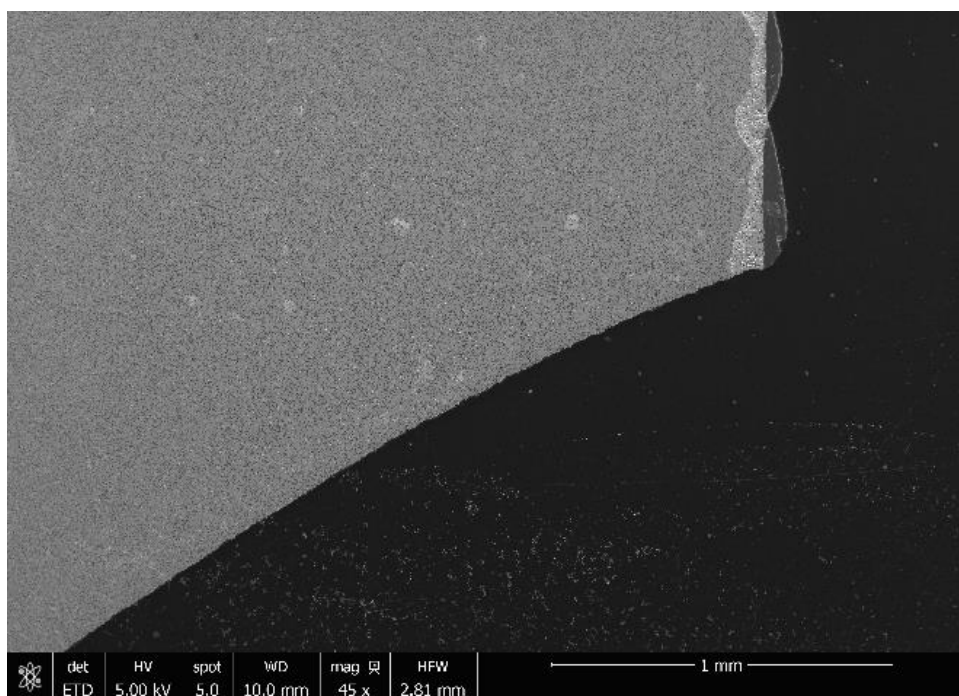
Figure 184. SEM Micrograph of HfB$_2$-20%SiC-11 fracture surface. Test ran at 75 MPa for 18 hours at 1500°C in air. The intergranular fracture surface exhibits virtually no oxide scale.
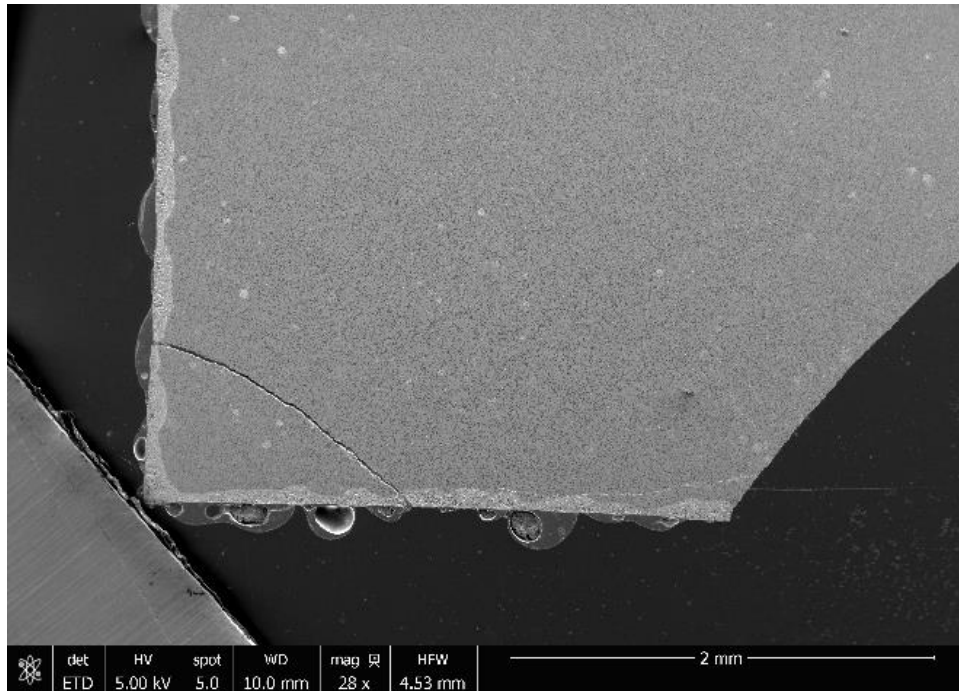
Figure 185. SEM Micrograph of HfB$_2$-20%SiC-11 fracture surface. Test ran at 75 MPa for 18 hours at 1500°C in air. The intergranular fracture surface exhibits virtually no oxide scale.
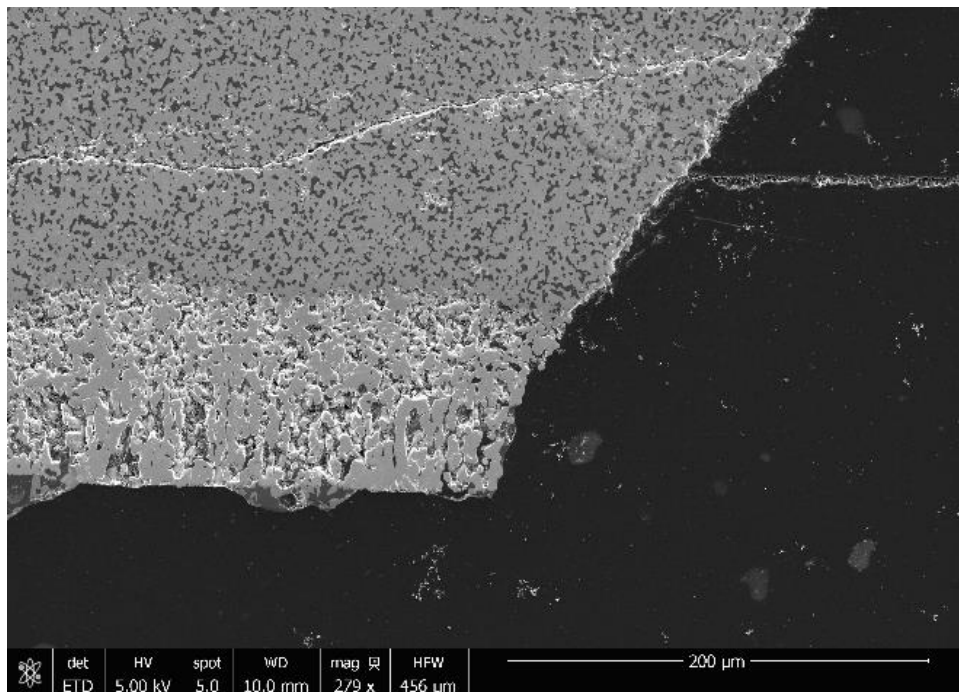
Figure 186. SEM Micrograph of HfB$_2$-20%SiC-11 fracture surface. Test ran at 75 MPa for 18 hours at 1500°C in air. The intergranular fracture surface exhibits virtually no oxide scale. The crack running into the sample was induced during sectioning.
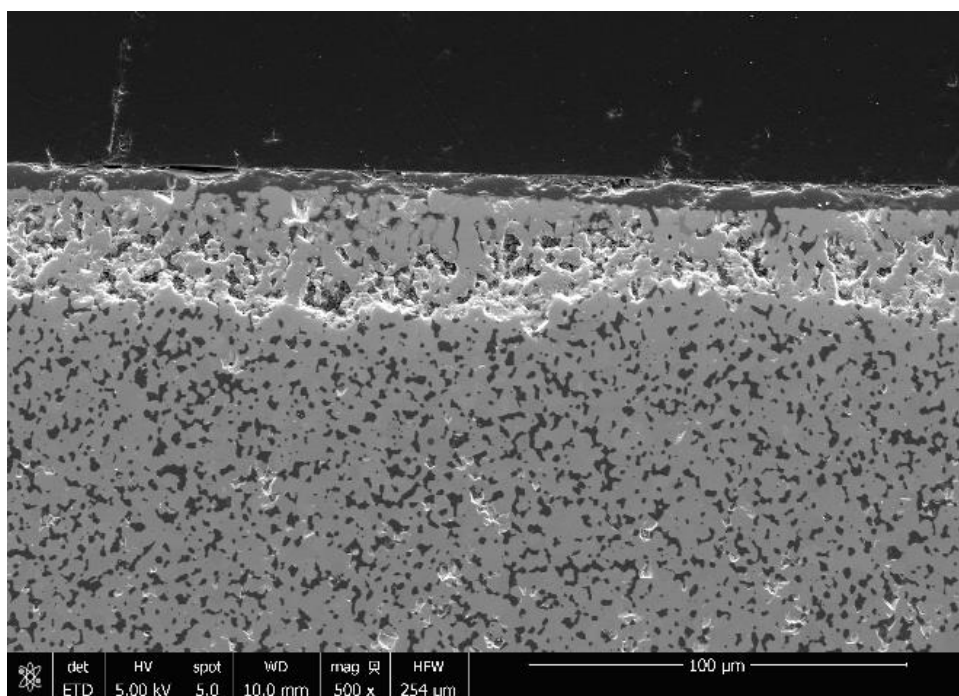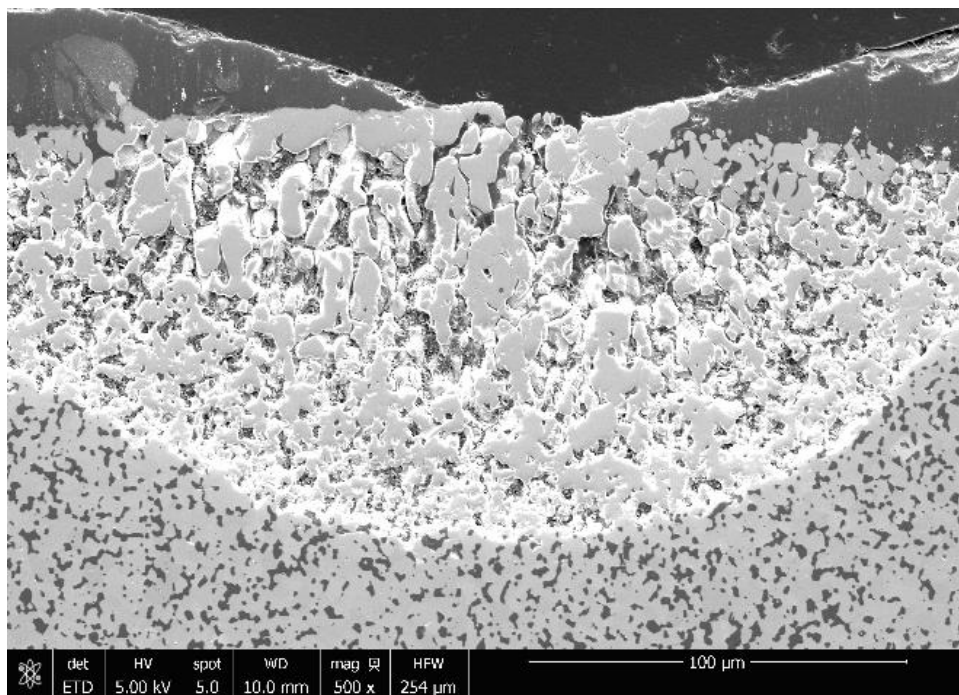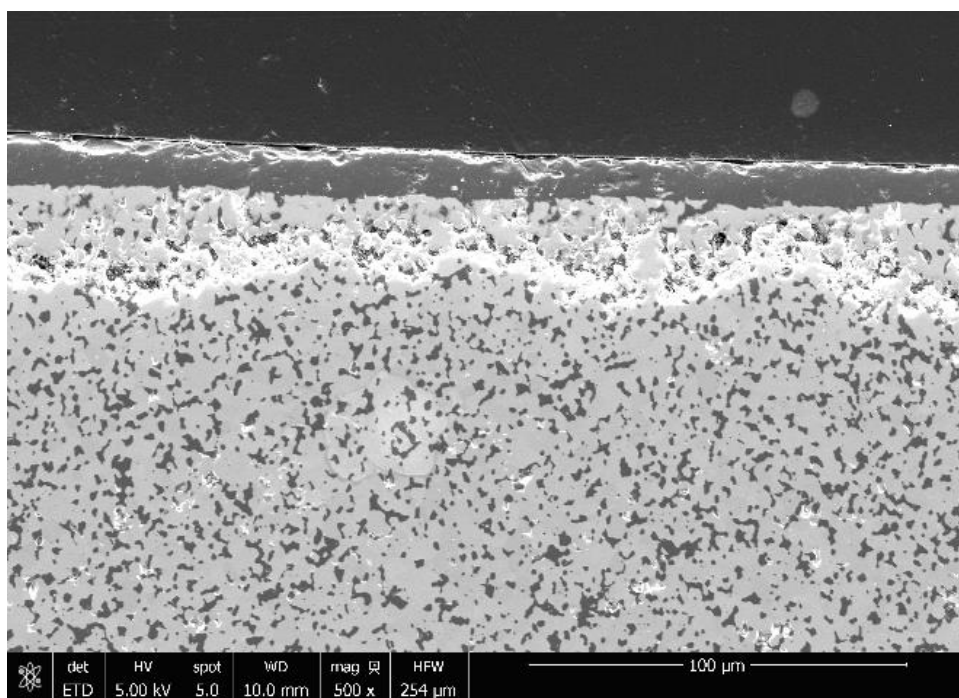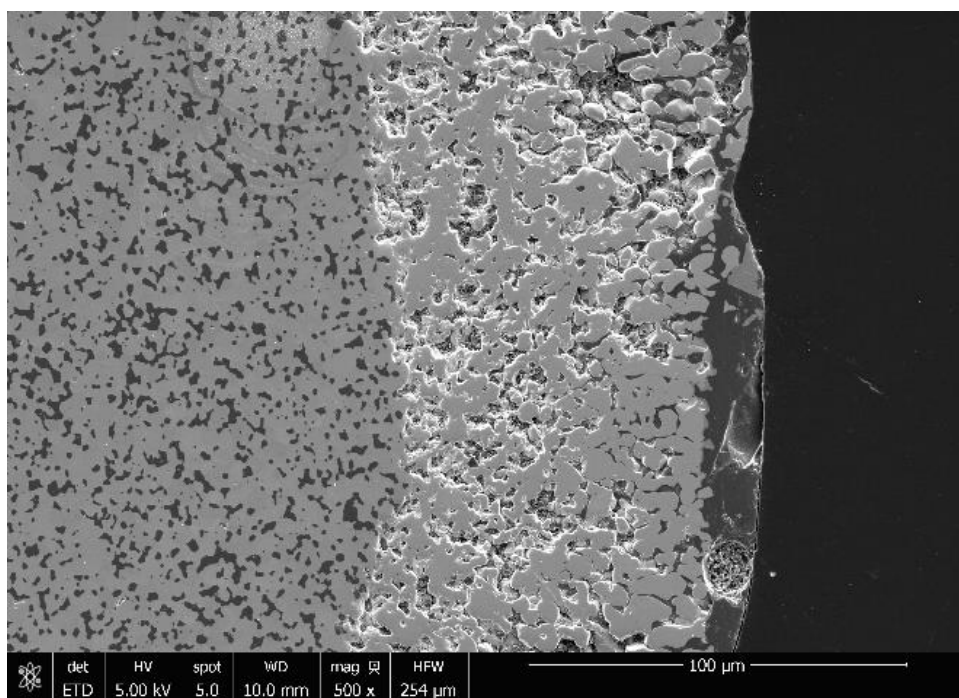
Figure 187. SEM Micrograph of HfB$_2$-20%SiC-11 oxide scale. Test ran at 75 MPa for 18 hours at 1500°C in air.
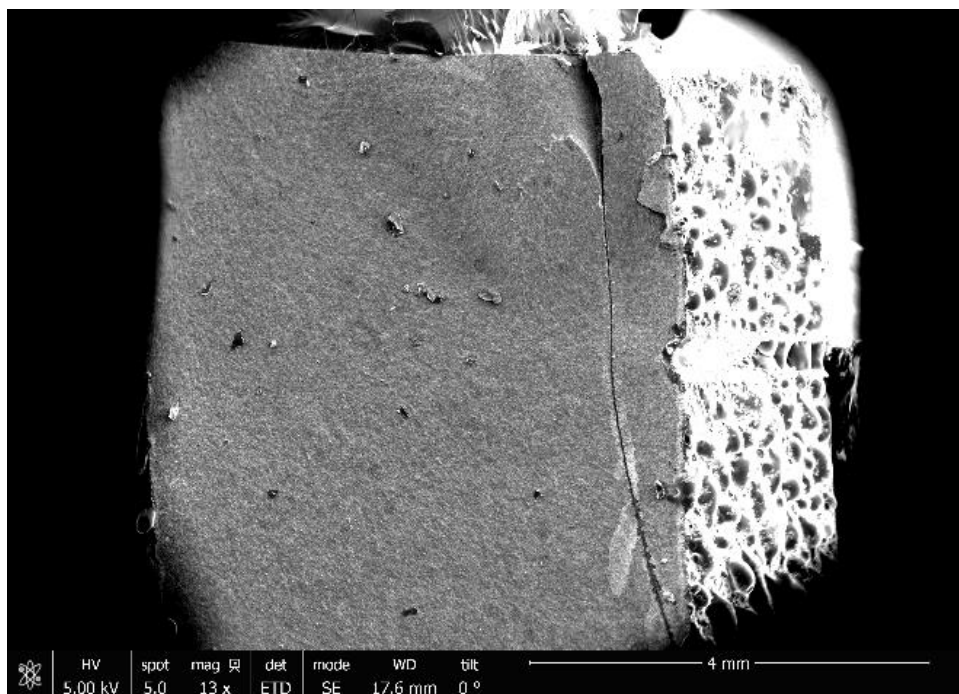
Figure 188. SEM Micrograph of HfB$_2$-20%SiC-11 fracture surface. Test ran at 75 MPa for 18 hours at 1500°C in air. Note the fracture appears to originate from the interface with the sapphire spacer remnants fused to the top of the specimen.
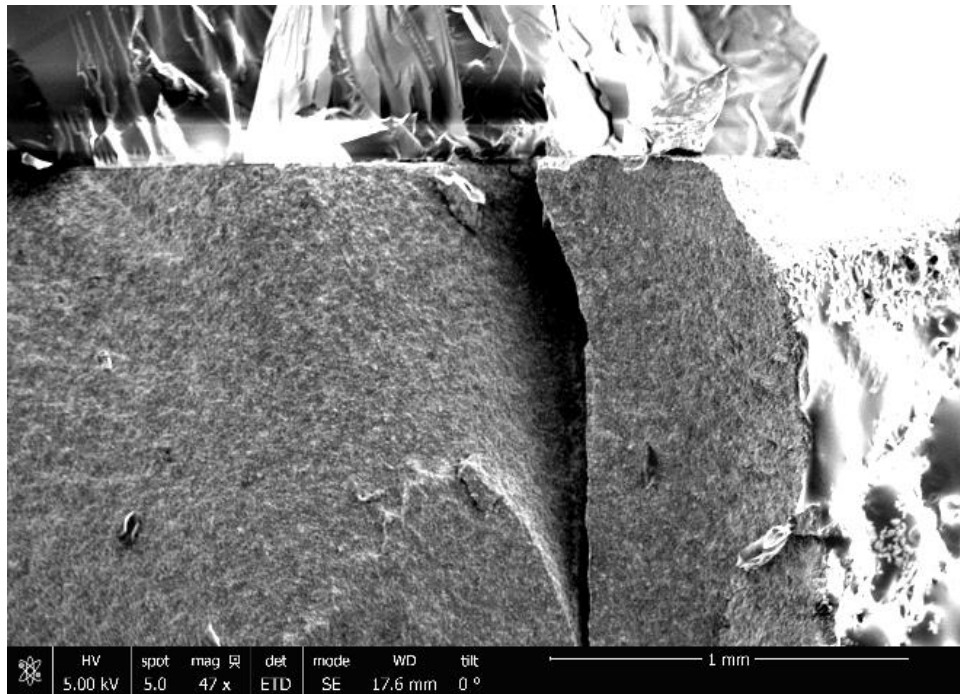
Figure 189. SEM Micrograph of HfB$_2$-20%SiC-11 fracture surface. Test ran at 75 MPa for 18 hours at 1500°C in air. Note the fracture appears to originate from the interface with the sapphire spacer remnants fused to the top of the specimen.
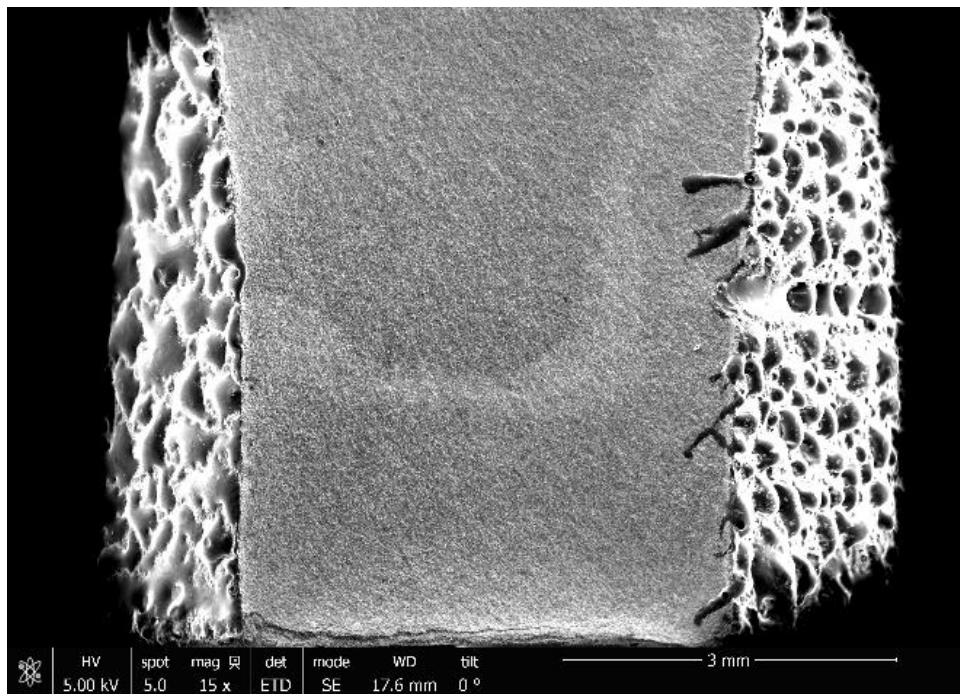
Figure 190. SEM Micrograph of HfB$_2$-20%SiC-11 fracture surface. Test ran at 75 MPa for 18 hours at 1500°C in air. Note the fracture surface appears to be uneven.
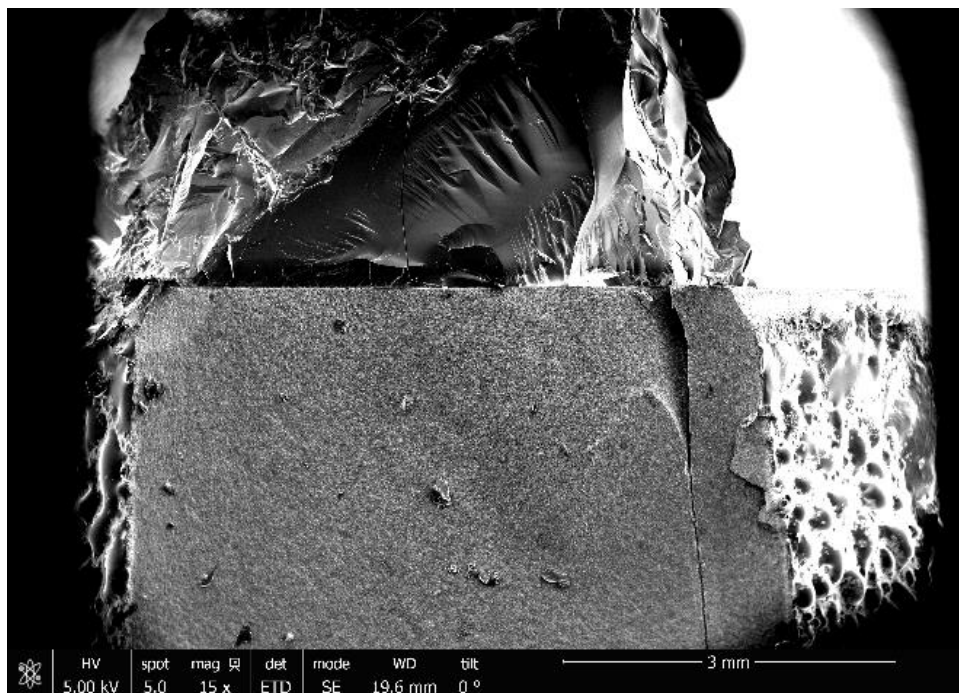
Figure 191. SEM Micrograph of HfB$_2$-20%SiC-11 fracture surface. Test ran at 75 MPa for 18 hours at 1500°C in air. Note the fracture appears to originate from the interface with the sapphire spacer remnants fused to the top of the specimen.
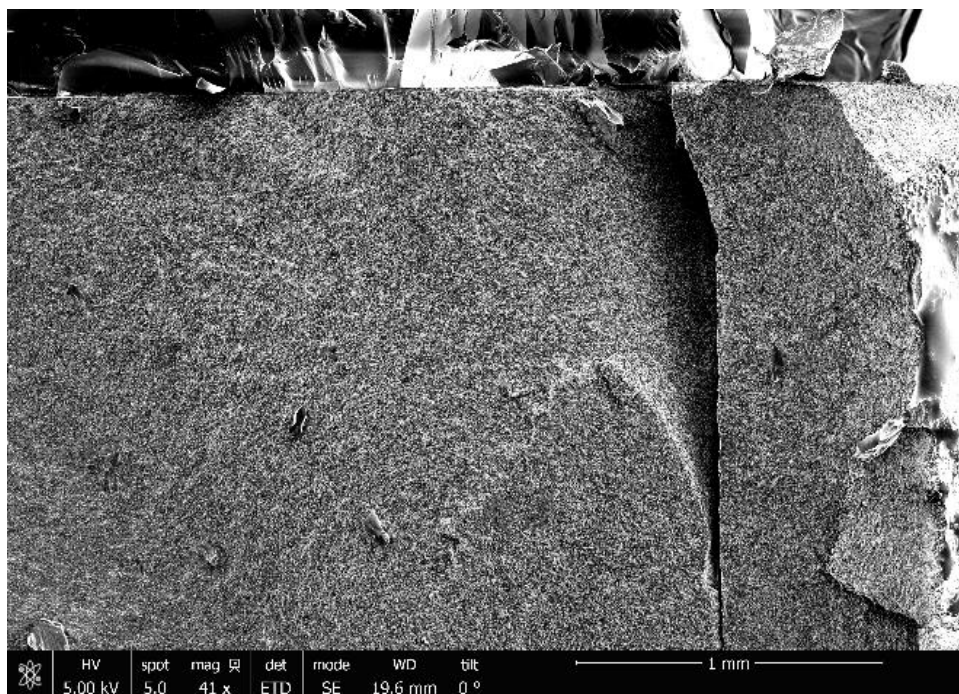
Figure 192. SEM Micrograph of HfB$_2$-20%SiC-11 fracture surface. Test ran at 75 MPa for 18 hours at 1500°C in air. Note the fracture appears to originate from the interface with the sapphire spacer remnants fused to the top of the specimen.
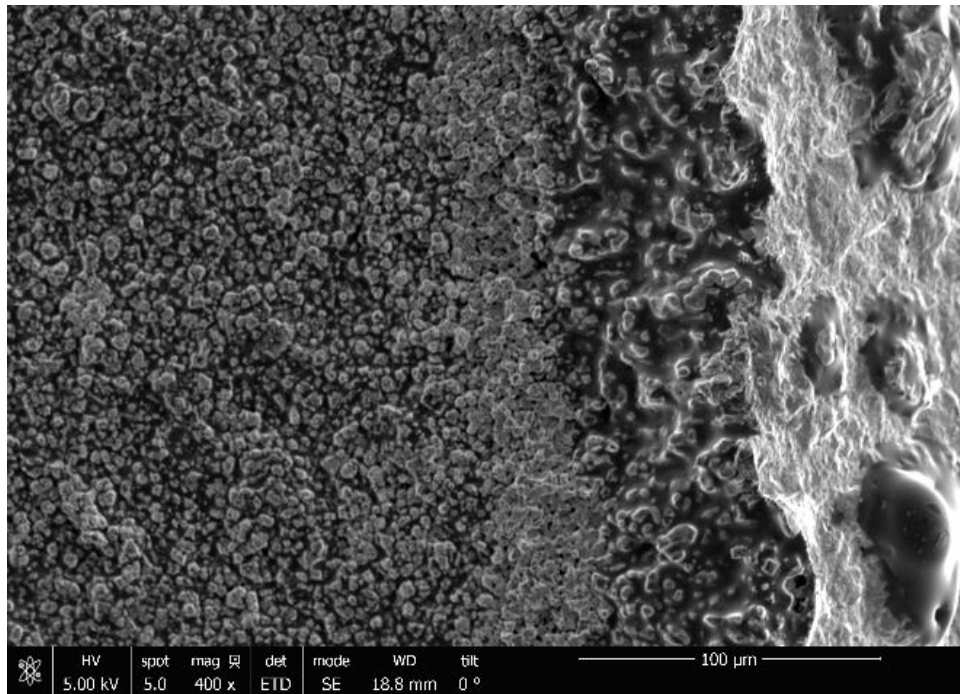
Figure 193. SEM Micrograph of HfB$_2$-20%SiC-11 fracture surface. Test ran at 75 MPa for 18 hours at 1500°C in air. Note the rightmost portion of the image shows the glassy surface. Directly under the glassy surface is thin oxide layer followed by unpolished, HfB$_2$-20% SiC.
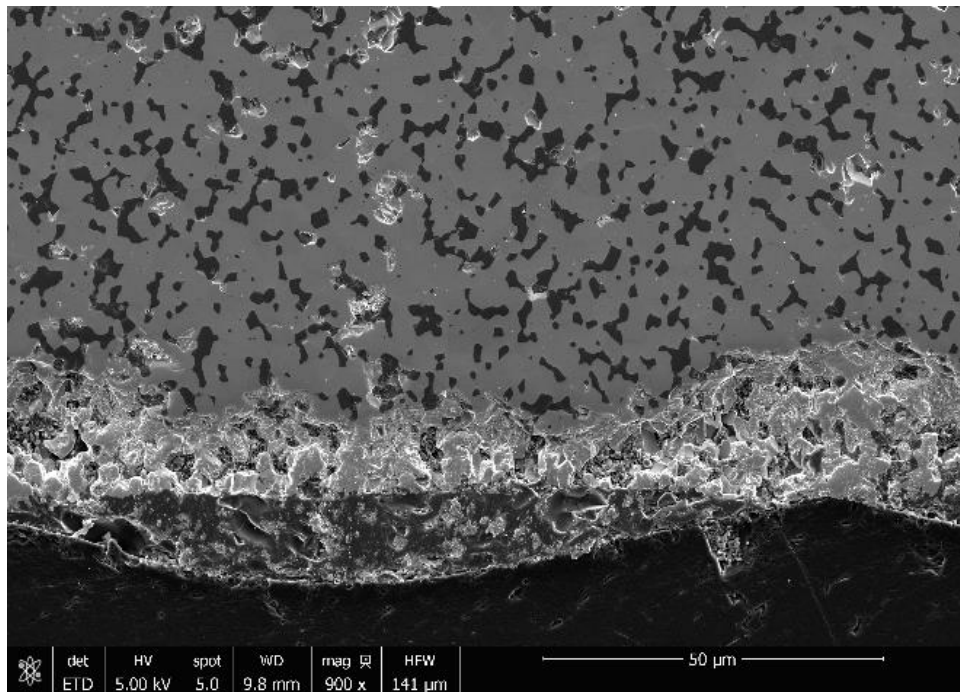
Figure 194. SEM Micrograph of HfB$_2$-20%SiC-12 oxide scale. Test failed during load up to 200 MPa. Specimen was subjected to 1500°C under 10 MPa for approximately 1 hour.

137
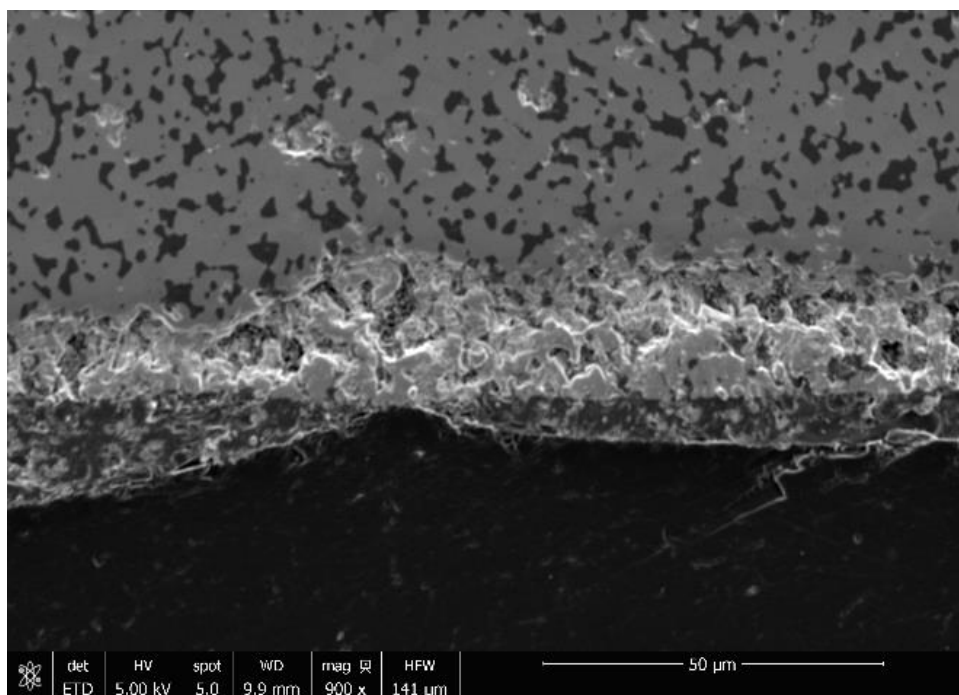
Figure 195. SEM Micrograph of HfB$_2$-20%SiC-12 oxide scale. Test failed during load up to 200 MPa. Specimen was subjected to 1500°C under 10 MPa for approximately 1 hour.
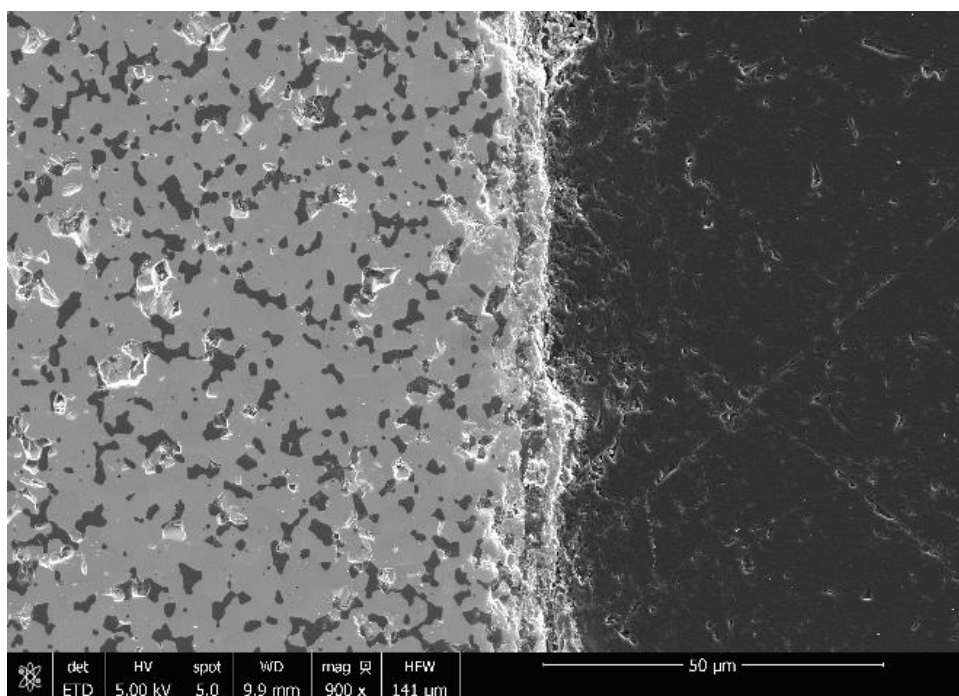
Figure 196. SEM Micrograph of HfB$_2$-20%SiC-12 oxide scale. Test failed during load up to 200 MPa. Specimen was subjected to 1500°C under 10 MPa for approximately 1 hour.
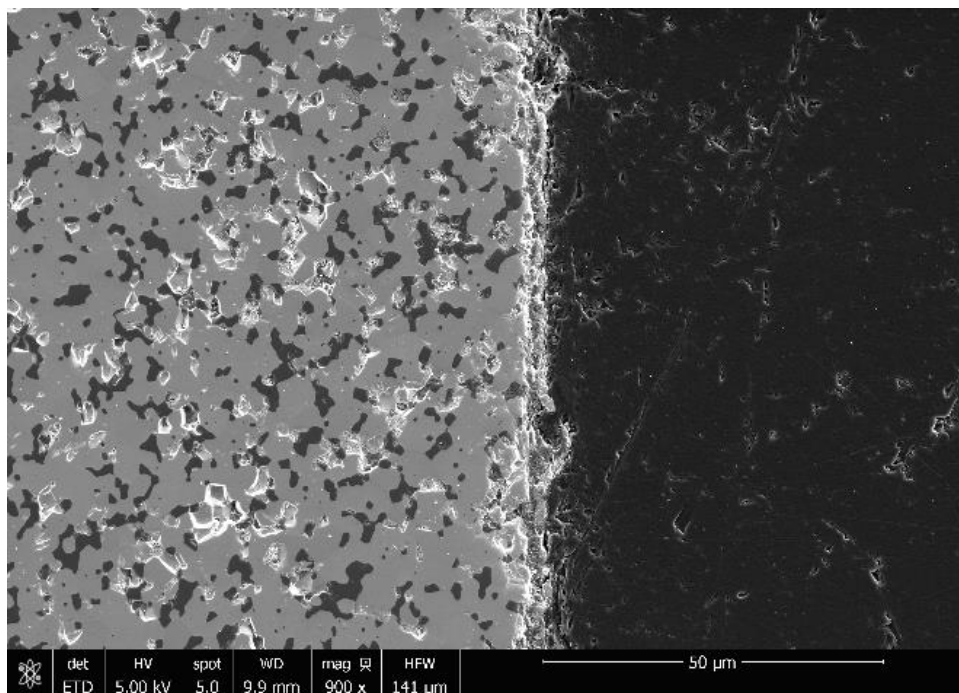
Figure 197. SEM Micrograph of HfB$_2$-20%SiC-12 oxide scale. Test failed during load up to 200 MPa. Specimen was subjected to 1500°C under 10 MPa for approximately 1 hour.
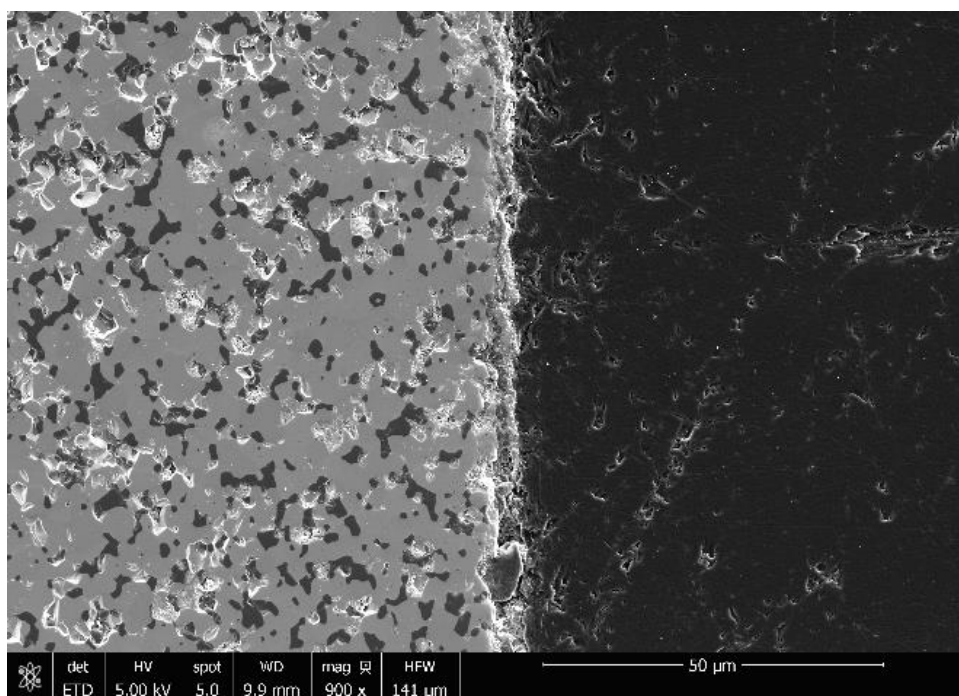
Figure 198. SEM Micrograph of HfB$_2$-20%SiC-12 oxide scale. Test failed during load up to 200 MPa. Specimen was subjected to 1500°C under 10 MPa for approximately 1 hour.
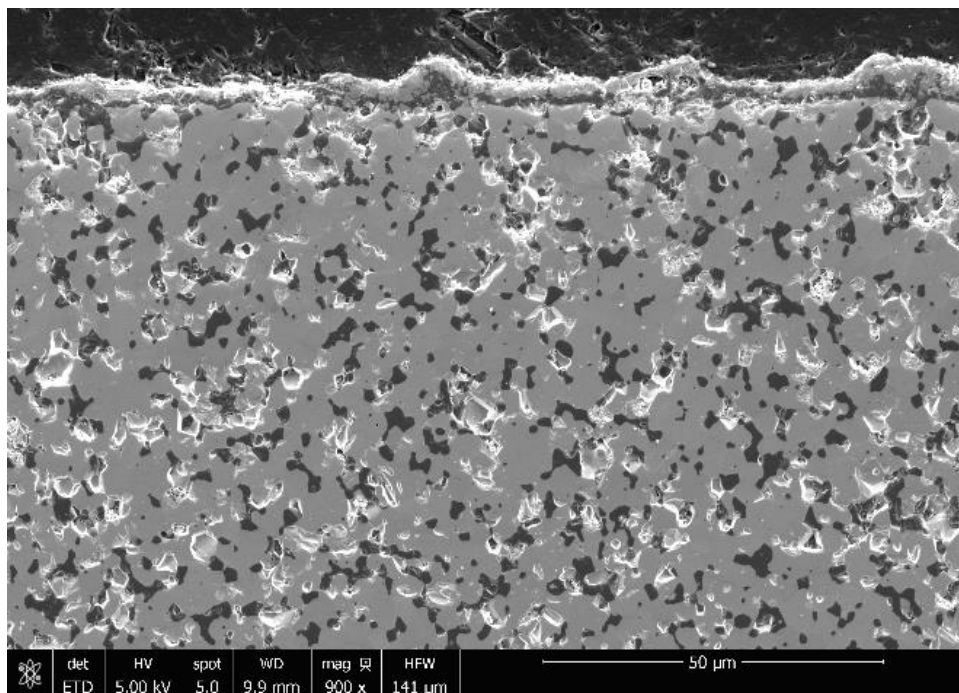
Figure 199. SEM Micrograph of HfB$_2$-20%SiC-12 oxide scale. Test failed during load up to 200 MPa. Specimen was subjected to 1500°C under 10 MPa for approximately 1 hour.
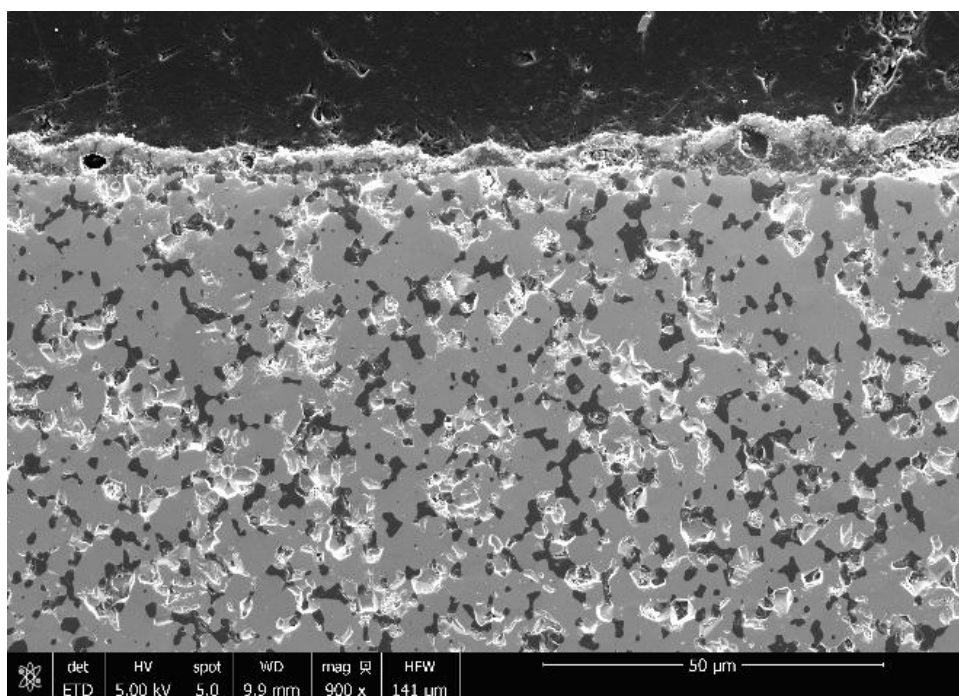
Figure 200. SEM Micrograph of HfB$_2$-20%SiC-12 oxide scale. Test failed during load up to 200 MPa. Specimen was subjected to 1500°C under 10 MPa for approximately 1 hour.
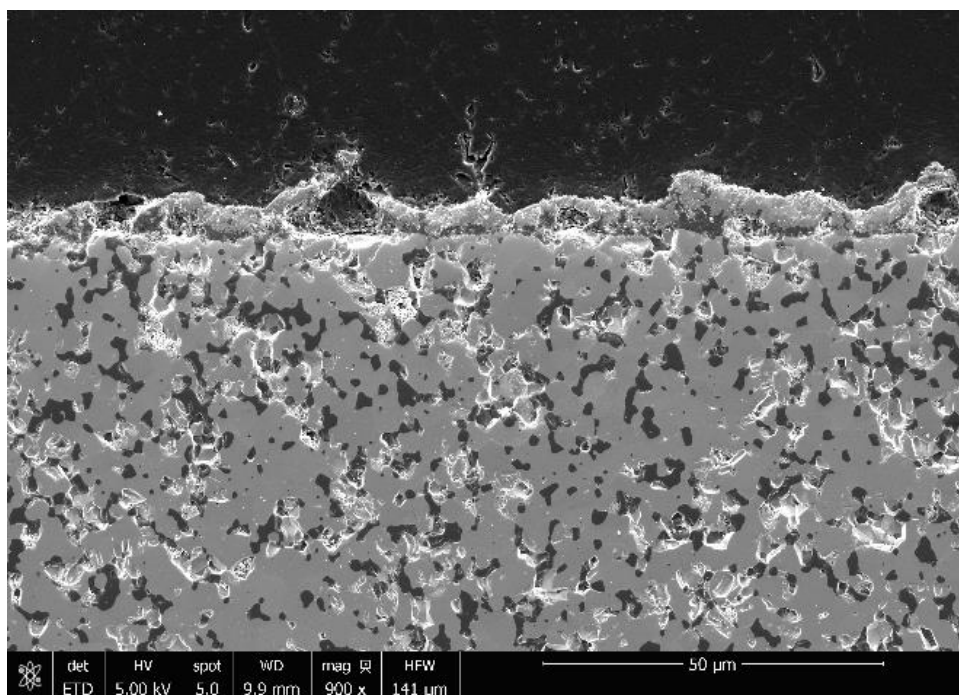
Figure 201. SEM Micrograph of HfB$_2$-20%SiC-12 oxide scale. Test failed during load up to 200 MPa. Specimen was subjected to 1500°C under 10 MPa for approximately 1 hour.
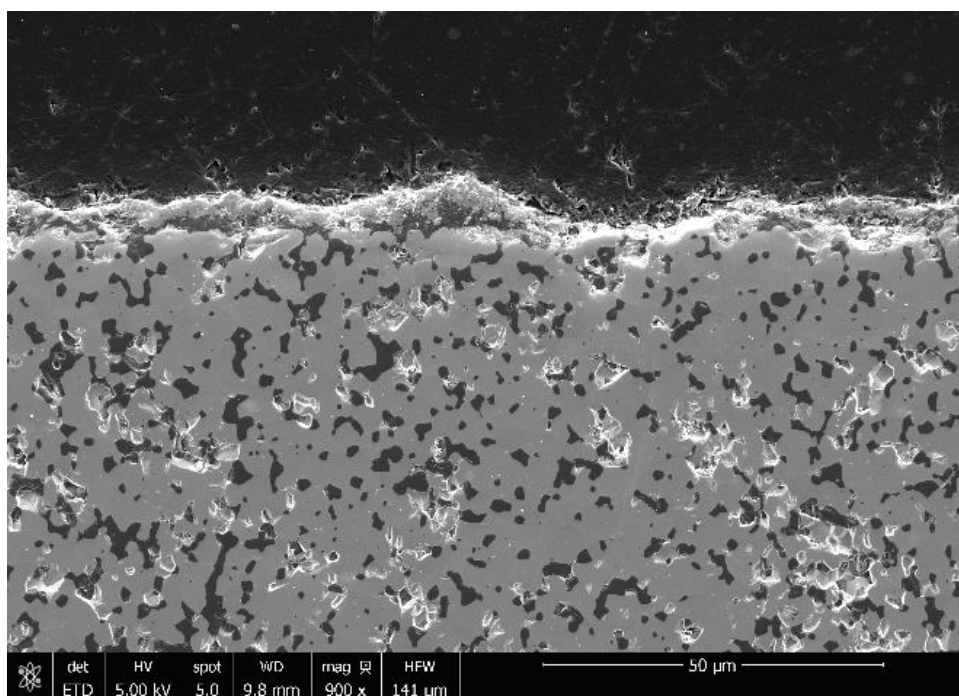
Figure 202. SEM Micrograph of HfB$_2$-20%SiC-12 oxide scale. Test failed during load up to 200 MPa. Specimen was subjected to 1500°C under 10 MPa for approximately 1 hour.
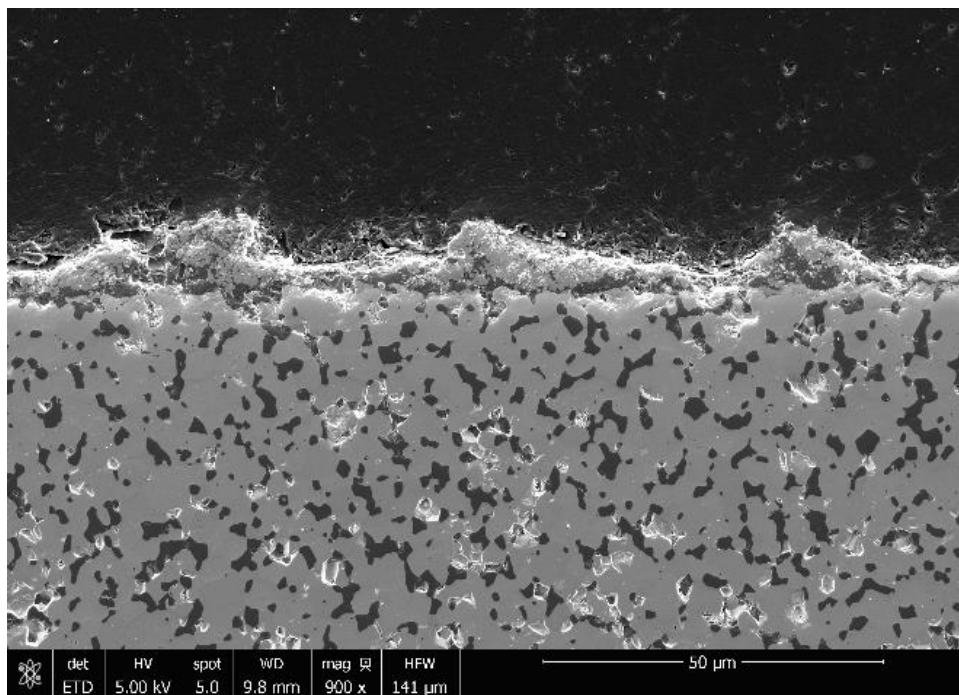
Figure 203. SEM Micrograph of HfB$_2$-20%SiC-12 oxide scale. Test failed during load up to 200 MPa. Specimen was subjected to 1500°C under 10 MPa for approximately 1 hour.
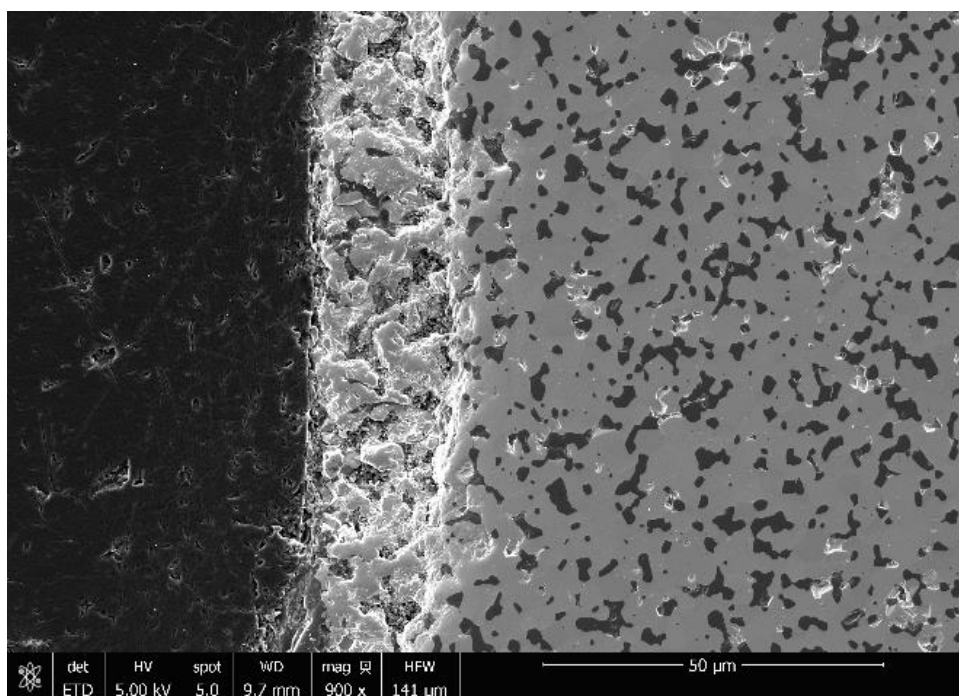
Figure 204. SEM Micrograph of HfB$_2$-20%SiC-12 oxide scale. Test failed during load up to 200 MPa. Specimen was subjected to 1500°C under 10 MPa for approximately 1 hour.
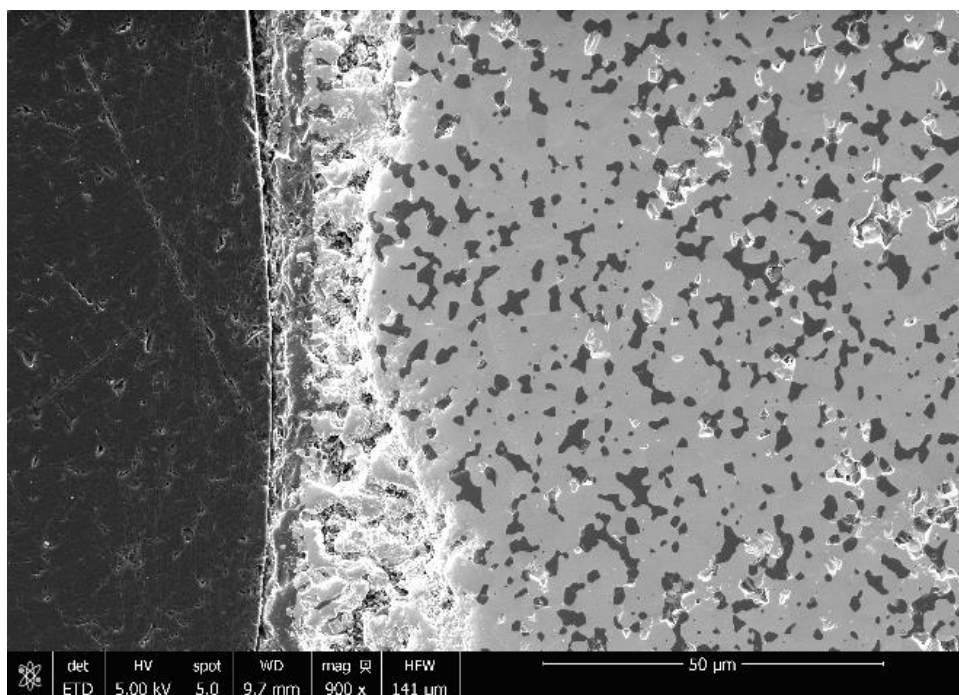
Figure 205. SEM Micrograph of HfB$_2$-20%SiC-12 oxide scale. Test failed during load up to 200 MPa. Specimen was subjected to 1500°C under 10 MPa for approximately 1 hour.
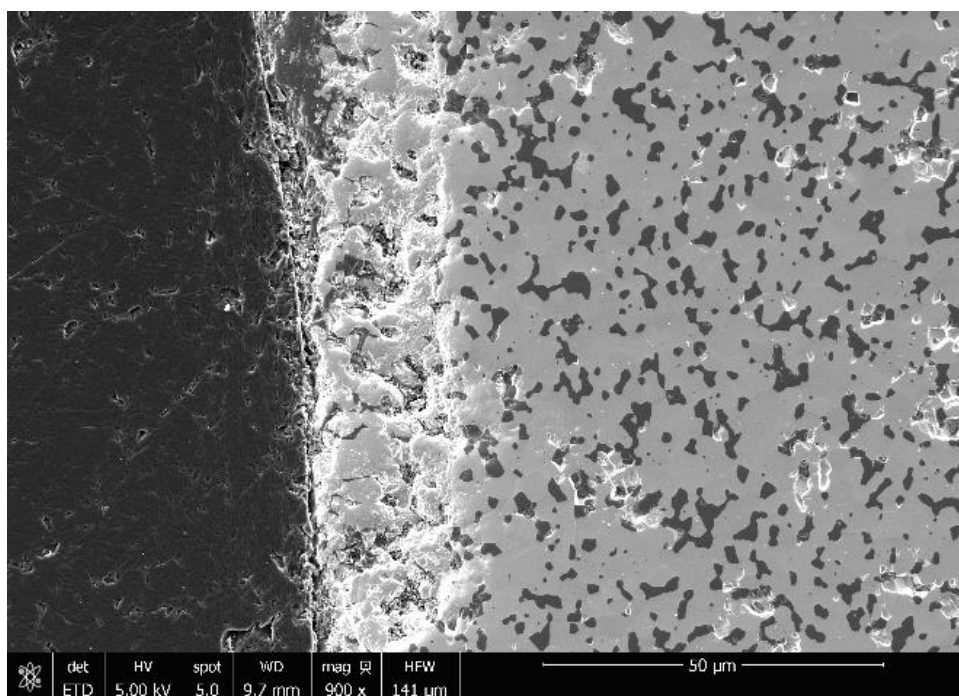
Figure 206. SEM Micrograph of HfB$_2$-20%SiC-12 oxide scale. Test failed during load up to 200 MPa. Specimen was subjected to 1500°C under 10 MPa for approximately 1 hour.
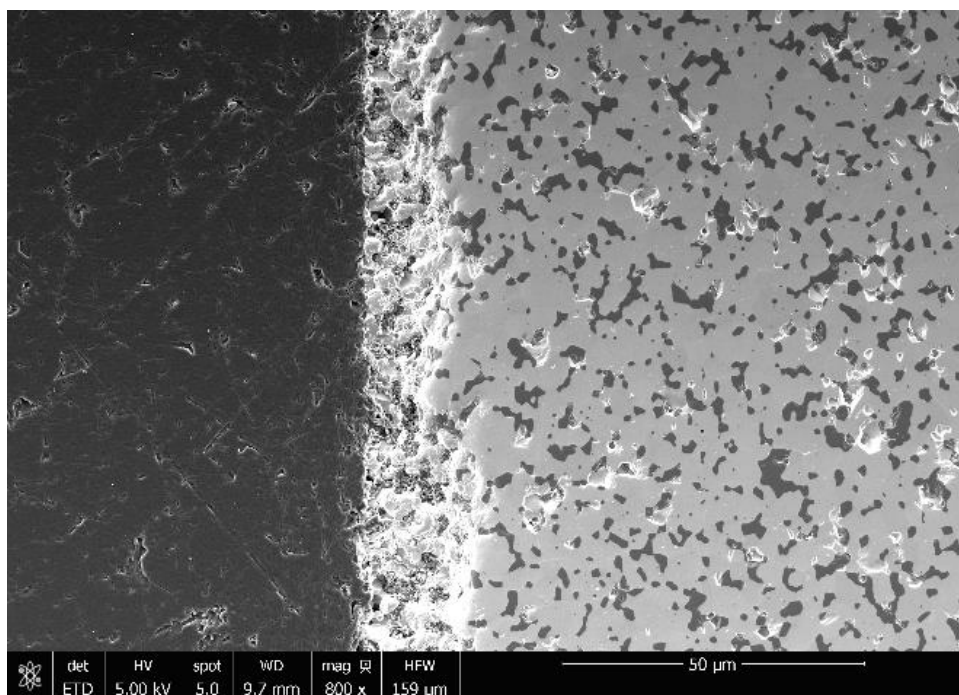
Figure 207. SEM Micrograph of HfB$_2$-20%SiC-12 oxide scale. Test failed during load up to 200 MPa. Specimen was subjected to 1500°C under 10 MPa for approximately 1 hour.
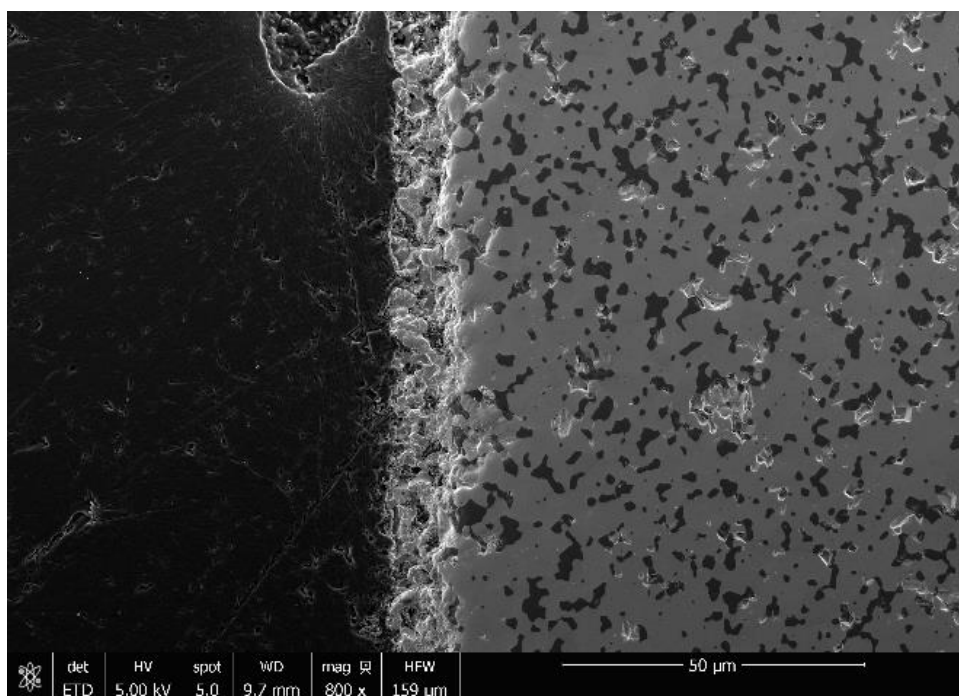
Figure 208. SEM Micrograph of HfB$_2$-20%SiC-12 oxide scale. Test failed during load up to 200 MPa. Specimen was subjected to 1500°C under 10 MPa for approximately 1 hour.
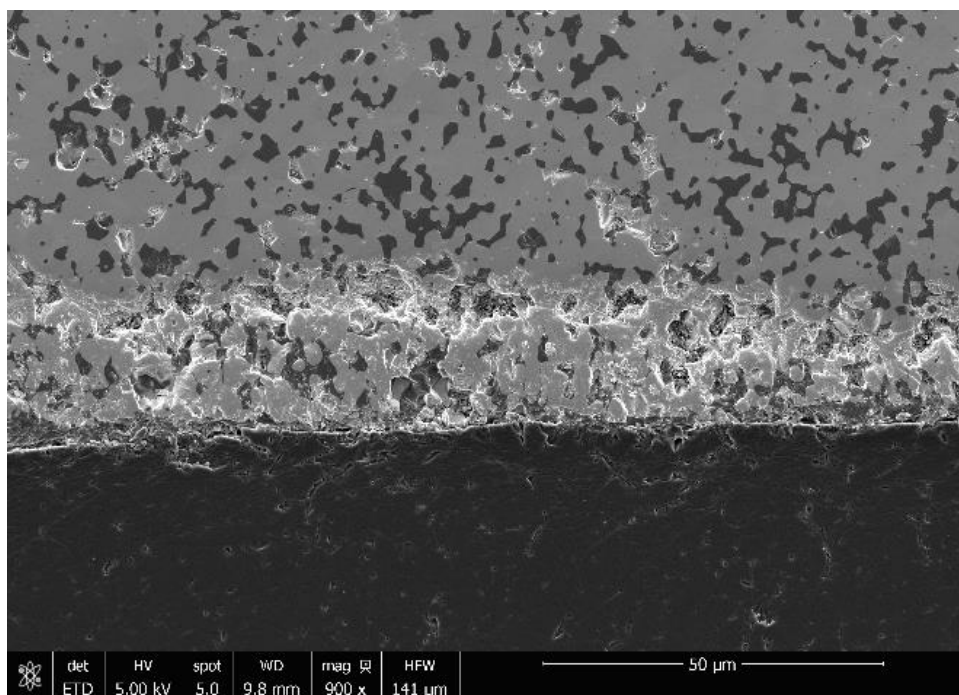
Figure 209. SEM Micrograph of HfB$_2$-20%SiC-12 oxide scale. Test failed during load up to 200 MPa. Specimen was subjected to 1500°C under 10 MPa for approximately 1 hour.

Appendix B: Test Procedures

<u>Pre-Test</u>

Specimen:

- Select specimen, new/refurbished YAG rods, new/refurbished sapphire extensometer rods, new sapphire spacers, temperature and stress for test

- Weigh, measure (caliper), and photo specimen. Take repeated measurements for completeness.

- Calculate load required for desired stress
MTS Station

- If MTS Station Manager needs to be opened, select "Temperature.cfg" and desired Parameters

- Select "New Specimen" on MTS Station Manager, enter specimen name, and hit <ENTER>

- Reset and edit procedure Creep.000 (load, temp, displacement limit detector values) and Save. Note: compressive loads are negative values. Set limit detector values to range from 9 mm → -3 mm.

- Check to ensure heating element leads are clear of metal-to-metal contact with the furnace and that the braids are securely connected (do not over tighten)

- Power on standalone hydraulic pump, Eurotherm controller, grip hydraulic power. Grip pressure should read about 2000 psi.

- Ensure manual command is disabled.

- Clear MTS Station Manager limit detectors, reset/override if needed, and start hydraulics (low then high)

- Start function generator (1 Hz, 5 mm sine wave) to warm up hydraulics/ MTS

- Stop function generator after a minimum of 30 minutes

<u>Load Train Assembly:</u>

- Clean specimen, sapphire spacers and YAG rods with acetone, ethanol or pure alcohol. Ensure mating interfaces are clear from any debris/ particulates.

- Assemble custom YAG holder with silver plated screws and spring washers

- Wrap steel shims around alignment rod

- Insert alignment rod into custom holder, finger tighten setscrews so rod is snug

- Insert assembly into MTS grips with 5mm separation between custom holder and MTS grip with both holders touching rear L-brackets, close top grip

- In displacement control, zero force via MTS interface, switch to force control with 0 lbf command, close bottom grip

- Ensure alignment rod is still free to move (i.e. not loaded)

- Return to displacement control, raise top crosshead, remove alignment rod

- Insert copper foil into slit at base of both custom holders

- Shim the YAG rods with enough copper foil to wrap one time around and insert into custom grips; secure set screws with hex key until finger tight

- Bring YAG rods together to verify alignment; repeat alignment procedure if not Aligned

- In displacement control, zero force

- Lower bottom crosshead, place wrap-around soft insulation through bottom YAG rod, raise crosshead

- Cut 2 pieces of Pt foil to size of a sapphire spacer

- Load one side of 3D printed alignment tool: Pt foil, 2 sapphire spacers, test specimen, 2 sapphire spacers, Pt foil

- Using other side of 3D printed tool bring YAG rods together so they are almost to the spacer cutouts.

- Carefully insert loaded half of alignment tool such that the YAG rods fit into their respective cutouts.

- Place other half of alignment tool on the exposed side, encasing load train with alignment tool.

- Holding the tool together, raise lower crosshead in 0.1mm increments until -10lbf is Reached

- Switch to force control and command -50lbf

- (Optional) Switch to displacement control, remove alignment tool, switch back to force control.

- Carefully remove alignment tool to verify everything within the load path is aligned.

- If adjustments are required rotate load train assembly using alignment tool; this may be accomplished at -50lbf but could require restarting

- Verify alignment; repeat alignment procedure if not aligned; zero displacement

- Set values for displacement limit detectors on MTS Station Manager, and activate for Station Power Off (+9/-3 mm)

- Replace extensometer rods (use fresh rods every time)

- Test extensometer on specimen; adjust rods as necessary; rods must be as centered in window as possible

- Zero strain; remove extensometer. Zero displacement and place blocks under lower ram.

Insulation:

- Slide furnace forward and secure; insert pie piece

- Place insulation around bottom YAG rod, between wrap around and furnace, to plug lower hole

- Wrap up wrap around soft insulation; secure with weight bar

- Place top soft insulation; secure with weights

- Support bottom of wrap around soft insulation with braces (metal ruler, wrenches)

- (Optional) Place side soft insulation

- Place extensometer; verify strain reading should be near zero with appropriate noise levels (<1%); zero strain

- Insert argon feeding tubes (even if testing in air), secure with tape to extensometer mounting brace

Heat:

- Turn on coolant to grips; ensure chiller is filled with distilled water

- Turn on heating element cooling fans and cooling air for extensometer

- Start procedure "Creep.000" (starts heat up and displays "Start", "End", and "ABORT" test buttons)

- Record lab temperature, relative humidity, and anytime the temperature goes into or out of limits

- When furnace begins to glow, visually verify the specimen and extensometer are in good position

- After reaching target temperature, wait for 1 hour of temperature soak
- Verify temperature and strain readings are steady before proceeding with Load
Load:

- Verify good thermal strain; verify temperature and strain are stable and within Limits

- Select "Start Test" button (loads up to desired load)

During Test:

- Check to ensure extensometer is clear of obstacles and is in grooves on specimen (use welding goggles)

- Check temperature, strain, displacement, and force values

- Check to ensure displacement is not too close to limit detector values

- Record strain, displacement, argon pressures, and time

Post Test:

- "End Test" button (commands -50 lbf and 0°C)

- Let cool naturally until 100°C (opening early can shock the YAG and crack them)

- Remove argon feeding tubes, extensometer, top and side soft insulations; raise topside of wrap around insulation

- Remove pie piece; photo specimen; "Release Specimen" button, switch to displacement control

- Lower bottom crosshead in 0.1 mm intervals until there's clearance to remove Specimen

- Remove, photo, and secure specimen

- Power down grip coolant, hydraulics on MTS Station Manager, Eurotherm Controller

- Remove bottom supports and wrap around insulation

- Push back furnace and secure

- Remove top and bottom custom grips and power down hydraulics for grips

- Power down standalone hydraulic pump

- Remove YAG rods from custom holders and turn in for repair if reparable

- Copy and analyze data from MTS computer

- Weigh and measure specimen; assess oxide scale and thickness

Appendix C: XRD Analysis

Figures X-X show XRD results and optical micrograph references for specimen HfB$_2$-20SiC-6 which exhibited dissimilar scale formations. This data was to be used in conjunction with EDS results presented in Chapter IV to examine the various types of oxide scales formed on the specimen's surface during testing. XRD analysis is able to provide information regarding the crystallographic structure of each type of oxide scale present. The XRD equipment used was a Rigaku Ultima IV X-Ray Diffractometer. Analysis was performed through the Rietveld refinement program MAUD to determine phase fractions from the X-ray diffraction patterns.

(i)   (ii)
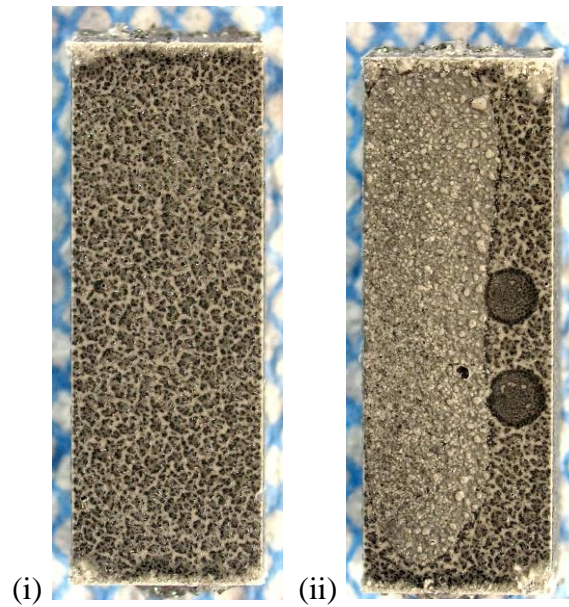
Figure 210. Post-test optical micrographs of specimen HfB$_2$-20SiC-6 showing (i) a visually uniform oxide scale and (i) visually dissimilar oxide scales.
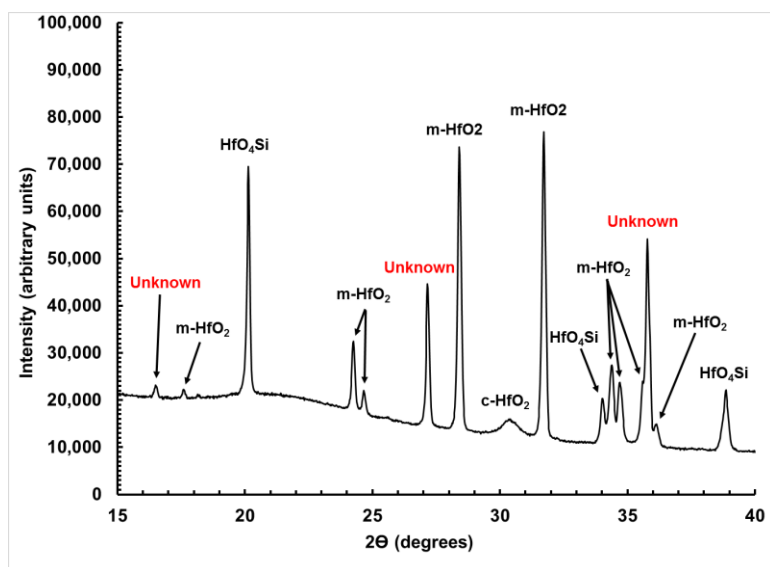
Figure 211. XRD results from a scan of the visually uniform oxide scale formation of specimen HfB_2-20SiC, represented by Figure 210(i). Known crystallographic formations are labeled above their respective intensity peaks. 'm-HfB_2' represents monoclinic hafnia. 'c-HfB_2' represents cubic hafnia. An unidentified crystallographic structure (labeled as 'unknown') was detected however, standard analysis methods could not identify the structure given the elements known to be present within the scale.
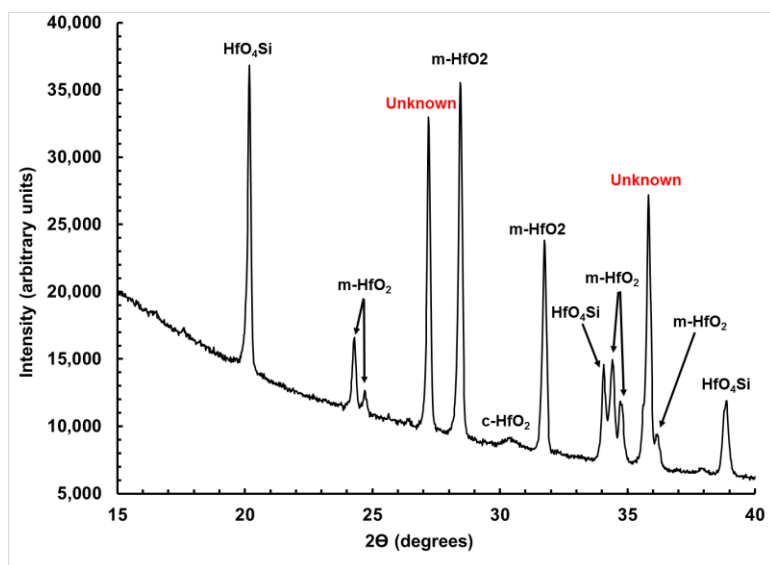
Figure 212. XRD results from a scan of the visually dissimilar oxide scale formations of specimen HfB_2-20SiC, represented by Figure 210(ii). Known crystallographic formations are labeled above their respective intensity peaks. 'm-HfB_2' represents monoclinic hafnia. 'c-HfB_2' represents cubic hafnia. An unidentified crystallographic structure (labeled as 'unknown') was detected however, standard analysis methods could not identify the structure given the elements known to be present within the scale.

152

The uniform scale and the dissimilar scale appear to contain the same basic crystallographic structures within their respective oxide scales. While peaks are present at the same 2Θ intervals for both figures, the relative intensities between the peaks are clearly different. This indicates that while the same crystallographic structures are present on the surface of these two side of specimen HfB_2-20SiC-6, they occur in different ratios.

Figures 213-216 show pole figures for both untested specimen HfB_2-20SiC-15 and tested specimen HfB_2-20SiC-9. Three orthogonal faces were scanned for each specimen and XRD analysis was performed to determine whether a preferred grain orientation was present within the specimen. Recall from the discussion in Chapter III, an MRD value of 1 represents a completely random grain orientation while an MRD value of infinity represents a perfectly oriented crystal (i.e. a single crystal). Figure 217 shows the 3 sides chosen for analysis for both specimen. Both specimen were polished to a surface finish of 45 μm for consistency. Specimen HfB_2-20SiC-15 was scanned in the original configuration from manufacture, dimensions: 6.5 x 6.5 x 19 mm. Since specimen HfB_2-20SiC-9 had undergone testing, it was necessary to remove the oxide scale to scan the grain structure under the surface. Therefore, specimen HfB_2-20SiC-9 was sectioned via a low concentration diamond blade and polished to the desired surface finish, final dimensions: 3 x 3 x 7 mm.
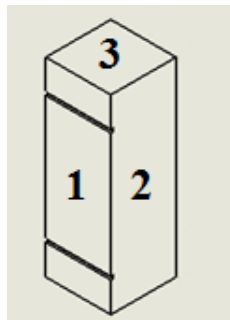
Figure 217. Representative of the 3 orthogonal sides scanned for each specimen to determine preferred grain orientation.

153

The pole figures in Figures 213-216 represent the degree of preferred grain orientation and preferred grain direction present within the specimens. Miller indices 001, 100, 101, and 110 were selected for representation in these figures because these planes indicated the highest MRD values detected. Table 6 in Chapter IV provides the MRD values and preferred grain orientation for each specimen. The pole figures below are plotted on an MRD spectrum ranging from either 0.8-1.2 or 0.0-2.0. The spectrum from 0.8-1.2 was chosen so that a preferred grain orientation could be detected. For example, in Figure 213, of the pole figures associated with specimen HfB_2-20SiC-15, side 1, the 001 plane provides the highest MRD value in the center ring (indicated by presence of dark red coloration). Although slight preferred orientations are discernable at a narrow MRD scale of 0.8-1.2, this range is so close to an MRD scale of 1, that any detected preferred orientation would still be considered slight. For context, Figures 215 and 216 show the same data plotted on pole figures with MRD scales ranging from 0.0-2.0. In these figures, preferred orientations are barely identifiable. Given that the MRD scale ranges from one to infinity, these figures represent how slight a preferred orientation is present in these specimens.
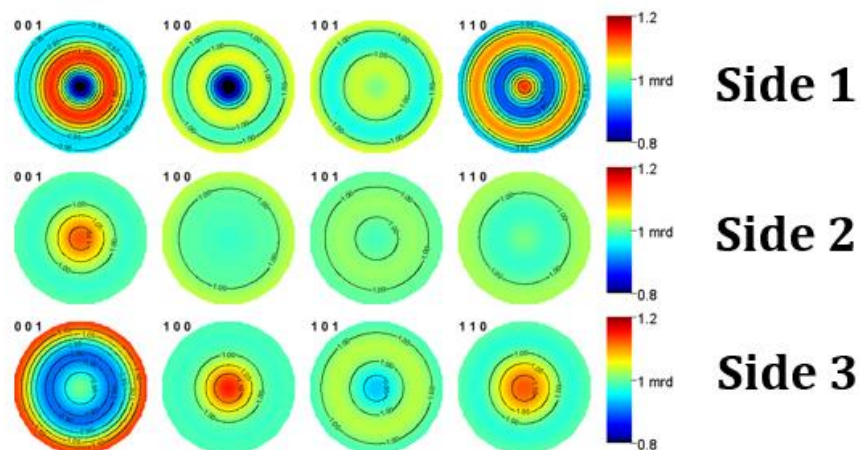
Figure 213. Pole figures for untested specimen HfB$_2$-20SiC-15. MRD scale: 0.8-1.2. Dark red coloration indicates the presence of a preferred orientation. For any side, the darkest red within the centermost ring of an individual pole figure indicates the miller index associated with the direction of preferred orientation.
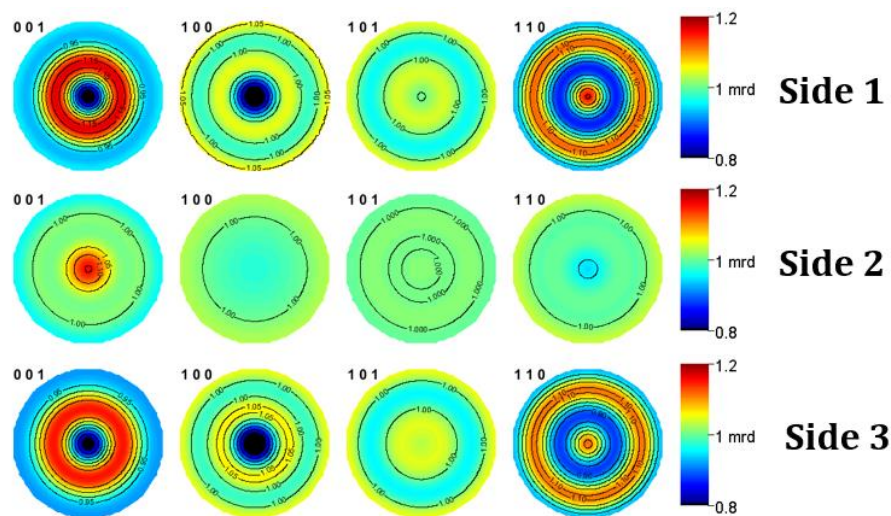
Figure 214. Pole figures for specimen HfB$_2$-20SiC-9 subject to 150 MPa for 6.03 hours. MRD scale: 0.8-1.2. Dark red coloration indicates the presence of a preferred orientation. For any side, the darkest red within the centermost ring of an individual pole figure indicates the miller index associated with the direction of preferred orientation.
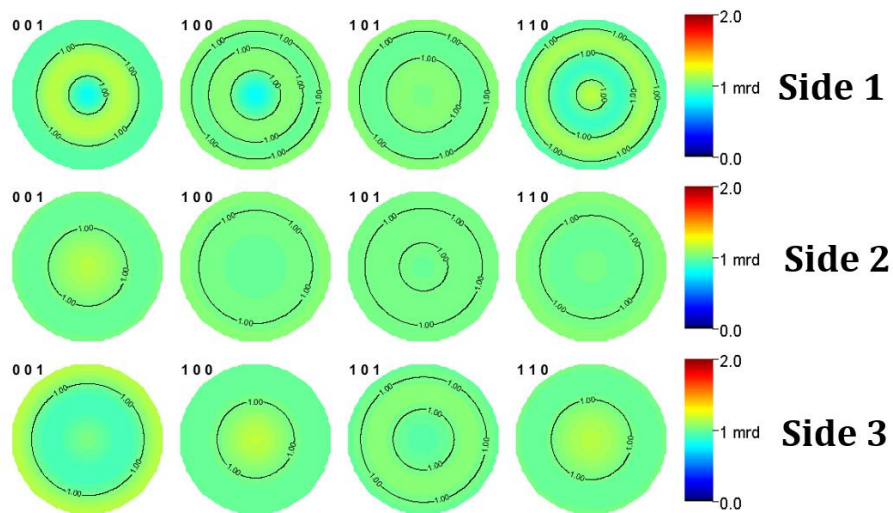
Figure 215. Pole figures for untested specimen HfB$_2$-20SiC-15. MRD scale: 0.0-2.0. This scale shows a hardly identifiable orientation at a slightly larger scale. When compared to the full MRD scale of 1-∞, the degree of preferred orientation in this specimen is quite small.
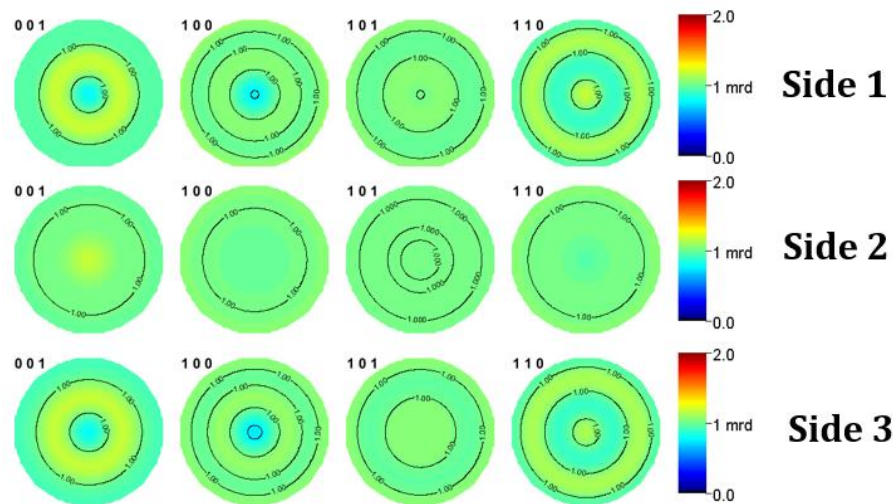
Figure 216. Pole figures for specimen HfB$_2$-20SiC-9. MRD scale: 0.0-2.0. This scale shows a hardly identifiable orientation at a slightly larger scale. When compared to the full MRD scale of 1-∞, the degree of preferred orientation in this specimen is quite small.
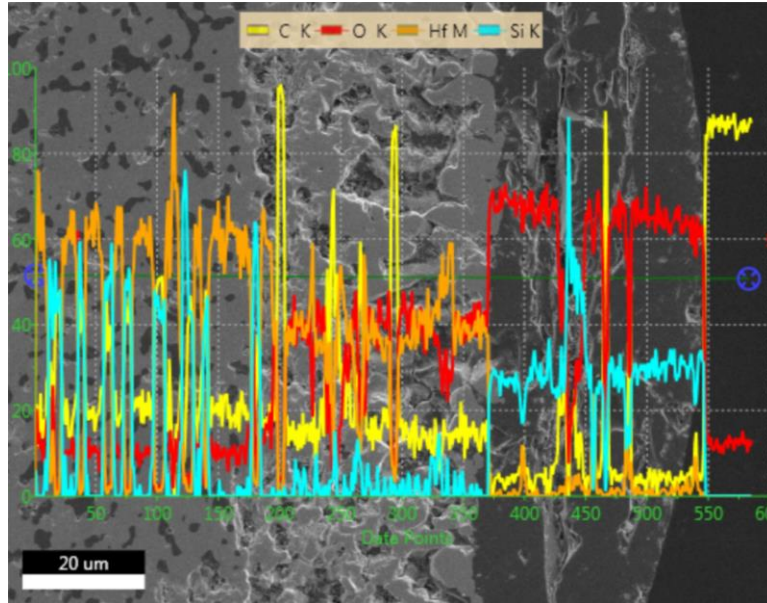
Figure 218. EDS line scan of the oxide scale of specimen HfB$_2$-20SiC-5. Elemental analysis shows varying amounts of carbon, oxygen, hafnium and silicon through different regions of the specimen. This line scan data is the same as in Figure 17 in Chapter III, the concentration of various elements have simply been overlaid onto the same figure.
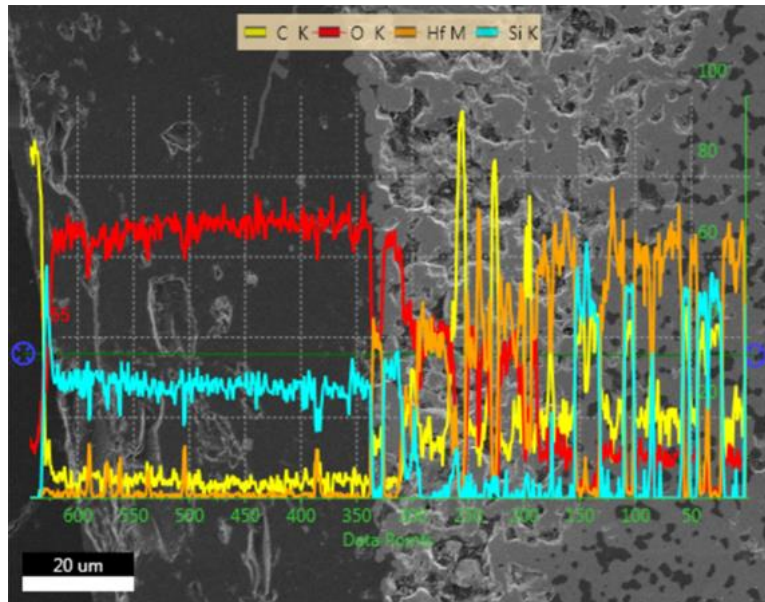
Figure 219. EDS line scan of the oxide scale of specimen HfB$_2$-20SiC-5. Elemental analysis shows varying amounts of carbon, oxygen, hafnium and silicon through different regions of the specimen. This line scan data was taken from a separate area of the specimen than the data in Figure 17. Analysis of this area provided the same conclusions as those detailed in Chapter III.
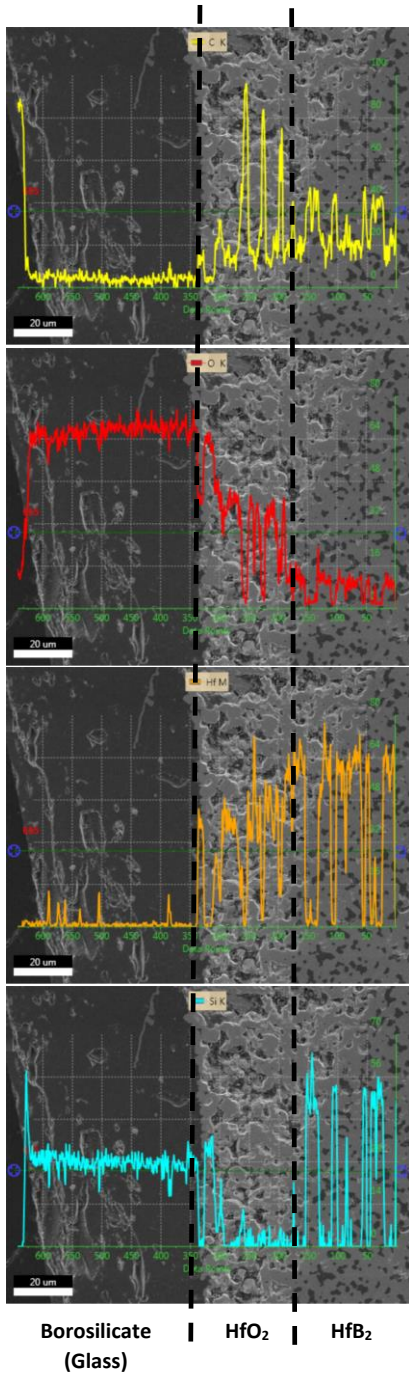
Figure 220. EDS line scan of the oxide scale of specimen HfB$_2$-20SiC-5. Elemental analysis shows varying amounts of carbon, oxygen, hafnium and silicon through different regions of the specimen. This line scan data was taken from the same area as Figure 219. Analysis of this area provided the same conclusions as those detailed in Chapter III.

EDS analysis of the oxide scale of specimen HfB$_2$-20SiC-6 was performed in a similar manner to the analysis detailed in Chapter IV for specimen HfB$_2$-20SiC-9. As evidenced by the optical micrographs in Appendix A, Specimen HfB$_2$-20SiC-6 exhibited at least three visually dissimilar oxide scales on its surface during testing. This work examined the elemental composition of these three dissimilar oxide areas. Figure 221 shows an SEM image of a region on the surface of specimen HfB$_2$-20SiC-6 exhibiting dissimilar oxide scale formations. The red squares indicate areas scanned and analyzed by EDS. EDS analysis of specimen HfB$_2$-20SiC-6 provided the same results as the EDS analysis of specimen HfB$_2$-20SiC-9 discussed in Chapter III. Results for Area 4 were corrupted and not included in this discussion.
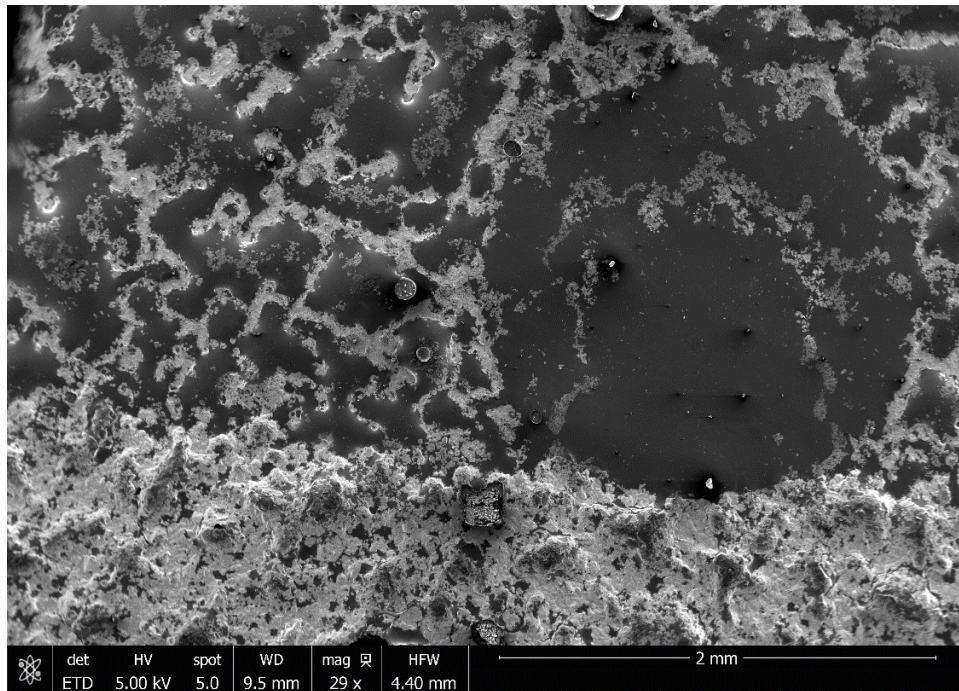
Figure 221. SEM micrograph of the oxide scale of specimen HfB$_2$-20SiC-6 showing the presence of three distinct regions of oxide scale. This region is the focus of the EDS analysis discussed herein.
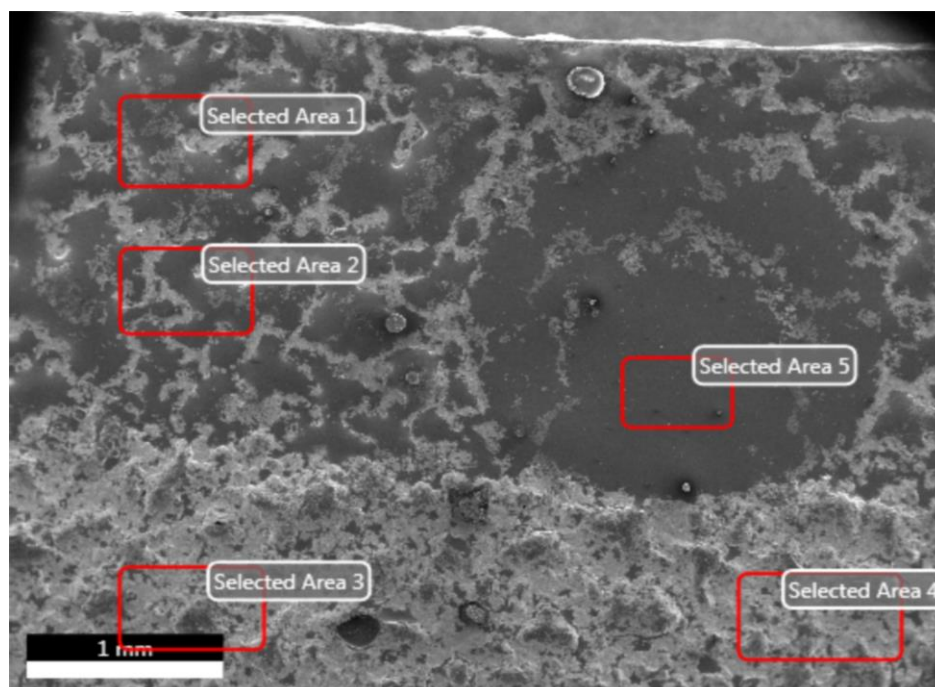
Figure 222. SEM image of the oxide scale of specimen HfB$_2$-20SiC-6 showing the presence of three distinct regions of oxide scale. A darker region interspersed with lighter colored veins (Areas 1 and 2), a lighter region (Areas 3 and 4) and a smooth, dark area (Area 5). The red squares represent areas scanned with EDS for elemental analysis.

Figure 223. EDS analysis of Area 1 (as indicated in Figure 222) of specimen HfB$_2$-20SiC-6. Analysis indicates the presence of silicon, hafnium and oxygen. Given the presence of these elements, it is most likely that the dark, amorphous material in Figure 221 is borosilicate glass (B$_2$O$_3$+SiO$_2$) and the lighter crystalline material is hafnia (HfO$_2$).

Figure 224. EDS analysis of Area 2 (as indicated in Figure 222) of specimen HfB_2-20SiC-6. Analysis indicates the presence of silicon, hafnium and oxygen. Given the presence of these elements, it is most likely that the dark, amorphous material in Figure 221 is borosilicate glass ($B_2O_3+SiO_2$) and the lighter crystalline material is hafnia (HfO_2).

Figure 225. EDS analysis of Area 3 (as indicated in Figure 222) of specimen HfB_2-20SiC-6. Analysis indicates the presence of silicon, hafnium, oxygen and carbon. Given the presence of these elements, it is most likely that lighter crystalline material in Figure 221 is hafnia (HfO_2) and there is a dispersion of borosilicate glass filling in cracks and voids.

Figure 226. EDS analysis of Area 5 (as indicated in Figure 222) of specimen HfB_2-20SiC-6. Analysis indicates the presence of silicon, oxygen and carbon. Given the presence of these elements and the processes known to have taken place during testing, it is most likely that the dark, amorphous material in Figure 221 is borosilicate glass ($B_2O_3+SiO_2$).

161

Optical micrographs in Appendix A show that specimen HfB_2-20SiC-12 exhibited a unique reddish hue following testing. Both Winder and Bowen observed similar discoloration in their testing. Composition analysis of Winder and Bowen revealed the presence of aluminum deposits on the surface, responsible for the discoloration. Similar EDS analysis was performed on specimen HfB2-20SiC-12 with identical results. The presence of aluminum was responsible for the discoloration. Aluminum deposits most likely occurred after the test for HfB_2-20SiC-12 failed due to spacer failure and the specimen came to rest against the alumina furnace for approximately 2 hours as the furnace cooled from 1500°C. Figures 227-234 show results of EDS analysis of specimen HfB_2-20SiC-12.
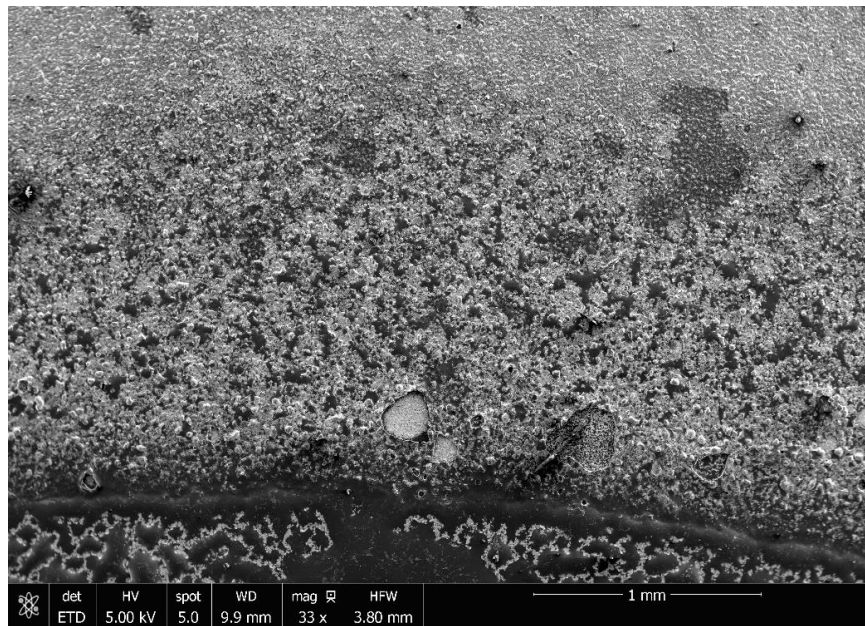
Figure 227. Post-test SEM micrograph of specimen HfB2-20SiC-12 showing a region of the external surface of the specimen exhibiting a reddish discoloration. This region was the focus of EDS compositional analysis.
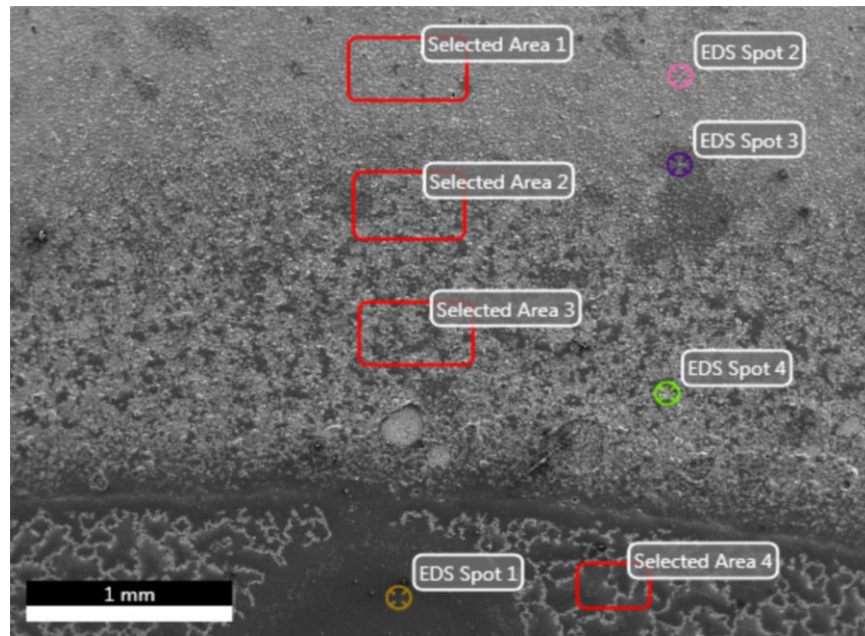
Figure 228. Post-test SEM micrograph of specimen HfB2-20SiC-12 showing the same area as Figure 227, a region of the external surface of the specimen exhibiting a reddish discoloration. This region was the focus of EDS compositional analysis. Red squares and colored bullseyes indicate the areas scanned for analysis.
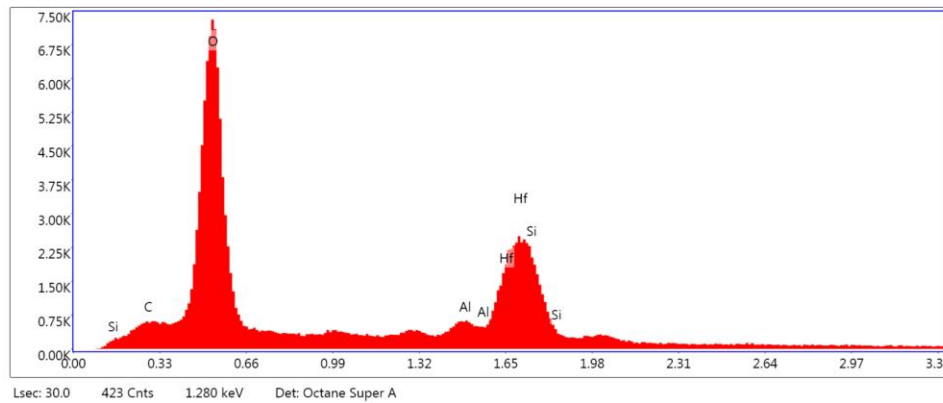
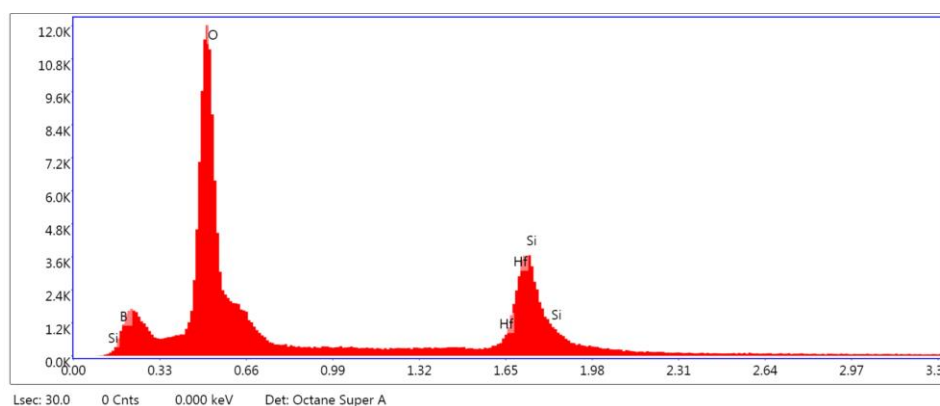Figure 229. EDS analysis of Area 1 (as indicated in Figure 228) of specimen HfB_2-20SiC-12. Analysis indicates the presence of silicon, oxygen, hafnium, carbon and aluminum. Aluminum is the only unexpected element present and is likely the cause of the reddish discoloration.

163
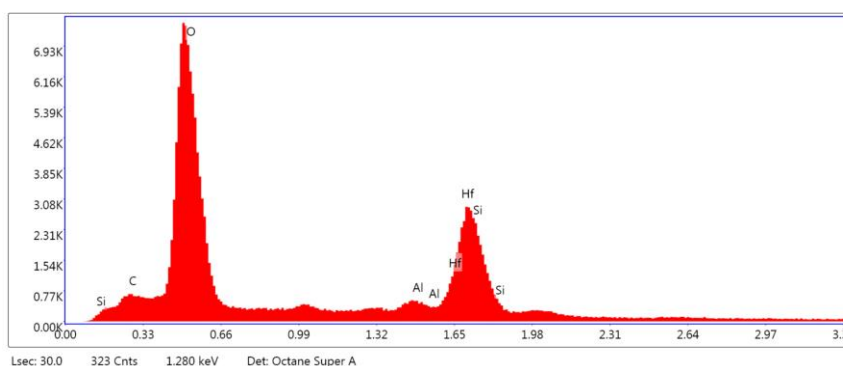
Figure 230. EDS analysis of Area 2 (as indicated in Figure 228) of specimen HfB₂-20SiC-12. Analysis indicates the presence of silicon, oxygen, hafnium, carbon and aluminum. Aluminum is the only unexpected element present and is likely the cause of the reddish discoloration.
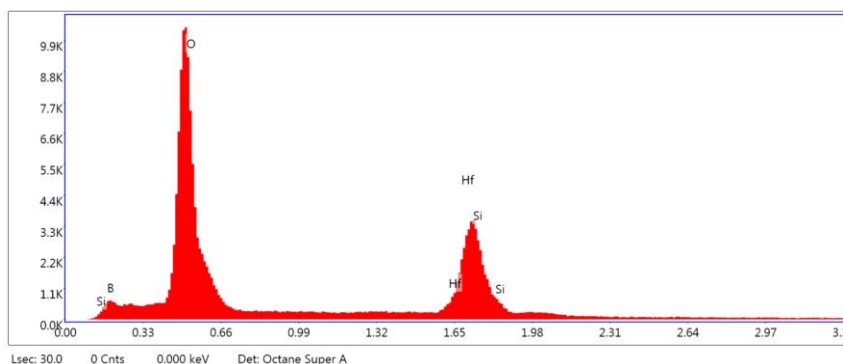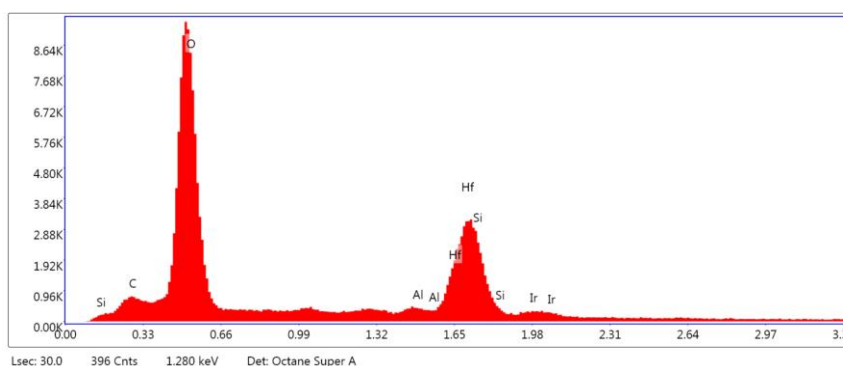

Figure 231. EDS analysis of Area 3 (as indicated in Figure 228) of specimen HfB₂-20SiC-12. Analysis indicates the presence of silicon, oxygen, hafnium, carbon and aluminum. Aluminum is the only unexpected element present and is likely the cause of the reddish discoloration.
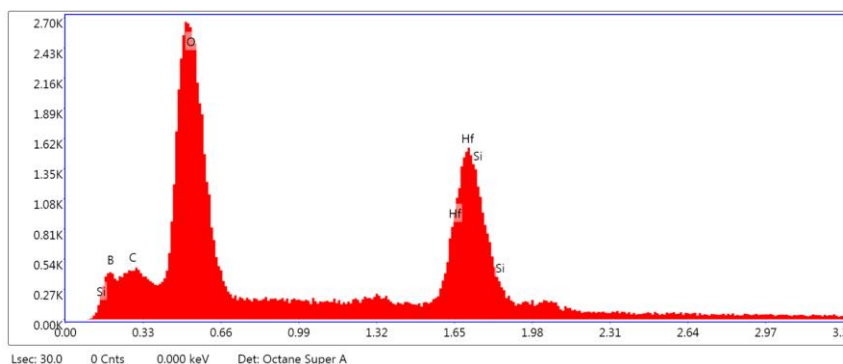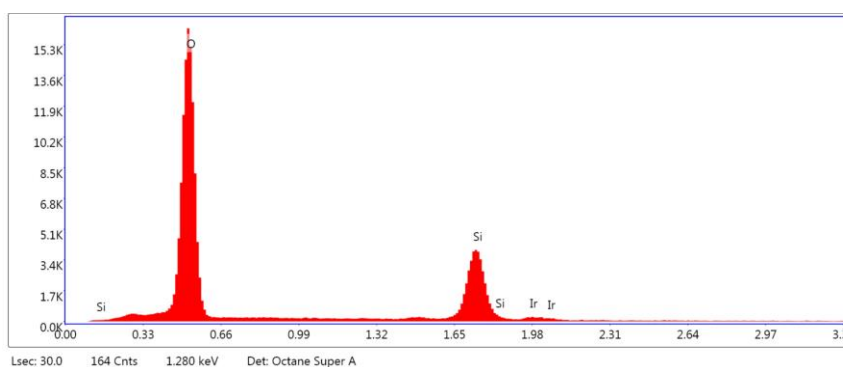

Figure 232. EDS analysis of Spot 1 (as indicated in Figure 228) of specimen HfB₂-20SiC-12. Analysis indicates the presence of silicon, oxygen, and iridium. This area was not exhibiting discoloration and aluminum is not present. A thin coating of iridium was used to coat the specimen to prevent surface charging in the SEM.

164
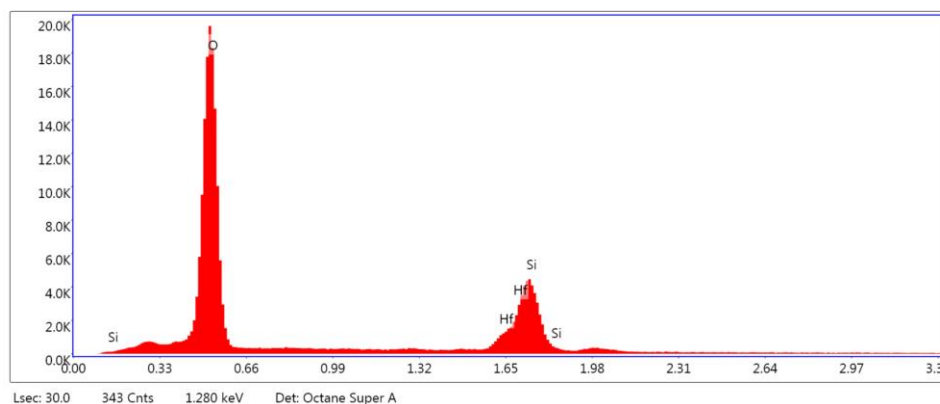
Figure 233. EDS analysis of Area 4 (as indicated in Figure 228) of specimen HfB$_2$-20SiC-12. Analysis indicates the presence of silicon, oxygen, and hafnium. This area was not exhibiting discoloration and aluminum is not present.
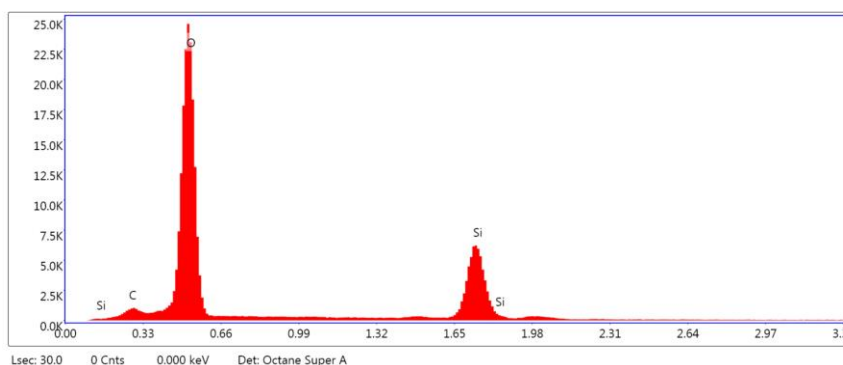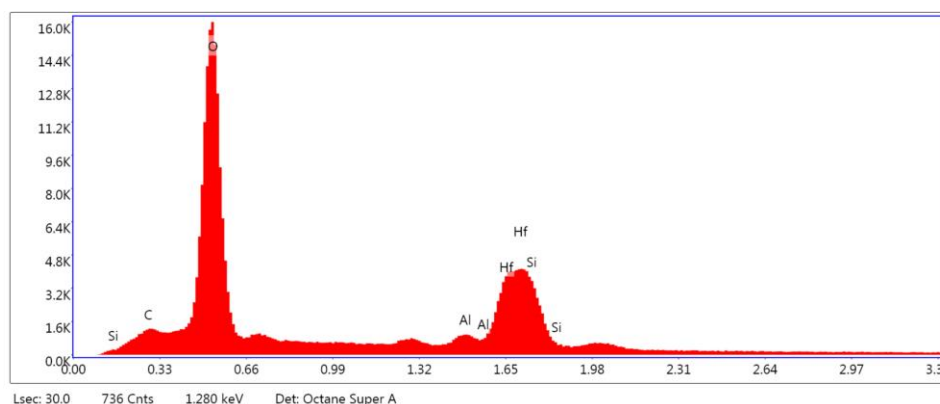

Figure 234. EDS analysis of Spot 2 (as indicated in Figure 228) of specimen HfB$_2$-20SiC-12. Analysis indicates the presence of silicon, oxygen, hafnium, carbon and aluminum. Aluminum is the only unexpected element present and is likely the cause of the reddish discoloration.

References

[1] K. K. Chawla, Ceramic matrix composites. London: Chapman & Hall, 1993.

[2] S. Musikant, What Every Engineer Should Know About Ceramics. New York: Marcel Dekker, Inc., 1991.

[3] "THE X-15 PROGRAM IN RETROSPECT," NASA. [Online]. Available: http://history.nasa.gov/x15lect/structur.html. [Accessed: 02-Aug-2017].

[4] "Ceramic History." [Online]. Available: http://depts.washington.edu/matseed/mse_resources/Webpage/Ceramics/ceramichistory.htm. [Accessed: 20-Jul-2017].

[5] R. W. Davidge, Mechanical Behaviour of Ceramics. Cambridge: Cambridge University Press, 1979.

[5] A. Shaffer, "Precision Strike Annual Review," 17-Mar-15. [Online] Available: http://www.dtic.mil/ndia/2015PSAR/AlShaffer.pdfA. [Accessed: 02-Aug-2017].

[6] E. Wuchina, E. Opila, M. Opeka, W. Fahrenholtz and I. Talmy, 'UHTCs: Ultra-High Temperature Ceramic Materials for Extreme Environment Applications,' *Electrochem. Soc. Interface*, Winter 30-36 (2007).

[7] W. G. Fahrenholtz, G. E. Hilmas, I. G. Talmy and J. A. Zaykoski, 'Refractory Diborides of Zirconium and Hafnium,' *J. Am. Ceram. Soc.*, 90 [5] 1347-1364 (2007).

[8] W. G. Fahrenholtz and G. E. Hilmas, 'Ultra-High Temperature Ceramics – An Introduction to Ultra-High Temperature Ceramics,' *The A to Z of Materials*, 2012.

[9] W. Guo and G. Zhang, 'Oxidation Resistance and Strength Retention of ZrB_2–SiC Ceramics,' *J. Eur. Ceram. Soc.*, 30 [11] 2387-2395 (2010).

[10] M. Opeka, J. Zaykoski, I. Talmy and S. Causey, 'Synthesis and Characterization of Zr_2SC ceramics,' *Materials Science & Engineering: A*, 528 [4–5] 1994-2001 (2011).

[11] I. G. Talmy, J. A. Zaykoski and C. A. Martin, 'Flexural Creep Deformation of ZrB_2-SiC Ceramics in Oxidizing Atmosphere,' *J. Am. Ceram. Soc.*, 91 [5] 1441-1447 (2008).

[12] I. G. Talmy, J. A. Zaykoski and M. M. Opeka, 'High-Temperature Chemistry and Oxidation of ZrB_2 Ceramics Containing SiC, Si_3N_4, Ta_5Si_3, and $TaSi_2$,' *J. Am. Ceram. Soc.*, 91 [7] 2250-2257 (2008).

[13] T. A. Bowen, "Stressed Oxidation of Hafnium Diboride in Air at 1500°C", Thesis, Defense Technical Information Center, 2017.

[14] M. M. Opeka, I. G. Talmy and J. A. Zaykoski, 'Oxidation-Based Materials Selection for 2000°C+ Hypersonic Aerosurfaces: Theoretical Considerations and Historical Experience,' *J. Mater. Sci.*, 39 [19] 5887-5904 (2004).

[15] M. M. Opeka, I. G. Talmy and E. J. Wuchina, 'Mechanical, Thermal, and Oxidation Properties of Refractory Hafnium and Zirconium Compounds,' *J. Eur. Ceram. Soc.*, 19 2405-2414 (1999).

[16] E. Wuchina, M. Opeka, S. Causey, K. Buesking, J. Spain, A. Cull, J. Routbort and F. Guitierrez-Mora, 'Designing for Ultrahigh-Temperature Applications: The Mechanical and Thermal Properties of HfB_2, HfC_x, HfN_x and $aHf(N)$,' *J. Mater. Sci*, 39 [19] 5939-5949 (2004).

[17] S. C. Zhang, G. E. Hilmas and W. G. Fahrenholtz, 'Pressureless Densification of Zirconium Diboride with Boron Carbide Additions,' *J. Am. Ceram. Soc.*, 89 [5] 1544-1550 (2006).

[18] S. C. Zhang, G. E. Hilmas and W. G. Fahrenholtz, 'Oxidation of Zirconium Diboride with Tungsten Carbide Additions,' *J. Am. Ceram. Soc.*, 94 [4] 1198-1205 (2011).

[19] X. Zhang, G. E. Hilmas and W. G. Fahrenholtz, 'Densification, Mechanical Properties, and Oxidation Resistance of TaC-TaB_2 Ceramics,' *J. Am. Ceram. Soc.*, 91

[20] L. Kaufman and E. V. Clougherty, "Investigation of boride compounds for very high temperature applications (Technical Documentary Report No. RTD-TDR-63-4096)," Wright-Patterson AFB, Ohio, 1963.

[21] C. B. Bargeron, R. C. Benson, R. W. Newman, A. N. Jette, and T. E. Phillips, "Oxidation Mechanisms of Hafnium Carbide and Hafnium Diboride in the Temperature Range 1400 to 2100˚C," John Hopkins APL Tech Digest, vol. 14, no. 1, pp. 29–36, 1993.

[22] S. L. Winder, "Mechanical Testing of Ultra-High Temperature Ceramics at 1500°C in Air – Development of an Experimental Facility and Test Method," dissertation, Defense Technical Information Center, 2015.

[23] A. DeGregoria, "Creep and Oxidation of Hafnium Diboride-Based Ultra High Temperature Ceramics at 1500˚C," dissertation, Defense Technical Information Center, 2015.

[24] D. S. Wilkinson, "Creep mechanisms in multiphase ceramic materials," Journal of the American Ceramic Society, vol. 81, no. 2. pp. 275–299, Jan-1998.

[25] I. H. Shames and F. A. Cozzarelli, Elastic and inelastic stress analysis. Washington, DC: Taylor and Francis, 1997.

[26] W. F. Smith, Principles of materials science and engineering. New York: McGraw-Hill, 1996.

[27] M. W. Bird, R. P. Aune, F. Yu, P. F. Becher, and K. W. White, "Creep behavior of a zirconium diboride–silicon carbide composite," Journal of the European Ceramic Society, vol. 33, no. 13-14, pp. 2407–2420, 2013.

[28] R. T. DeHoff, Thermodynamics in Materials Science. Boca Raton: CRC/Taylor & Francis, 2006.

[29] M. Mallik, K. Ray, and R. Mitra, "Oxidation behavior of hot pressed ZrB2–SiC and HfB2–SiC composites," Journal of the European Ceramic Society, vol. 31, no. 1-2, pp. 199–215, 2011.

[30] T. A. Parthasarathy, R. A. Rapp, M. Opeka, M. K. Cinibulk, and N. Jacobson, "Modeling Oxidation Kinetics of SiC-Containing Refractory Diborides," *Journal of the American Ceramic Society,* vol. 95, no. 1. p. 338, Jan-2012.

[31] C. M. Carney, "Oxidation resistance of hafnium diboride-silicon carbide from 1400 to 2000°C," Journal of Materials Science, vol. 44, no. 20. p. 5673, Jan-2009.

[32] C. M. Carney, T. A. Parthasarathy and M. K. Cinibulk, 'Oxidation Resistance of Hafnium Diboride Ceramics with Additions of Silicon Carbide and Tungsten Boride or Tungsten Carbide,' *J. Am. Ceram. Soc.*, 94 [8] 2600-2607 (2011).

REPORT DOCUMENTATION PAGE

The public reporting burden for this collection of information is estimated to average 1 hour per response, including the time for reviewing instructions, searching existing data sources, gathering and maintaining the data needed, and completing and reviewing the collection of information. Send comments regarding this burden estimate or any other aspect of this collection of information, including suggestions for reducing the burden, to Department of Defense, Washington Headquarters Services, Directorate for Information Operations and Reports (0704-0188), 1215 Jefferson Davis Highway, Suite 1204, Arlington, VA 22202-4302. Respondents should be aware that notwithstanding any other provision of law, no person shall be subject to any penalty for failing to comply with a collection of information if it does not display a currently valid OMB control number.
PLEASE DO NOT RETURN YOUR FORM TO THE ABOVE ADDRESS.

1. REPORT DATE *(DD-MM-YYYY)*	2. REPORT TYPE	3. DATES COVERED *(From - To)*

4. TITLE AND SUBTITLE

5a. CONTRACT NUMBER

5b. GRANT NUMBER

5c. PROGRAM ELEMENT NUMBER

6. AUTHOR(S)

5d. PROJECT NUMBER

5e. TASK NUMBER

5f. WORK UNIT NUMBER

7. PERFORMING ORGANIZATION NAME(S) AND ADDRESS(ES)

8. PERFORMING ORGANIZATION REPORT NUMBER

9. SPONSORING/MONITORING AGENCY NAME(S) AND ADDRESS(ES)

10. SPONSOR/MONITOR'S ACRONYM(S)

11. SPONSOR/MONITOR'S REPORT NUMBER(S)

12. DISTRIBUTION/AVAILABILITY STATEMENT

13. SUPPLEMENTARY NOTES

14. ABSTRACT

15. SUBJECT TERMS

16. SECURITY CLASSIFICATION OF:			17. LIMITATION OF ABSTRACT	18. NUMBER OF PAGES	19a. NAME OF RESPONSIBLE PERSON
a. REPORT	b. ABSTRACT	c. THIS PAGE			
					19b. TELEPHONE NUMBER *(Include area code)*

INSTRUCTIONS FOR COMPLETING SF 298

1. REPORT DATE. Full publication date, including day, month, if available. Must cite at least the year and be Year 2000 compliant, e.g. 30-06-1998; xx-06-1998; xx-xx-1998.

2. REPORT TYPE. State the type of report, such as final, technical, interim, memorandum, master's thesis, progress, quarterly, research, special, group study, etc.

3. DATES COVERED. Indicate the time during which the work was performed and the report was written, e.g., Jun 1997 - Jun 1998; 1-10 Jun 1996; May - Nov 1998; Nov 1998.

4. TITLE. Enter title and subtitle with volume number and part number, if applicable. On classified documents, enter the title classification in parentheses.

5a. CONTRACT NUMBER. Enter all contract numbers as they appear in the report, e.g. F33615-86-C-5169.

5b. GRANT NUMBER. Enter all grant numbers as they appear in the report, e.g. AFOSR-82-1234.

5c. PROGRAM ELEMENT NUMBER. Enter all program element numbers as they appear in the report, e.g. 61101A.

5d. PROJECT NUMBER. Enter all project numbers as they appear in the report, e.g. 1F665702D1257; ILIR.

5e. TASK NUMBER. Enter all task numbers as they appear in the report, e.g. 05; RF0330201; T4112.

5f. WORK UNIT NUMBER. Enter all work unit numbers as they appear in the report, e.g. 001; AFAPL30480105.

6. AUTHOR(S). Enter name(s) of person(s) responsible for writing the report, performing the research, or credited with the content of the report. The form of entry is the last name, first name, middle initial, and additional qualifiers separated by commas, e.g. Smith, Richard, J, Jr.

7. PERFORMING ORGANIZATION NAME(S) AND ADDRESS(ES). Self-explanatory.

8. PERFORMING ORGANIZATION REPORT NUMBER. Enter all unique alphanumeric report numbers assigned by the performing organization, e.g. BRL-1234; AFWL-TR-85-4017-Vol-21-PT-2.

9. SPONSORING/MONITORING AGENCY NAME(S) AND ADDRESS(ES). Enter the name and address of the organization(s) financially responsible for and monitoring the work.

10. SPONSOR/MONITOR'S ACRONYM(S). Enter, if available, e.g. BRL, ARDEC, NADC.

11. SPONSOR/MONITOR'S REPORT NUMBER(S). Enter report number as assigned by the sponsoring/ monitoring agency, if available, e.g. BRL-TR-829; -215.

12. DISTRIBUTION/AVAILABILITY STATEMENT. Use agency-mandated availability statements to indicate the public availability or distribution limitations of the report. If additional limitations/ restrictions or special markings are indicated, follow agency authorization procedures, e.g. RD/FRD, PROPIN, ITAR, etc. Include copyright information.

13. SUPPLEMENTARY NOTES. Enter information not included elsewhere such as: prepared in cooperation with; translation of; report supersedes; old edition number, etc.

14. ABSTRACT. A brief (approximately 200 words) factual summary of the most significant information.

15. SUBJECT TERMS. Key words or phrases identifying major concepts in the report.

16. SECURITY CLASSIFICATION. Enter security classification in accordance with security classification regulations, e.g. U, C, S, etc. If this form contains classified information, stamp classification level on the top and bottom of this page.

17. LIMITATION OF ABSTRACT. This block must be completed to assign a distribution limitation to the abstract. Enter UU (Unclassified Unlimited) or SAR (Same as Report). An entry in this block is necessary if the abstract is to be limited.